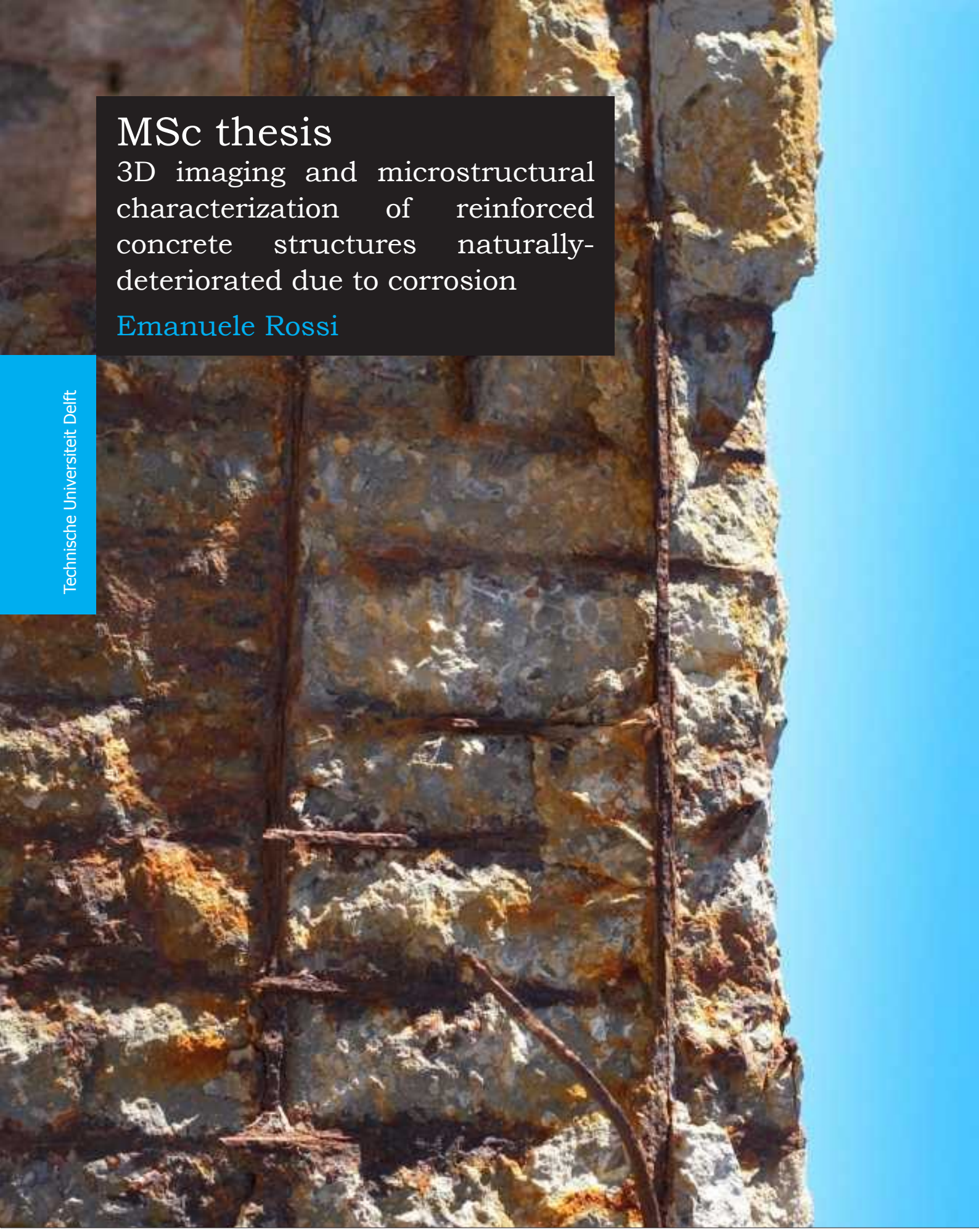

# MSc thesis

## 3D imaging and microstructural characterization of reinforced concrete structures naturally-deteriorated due to corrosion

Emanuele Rossi

Technische Universiteit Delft

TU Delft Delft University of Technology

Challenge the future

# MSc thesis

## 3D imaging and microstructural characterization of reinforced concrete structures naturally-deteriorated due to corrosion

by

**Emanuele Rossi**

in partial fulfillment of the requirements for the degree of

**Master of Science**
in Building Engineering

at the Delft University of Technology,
to be defended publicly on Wednesday, 3rd of October, 2018 at 2:00 PM.

| | | |
|---|---|---|
| Supervisor: | Dr. O. Copuroglu | TU Delft, CiTG, Materials & Environment |
| Thesis committee: | Prof. dr. R. B. Polder | TU Delft, CiTG, Materials & Environment |
| | Dr. B. Savija | TU Delft, CiTG, Materials & Environment |
| | Ir. S. Pasterkamp | TU Delft, CiTG, Building Engineering |
| | Dr. T. Nijland | TNO, Structural Reliability |

*Cover image from: https://gharpedia.com/factors-causing-steel-corrosion-concrete-structures/.*



TU Delft Delft University of Technology

# Acknowledgements

This Master of Science thesis is the result of a research conducted between January and September 2018, as a collaboration between the MicroLAB at the Materials & Environment Department at TU Delft and TNO. During the whole duration of this research I met and collaborated with experts, scientists and technicians that guided me through the essence of being a Master in the field of material science, with incredible effort and patience. Without their help and the support of my family and my friends, I would have probably failed along the way, so the least thing that I can do is to thank them all.

Above all, I want to immensely thank my parents. Apart from their never-ending love and support, they always pushed me to try to become the person that I wanted to be and doing the things that I wanted to do. They gave me the freedom to choose but at the same time the they were always present at my side, taking out the best version of myself. I thank you and always love you.

A sincere thank you goes to all the committee members of this thesis. Thank to Dr. Oguzhan Çopuroglu, my daily supervisor, who, since the beginning of this research, taught me not what to think, but how. He stimulated me since the very first days, challenging me once every while to take the best I could do out of this research, and I will always be grateful for that. I want to thank Dr. Branko Savija, for his support and effort he focused on me day by day and for helping me with experiments, analysis of results and many more things, since the beginning of the research and even if I was only a stranger. I want to thank Prof. Rob Polder, who was not only a professor, but more a mentor since the very beginning of my Master. His advices, suggestions, knowledge and expertise in and out the field of corrosion and material science are lessons that I will always bring with me during the future. I want to thank Dr. Timo Nijland, who gave me the possibility to conduct this research at TNO and supervised me with great patience and interest even when his agenda was completely busy, helping me to think out of the box. Finally, I want to thank ir. Sander Pasterkamp, for showing great interest into my research and helped me to keep in mind the potential practical implications that this and further research could have, which is the essence of being an engineer. Personally, I feel incredibly lucky that I have met you all during this research, and I thank you all again.

A special thank you goes to Maiko van Leuween, Arijan Thijssen, Ton Blon, Hongzhi Zhang and all the other people of the MicroLAB that helped me with specimen preparation, experimental set up and gave me wonderful advices on the way, always answering my tireless will of asking questions. I want to thank especially Juan and Claudia, for the interesting discussions we had, the advices we shared and the training they gave me to become a master Spanish speaker.

An immense thank you goes to my sister, Sara, and my brother, Fede. As you were at my side when I needed you both, I will always be at yours. To the members of my wonderfully enlarged family, Linda, Diana and Cecco, hoping that the way to go together will be still long and great. To my family all and to my grandparents, inspirations of unconditioned love. To my blood brothers at home, and especially to Ghigo, Mat, Bob, Pip & Chiara, Elio, Rodo, Bedo and all the others. To my flat mates and great friends Edo and Fede for the way we went together and for sharing every day of the last two years, like if we had a piece of home even if we were abroad. To the most amazing people that I met here in Delft, who became great friends that I will always keep as close as possible: among others to Andy, Lore, Michi, Paolino, Kevin, Badi, Ari, Angeles, Firmino, Saskia, Nico & Fra. Thank you to all the friends I graduated with during the Bachelor at the Politecnico di Milano, and to the groupmates of Shock Safe Nepal. Thank you Annamaria for inspiring me while sitting at the feet of the Himalayas. Last but not least, the most special thank you goes to my girlfriend, Eli, who made all the way up to here always more senseful and beautiful.

*Emanuele Rossi*
*Delft, October 2018*

*Alla mia mamma ed al mio babbo.*
*Grazie di cuore*

*and I will love to see that day*
*that day is mine*
*when she will marry me outside*
*with the willow trees*
*and play the songs we made*
*they made me so*
*and I would love to see that day*
*that day was mine*

*Postcards from Italy, Beirut*

# Abstract

In this study, a three-scale characterization of eight 20-years-old reinforced concrete specimens naturally deteriorated due to chloride-induced corrosion was carried out. The main aim of this research was to investigate some relevant parameters to accurately model corrosion of reinforced concrete structures, such as which are the locations where corrosion pits are more likely to initiate as well as if the Elastic modulus of corrosion product depends on the concrete mix that the reinforcement was embedded in. Each scale of characterization had a specific goal: the macro-scale characterization aimed to analyze the state of the specimens after 20 years of outside (unsheltered) exposure through Non-destructive techniques (i.e. potential measurements, corrosion rate, resistivity of concrete), visual inspections and analysis of historical records. Also, since specimens were mis-labelled during the years, the cement type that each specimen was cast with was identified through polished sections of concrete portions analyzed under the Scanning Electron Microscope (SEM). The meso-scale characterization of the reinforcement aimed to quantify the volume loss of the steel as well as to investigate which were the locations where corrosion pits occurred the most. Out of each reinforced concrete specimen, a core of 20 mm diameter and 100 mm height has been drilled, embedding a steel bar of 8 mm diameter. Each core has been then analyzed through X-ray Computed Tomography (CT-scan) and image analysis was performed. Apart from revealing different volume loss for bars embedded in different mixes (i.e. CEM I was the most corroded, CEM III/B the least), this characterization suggested that the most influencing factor for corrosion pits to form is the presence of defects (i.e. air voids) at the steel/concrete interface. Finally, the micro-scale characterization of corrosion product aimed to investigate the relation between Elastic modulus of corrosion product ($E_{cp}$), its micro-structure and its chemical composition, with regard to the different concrete mix that steel was embedded into. $E_{cp}$ was measured through Nano-indentation, while chemical composition was measured through SEM/EDS (Energy Dispersive Spectrometry) elemental mapping and spot analysis. This phase of the research revealed that differences between Elastic modulus of corrosion product generated in different mixes are not significant, and that the relation between $E_{cp}$ and Fe/O seems to be (linearly) proportional. In the last chapter, the findings of the research are summarized and some recommendations are made regarding future endeavors.

# Contents

# 1

# Introduction

## 1.1. General

The service life of civil engineering structures is one of the main parameter to consider during the design phase. In practice infrastructures are designed considering, among others, the needed structural capacity, the physiognomy of the structure (i.e. dimensions, geometry, etc.) and the environmental conditions that the structure will be exposed to. However, when deterioration occurs, structural- and service-life properties of the structures can be compromised.

When dealing with reinforced concrete structures, one of the main degradation mechanism they are subjected to is corrosion of the steel reinforcement. Even though engineers and scientists studied this topic for decades, there are still open questions about the fundamentals of how corrosion initiation and especially propagation affect the degradation resistance and structural performance of infrastructures. During the last 50 years, huge attention has been focused on repair and maintenance of corroding structures through different techniques. For instance, corrosion of reinforcement is highly depending on the quality of the concrete matrix and the thickness of the concrete cover, hence the combination of accurate concrete mix design and proper safety factors helped to post-pone corrosion in practice. Furthermore, cathodic protection, stainless steel bars and concrete surface treatments demonstrated to be effective corrosion prevention techniques commonly used in practice. Even though these techniques contributed to tackle degradation in practice, none of them gives a better understanding about corrosion progress. Furthermore, they require interventions directly on site, which are generally expensive, time-consuming and they would rely on the expertise of the workers. Among others, these reasons stimulated scientists to develop a more accurate and effective method to predict and tackle corrosion of steel in concrete, that they found in modelling. Ideally, models would help to analyze the volume loss of reinforcement due to corrosion during time, to quantify the pressure induced by formation of corrosion product on the surrounding matrix, to simulate the degradation mechanism during time and hence to elaborate accurate and effective repair and maintenance plans. However, due to the complexity of the mechanisms and the huge amount of interrelated parameters, to rely on accurate models there is still a long way to go.

It must be specified that the evaluation of corrosion on reinforced concrete structures generally relies on laboratory experiments and results, where specimens are exposed to controlled environmental conditions and loads. However, real structures are subject to conditions that change daily. Very little research focused on characterizing the corrosion state of naturally deteriorated structures, which is an added value of this research. Results obtained after several years of natural exposure may provide vital information that may help to better understand how degradation propagates during time as well as the effects of this propagation.

## 1.2. Summary of this study

The main objective of this study was to characterize the corrosion state of reinforced concrete specimens naturally deteriorated due to corrosion: more specifically, main points of investigation were the analysis of relation between corrosion pits and concrete defects at the steel/concrete interface as well as analyzing the micro-mechanical properties of corrosion product (i.e. Modulus of Elasticity) in relation to its chemical composition, its micro-structure and the concrete environment where corrosion products have been formed. Eight 20-years-old specimens were used as object of this study. Specimens were part of a group of specimens cast in 1998 and analyzed for the first 2,5 years and after 12 years [78]-[8]. In this research, these specimens were subjected to a three-scale characterization procedure. The macro-scale characterization of reinforced concrete prisms consisted of corrosion-related electro-chemical measurements (i.e. potential, corrosion rate and resistivity) of specimens, carbonation depth measurements and analysis of historical records. The meso-scale characterization of steel reinforcement consisted of using X-ray Computed Tomography on reinforced concrete cores, and analyzing the internal state of the reinforcement. The micro-scale characterization of corrosion product consisted on evaluating the Elastic modulus of corrosion product, its chemical composition and its micro-structure, and the relation between these three. Finally, information about the characteristics of the steel/concrete interface and the penetration of corrosion product into surrounding matrix and defects were collected.

## 1.3. Outline of this report

This report is divided in seven chapters beside the present introduction (Chapter 1): the contents treated in each chapter are briefly described below.

In Chapter 2, background information about reinforced concrete structures durability, service life and degradation mechanisms are reported, with deeper attention on their deterioration due to corrosion induced by chlorides ingress. Besides the scientific background about this mechanism, also a description of the monitoring techniques used in the introduction of the present research is given. In this literature review, significant attention has been given to analysis of previous results about the relation between corrosion pits and concrete defects at the steel/concrete interface, as well as the micro-mechanical properties and micro-structure of corrosion product, as investigated by others.

In Chapter 3 a summary of the previous work conducted on the specimens is given, as reported by TNO from 1998 until 2010. This summary includes information about the materials used to cast the specimens, the environmental conditions they were exposed to and the analysis that they were subjected to during the first 12 years after casting. At the end of the chapter, the state at which specimens were found at the beginning of this research is described, followed by the selection of the eight specimens that were analyzed in this research. A brief description of the experimental plan that these specimens were subjected to is also given.

Chapter 4 described the identification of the cement type that the specimens were cast with. Since it will be shown that specimens were mislabeled between 2002 and 2010, microscopy analysis was necessary to identify what was the mix design of each prism object of this research. The identification procedure included analysis of polished concrete portions under BSE mode, of which images are also reported in Appendix A.

In Chapter 5 non-destructive electro-chemical measurements related to the corrosion state of the specimens are reported. These measurements were also analyzed with respect to historical measurements taken in 2010, in order to gather information about the on-going corrosion state of the specimens. Carbonation depth was also measured destructively. Raw data and images about this characterization and historical analysis are also reported in Appendix B.

Chapter 6 describes the characterization of the corrosion state of the steel reinforcement after 20 years of exposure. This analysis relied on images representative of the internal state of each specimen

acquired through X-ray Computer Tomography and then processed with the freeware Fiji. In this way, the volume loss due to corrosion as well as the distribution of corrosion pits along the length of each bar was determined. These two parameters were then analyzed with regard to information given by previous non-destructive measurements (i.e. corrosion rate and potential of the steel). Beside this analysis, high attention was focused on analyzing the relation between corrosion pits, defects at the steel/concrete interface and orientation of the reinforcement. To do so, corrosion pit depths were measured in the horizontal 2D cross section plane. Analysis on the relation between pit depths, the side of the reinforcement at which they were found (outside- and inside-exposure surfaces) and the proximity of concrete defects were then conducted. CT-scans that were object of this analysis are visible consulting Appendix C.

In Chapter 7 the micro-scale characterization of corrosion product is reported. This part of the research included: the determination of the Elastic modulus of corrosion product through Nano-indentation; analysis of the chemical composition of corrosion product through SEM/EDS elemental mapping and spot analysis; the investigation about the micro-structure of corrosion product through SEM/EDS elemental mapping (for all the specimens), standard-based EDS spot analysis (for one specimen only) and XRD on corrosion product powder. Analysis about how chemical composition and micro-structure of corrosion product (might) affect its Modulus of Elasticity were also conducted. Observations about corrosion product penetrating into the surrounding matrix and defects at the steel/concrete interface through analyzing BSE images are also reported. BSE images and graphs representative for the relation between all these parameters are also reported in Appendix D.

Finally, Chapter 8 presents the conclusions that could be deduced from what was found in this research, as well as recommendations for future work. The list of references that were used to analyze and compare the results collected in the present research is reported at the end of the report.

# 2

# Deterioration of reinforced concrete structures due to corrosion

## 2.1. Introduction on corrosion of reinforced concrete structures

Since the beginning of the 20th century, durability of materials started to be one of the main aspect to consider in the construction field. Design codes were introduced to improve the durability of infrastructures and extend their life-span [1] [2]. Because reinforced concrete is the most used construction material all over the world, the causes of its deterioration became main points of interest for scientists and engineers. Uncontrolled degradation of reinforced concrete structure would lead to unforeseen maintenance and repair costs and to safety-related issues.

The durability of reinforced concrete structures is defined as "their ability to maintain serviceability in a given environment over a specified time" [3]. The service-life of a structure is a parameter that is established during the design phase by means of deterministic or stochastic measures. Reinforced concrete structures are commonly designed with service life spans between 50 and 100 years. Measures have been used world-wide to prevent deterioration, such as adequate cover depth, water/binder ratio, curing, coating, etc. [4]. Nevertheless, degradation might still occur under certain conditions. Concrete and steel may be subjected to diverse degradation mechanisms, highly depending on the environmental conditions where the structure stands. An overview of the most common degradation processes and their main causes for reinforced concrete structure is given here (Figure 2.1) [4].

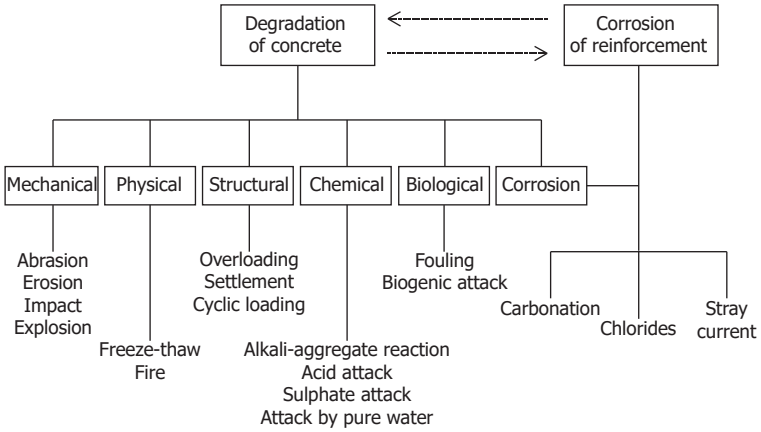


Figure 2.1: Degradation of concrete and their possible causes [4]

Steel reinforcement is embedded into the concrete to improve its tensile strength. Corrosion of reinforcement has been defined as the main degradation issue in the construction industry all over

the world [5]. It involves the dissolution (oxidation) of iron of the steel reinforcement, compromising the structural capacity of the structure and inducing tensile stresses to the surrounding concrete. The concrete around the reinforcement has a double function: firstly, it acts as physical barrier for aggressive components that might get in the concrete from the environment; secondly, the high pH of the concrete pore solution provides thermo-dynamically stable environment for the steel reinforcement, avoiding or reducing aggressive corrosion. For these reasons, the combination of steel and concrete makes a reliable solution as construction material.

### 2.1.1. Electrochemistry of corrosion

The corrosion reaction is driven by an electrical flow of current, like a voltaic cell. A voltaic cell is made of two half-cells, connected by a medium. The two half-cells are subjected to two different electrochemical reactions: on the one half-cell, dissolution of the metal occurs. This cell is called oxidation (or anodic) cell. On the other half-cell, reduction of oxygen occurs. This latter cell is called reduction (or cathodic) cell. The current flowing between the two half-cells is carried by ions contained in the pore solution, which works as an electrolyte. Ions are transported through pores and provide electrical conductivity of the medium.

The electrochemical corrosion process is made by two contemporary stages. The steel bar is subjected to the oxidation half-reaction (anode) cell according to:

$$Fe \longrightarrow Fe^{2+} + 2\,e^{-}$$

The reduction half-reaction (cathode) occurs on the un-corroded steel surface:

$$\frac{1}{2}\,O_2 + 2\,H_2O + 2\,e^{-} \longrightarrow 2\,OH^{-}$$

The oxidation and reduction reactions are kept in contact due to the presence of the steel bar, which works as electron conductor, and of the water-filled pores, allowing conduction of ions. In this way, an electrical circuit is formed. Between the anodic and cathodic regions of the steel reinforcement, an electrochemical potential difference occurs. This difference is a relevant parameter for knowing the intensity of the corrosion process affecting a certain structure [6].

### 2.1.2. Passivity of reinforcement

During the hydration of cement, the soluble alkali oxides ($N_2O$, $K_2O$) produce an alkaline solution which provides an environment with kinetically stable conditions for the embedded steel reinforcement. When hardened, the pH of the pore solution in a hydrated cement matrix remains around 13. Depending on the type of cement used, this value might change for different mix design; however, their alkalinity is overall ensured. In an alkaline environment, a thin and dense layer of oxides (”passive layer”) is formed spontaneously on the surface of the steel reinforcement [7]. This layer works as protective layer for the anodic reaction that could affect the steel reinforcement. Nevertheless, when aggressive ions are locally contained above a certain threshold level or when the pH of the environment is too low, the passive layer may be broken. If de-passivated, no protective layer can protect the steel reinforcement from degradation processes anymore, and dissolution of iron might initiate.

### 2.1.3. Corrosion initiation

When aggressive components (such as chlorides) penetrate the concrete matrix, reaching the embedded steel reinforcement and breaking the passive layer, corrosion initiates. This would only occur in presence of oxygen also. The time that is taken by agents to reach the reinforcement and then to start the dissolution of iron is called corrosion initiation period [8]. The intensity of this process depends, among other causes, on how quickly and easily the aggressive components are accumulated close to the reinforcement. Beyond a certain concentration, the conditions of stability for the passive layer are not present anymore, and corrosion is initiated.

Agents that cause iron dissolution might be different in nature. These differences play a role in determining the characteristics and intensity of the eventual corrosion mechanisms that would affect the reinforcement. The development of corrosion affecting a structure and how the service life is affected is schematically given below (Figure 2.2) [9].

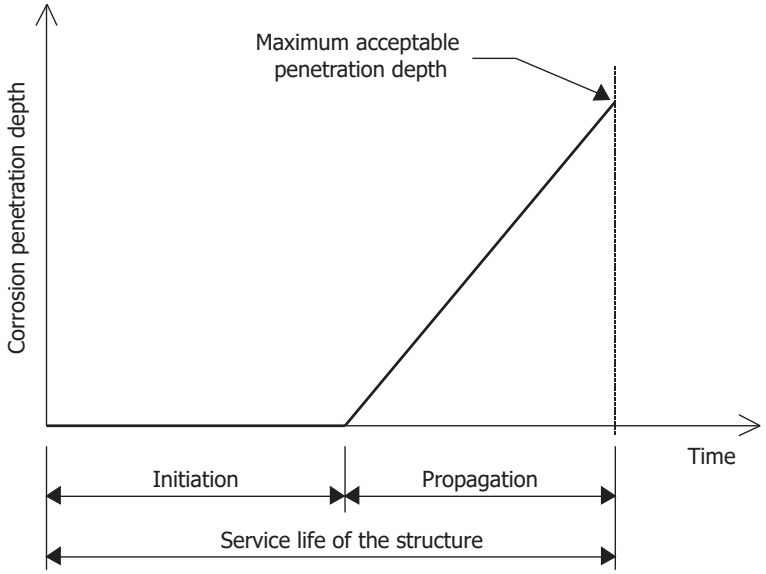


Figure 2.2: Time span of service life in concrete structures subjected to corrosion of reinforcement [9]

The nature of the corrosion may be different per each situation. The most common corrosion processes found in practice are caused by chloride and carbon dioxide ingress. The former is responsible for localized pitting corrosion, while the latter for uniform corrosion due to carbonation. Furthermore, bacteria, stray currents and stresses may cause corrosion to develop [6].

### 2.1.4. Chloride ingress and pitting corrosion

Chloride-induced corrosion is considered the most dangerous for the structural performance of the einforcement. Depending on the chloride concentration, chloride ions influence the steel potential: higher the chloride content, higher the anodic current density in the cell. An overview of the changes in potential that the steel is subjected to when in contact with chlorides is given below (Figure 2.3) [6].

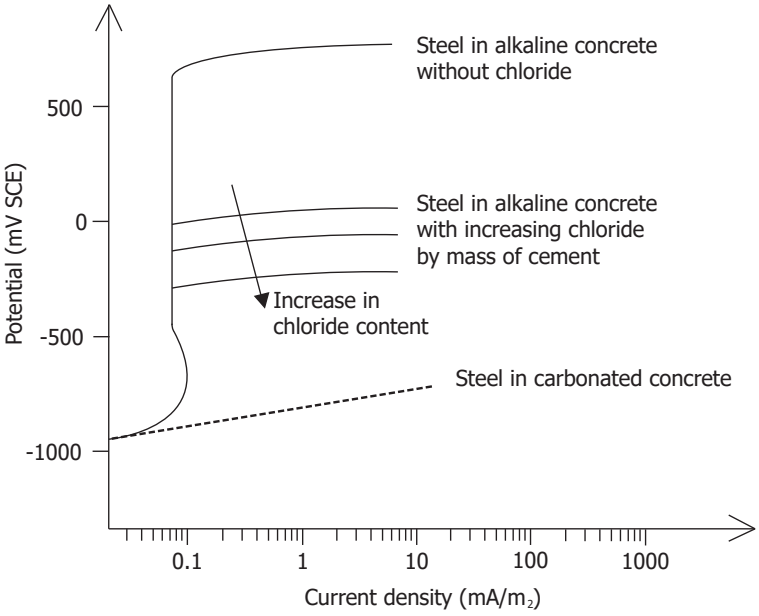


Figure 2.3: Influence of chlorides concentration in steel potential of embedded reinforcement [6]

A chloride concentration higher than the chloride threshold limit produces localized breakdown of the passive layer of the reinforcement. When de-passivated, steel starts to dissolve, forming pitting corrosion at localized spots along the reinforcement. Those pits are the spots where oxidation of iron would occur (anodic zone). On the other hand, reduction of oxygen would occur at the adjacent non-corroding steel surface (cathodic zone). In this process, the transfer of electrons between the anode and the cathode is driven by the electrolytic solution surrounding the reinforcement (Figure 2.4).

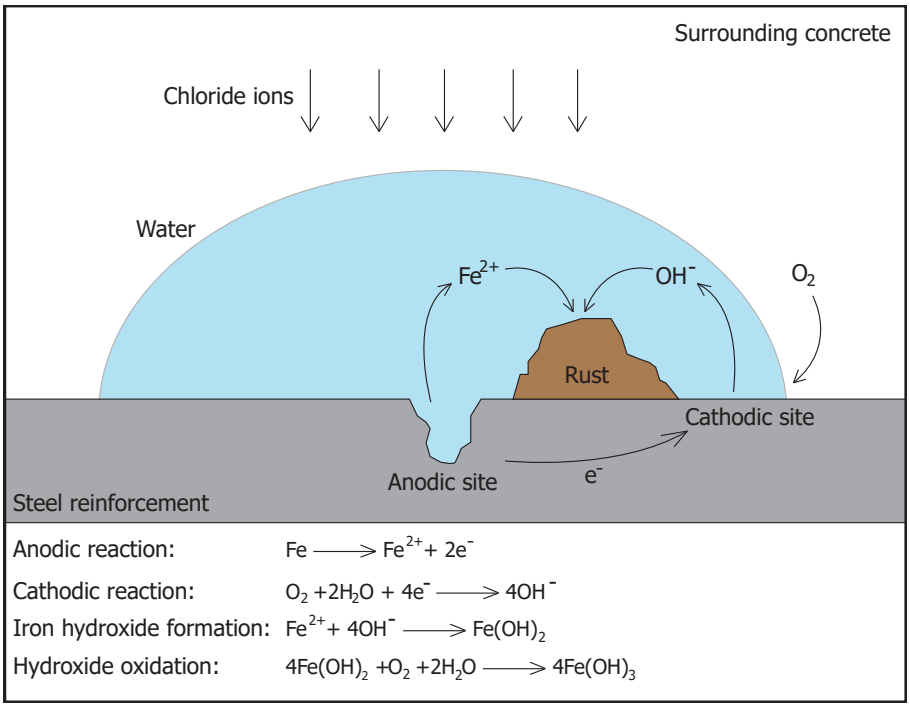


Figure 2.4: Pitting corrosion due to chlorides ingress

Inside the corrosion pit, iron reacts with chloride ions in presence of water as follows:

$$Fe^{2+} + 2\,Cl^{-} + 2\,H_2O \longrightarrow Fe(OH)_2 + 2\,HCl$$

The hydrochloric acid that is produced is responsible of the low pH inside the pit, constituting an aggressive environment for the surrounding steel reinforcement. The low pH inside a corrosion pit works as propulsor for the growth of the pit itself, getting deeper over time. The rate of iron dissolution is strongly dependent on the amount of oxygen and chlorides in the corrosion pits. A continuous availability of them leads to corrosion propagation over time, resulting in a localized reduction of the cross section of the steel reinforcement bars and so of its structural capacity. The rate of chloride ingress depends on the pore micro-structure of concrete. Denser mixes, such as adding fly ash and blast furnace slag, can generally hold higher concentrations of chlorides before any corrosion starts [8].

### 2.1.5. Carbonation

With the term "carbonation" it is meant the degradation of reinforced concrete caused by the ingress of carbon dioxide present in the atmosphere. When penetrating the concrete, $CO_2$ causes a reduction of the pH of the concrete down to around 9. In this situation, the thermodynamic conditions that produced the passive layer of steel bars are no longer present at the interface between concrete and reinforcement, causing the destruction of the passive layer and therefore the initiation of corrosion. The carbonation reaction occurs in all the volume of concrete that is in contact with carbon dioxide, and the penetration depth of $CO_2$ increases over time [8]. The loss of the passivity layer and further dissolution of steel begin when the concrete surrounding the reinforcement is carbonated, degrading the rebar for its whole length. The loss of alkalinity in concrete due to carbonation occurs according to the following reaction:

$$CO_2 + Ca(OH)_2 \longrightarrow CaCO_3 + H_2O$$

The rate of carbonation depends on many concrete properties, like cement type, water-binder ratio and curing. Environmental conditions like $CO_2$ concentration and relative humidity play a relevant role as well. For instance, when RH is between 60-70%, carbon dioxide can diffuse more easily through the pores than in saturated conditions. This latter case prevents carbonation thanks to the difficulties that $CO_2$ encounters when penetrating the concrete. On the other hand, very dry conditions also prevent degradation caused by carbonation thanks to the unavailability of water to make the carbonation reaction occur. For this reasons, a "moderate" RH of the concrete is the most sensitive environment for carbonation of concrete to occur.

## 2.2. Effects of corrosion and monitoring techniques

Beside the reduction of the cross section of the reinforcement, compromising its structural capacity, corrosion has further side-effects with regard to surrounding concrete. The corrosion reaction produces ferric hydroxides, also known as corrosion product or rust, which occupies a volume larger than the initial volume of steel [10]. This expansion in volume induces internal stresses within the concrete matrix. Since the tensile strength of the concrete is relatively low, cracking, delamination and finally spalling of the surrounding concrete might be caused eventually. Due to cracking, higher penetration of aggressive ions from the outside is enabled, accelerating the corrosion rate of the reinforcement and making the reduction of structural capacity faster. These and other side-effects that corrosion leads to for reinforced concrete structures are schematically shown below (Figure 2.5) [4].

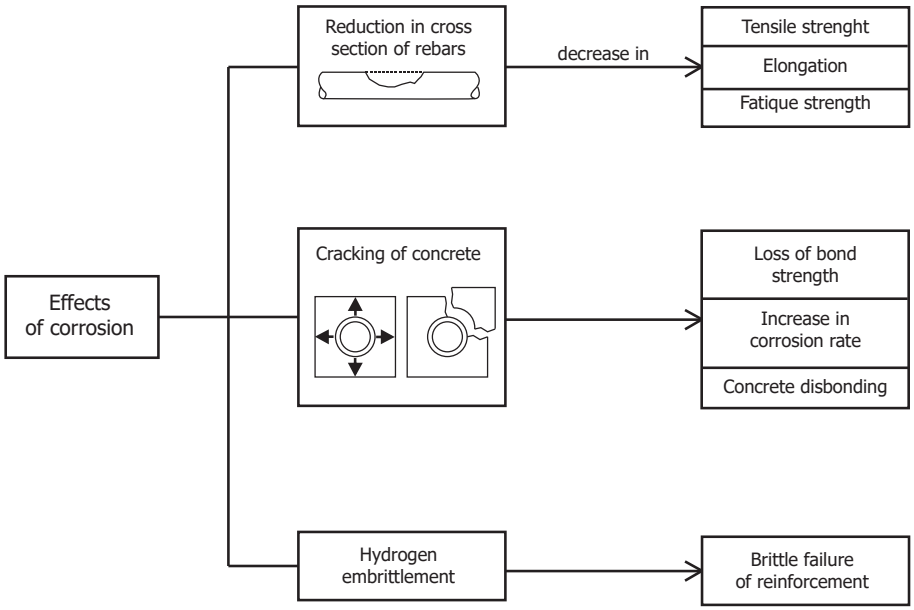


Figure 2.5: Effects of steel corrosion for concrete [4]

The effects that corrosion of reinforcement has on both the structural capacity of a structure and to the cracking of the concrete cover have been deeply studied by many engineers and scientists, as described later in this report (Section 2.3). To evaluate the state of corrosion for steel reinforcement, many techniques are available. These can be divided in Non-Destructive (NDT) and Destructive Techniques (DT). The former aim to evaluate and monitor corrosion development as less intrusively as possible, keeping the state of the structure intact. Among others, these techniques are: potential mapping of the steel reinforcement, linear polarization resistance of bars (LPR), concrete resistivity measurements and electric pulse velocity. In this project, potential of steel reinforcement and concrete resistivity were measured before conducting destructive testing on the specimens to evaluate their corrosion state 20 years after casting. A description of how these parameters are usually recorded in practice and their importance to evaluate deterioration due to corrosion is given below.

### 2.2.1. Steel potential (E)

The potential of steel in concrete is indicative of the passivity state of steel. Potential can be measured with the use of either embedded reference electrodes or external reference electrodes (RE). In both cases, a high impedance voltmeter (>10 MOhm) is required to record stable measurements. The voltmeter must be connected to both the steel reinforcement and the RE. Adequate electrolytic connection between the RE and the reinforcement must be guaranteed. When using an external RE, a wet cloth is placed between the RE and the measurement point. A schematic representation of this measurement procedure is given below (Figure 2.6).

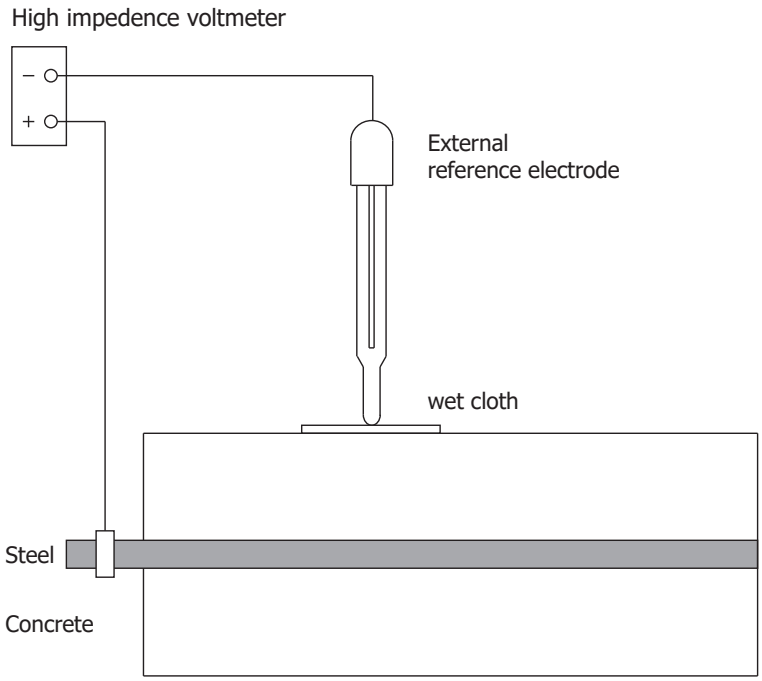


Figure 2.6: Potential measurement of steel vs external reference electrode

The relative potential of the steel reinforcement depends on the reference electrode that has been used. Each electrode has a potential difference with regard to the Standard Hydrogen Electrode (SHE). The common values of potential difference (ΔE) between reference electrodes and the SHE are given below (Table 2.1).

Table 2.1: Standard potentials of reference electrodes vs SHE

| **Electrode** | **Potential vs SHE (mV)** |
|---|---|
| Saturated calomel electrode (SCE) | +244 |
| Silver/Silver Chloride (SSE) Ag/AgCl | +199 |
| Copper/Copper Sulphate (CSE) $Cu/CuSO_4$ | +316 |
| Manganese dioxide | +365 |
| Graphite | +150±20 |
| Activated Titanium (Ti*) | +150±20 |
| Stainless steel | +150±20 |

Analyzing the potential of the steel, the probability of current corrosive state of the bar can be supposed. A schematic scale for determining the state of embedded steel reinforcement in concrete with reference to a Saturated calomel electrode (SCE) is given below (Figure 2.7).

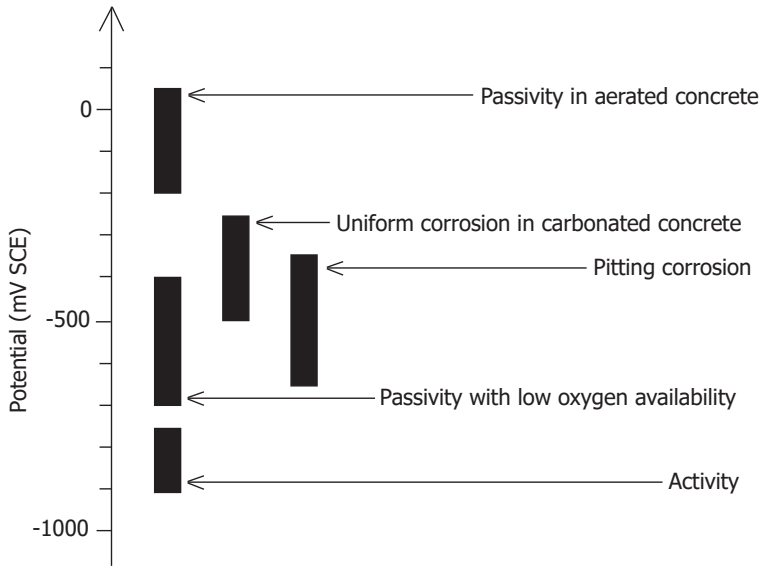


Figure 2.7: Interpretation of potential measurements vs SCE of steel embedded into concrete

Figure 2.7 shows the relation between potential measurements of steel reinforcement (E) and the different conditions of corrosion of the steel itself. A potential between 0 and around -200 is associated to a passive state of steel, while pitting corrosion is mostly found when corrosion potential is between -400 and -700mV. It must be said that it is not possible to assure which deterioration mechanism is affecting the steel only by measuring corrosion potential, nor describing the corrosion that affected the bar earlier in time, if any. Additional tests like concrete resistivity and LPR give additional insights to identify the most probable degradation mechanism affecting reinforced concrete structures as well as its aggressivity [8].

### 2.2.2. Linear Polarization Resistance (LPR) and corrosion rate

Linear polarization resistance is a technique which estimates the corrosion rate (CR), representative for the degree of degradation of the metal due to corrosion in terms of loss of material ($\mu m/year$). The theoretical principle of this measurements consist on applying small potential differences (ΔE) around the corrosion potential ($E_{corr}$) of the steel and to measure the current ($i_{corr}$) changes related to these ΔE. A current-potential plot is generated which represents a quasi-linear relationship between $i_{corr}$ and $E_{corr}$. To guarantee this quasi-linearity, the applied ΔE must not exceed 50 mV [13]. The slope of this curve within a ΔE = ±10 mV is called Linear Polarization Resistance (LPR). Within these limits, the relation between $i_{corr}$ and $E_{corr}$ is as assumed to be linear (Figure 2.8).

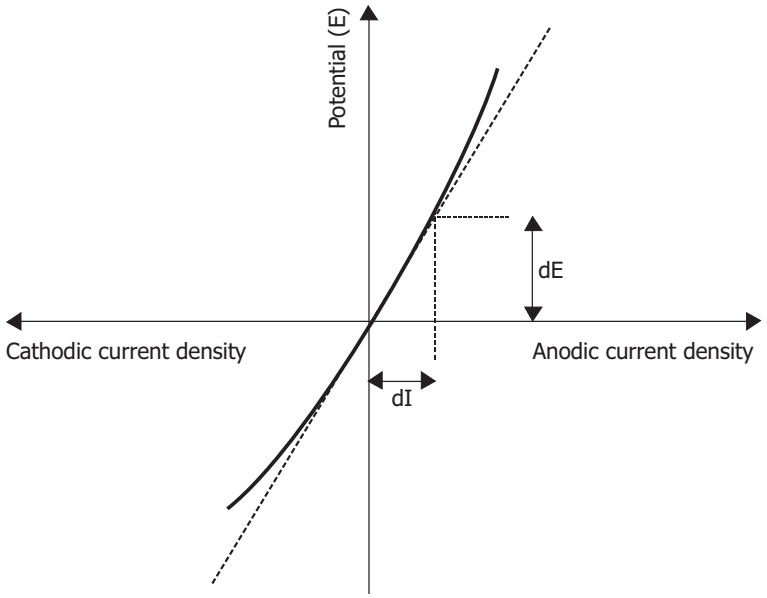


Figure 2.8: Linear Polarization resistance [13]

The application of this technique is derived from the anodic and cathodic curves proposed by Stern and Geary [14], whose equation is defined as:

$$i_{corr} = \frac{\beta_a * \beta_c}{2.3 * (\beta_a * \beta_c)} * \frac{1}{R_p}$$

where $i_{corr}$ is the corrosion current, $\beta_a$ is the anodic slope of the $R_p$ curve and $\beta_c$ is the cathodic slope. Because $\beta_a$ and $\beta_c$ are constants, the Stern-Geary equation can be re-defined as follows:

$$i_{corr} = \frac{B}{R_p}$$

The term B is related to both the slopes $\beta_a$ and $\beta_c$, which are usually found in the range between 12 mV and 52 mV depending on the system. For steel embedded in concrete, B=52 mV when considering passivated steel, while B=26 mV is when considering active steel [10]. Generally, a corrosion rate higher than 1 $\mu m/cm^2$ is considered to indicated active corrosion affecting the reinforcement [10] [15]. An interpretation of different corrosion currents is given below (Table 2.2) [8]:

Table 2.2: Interpretation of corrosion current values

| **Corrosion current** | **Interpretation** |
|---|---|
| 0 to 200 $mA/cm^2$ | Low |
| 200 to 500 $mA/cm^2$ | Low to moderate |
| 500 to 1000 $mA/cm^2$ | Moderate to high |
| > 1000 $mA/cm^2$ | High |

The corrosion rate, CR, or corrosion velocity, $V_{corr}$, represents the volume loss of material by unit of area during time. Through Faraday's Law, the corrosion rate (mm/year) can be obtained from the corrosion current and the density of the metal affected by corrosion. For steel embedded into concrete, corrosion rate can be estimated according to:

$$V_{corr}(\mu m/year) = 11.6 * i_{corr}(\mu A/cm^2)$$

Knowing the volume loss of steel reinforcement due to corrosion, the actual structural response of structures can be addressed during time.

### 2.2.3. Concrete resistivity

The electrical resistivity of concrete is a useful property to monitor and inspect corrosion affecting reinforced concrete structures [12]. It describes the electrical resistance of the material, defined as the ratio between an applied voltage and the resulting current in a unit cell (Figure 2.9). The unit cell is made of two electrodes located at a certain distance from each other, depending on the measurement technique (i.e. two-points method or Wenner probe). The electrical current resulting from the voltage application is carried by ions in the pore solution of the concrete. Higher amount of pore water as well as larger and more pores of the mix result in lower resistance to the ionic flow [12].

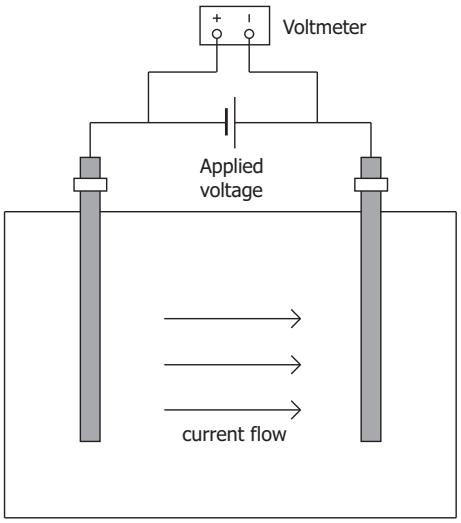


Figure 2.9: Concrete resistivity measurements (two-points method)

Resistivity is an important parameter to analyze the environment in which steel reinforcement is embedded into. Higher availability of oxygen and water leads to more intense electrochemical reaction at the cathodic site of the corrosion process. Resistivity is calculated by using the following formula [16]:

$$\rho = A * R_2$$

where $\rho$ is the concrete resistivity [Ωm], A is the cell constant which depends on the geometry of the specimen and the arrangement of steel reinforcement [m] and $R_2$ is the electrical resistance measured as the ratio between an applied voltage in AC and the resulting current [Ω].

In this research, macro-scale characterization of 20-years-old reinforced concrete specimens is reported. This characterization was performed by means of both non-destructive and destructive analysis: electro-chemical measurements were recorded to evaluate the steel potential and concrete resistivity 20 years after casting, contemporary to visual inspections and analysis of historical measurements. Carbonation depth was also measured, and its influence on the corrosion state of steel reinforcement was analyzed. Characterization of both steel reinforcement (meso-scale) and corrosion product (micro-scale) are also part of this research. Information about the state of the art related on these two topics is given below.

## 2.3. Characterization of steel reinforcement and steel/concrete interface

Pitting corrosion is known as a localized breakdown of the passivation layer of steel reinforcement caused by the chloride critical content (or chloride threshold value). This value corresponds to the chloride content at the location of the steel reinforcement that causes the transition from initiation to propagation phase [17]. Diffusion of chlorides within the concrete pore structure highly varies for different concrete mixes in terms of both time needed for chlorides to reach the reinforcement and chlorides content at the steel/concrete interface (SCI). It is common practice to keep the w/c of concrete as low as possible to reduce the porosity of the matrix, thus preventing an excessive amount (lower than the threshold level) of chlorides to reach the reinforcement. Also the use of blended cements are beneficial for long-term corrosion resistance of reinforced concrete, especially those containing fly ash and slag [17]. Chloride critical content is known as the main parameter that governs de-passivation of the reinforcement. Generally in practice, a chloride content of 0,4% by mass of cement is indicated as threshold value. However, it was observed by many researchers that critical chloride content highly depends on interrelated parameters, such as the quality of steel/concrete interface, the chemistry and structure of the concrete pore solution, the steel potential and the exposure conditions of reinforced concrete structures [17].

Strong and dense contact between steel and concrete provides physico-chemical protection of corrosion thanks to the buffering effect as well as the physical concrete matrix barrier that blocks dissolution of iron [18]. Good adhesion at the steel/concrete interface (SCI) limits both chlorides and oxygen to reach the steel reinforcement, therefore limiting the risk of corrosion. For this reason and for their denser micro-structure, improving resistance to chloride diffusion within the concrete matrix, blended cements are usually preferred to Ordinary Portland Cement in terms of corrosion resistance. However, also for good-quality blended-cement mixes the risk of corrosion might occur if concrete defects are present at the steel/concrete interface [19].

No matter what cement type the concrete is cast with, defects at the SCI are often reported to be required for initiation and further propagation of corrosion [18] [20] [21] [22] [23]. Soylev [18] characterized defects at the steel/concrete interface in three main groups: intrinsic, visible and invisible defects. Intrinsic defects are representative of the porosity of the concrete cover surrounding the steel reinforcement. Visible defects (or macro-defects) include air voids that are detectable even by naked eyes, caused by bleeding and settlement of fresh concrete. Invisible defects are representative of micro-defects at the SCI caused, for instance, by the rupture of adhesion between steel bars and concrete due to slipping of reinforcement under loading, and they can be detected through microscopy analysis. Only invisible defects are reported not to have an influence on corrosion progress in reinforced concrete structures. Intrinsic defects are significant especially for high w/c concrete, resulting in more porous concrete surrounding the reinforcement. These porous portions allow for oxygen and chlorides to reach the reinforcement more easily and thus resulting in sites more sensitive to corrosion pit formation and growth. Visible defects have, however, the highest influence on corrosion initiation and propagation. They are generally related to inadequate compaction of concrete, as result of segregation, settlement and bleeding of fresh concrete, and corrosion is reported to vary directly with their quantity in the concrete mix [18].

Concrete defects at the SCI influence corrosion initiation because, in partially or completely saturated conditions, high content of electrolyte would be present at the location of defects, thus facilitating corrosion progress. If the presence of voids at the SCI decreased, the corrosion would be significantly inhibited [19]. This statement is confirmed by Glass et al [24], who observed that the chloride threshold value for corrosion propagation of steel reinforcement increases if the percentage of air voids at the steel/concrete interface decreases (Figure 2.10).

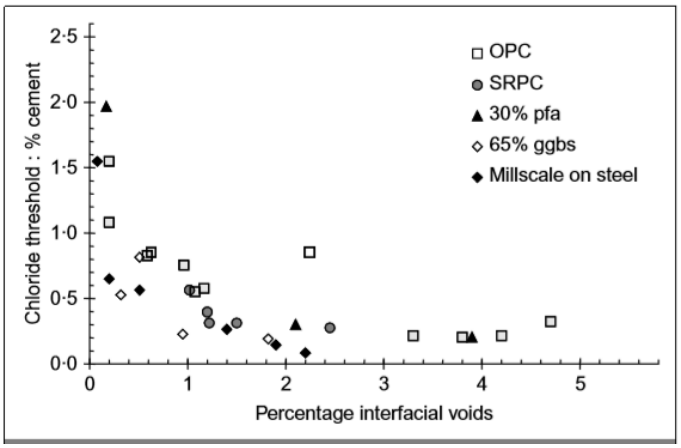


Figure 2.10: Published relationship interfacial voids and chloride threshold level (OPC, ordinary portland cement; SRPC, sulphate-resisting Portland cement) [24]

To be sensitive locations for corrosion propagation, concrete defects and especially air voids must be partially or completely saturated, thus containing an electrolyte that would allow corrosion to proceed. In dry conditions, significant corrosion does not occur [19], thus corrosion process is also to some extent dependent on the environmental conditions which the structure is exposed to, and especially to the moisture content of the concrete [25]. These observations are confirmed by Angst [17], who observed by visual examinations of the SCI that the location of corrosion onset did never coincide with the location of macro-pores because these latter ones never became saturated. He also observed that corrosion almost exclusively started on the back side of the reinforcement, thus the one with lower chloride concentration (because less close to the outside environment), and that concrete portions on the upper and lower sides of the rebar exhibited different characteristics. Because bleeding water and plastic settlement of concrete made the SCI weaker at the lower side of the rebar due to water raising from vibration of the mix, more likely corrosion initiation sites were found at the bottom side of the steel (Figure 2.11) [17] [26] [27]. In his research, reinforced concrete specimens were cast embedding steel rebars perpendicularly to the concrete casting direction. Similar results about the influence of casting direction and corrosion initiation sites were observed by other scientists [18] [22] [28]. Also high w/c ratio and porosity sites might weaker the SCI and thus be sensitive sites to corrosion pit formation and growth [29] [30].

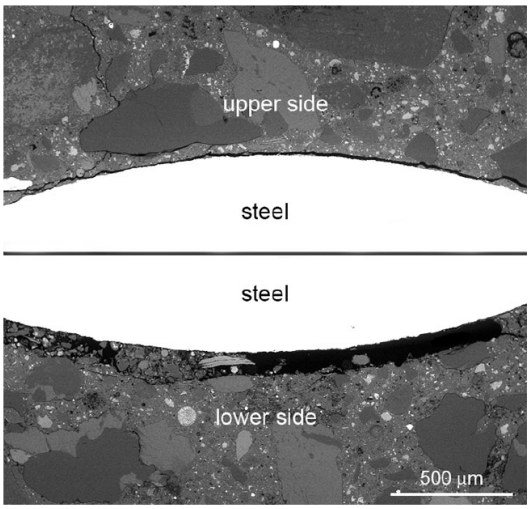


Figure 2.11: Bleed water zone at the underside of a rebar; backscattered electron micrograph of polished sections showing upper and lower SCIs in a specimen (Portland cement with 20% fly ash replacement, w/b = 0.5, hardened under sealed conditions for 1,5 years) from [26]

To summarize, corrosion progress is known to be highly dependent on many interrelated parameters. Among others, the most significant factors that influence the sensitivity of SCI sites for corrosion initiation are environmental conditions (i.e. chloride load and concrete moisture), the presence of defects (i.e. visible and intrinsic defects, dependent on the casting operations and the concrete mix respectively) and orientation of steel reinforcement (with respect to the casting direction and to the exposure conditions).

In this research, characterization of steel reinforcement embedded in 20-years-old concrete prisms is reported. This characterization included the quantification of volume losses of reinforcement due to corrosion and analysis of the observed corrosion pits. These latter analyses are about the distribution of corrosion pits along the rebar length as well as the relation between corrosion pit depths, orientation and presence of concrete defects. These analyses were conducted by means of processing X-Ray Computed Tomography images. The working principle behind this technique is described later in this report (Section 2.3.1).

### 2.3.1. X-ray Computed Tomography

Among novel Non-Destructive techniques, X-ray Computed Tomography (CT-scanning) is reported to be really effective to monitor degradation of construction materials [11]. The aim of this technique is to identify the nature of a certain material occupying an exact position inside a body [31]. The principle behind CT-scanning is shown below (Figure 2.12) [11].

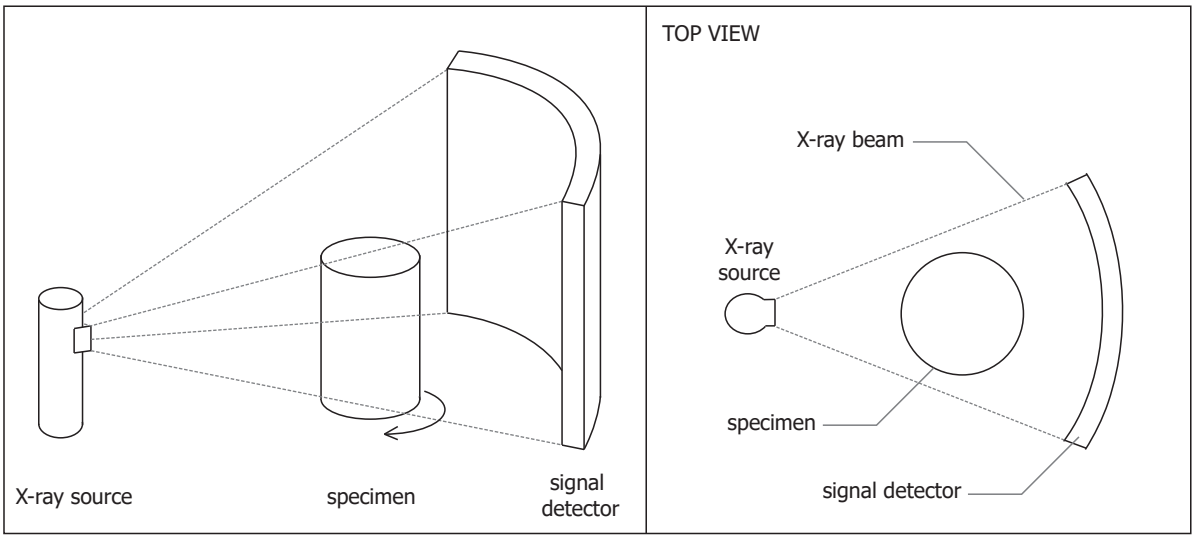


Figure 2.12: measurement principle of CT-scanning [11]

An X-ray tube works as signal source that is sent to the analyzed specimen. The different components inside the specimen absorb X-rays differently, depending on their state and chemical composition. When the signal gets to the detector, which is located behind the specimen, it carries information about X-ray absorption in the specimen [32]. CT images are taken rotating the specimen 360° within a time span set up beforehand. Using a reconstruction algorithm, images are processed and a map of the internal structure is provided.

CT scanning is increasingly used in non-destructive testing and monitoring practice, also for construction materials. Recently, image processing has been widely used as a reliable technique to study more deeply the micro-structure of mortar [32]-[35] and the development of corrosion in reinforced concrete [11] [36]-[38]. Trainor [32] used CT-scanning to monitor the internal structure of fiber-reinforced cement-based composites when subjected to fracture, while Landis et al. [33] used X-ray microtomography to make high-resolution three-dimensional digital of small concrete specimens under controlled load.

Quantitative analysis has been also extended to the evaluation of the volume loss of steel reinforcement due to corrosion thanks to X-Ray image processing. Despite the relatively low number of researches conducted related to this topic, image processing of CT scans shown already promising results. Filho et al. [36] quantified the volume loss of steel bars exposed uncovered to NaCl solution through processing CT images. The volume loss estimated by image processing was then compared to the one measured by gravimetric analysis of the steel reinforcement, resulting in slight differences between these two. In a less recent paper [37], he also quantified the volume loss due to corrosion in steel reinforcement embedded into cement mortar, and then comparing the results to estimations using Faraday's law. Here the differences were more relevant, but the overestimation of the latter measurements was justified by the fact that using Faraday's law it is assumed a general corrosion of the steel bars, which was not specifically that case.

Dong et al. [38] monitored the corrosion behavior of steel reinforcement embedded in a novel self-healing concrete. In this case, the volume loss due to corrosion was firstly quantified and then used to estimate the corrosion rate at which the rebars were subjected to.

Further studies have been conducted using X-ray tomography to qualitatively but not quantitively analyze the corrosion progress of steel reinforcement [11] [40] [41]. Itty et al [40] and Ghahari et al [41] used X-ray tomography to analyze the in-situ behavior of different types of steel with regard to the pitting corrosion they were subjected to. Cesen et al [42] analyzed and compared different electrochemical and physical techniques to characterize the corrosion of steel reinforcement in mortar, including also X-ray computed tomography. According to them, CT-scanning was found to be a very effective, non-destructive tool for the assessment of the corrosion of steel in mortar, including the type and the dimensions of the damage.

Savija et al [11] used X-ray computer tomography for monitoring rust formation during accelerated corrosion of reinforcement, and subsequent cover cracking in reinforced concrete cores. Beside confirming the usability of this technique for monitoring corrosion development, he found interesting behavior of rust with regard to the composition of the surrounding concrete. Two reinforced concrete specimens were CT scanned in this study. The two specimens were made of strain hardening cementitious composite (SHCC) mixed with Portland cement (CEM I 42.5N). The first specimen was cast with PVA fibers (named SHCC mixture), while the second one without (control mixture). Some slices of these specimens were analyzed. In one slice of SHCC mixture, a relevant air void was visible close to the steel-paste interface. Inducing accelerated corrosion, the rust amount increased and penetrated into this air void, thereby relieving some of the pressure which would otherwise be exerted onto the surrounding concrete. The rate of the rust production was also higher close to the air void compared to what was found in the bulk material. This might be explained by the higher speed that cathodic reaction could have close (or into) air voids due to the higher availability of oxygen in the air voids with respect to the dense matrix. The same rust penetration was also visible into open cracks (Figure 2.13) [11].

Rust formed at the interface zone was also found to be discontinuous as it was apparently made of overlapping layers. However, at the experimental magnification this possibility could not be confirmed. The discontinuity of the rust layer found for the control mixture specimen is shown below (Figure 2.13) [11].

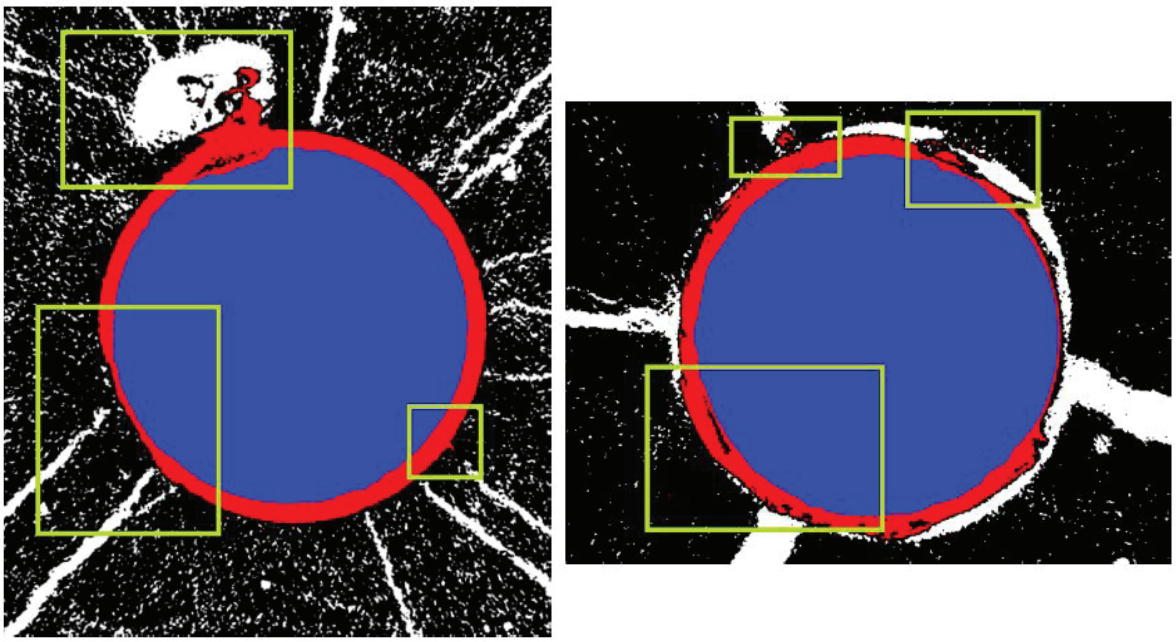

Figure 2.13: rust (red) penetration into air void (white) [left], layered rust formation (red with black layers) [right] [11]

When comparing the two tested specimens, it is visible that the control mixture specimen showed more brittle behavior, while SHCC specimen showed higher resistance to corrosion progress, even though corrosion was accelerated to the same extent. This is a further confirmation that characteristics of surrounding concrete and the quality of the steel/concrete interface are significant parameters for the corrosion progress. In numerical models about cover cracking, researchers already tried to consider these differences of corrosion development (and the pressure induced by the corrosion product to the concrete matrix) depending on the surrounding environment (i.e. concrete properties, presence of voids, etc.) [43] [44]. However, the quantification of this effect remains an issue [11].

## 2.4. Characterization of corrosion product

Many models simulating the effects of corrosion in reinforced concrete structures are available in the literature. Computational models allow experts to evaluate the development of this degradation process during time and to predict the cracking time of the surrounding concrete due to the tensile stresses induced by the formation of corrosion product. In cracking models of reinforced concrete due to corrosion, properties such as the volume expansion coefficient ($\alpha_{exp}$) and the E modulus ($E_{cp}$) of corrosion product play a significant role to develop accurate models. These two parameters have been widely studied and estimated by many scientists. However, it will be shown that there is no agreement about what are the most likely values of $\alpha_{exp}$ and $E_{cp}$, and that these values differ significantly in the current literature (Section 2.4.1 - Section 2.4.2). This disagreement among scientists is probably caused by the fact that formation, composition and structure of corrosion product are highly influenced by the environmental conditions where corrosion occurs, such as humidity, temperature, oxygen supply and presence of harmful agents (i.e. chloride ions) [45] [46] [47] [48].

The main components of corrosion product that have been observed in the literature are $\beta$-FeO(OH) (akaganeite), $\alpha$-FeO(OH) (goethite), $\gamma$-FeO(OH) (lepidocrocite), $Fe_3O_4$ (magnetite), $\alpha$-$Fe_2O_3$ (hematite), $\gamma$-$Fe_2O_3$ (maghemite) and green rusts [45]-[53]. Also amorphous $\delta$-FeO(OH), $Fe_8(O,OH)_{16}Cl_{1.3}$ and ferrihydrite have been observed under specific conditions [46] [47]. The presence and content of each corrosion product highly depends on interrelated parameters: for instance, Oh et al. observed that the same steel is exposed to different environmental conditions, the composition of corrosion product changes considerably in terms of components and their content [49].

Zhao et al. investigated the composition of corrosion product naturally-generated in different environments by means of XRD and thermal expansion analysis [45]. They confirmed the influence of exposure conditions on the composition of corrosion product. For instance, rich oxygen can improve the content of high-valency (threevalent) iron ions, while poor oxygen supplementation induces low-valency iron ions. The valency of iron ions is also related to the colour of corrosion product: black and dark brownish corrosion product are representative for a low oxygen supply, while yellow- and red-brownish corrosion product are usually found in direct contact with air [46].

Environmental conditions, such as humidity and temperature, affect the content of hydroxy-oxides of the corrosion product. Humidity directly affects the electrolytic resistance of the medium and thus the transport of hydroxyl ions within that, which are the producers of hydroxy-oxides [45].

In environment containing rich chloride ions the content of $\beta$-FeO(OH) is usually high: the significant influence that chlorides have on the composition of rust have been observed by many researchers [45] [47] [50] [51]. $\alpha$-FeO(OH) and $\gamma$-FeO(OH) were generally found in presence of $SO_4^{2-}$ and $NO_3^-$ [52]. Under certain humidity conditions and without ion ingress, $\gamma$-FeO(OH) slowly transforms to $\alpha$-FeO(OH). This transformation was observed by Wang et al. when investigating the corrosion product of weathering steel exposed to industrial atmosphere in Taiwan [53]. The outcome $\alpha$-FeO(OH) works as additional resistance layer against further development of corrosion. The formation of $Fe_2O_3$ requires extreme temperature that are (usually) not reached within the service-life of structures [45]: for this reason, some scientists think that it cannot be a component of the corrosion product but more likely a result of the hot treatment that steel is subjected to during industrial production ("mill scale"). Therefore, $Fe_2O_3$ has been considered as non-contributing to concrete cover cracking [45].

### 2.4.1. Volume expansion coefficient of corrosion product

The corrosion reaction produces ferric hydroxides, which occupy a volume larger than the initial volume of iron [10]. This expansion in volume induces internal stresses within the concrete matrix. Since the tensile strength of the concrete is relatively low, cracking, delamination and finally spalling of the surrounding concrete might be caused. Due to cracking, higher penetration of aggressive ions from the outside is enabled, accelerating the corrosion rate of the reinforcement and making the reduction of structural capacity faster.

The expansion coefficient of corrosion product ($\alpha_{exp}$) is defined as the ratio between the volume of the corrosion product and the volume consumed by the corrosion process [54]. This latter one is also known as "volume loss". Due to the influence that rust formation and then expansion in volume have with regard to the surrounding concrete matrix, and thus the durability of the whole structure, the rust expansion coefficient has received much attention from both scientists and practical engineers [45].

In previous research on concrete cracking models due to corrosion, values of rust expansion coefficient varied between 2 and 4 [45]. The value of 2.0 was used by Molina [55], Noghabai [56], Lundgren [57] and Wang [58]. Higher values of 2.7, 3.0 and 4.0 were used by Lu [59], Zhao [60] and Liu [62] respectively in their analysis and models of concrete cracking due to corrosion. In their thermal simulation Bhargava [63] and Val [61] used rust expansion coefficient equal to 2.94 and 3.39 respectively.

Tuuttii estimated that the expansion coefficient of corrosion product varies between 2.2 and 6.4 [9]. Carè and Nguyen [54] tried to determine the expansion coefficient for each corrosion product with a modelling approach, considering the interfacial zone between steel and surrounding concrete as a three-phase material (steel/rust/mortar) and analyzing its varying thickness [45]. In this case, $\alpha_{exp}$ were in line with those found in previous research [9]. Zhao [45] measured the expansion coefficient of different rust also considering the different composition of the corrosion product exposed to different environmental conditions, by means of X-ray diffraction and thermal analysis. For his eight rust specimens, he found rust expansion coefficients varying between 2.64 and 3.24. These differences were attributed to the different composition that rust specimens had because of the different environmental conditions they were exposed to (Section 2.4).

In Figure 2.14, the volume expansion coefficient for each type of corrosion product is visible [67], while Figure 2.15 shows the $\alpha_{exp}$ considered in the available literature.

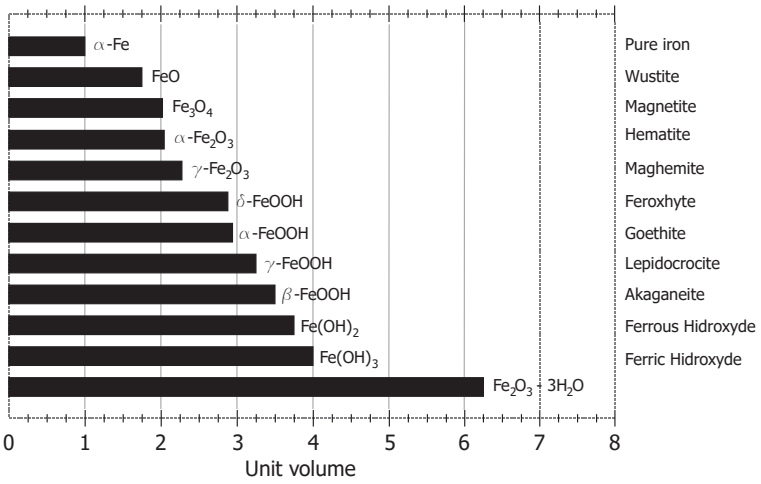


Figure 2.14: Volume expansion coefficients of each type of corrosion product

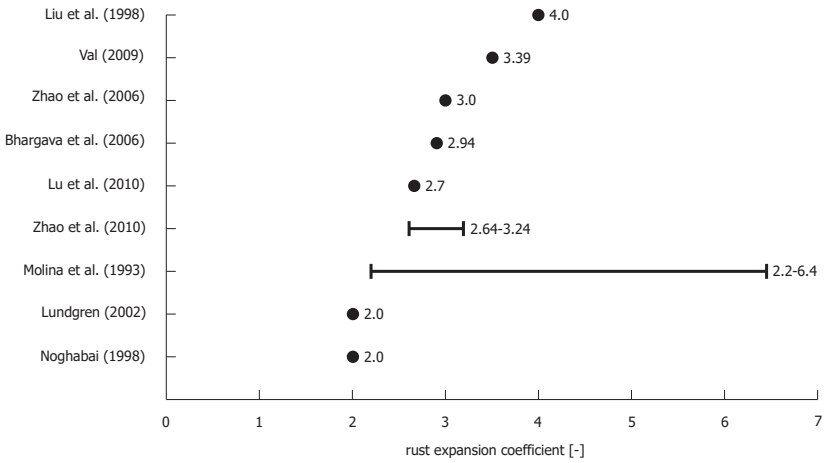


Figure 2.15: Volume expansion coefficients of corrosion product considered in previous studies

### 2.4.2. Elastic modulus of corrosion product ($E_{cp}$)

Apart from inducing stresses by their volume expansion, the corrosion products also participate in the mechanical interaction between the concrete cover and the steel during the concrete cracking process due to corrosion [64]. The corrosion product around the reinforcement acts as interlayer at the interfacial zone between steel and concrete, transferring the loads to the surrounding concrete matrix. Therefore, mechanical properties of corrosion product, and especially its E modulus ($E_{cp}$), are relevant when modelling concrete cracking. The relevance of this parameter is confirmed by the number of researchers that have studied the topic. Despite the relatively high number of publications, there are large differences between the values of $E_{cp}$ found in the literature.

In 1973, Samsonov [65] estimated the Elastic modulus of iron oxide crystals between 215 and 360 GPa. However, these values reflected more the E modulus of single components of corrosion product

($Fe_2O_2$ and $Fe_3O_4$) instead of those of the rust itself. These values are in line with those found by Ouglova et al., who estimated $E_{cp}$ of 360 GPa [66]. In this latter case, rust samples were appositely prepared, made in different size (from 0.4 to 8.7 μm) and then analyzed by oedometer test. It seems, however, unlikely that $E_{cp}$ would be higher or comparable to the one of uncorroded steel (generally 210 GPa). Apparently, corrosion product is made of iron oxides and hydroxy-oxydes layers overlapping each other. Both the porosity and oxygen content of the corrosion product is higher than that of uncorroded steel, which is likely to reduce its $E_{cp}$ modulus as well.

Corrosion product composition, and so likely its mechanical properties, is influenced also by which iron compounds are formed and its porosity. Zhao et al. [64] found that $E_{cp}$ is proportional to its $Fe/O$. According to Shahzma et al. [67], longer the corrosion of the reinforcement, lower the $Fe/O$ of the corrosion product, reducing the $E_r$ of the rust. Zhao et al. also found two distinct (outer and inner) layers of rust when inspecting samples through SEM. The Elastic modulus of inner rust layer ranged between 47 and 86 GPa, while the E of the outer layer ranged between 98 and 122 GPa. While the inner rust is thought to be generated by the corrosion process, the outer rust seems to be formed by heat treatment, hot rolling and forging processes that steel is subjected to [68]. The different $Fe/O$ ratios of corrosion product layers have been identified as the main reason why relevant differences between $E_{cp}$ are found. Different rust layers have been found also by Hosemann et al. on prepared rust samples [69], with $E_{cp}$ ranging between 70-100 GPa measured through nano-indentation.

Savija et al. [11] performed nano-indentation tests on reinforced concrete specimens previously subjected to induced accelerated corrosion. In line with the values measured by Zhao [64], they found that the $E_{cp}$ ranged between 49.4 and 67.9 GPa. However, no distinct corrosion product layers were identified, probably because corrosion of steel was anodically accelerated.

In their model for concrete cover cracking as a function of reinforcement corrosion, Molina et al. [55] assumed that rust was perfectly elastic and that It could be considered as a fluid with Poisson's ratio of $v_r = 0.5$ and bulk modulus of $K_r = 2.0GPa$. Using the equation $E_{cp} = 3(1 - 2v_r) * K_r$ they determined an E modulus of rust ($E_{cp}$) of 12 MPa.

Bhargava et al. [63] investigated the time to cracking of concrete cover due to corrosion. In doing so, they assumed that E modulus and Poisson's ratio of rust were identical to those of the steel reinforcement, i.e. $E_{cp}$=200 GPa and $v_r$=0,3. This assumption seemed to be implausible by other researches due to the different hardness and density of the two components [70].

Lundgren [71] proposed a stress-strain formula for the mechanical properties of the rust ($\sigma_r = K_r * \varepsilon_r$) based on the two-dimensional relation between the components at the interface zone (rebar, rust and concrete). After evaluating the stress by analysing different combinations of experimental results, he estimated a modulus coefficient ($K_r$) of 14 GPa. Suda et al. [72] found that $E_{cp}$ ranged between 0.1 and 0.5 GPa through nonlinear finite element analysis. Low values of $E_{cp}$ have been proposed by Balasaf [73] also, ranging between 40 and 87 MPa, and by Zhao [70], who performed cyclic low-compression tests and oedemeter tests on naturally generated rust. In this latter paper, they found that the magnitude of the $E_{cp}$ was around 100 MPa.

An overview of $E_{cp}$ values found or estimated in the current literature is given below (2.16).

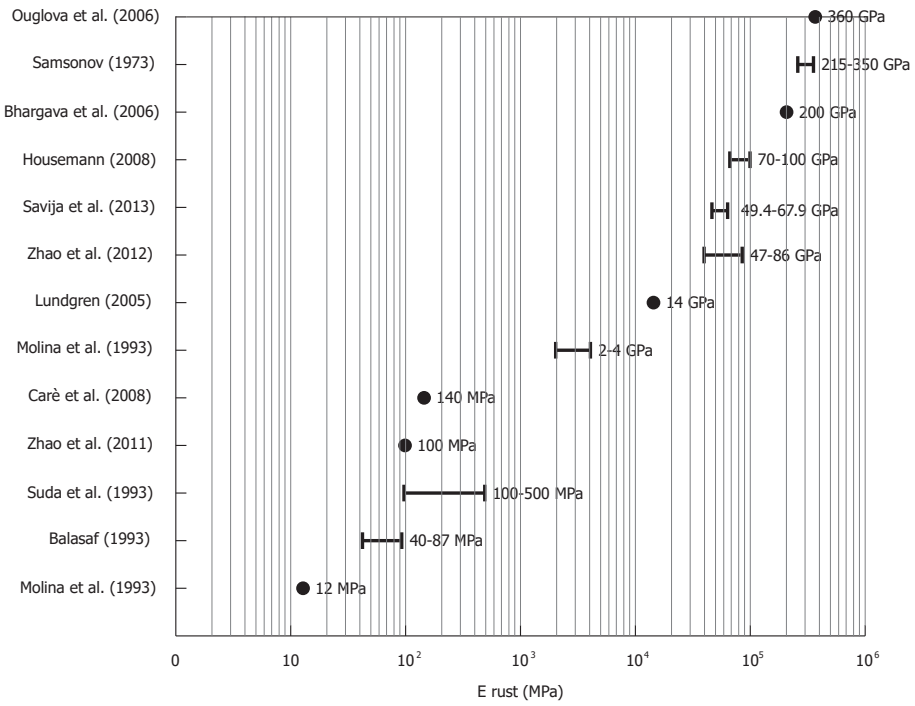


Figure 2.16: Elastic modulus results found in previous studies

As shown in Figure 2.9, $E_{cp}$ values found in the literature can vary by a factor of $10^6$, from a minimum value of 12 MPa [55] to a maximum value of 360 GPa [65] [66]. There is no agreement between scientists about which value of $E_{cp}$ is the most likely nor about what it is mostly influenced by. It seems that $E_r$ depends on interrelated parameters: for instance, the composition and microstructure of the corrosion product that is analyzed, and so the environmental conditions it was exposed to [45]. Also the technique that is used to measure $E_{cp}$ might play a significant role at this stage: both Savija et al. [11] and Zhao et al. [64] used nanoindentation to measure $E_{cp}$, and the output values are comparable with each other (between around 50 and 80 GPa). On the other hand, Zhao et al. [70] measured $E_{cp}$ by means of loading-unloading cycles, and the output was significantly lower, equal to around 100 MPa. Since in this research the mechanical properties of corrosion product were tested through nano-indentation, a description of this technique and its working principle is given below (Section 2.4.3).

### 2.4.3. Nano-indentation

Nanoindentation is a technique used to assess the mechanical properties of materials at a micro-scale. If it is possible to assess mechanical properties of materials at a state where they manifest themselves in a chemically stable state, it is also possible to translate chemical equilibrium states to bigger-scales material properties [74]. Mechanical properties of materials can be characterized based on the localized contact response of the material itself when subjected to localized loads. With this technique, the variation of penetration depth of the indenter, *h*, and the imposed indentation load, *P*, are continuously recorded and then plotted together. Indentation data are then empirically correlated to mechanical properties of the indented material.

The working principle behind this technique has been studied at the beginning of 1900 by the Swedish engineer Brinell [75]. By pushing a small ball of hardened steel or tungsten carbide against the surface of a specimen, he empirically correlated the shape imprinted permanently on the specimen

with the strength of metal alloys [74]. Eventually, other scientists suggested others empirical relations to translate indentation data into mechanical properties for different indenter geometries [76] [77]. However, by means of finite elements analysis it has been found that using indenters with other shapes than the pyramidal one, the variations between *P-h* curves during unloading are negligible [74].

A typical indentation test is composed by a loading-phase and an un-loading response of the specimen. During unloading, the material is assumed to behave purely elastic. In this case, elastic punch theory can be applied to the curve *P-h*, extrapolating the elastic properties of the material as the slope of the curve itself. An example of *P-h* curve and a sketch of the working principle behind this technique is given below (Figure 2.17) [74].

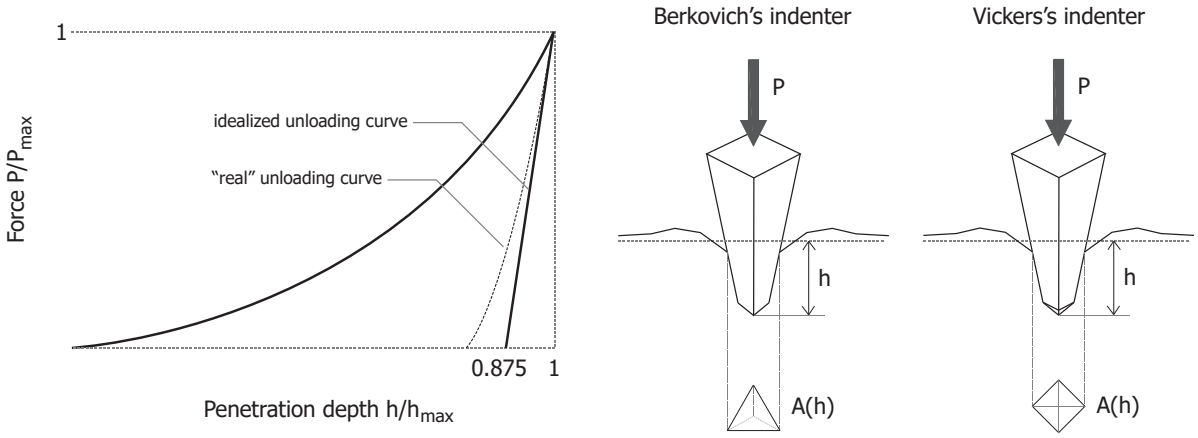


Figure 2.17: Example of P-h curve (left) and sketch of parameters measured by nanoindentation (right)

The elastic modulus of the indented material can be calculated using the following formula [11]:

$$\frac{1}{E} = \frac{1 - v_s^2}{E_s} + \frac{1 - v_{in}^2}{E_{in}}$$

where, $v_s$ is the Poisson's ratio of the intended material, $v_{in}$ is the Poisson's ratio of the indenter, $E_s$ is the Young modulus of the intended material and $E_{in}$ is the Young modulus of the indenter. By assuming that during unloading only the elastic displacements are recovered, the reduced elastic modulus ($E_r$) can be determined from the slope of the unloading curve, as:

$$S = \frac{dP}{dh} = c * \sqrt{A} * E_s$$

where, *S* is the elastic unloading stiffness (equal to the slope of the upper unloading curve during the initial unloading phase), *P* is the indented load, *h* is the displacement with respect to the initial undeformed surface, *A* is the projected contact area at the peak load and *c* is the indenter constant. For the Vickers pyramid indenter (Figure 2.16), a constant *c* of 1.142 is used. For the Berkovich indenter (triangular cross section) *c* is equal to 1.167, while it is equal to 1.1284 for the flat cylindrical indenter. However, by means of relatively low differences between the constant c for differently shaped indenters, *dP/dh* can be calculated without large errors with different indenters [74].

To determine the $E_r$ modulus of the rust, the Poisson's ratio, $v$ of the rust has to be specified. This value has been differently assumed by many scientists when developing concrete cracking models [66] [55]. Despite the differences present in the literature, Zhao et al [64] found that Poisson's ratios estimated between 0.2 and 0.3 yield to marginally different results.

According to Constantinides [74], elastic modulus of indented materials can be also determined directly from the sharp *P-h* response obtained during the complete loading/unloading cycle using the following formula:

$$E = d * \frac{H}{1 - \frac{W_p}{W_t}}$$

where, *H=P/A* (h) is the average pressure under the indenter, $\int_0 hP(s) * ds$ is the total work performed by the indenter during deforming the indented material, and $W_p$ is the plastic work. These quantities are extracted directly from the *P-h* as sketched previously (Figure 2.17). However, in practical applications E is determined for the maximum $P_{max}$ and penetration depth $h_{max}$ only, which are associated with a specific material scale under consideration [74].

## 2.5. Synopsis

In Section 2.4.1-2.4.2, the volume expansion coefficient and E modulus of corrosion product given by the current state of the art were reported. As previously pointed out, significant differences are found among the values given for these two parameters in literature. It is likely that characteristics of corrosion product vary so significantly because they are highly dependent on many interrelated parameters. However, when modelling concrete cover cracking progress, no distinctions are made between different types of corrosion product that are likely to be found under different conditions. Different composition of corrosion product influences its chemical composition and mechanical properties, so influencing the concrete cover cracking process. To model this process more accurately, these differences should be probably included.

The influence that environmental conditions have on the composition of corrosion product have been widely studied, especially with regard to aggressive exposures [45]. However, the influence that the concrete environment might have on the composition of the corrosion product, and so on its characteristics, has not been investigated. Even though Angst [17] pointed that the binder type used to cast concrete seems to be a secondary factor on corrosion progress and especially on the quality of the steel/concrete interface, this research aims to investigate if (and how) different concrete mixes might influence (directly or indirectly) the composition and Elastic modulus of corrosion product. Differences in composition of corrosion products of steel embedded in different mixes might be of interest when modelling concrete cover cracking processes, allowing for potentially more accurate output depending on the characteristics of a certain structure. Different techniques will be used to characterize steel reinforcement embedded in different concrete mixes as well as its corrosion product: these techniques include X-ray Computed Tomography (CT-scan), Nano-indentation and Scanning Electron Microscopy (SEM). A brief description of the former two techniques has been previously given, while the whole experimental plan will be described later in this report (Section 3.4).

# 3

# Specimens' historical records (1998-2010) and current state (2018)

## 3.1. Introduction

In the present research a three-scale characterization of eight reinforced concrete specimens was carried out. These specimens were 20-years old and naturally-deteriorated due to corrosion. In 1998, they were cast with w/c of 0,55 and with four different cement types (CEM I, CEM II/B, CEM III/B-V, CEM V/A). During their first 6 months after casting, they were exposed to NaCl wet/dry cycles to accelerate chloride-induced corrosion. These specimens were part of a group of 192 prisms cast in 1998 by Polder et al. [78]. In this chapter, historical records and information about the whole group of specimens are given (Section 3.2), as well as the state at which specimens were found at the beginning of the present research (Section 3.3). An overview of the experimental plan conducted on these specimens is also described (Section 3.4).

## 3.2. Previous work (1998-2010)

In 1998, 192 reinforced concrete prisms were cast to study of corrosion initiation and propagation of steel reinforcement embedded in different concrete mixes and under different exposure conditions [78]. The composition of the specimens was defined as a combination of four different cement types and three water/binder ratios [8] [78]. The cement types that were used according to ENV 197-1:1992 are:

- CEM I 32.5 R Portland cement;
- CEM II/B-V 32.5 R fly ash cement (27% fly ash);
- CEM III/B 42.5 N blast furnace slag cement (75%);
- CEM V/A 42.5 N fly ash and slag composite cement (25% fly ash, 25% slag);

while the water/binder ratio are:

- 0.40;
- 0.45;
- 0.55;

Based on their w/c and their cement type, 12 concrete mixes were made. Per each mix, 16 specimens were cast, of which 6 included adding 2% of $CaCl_2$ (labelled as "mixed-in chlorides specimens") and 10 did not. Mixed-in chlorides specimens were not analyzed in this research; for this reason, the information reported here must be considered about the specimens without chloride addition only (10 per concrete mix). More information about all specimens can be found elsewhere [78]-[81].

The prisms were made with siliceous river material with a maximum size ($D_{max}$) of 8 mm as aggregate. The geometrical representation of the specimens is shown in Figure 3.1. Prisms were cast with dimensions equal to 100 x 100 x 300 mm. In each prism, two groups of three smooth steel bars of 8 mm in diameter were embedded at 10 mm and 30 mm of cover depth from one mold face, cast parallel to the bars. Each bar had an embedded length of around 80 mm. The top and the bottom portion of each bar was covered with a protective coating to avoid side-effects from the exposure. In doing so, the exposed (uncovered) length of the reinforcement was 45 mm (with exposed lateral surface of around 1090 $mm^2$), starting at 10 mm from the top side of the prism. Two groups of two stainless steel bars with 6 mm in diameter were placed at both 10 mm and 50 mm in depth for resistance measurements. Two activated titanium wire electrodes with length of 20 mm were cast-in for each group of embedded mild steel bars, working as reference electrodes for steel potential measurements [8] [78].

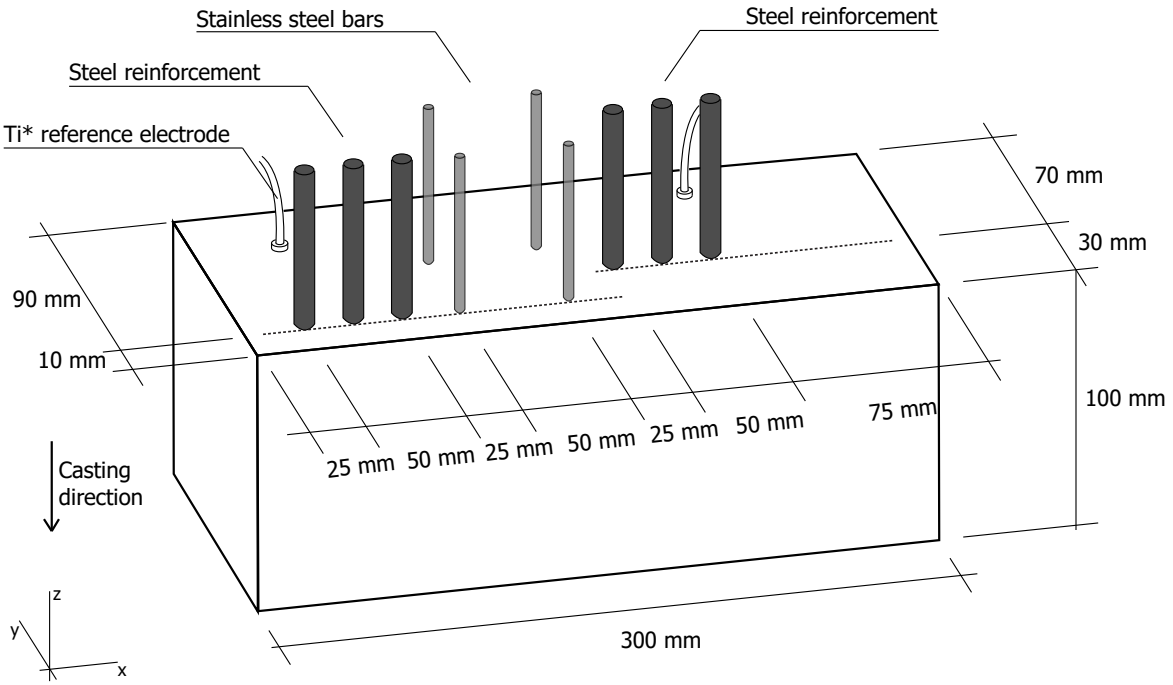


Figure 3.1: Geometrical representation of concrete specimens

A resume of properties of concrete mixes in both fresh and hardened state is given in Table 3.1 [78].

Table 3.1: Properties of fresh and hardened concrete specimens after 280 days [78]

| Cement type | w/b | Chloride content (%) | Slump (mm) | Flow (mm) | Specific gravity fresh mix (kg/m^3) | Air content (%) | Compressive strength (MPa) | Specific gravity cube (kg/m^3) |
|---|---|---|---|---|---|---|---|---|
| CEM I | 0.40 | 0 | 10 | 360 | 2267 | 3.9 | 45.7 | 2338 |
| | 0.40 | 2 | 20 | 310 | 2068 | 6.8 | 44.4 | 2290 |
| | 0.45 | 0 | 4 | n.b. | 2260 | 2.1 | 42.0 | 2314 |
| | 0.45 | 2 | 55 | 360 | 2042 | 12.5 | 39.3 | 2229 |
| | 0.55 | 0 | 10 | 290 | 2280 | 4.3 | 23.4 | 2256 |
| | 0.55 | 2 | 20 | 440 | 1986 | 12.0 | 27.4 | 2227 |
| CEM II | 0.40 | 0 | 120 | 420 | 2287 | 4.4 | 53.2 | 2345 |
| | 0.40 | 2 | 37 | 335 | 2238 | 5.5 | 48.7 | 2250 |
| | 0.45 | 0 | 70 | 380 | 2280 | 4.0 | 40.8 | 2337 |
| | 0.45 | 2 | 100 | 400 | 2230 | 7.4 | 37.4 | 2225 |
| | 0.55 | 0 | 20 | 320 | 2270 | 4.6 | 36.5 | 2339 |
| | 0.55 | 2 | 200 | 500 | 2091 | 11.5 | 25.6 | 2197 |
| CEM III | 0.40 | 0 | 10 | 320 | 2319 | 3.7 | 43.0 | 2345 |
| | 0.40 | 2 | 10 | 280 | 2222 | 6.7 | 50.8 | 2276 |
| | 0.45 | 0 | 10 | 300 | 2296 | 4.3 | 41.5 | 2335 |
| | 0.45 | 2 | 70 | 360 | 2126 | 9.0 | 36.8 | 2218 |
| | 0.55 | 0 | 110 | 460 | 2313 | 3.5 | 34.6 | 2357 |
| | 0.55 | 2 | 250 | 540 | 2176 | 8.3 | 38.1 | 2247 |
| CEM V | 0.40 | 0 | 10 | 270 | 2300 | n.b. | 60.8 | 2329 |
| | 0.40 | 2 | 0 | 280 | 2290 | 4.4 | 51.1 | 2275 |
| | 0.45 | 0 | 70 | 370 | 2355 | 1.9 | 46.2 | 2322 |
| | 0.45 | 2 | 130 | 420 | 2259 | 5.0 | 47.3 | 2244 |
| | 0.55 | 0 | 120 | 460 | 2278 | 3.0 | 35.8 | 2327 |
| | 0.55 | 2 | 220 | 510 | 2096 | 10.0 | 32.9 | 2202 |

Specimens were cast between August and October 1998 [78]. They were left in their molds for 24 hours after casting, covered with plastic foil. When de-molded, all the specimens were stored in a fog room (20°C, RH>95%) for their first week after casting. When specimens were 1-month old, they were exposed to different environmental conditions. These conditions included accelerated carbonation (storage in a 5% CO2, 20°C and 50% RH) and accelerated chloride ingress. This latter exposure included the application of 3,5% NaCl solution on the face with the lowest cover depth of the mild steel bars for 24 hours and then drying the specimen in a 20°C and 50% RH environment for six days. These exposure conditions were applied until specimens were around 6-months-old. Between 6 months and 2,5 years old, specimens were divided in different groups and exposed to different environmental conditions, which included a fog room (RH>95%), outside (unsheltered) and at 20°C-80% RH.

The corrosion progress of steel embedded in each prism was monitored for the first 2,5 years by means of measuring Potential (E) and Linear Polarization Resistance (LPR) of the mild steel [78]-[81]. E measurements were recorded for each steel bar in relation to the closest cast-in titanium electrode. LPR measurements were taken for each steel bar, using the other two bars with equal cover depth as reference and counter electrodes respectively. Concrete resistance was also measured between each

pair of stainless steel bars with equal cover depth and through a Wenner probe placed on the opposite face. All resistivity measurements applied 120 Hz AC.

Between 2003 and 2009, specimens were not further studied and they were left unsheltered exposed to outside environment. During this period, the TNO Mec LAB (where specimens were kept) was re-located, causing loss and mislabeling of some of the specimens. In October and November 2009, specimens were characterized at 11 years after casting by Pacheco [8]. At that time, the number of specimens available was 123 out of the initial 192, and most of the labeling was lost. The purpose of that research was to analyze the corrosion progress of steel embedded in 11 years old concrete, and studying if (and how) corrosion development depended on the characteristics of the specimens themselves. For this purpose and due to specimens mislabeling, a three-phases identification procedure was carried out prior to evaluate the corrosion state and progress of specimens. This procedure included visual analysis, statistical analysis and Non-Destructive techniques.

Based on this identification procedure, the composition of the salt/dry-exposed specimens (i.e. w/c and cement type) was identified with a degree of confidence of 95%. However, it was not possible to identify which were the environmental conditions to which specimens were exposed between 6-months and 2,5-years-old (i.e. fog room, 20°C-80% RH or outside). A detailed explanation of this investigation is given elsewhere [8]. When specimen composition was identified, potential and LPR of the mild steel bars and the resistance of the concrete were measured three times (November 2009, February and April 2010).

## 3.3. State of the specimens (2017-2018)

In December 2017, the state of the specimens was visually investigated as part of this project. Since 2010, they were left outside (unsheltered) the TNO Laboratory in Delft, the Netherlands. The number of specimens was 97, of which 84 had labels according to Pacheco [8] and 13 did not. The purpose of the present research is to investigate the influence of different cement types on the properties of the corrosion product and on the corrosion state of steel reinforcement. The influence of different water/binder ratios is not investigated: only specimens cast with w/c of 0,55 ("poor quality concrete") were then considered.

Specimens were also selected based on the conditions they were exposed to. The exposure to aggressive ions as chlorides increased the possibility to find more aggressive pitting corrosion if compared to those likely caused by carbonation ("carbonated specimens"). This was also confirmed by visual inspections conducted in December 2017, where in some salt/dry specimens brownish spots were visible on the surface of the prisms, suggesting presence of internal corrosion, which was not so visible for some of the carbonated specimens. According to the labels given in 2010 [8], the specimens cast with a water/cement ratio equal to 0,55 and exposed to NaCl cycles were 15 in total, divided as follows (Table 3.2):

Table 3.2: Number of specimens exposed to salt-dry cycles and w/c of 0,55 according to labelling given in 2018 [8]

| Water/binder | CEM I | CEM II | CEM III | CEM V |
|---|---|---|---|---|
| **0.55** | 2 | 3 | 4 | 6 |

Some of these 15 specimens showed characteristics that suggested they belonged to different exposure conditions or mixes (i.e. no presence of silicone to keep the solution in place). More information about these relevant characteristics can be found elsewhere [8]. After leaving out those specimens that did not show signs of salt/dry cycle exposure, the total amount of specimens was equal to 12. Out of 12 specimens, 8 specimens (2 per cement type) were considered for this research, which are listed below (Table 3.3):

Table 3.3: Specimens object of this research

| Sample label (2010) | Cement type | w/c |
|---|---|---|
| 1550-A | CEM I | 0.55 |
| 1550-B | CEM I | 0.55 |
| 2550-A | CEM II | 0.55 |
| 2550-C | CEM II | 0.55 |
| 3550-B | CEM III | 0.55 |
| 3550-D | CEM III | 0.55 |
| 5550-D | CEM V | 0.55 |
| 5550-F | CEM V | 0.55 |

The specimens were labeled by four digits with the following codes according to previous researches [78]:

- The first digit indicates the cement type (1 for CEM I, 2 for CEM II, 3 for CEM III and 5 for CEM V);
- The second and third digits for the water/binder ratio (40 for 0.40, 45 for 0.45, 55 for 0.55; in this research, only 55 is present);
- The fourth digit for the chloride content (0 for 0% of mixed-in $CaCl_2$, 2 for 2% of mixed-in $CaCl_2$; in this research, only 0 is visible);
- The last digit (letter) was added to label different specimens from the same concrete mix;

Following this way of labeling, the specimen 1550-A corresponds to one sample with CEM I, with 0.55 water/binder ratio and 0% of mixed-in chlorides. To summarize the exposure conditions and operations related to specimens object of this research, a time line is given below (Figure 3.2):

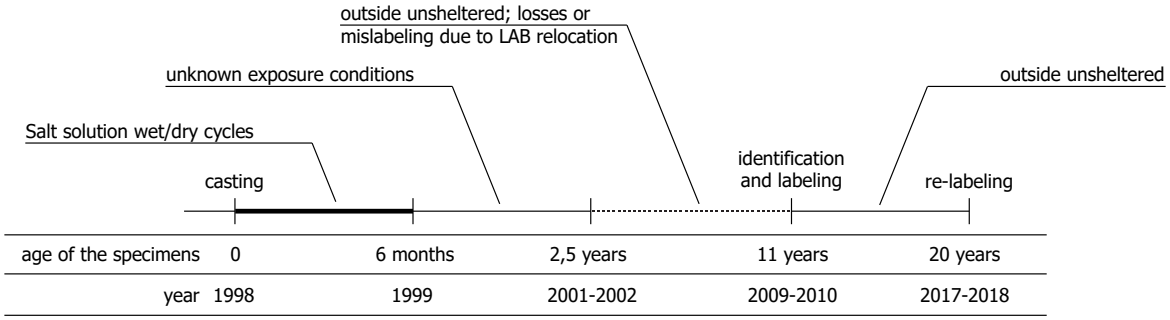


Figure 3.2: Timeline of exposure conditions and operations related to NaCl exposed specimens with w/c=0,55

## 3.4. Experimental plan overview

After specimen selection, the cement type for specimen was identified to ensure that the identification procedure conducted by Pacheco [8] was accurate. Polished sections of concrete portions were analyzed by means of Scanning Electron Microscope (SEM). This identification procedure is described in Chapter 4.

As soon as each cement type was identified, a three-scale characterization was carried out. Chapter 5 reports the macro-scale characterization conducted on the reinforced concrete prisms by means of electro-chemical measurements, carbonation depth and visual inspection. These analyses were used to evaluate the state of the concrete environment as well as the likely corrosion state of the reinforcement, even with regard to the available historical measurements.

In chapter 6 the meso-scale characterization of the steel reinforcement conducted by means of X-ray computed tomography (CT-scan) is reported. One core embedding one reinforcement bar was drilled out of each specimen. A length of 44 mm was CT-scanned and the internal state of the specimen was analyzed (Figure 3.3). By means of image processing, the volume loss due to corrosion was quantified as well as the influence of orientation and defects at the steel/concrete interface on corrosion initiation and propagation.

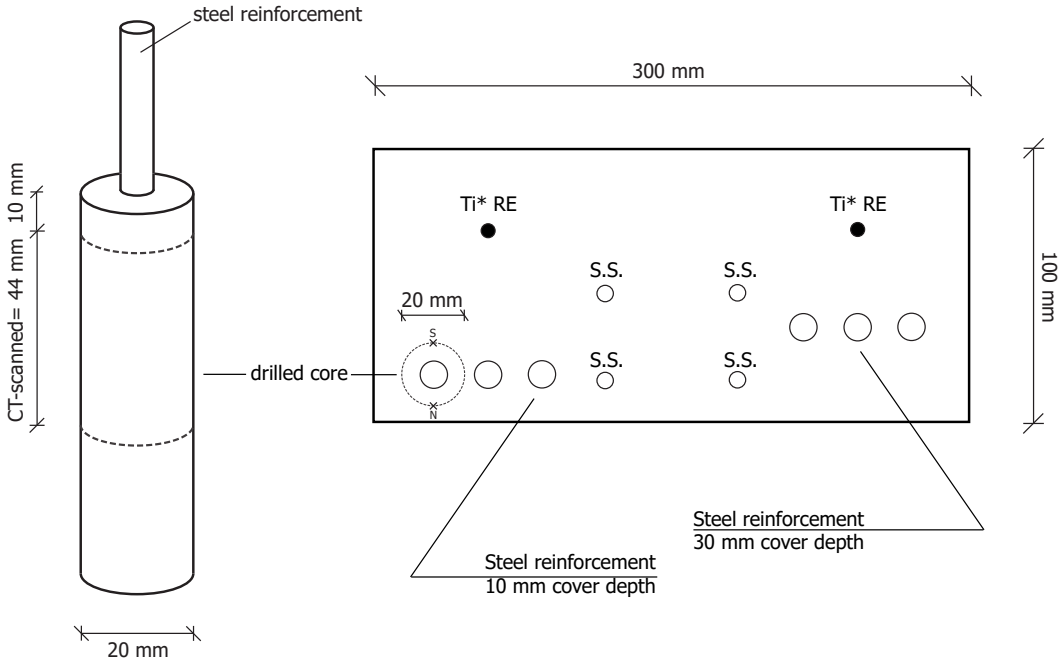


Figure 3.3: Visualization of one core drilled out of each prism that was then analyzed by means of X-ray computed tomography (out of scale)

Chapter 7 describes the micro-structural characterization of corrosion product through nano-indentation and SEM/EDS point analysis. The cores were side-impregnated with fluorescent epoxy and slices were sawn, grinded and polished (Figure 3.4).

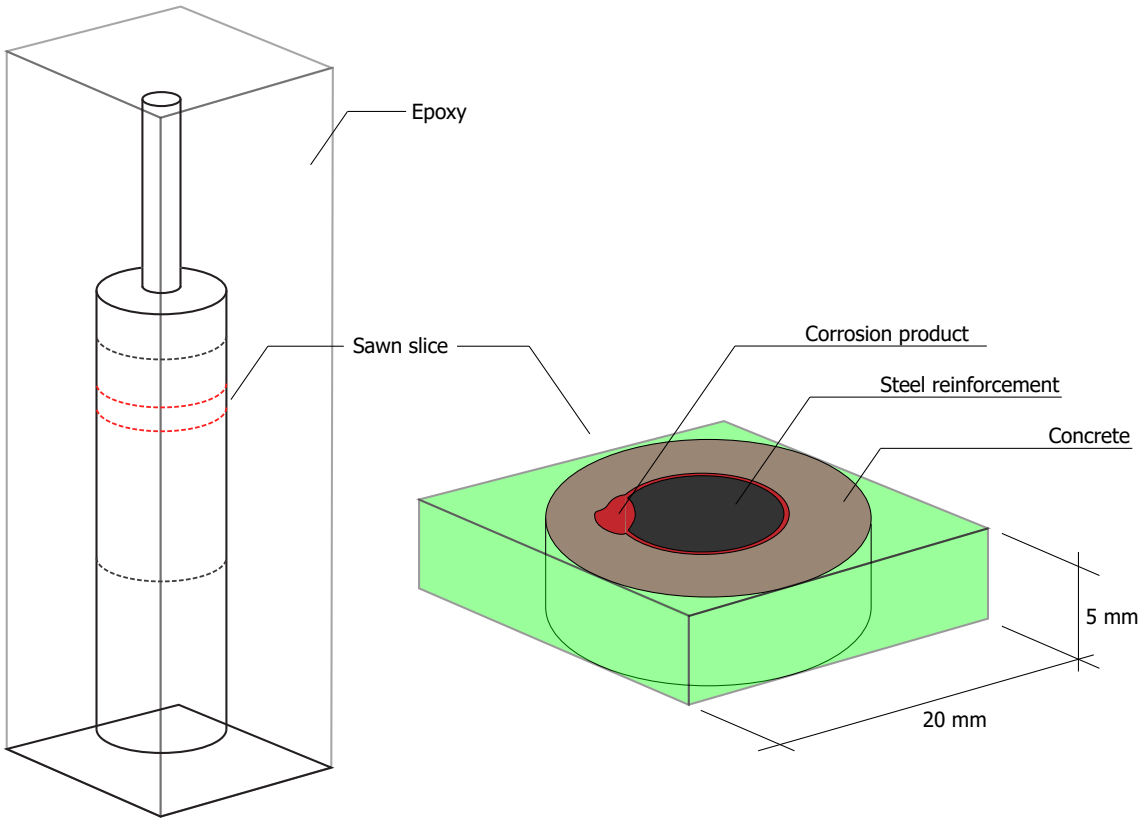


Figure 3.4: Visualization of reinforced concrete slices sawn for micro-scale analysis

Nano-indentation was performed to determine the micro-mechanical properties (i.e. Elastic modulus) of corrosion product at the steel/concrete interface of each specimen. To evaluate the influence of corrosion product composition on these properties, EDS elemental mapping (for all the specimens) and standard-based SEM/EDS spot analysis (for one specimen only) were conducted at the locations where nano-indentation was performed. Experimental set up, methodology and output of this characterization is described in more detail in both Chapter 7 and Appendix D. X-Ray Diffraction (XRD) was also conducted on corrosion product powder to characterize its crystalline composition, as reported in Section 7.5.

# 4

# Cement type identification through SEM and samples labeling

## 4.1. Purpose, procedure and results

Since the identification conducted by Pacheco was based on statistical analysis and Non-Destructive techniques only, his research did not completely ensure the composition of the prisms, although the degree of confidence of the analysis equaled 95% [8]. Following his recommendations, the cement type used to cast each prism was ensured by means of microscopy analysis. Concrete portions were sawn from each concrete prism. Once sawn, samples were manually ground with #120, #220, #280, #320, #600, #800 and #1200 grinding silcone carbide sanding paper and polished with 6, 3, 1 and 0.25 $\mu m$ polishing diamond paste on a lapping table. 100% ethanol and non-water based polishing paste were used for grinding and polishing, respectively.

The identification of each cement type was based on the visible presence of fly ash (CEM II), slag (CEM III), both fly ash and slag (CEM V) or none of them (CEM I). Fly ash and slag particles were identified based on their shape, dimensions and color: fly ash is known to be round-shaped with diameter generally around 20-50 $\mu m$, while slag particles are angular-shaped and heavier than both fly ash and cement paste (hence brighter in BSE images). BSE images were acquired at 20 kV acceleration voltage and 500x-1000x of magnification. A selection of BSE images for each specimen is given below: in each image fly ash and slag, if present, are pointed by yellow and green arrows respectively (Figure 4.1-4.4). Further BSE images are reported in Appendix A at the end of this report.

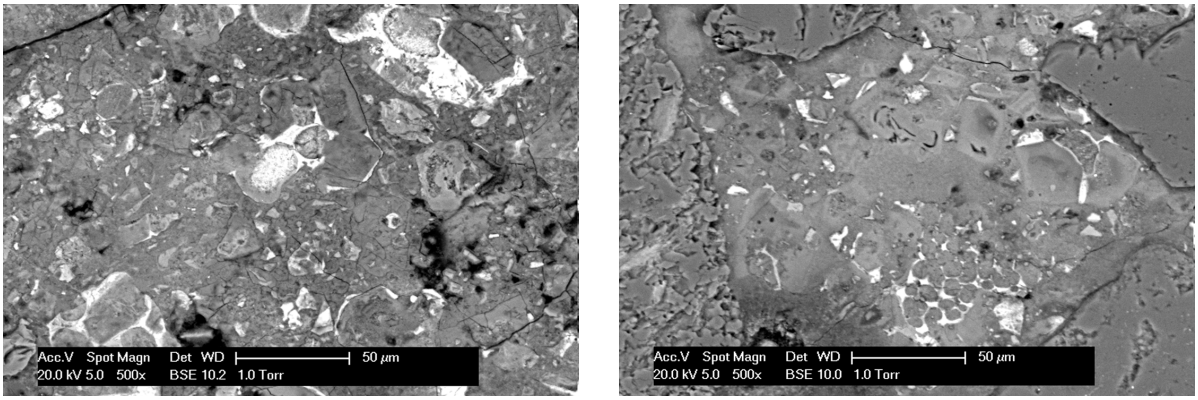


Figure 4.1: 1550-S1 (left) and 1550-S2 (right) BSE images

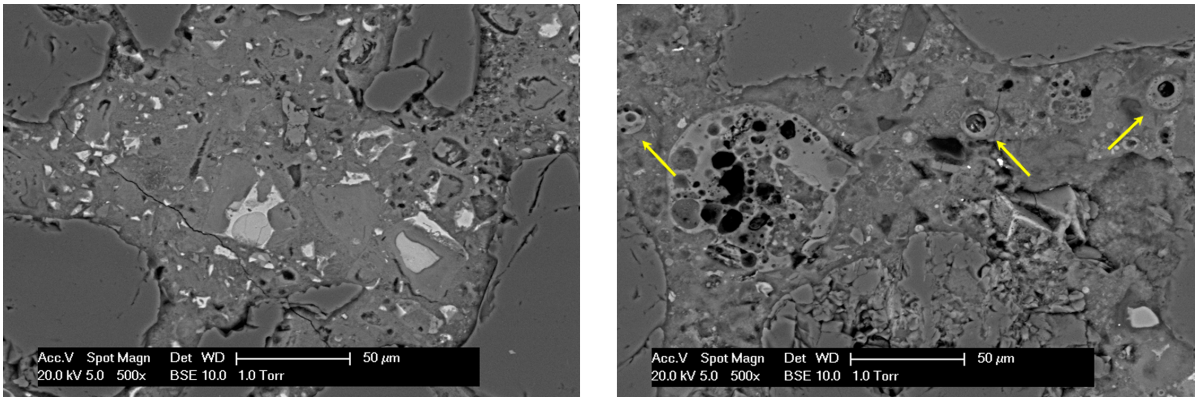


Figure 4.2: 2550-S2 (left) and 2550-S3 (right) BSE images (yellow arrows=fly ash)

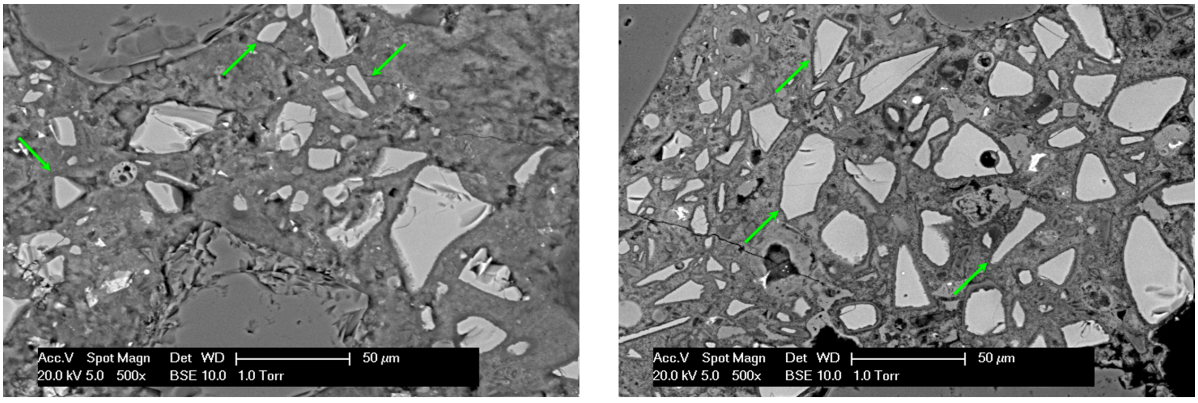


Figure 4.3: 3550-S1 (left) and 3550-S2 (right) BSE images (green arrows=slag)

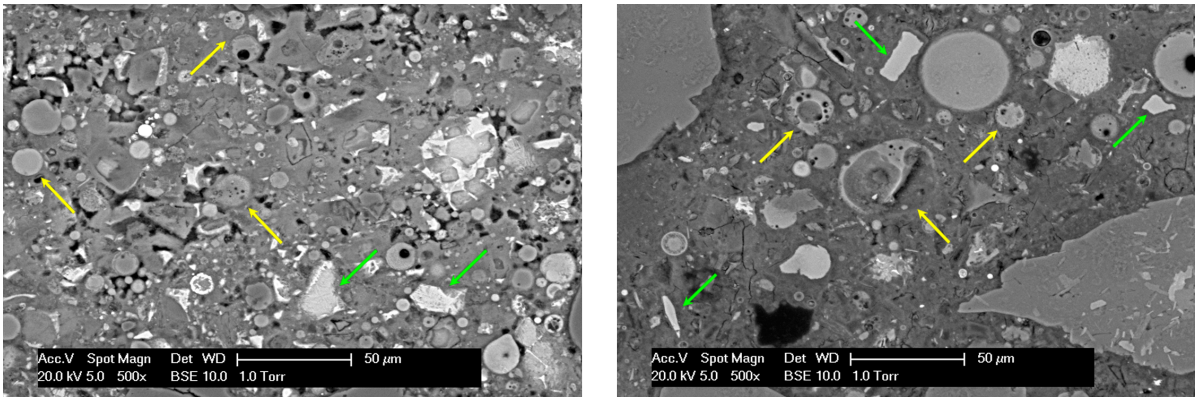


Figure 4.4: 5550-S1 (left) and 5550-S2 (right) BSE images (yellow arrows=fly ash; green arrows=slag)

In Figure 4.1-4.4 BSE images of concrete portions of each specimen are visible. As 1550-S1 and 1550-S2 did not have any fly ash nor slag particles, meaning they were cast with CEM I (Figure 4.1). 2550-S3 was cast with CEM II/B since only fly ash particles were visible (Figure 4.2). In 3550-S1 and 3550-S2 only a significant amount of slag particles was visible, suggesting that they were cast with CEM III/B (Figure 4.3), while 5550-S1 and 5550-S2 showed both slag and fly ash, meaning that they were cast with CEM V/A (Figure 4.4).

On the contrary, the composition of 2550-A was not so clear. It was clear that it was not cast with CEM II nor CEM V because no fly ash was observed, while a few slag particles were visible, suggesting that it was cast with CEM III. However, the amount of slag was not convincing for a CEM III/B, which contains 75% of slag (as visible for other CEM III/B specimens in Figure 4.3). Observations of polished sections were combined with analysis of historical concrete resistivity measurements [8]; in 2010, resistivity of 2550-A was much lower than blended-cement specimens and comparable to CEM I specimens. Therefore, it was concluded that 2550-A was cast with CEM I.

The BSE images (Figure 4.1-4.4) revealed that previous identification [8] was accurate for 7 out of 8 specimens. Only 2550-S2 included CEM I instead of the previously-identified CEM II/B; 2550-S2 was then re-labeled in 1550-S3. The identification of each water/cement ratio was not carried out in this research. Labels of each specimen were then confirmed or updated based on the output given by the cement type identification procedure, according to Table 4.1:

Table 4.1: Specimens selected for nano-scale analysis

| Re-label (2018) | Old label (2010) | Cement type | w/c |
|---|---|---|---|
| **1550-S1** | 1550-A | CEM I | 0.55 |
| **1550-S2** | 1550-B | CEM I | 0.55 |
| **1550-S3** | 2550-A | CEM I | 0.55 |
| **2550-S3** | 2550-C | CEM II | 0.55 |
| **3550-S1** | 3550-B | CEM III | 0.55 |
| **3550-S2** | 3550-D | CEM III | 0.55 |
| **5550-S1** | 5550-F | CEM V | 0.55 |
| **5550-S2** | 5550-D | CEM V | 0.55 |

From this point of the report, samples will be identified according to the above-mentioned re-labeling (Table 4.1).

# 5

# Characterization of reinforced concrete specimens

## 5.1. Intake measurements

In February 2018, resistivity (ρ) and potential (E) measurements of the 8 specimens cast with w/c=0.55 and exposed to NaCl cycles were measured. The measuring procedure followed the one already conducted on those specimens according to Polder et al [12] [78] [81], as previously described (Section 2.2.1). Before measuring, the external parts of the steel bars were cleaned mechanically with sanding paper and driller with sanding head to guarantee good electrical contact. Specimens were left unsheltered outside since 2010, directly exposed to weather precipitations and changes in temperature and humidity. At the time of measuring (in 2018), the daily average outside temperature was 4°C.

The E and ρ measurements measured in 2018 are plotted below (Figure 5.1). For each specimen, the potential was measured of all the 6 bars. A potential mean value was calculated between the 3 bars with same cover depth, 10 mm and 30 mm respectively. The mean potential of the steel with 10 mm of cover depth is plotted against resistivity measurements recorded between stainless steel bars with equal concrete cover, representative for the outer portion of the specimen ("X550-SY(10)", plotted in circles); The mean potential of the steel with 30 mm of cover depth is plotted against resistivity measurements recorded between stainless steel bars with 50 mm of concrete cover, representative of more internal concrete portion ("X550-SY(30)", plotted in triangles).

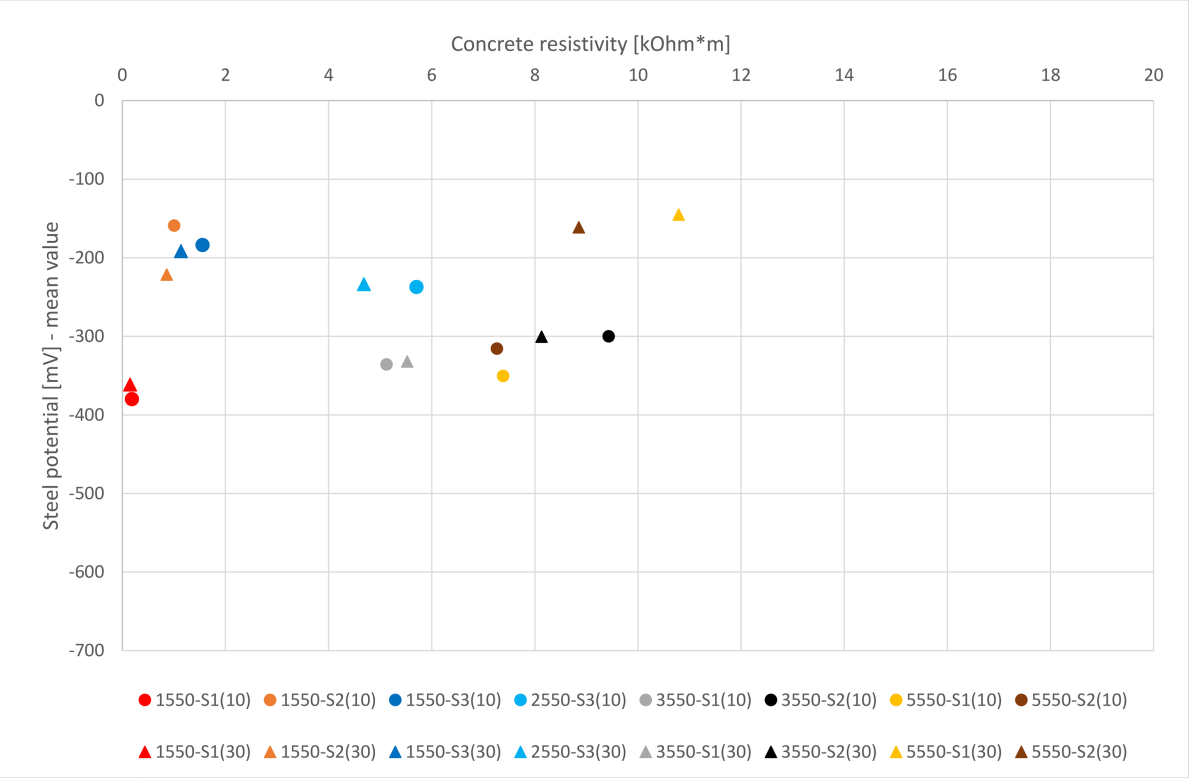


Figure 5.1: Steel potential (mV) against resistivity measurements (kOhm*m) recorded at T=4°C in February 2018

Figure 5.1 shows the potential and resistivity measurements recorded in February 2018. Considering a minimum threshold that suggests on-going corrosion of E equal to -300 mV (versus Ti*), it is visible that only 1550-S1 clearly had on-going corrosion, as it was slightly also for CEM III specimens and the bars at 10mm of cover depth of CEM V specimens. For the other specimens, E measurements were more positive than -250 mV, suggesting no likely on-going corrosion.

The resistivity of CEM I specimens was significantly lower than of blended-cement specimens. Since a relatively high resistivity is related to the high density in the pore structure, these measurements are in line with what was expected. According to Table 5.1, resistivity measurements of most of the specimens were representative for carbonated concrete, except for 1550-S1, of which resistivity was suggesting wet (outside) conditions.

Table 5.1: Electrical resistivity (Ohm*m) of existing structures (>10 years old) and comparable laboratory conditions [81]

| **Environment** | **Ordinary Portland cement** | **Blended cements** |
|---|---|---|
| very wet, submerged [fog room] | 50-200 | 300-1000 |
| Outside, unsheltered | 100-400 | 500-2000 |
| Outside, coated [20°C, 80%RH] | 200-500 | 1000-4000 |
| Carbonated | 1000 and higher | 2000-6000 |
| 20°C, 50%RH [carbonated] | 3000 and higher | 4000-10000 |

Comparing potential and resistivity recorded at different cover depth, it is interesting to notice that only CEM V specimens show differences between bars at 10 mm and 30 mm depth. CEM I, CEM II and CEM III specimens suggest that corrosion and the state of the concrete did not change considerably for the outer and inner portions of the specimens. On the other hand, differences of around 200 mV

in potential and 2-4 kOhm*m in resistivity are recorded for CEM V specimens. These differences are probably caused by the different moisture content of the two portions of the specimens.

According to Pacheco [8], the steel potential measured in April 2010 were much more negative than those recorded in 2018, as visible in Figure 5.2:

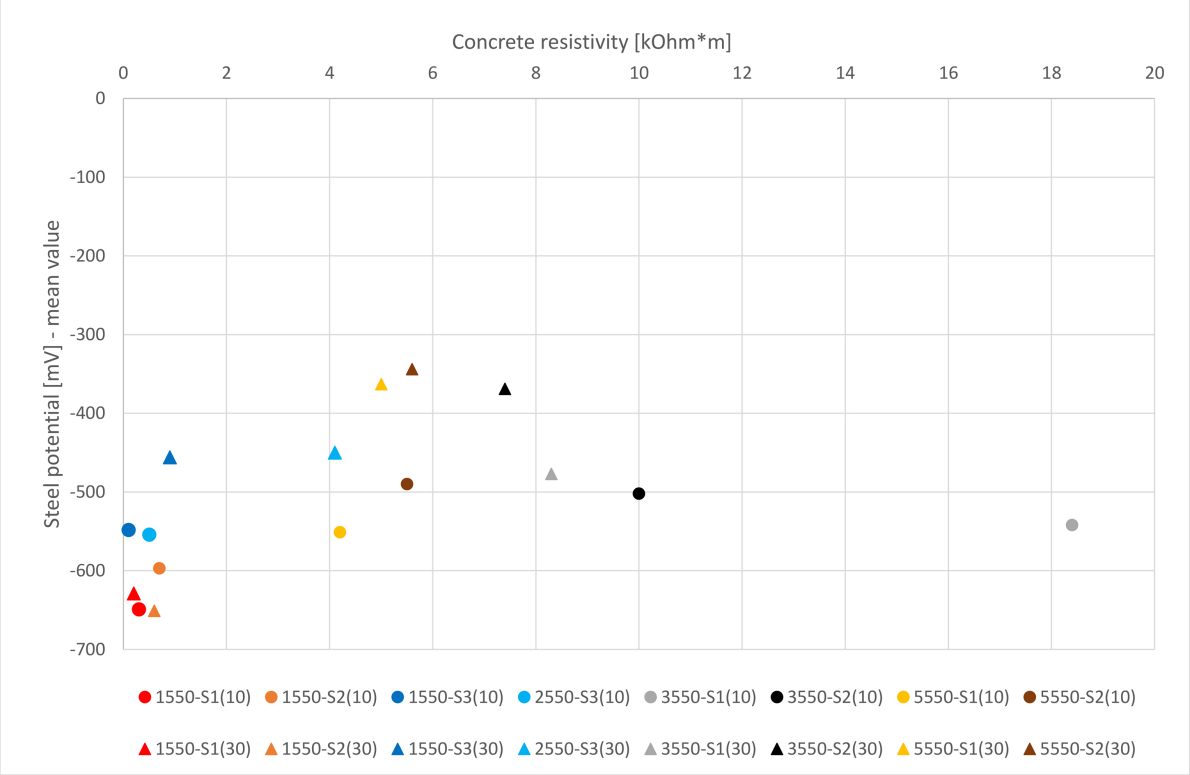


Figure 5.2: Steel potential (mV) against resistivity measurements (kOhm*m) recorded in April 2010

Considering the mean values, in 2010 CEM I specimens had around -600 mV of potential, CEM II and CEM III specimens had -500 mV and CEM V specimens had around -400 mV (see also Appendix B.1). For all the specimens, in 2010 a decrease in potential was measured of around -100 mV in 6 months (from November 2009 to April 2010), suggesting corrosion progress during this period. All these measurements were more negative than the threshold representative for on-going corrosion. It would be likely to think that corrosion would have continued between 2010 and 2018, contrarily to what 2018-measurements might suggest. Environmental conditions that specimens were exposed to might have influenced these measurements. Specimens might have been water-saturated due to the common relatively high precipitations in the Netherlands. However, this is not in line with resistivity measurements where concrete of most of the specimens was found to be relatively dry (but not for 1550-S1 and 1550-S3). The low temperature and dry conditions of the specimens might have played a relevant role at this stage, making the polarization of the steel reinforcement when measuring its potential more difficult and resulting in unlikely values. The influence of low temperature on corrosion-related electro-chemical values was already encountered for previous sessions of intake measurements [8].

Measurements of April 2010 (Figure 5.3) were recorded when the average outside temperature was higher than 10°C. Furthermore, in April 2010 it was also possible to measure the corrosion rate of steel reinforcement by means of Linear Polarization Resistance technique. The combination of steel reinforcement potential and corrosion rate measurements allow for broader and more accurate analysis on the corrosion progress of the specimens (Figure 5.3).

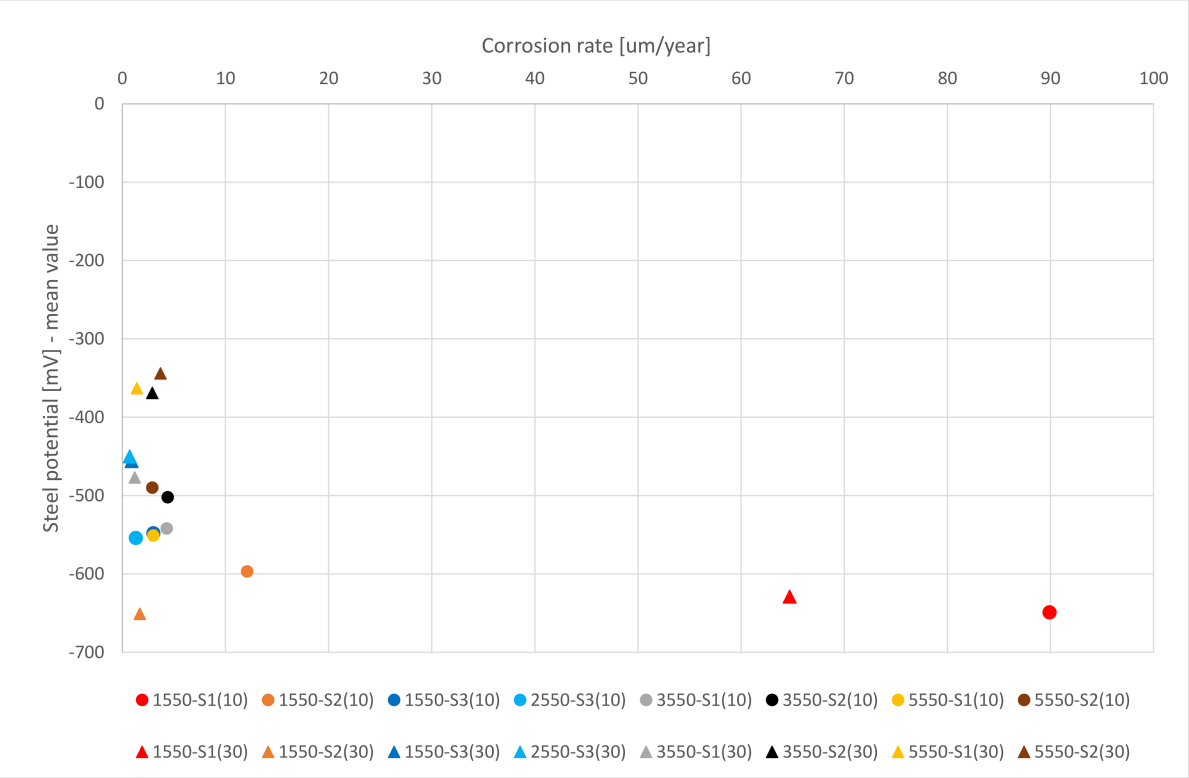


Figure 5.3: Steel potential (mV) against corrosion rate (um/year) recorded in April 2010

No temperature nor relative humidity were relatively extreme as they were in both February 2010 and 2018, avoiding any compromise of measurements. According to COST 509 [16], corrosion rates of reinforcement can be considered as follows (Table 5.2):

Table 5.2: Interpretation of corrosion rates values [16]

| **Corrosion rate** | **Interpretation** |
|---|---|
| <1 $\mu m/year$ | Negligible |
| 1-5 $\mu m/year$ | Low |
| 5-10 $\mu m/year$ | Moderate |
| >10 $\mu m/year$ | High/aggressive |

As suggested by Pacheco [8], in 2010 E and CR measurements were representative of aggressive corrosion for CEM I specimens (especially for 1550-S1) and of moderate low/moderate ongoing corrosion for the other specimens. Also the decrease in potential that was recorded within 6 months (from November 2009 to April 2010, see Appendix B.1) was suggesting that aggressive corrosion increased considerably. These measurements will be compared to the corrosion state of reinforcement investigated in 2018 later in this report (Section 6.4).

## 5.2. Carbonation depth

Carbonation depth was measured for each of the prisms from which cores were drilled. Prisms have been split at the centre of the distance between the stainless steel bars that were used to record resistance measurements (Figure 5.4).

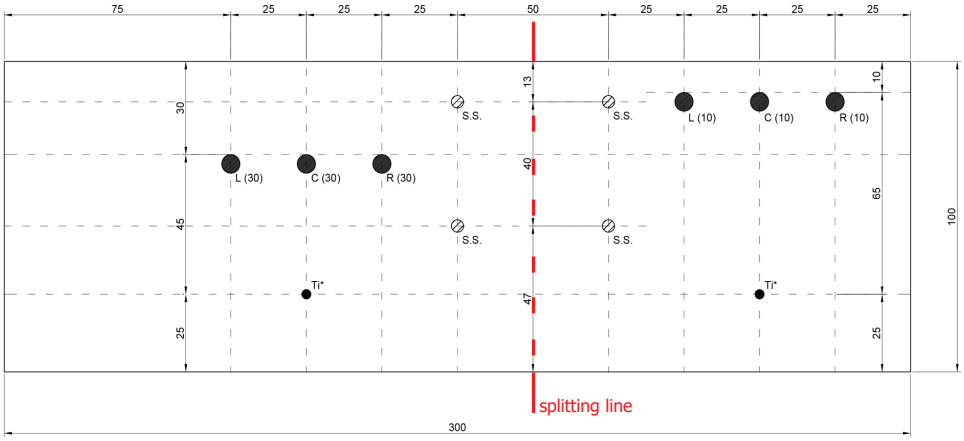


Figure 5.4: Splitting line for carbonation depth measurements (top view of the whole prism)

After splitting, a solution of phenolphthalein was sprayed on the freshly-broken concrete surface and allowed to dry for around 15 minutes. When dried, carbonation depth measurements were taken at the side exposed to the environment (i.e. the one parallel to the reinforcement, meaningful of the concrete cover). Measurements were recorded every 10 mm starting from the top side of the prism for its whole height (around 100 mm). The average carbonation depth of each prism is visible below (Table 5.3), while the carbonation depth profiles are reported in Appendix B.3.

Table 5.3: Average carbonation depth [mm]

| Specimen | Average carbonation depth |
|---|---|
| 1550-S1 | 7 mm |
| 1550-S2 | 3 mm |
| 1550-S3 | 3 mm |
| 2550-S3 | 10 mm |
| 3550-S1 | 18 mm |
| 3550-S2 | 9 mm |
| 5550-S1 | 0 mm |
| 5550-S2 | 4 mm |

Looking at Table 5.3, CEM III specimens are found to be the most deeply carbonated ones, with carbonation that reached the depth at which the reinforcement is located (10 mm). On the other hand, for CEM V specimens almost no carbonation had occurred. CEM I specimens shown slight differences between each other, with average carbonation depths of 7mm, 3mm and 3mm for 1550-S1, 1550-S2 and 1550-S3 respectively, while 2550-S3 was carbonated until 10mm deep. The influence that carbonation depth might have had with regard to the corrosion state of the reinforcement will be evaluated below (Section 6.4).

Because concrete prisms were cast with the same water/cement ratio, subjected to equal curing and exposed to the same environmental conditions for their 20 years of life, differences in carbonation depths might be addressed to the different micro-structures that the use of different cements implies for concrete. The fundamental factor controlling carbonation resistance of concrete is indeed the

diffusivity of the hardened cement paste, which is dependant on the pore structure [86]. Differences for prisms cast with same cement type might be due to different conditions that specimens were exposed to between 6 months and 2,5 years of age (20°C/80%RH, outside or fog room), which were not identifiable according to Pacheco [8]. Specimens exposed to more saturated conditions (i.e. fog room) when early-aged might have a denser micro-structure than those exposed to more dry conditions, hence resulting in lower diffusivity of the specimen pore structure.

The influence of different cement types on the carbonation resistance of concrete has been widely investigated. Bier [85] studied the progress of carbonation in different concrete mixes as function of different cement types used to cast the specimens. He found that carbonation depth is greater when $Ca(OH)_2$ content is lower. This statement is in line with the chemical mechanism of carbonation: blended cement leads to lower quantity of $Ca(OH)_2$ as result of the hydration process and the pozzolanic properties of the binders. The lower quantity of $Ca(OH)_2$ needs lower quantity of $CO_2$ from the outside environment to produce $CaCO_3$ and thus to cause carbonation of concrete. It follows that, with equal water/cement ratios, curing and exposure conditions, blended cements would allow for deeper carbonation of concrete than Ordinary Portland [86]. On the other hand, the micro-structure of blended-cement concretes results to be denser than the one of Ordinary Portland cement concrete: denser micro-structure lowers the diffusivity of the material, which would result in improving its carbonation resistance.

Pacheco [8] measured the carbonation depth of two specimens cast with CEM I and CEM III respectively in 2010. The former specimen had a water/cement ratio equal to 0.45, while the latter one had o,55. Both the specimens were subjected to NaCl wet/dry cycles, as the specimens of this research. He found that carbonation depth for CEM I was equal to 18 mm, while the one of CEM III was equal to 8 mm. These measurements were in contrast to what might be expected from literature [85] [86] and to the carbonation depth measured in 2018, where CEM III had higher carbonation depth than CEM I. This latter statement was expected due to the different microstructure of the two mixes (i.e. the lower content of $Ca(OH)_2$ in CEM III specimens). Also, carbonation depth of 18 mm for CEM III measured in 2018 suggest a carbonation progress during 8 years from the 8 mm of 2010.

Carbonation depth of CEM V specimens was comparable and even lower than the one of CEM I (0 mm and 4 mm for 5550-S1 and 5550-S2 respectively). This finding could be addressed to the microstructure of those concretes, as following. CEM III specimens contain 75% of blast furnace slag [78]. This might have reasonably resulted in relatively low content of $Ca(OH)_2$ after the hydration of cement, allowing for faster carbonation progress within the matrix. On the other hand, CEM V specimens were cast with 50% of slag and fly ash (Section 3.2). This probably led to higher content of $Ca(OH)_2$ than CEM III specimens, but still denser microstructure than CEM I ones, thus improving the carbonation resistance of CEM V concrete. Also the ingress of NaCl solution at an early stage could have caused a further densification of the pore structure, not allowing for carbonation within the concrete matrix (especially for CEM V specimens).

## 5.3. Cores drilling

After intake measurements, one core with 20 mm diameter was drilled out of each specimen (Figure 5.6). The cores were drilled for the whole height of the prism (around 100 mm) and embedding one steel bar as much centred as possible. Only the bars with 10 mm concrete cover have been considered for this research, because it was more likely to find more aggressive pitting corrosion there. Between the three bars with 10 mm concrete cover, only one per prism was drilled. Before drilling, the bottom side of the prism was marked with an arrow, indicating the direction of the outside exposure (N-direction).The selection of the one to drill has been based on visual inspections. Cores have been drilled where more rust was visible at the surface of the prism as well as based on the presence of cracks, as shown in the example below (Figure 5.5).


Figure 5.5: Example of visible cracks (red arrow) and rust (yellow arrow) at the surface of one prism (5550-S1); R, C and L to label the location of each bar.

As visible from Appendix B.2, CEM I and CEM V prisms had visible rust spots at the surface parallel to the steel bars located at 10 mm of cover depth (especially 1550-S3, 5550-S1 and 5550-S2). For 1550-S1 and 5550-S1 a corrosion-related crack was also present parallel to one of the bars. On the other hand, 2550-S3 and CEM III specimens did not have any corrosion spots nor visible cracks at the surface. On the portion of the surface parallel to bars at 30 mm of cover depth, no specimen presented visible corrosion product spots nor surface cracks. Each core drilled out of each specimen is visible below (Figure 5.6).

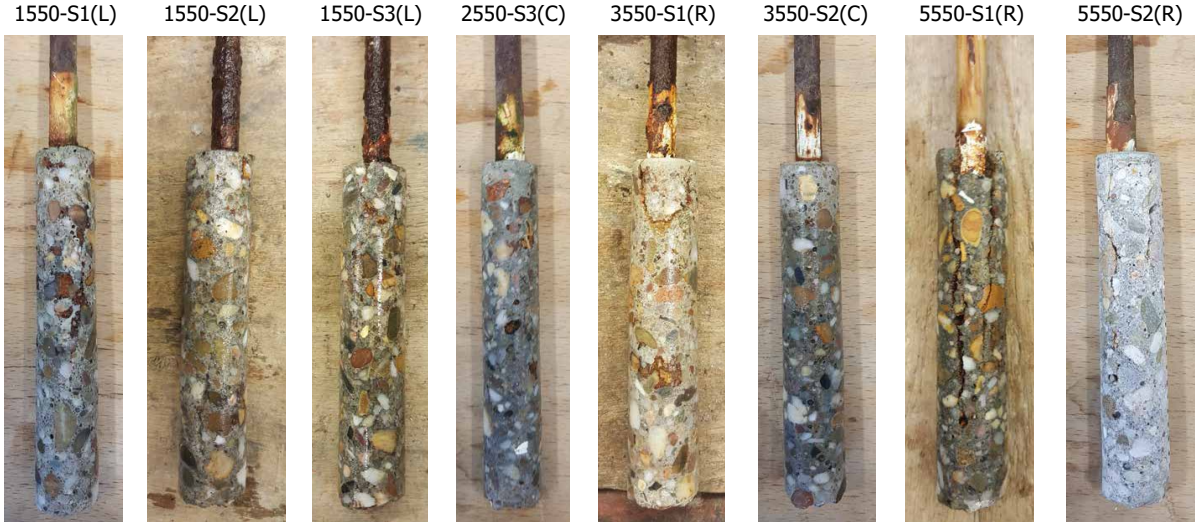


Figure 5.6: Drilled reinforced concrete cores

As visible in Figure 5.6, 1550-S1 and 5550-S1 showed visible signs of aggressive corrosion according to the visual inspections conducted on the whole prisms. In both of the cores, cracks parallel to the

bars are visible, which appear to be filled by corrosion product. Also 5550-S2 had two visible cracks parallel to the steel, but with no visible corrosion product at the surface. On the contrary, 1550-S3 did not have any crack, but surface rust spots are visible, similarly to 2550-S3. This is contrary to what the state of the whole prism surface suggested, as well as for 3550-S1, which was found to be heavily cracked on the top side of the core and with visible corrosion product spots. On the other hand, 1550-S2 and 3550-S2 did not show any sign of internal corrosion if looking at their surface. It looks like that corrosion propagation was constrained in blended-cement specimens (i.e. 2550-S2 and 3550-S1), but that was internally occurring without showing any signs at the surface., while for 1550-S2 and 3550-S2 it looked that no aggressive corrosion occurred.

# 6

# Characterization of reinfocement through X-ray computed tomography

## 6.1. Purpose and equipment

After drilling, cores were left drying for around 72 hours in a room at 20°C and 45% RH. When dried, CT scans were performed. The purposes of using this technique were:

- to observe corrosion pit size and distribution along the length of the steel reinforcement;
- to quantify the volume loss due to corrosion;
- to analyze the influence that orientation of reinforcement and macro-defects at the steel/concrete interface have on the presence and depth of corrosion pits;
- to identify relevant cross sections of the specimens to conduct further analysis (nanoindentation and EDS);

The CT scans were performed using a Phoenix Nanotom, which belongs to the Geo-technology department at Delft University of Technology. The machine consists of a transmission type x-ray tube, a sample stage and a 3072 x 2400 flat panel detector with pixel size of 100 um. The acquisition was performed using at 150 kV of transmission accelerating voltage, with a spatial resolution of 20 um. Each scan was composed of 2303 slices in the height direction (Z-axis) and 2283 slices in width (X-axis) and depth (Y-axis) directions. Each pixel of the performed scans contained 16 bits and displayed a grey scale value corresponding to the detected density. The reconstruction of each specimen was then performed through datos veloCt, the software provided by the equipment manufacturer.

## 6.2. Images acquisition, processing and 3D rendering

The first CT-image was taken at 10 mm from the top side of each specimen. With a spatial resolution of 20 um and 2303 slices along the Z-axis, the height of the specimen that was scanned was equal to around 46 mm. However, the first 50 images as well as the last 50 ones were not processed due to visible noise, which is likely to happen when using computed tomography to scan steel portions. The analyzed images along the Z-axis were then 2200 in total, resulting in a scanned height of 44 mm, which is almost equal to the whole exposed reinforcement length (45 mm). The scanned reinforcement was divided in 44 slices of 1 mm-thick each; 1 mm-thick slices were processed independently from each other, and settings were applied according to the image-processing procedure given by Filho et al. [36].

The image post-processing of each slice was conducted using the freeware Fiji. For each slice, the volume projection was generated using the 3D Project function (Figure 6.1).

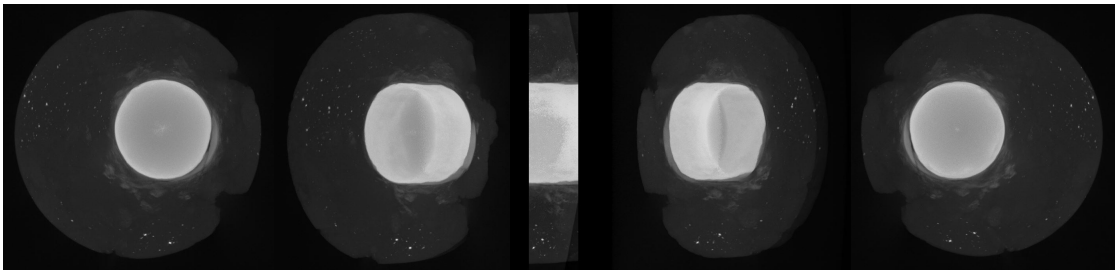


Figure 6.1: Volume projection example of one slice with rotation of 180° (5550-S1, slice 4 mm thick)

Segmentation was performed on each stack of images to highlight the uncorroded steel. The histogram of grey scale values for the whole stack of images was extrapolated and the portion of uncorroded steel was thresholded, analyzing both the progress of grey scale values within the histogram and visual analysis of the images when differently thresholded. This procedure has been repeated for each specimen. The GSV histograms of all the analyzed specimens with related distinguished components are visible in the Appendix C.1.

After thresholding, the volume projection of each slice was computed by the plugin 3D object counter. This tool allows to quantify voxels related to the thresholded component (in this case of uncorroded steel), and convert it into $mm^3$ using pixel and voxels statistics [38]. The volume of each slice can be quantified according to:

$$\eta_{vol} = \eta_{vox} * Z_{vox}$$

where $\eta_{vol}$ is the volume of the highlighted component ($mm^3$), $\eta_{vox}$ is the number of pixels (-) and $Z_{vox}$ represents the voxel volume ($mm^3$). The volume loss due to corrosion was then quantified as the difference between the initial volume of uncorroded steel [78] and the volume of uncorroded steel according to:

$$V_{loss} = \frac{V_0 - \eta_{vol}}{V_0} * 100$$

where $V_0$ is the initial volume of the reinforcement ($mm^3$) and $\eta_{vol}$ is the volume of the reinforcement 20 years after casting ($mm^3$).

3D rendering of the whole scanned-height of the specimens was also performed using the Volume Viewer plugin of the freeware Fiji. This allowed to perform qualitative analysis on the distribution of the pits along the bar as well as their orientation. Due to the relatively large dimensions of the CT-images, the 3D reconstruction has been conducted considering 1 of every 10 images and performing interpolation between them. In this way, the resulting file was much lighter, and 3D visualization of the steel reinforcement was fluent. This reconstruction was used for qualitative analysis only, thus a spatial resolution along the Z-axis of 0.2 mm was considered as suitable. The total amount of images that were processed were 220 per specimen, with a total height of 44 mm.

Volume loss of steel reinforcement is reported below as well as the 3D renders of each bar. A comparison of the total volume losses due to corrosion as well as the corrosion pit distribution along the steel reinforcement is reported (Section 6.3). The side exposed to the concrete cover was identified before drilling each specimen (Section 5.3), indicated as N-direction. The orientation and depth of corrosion pits will be analyzed as well as the relation between corrosion pit occurrence and presence of concrete defects (Section 6.5-6.6).

# 6.3. Volume loss quantification and 3D reconstruction

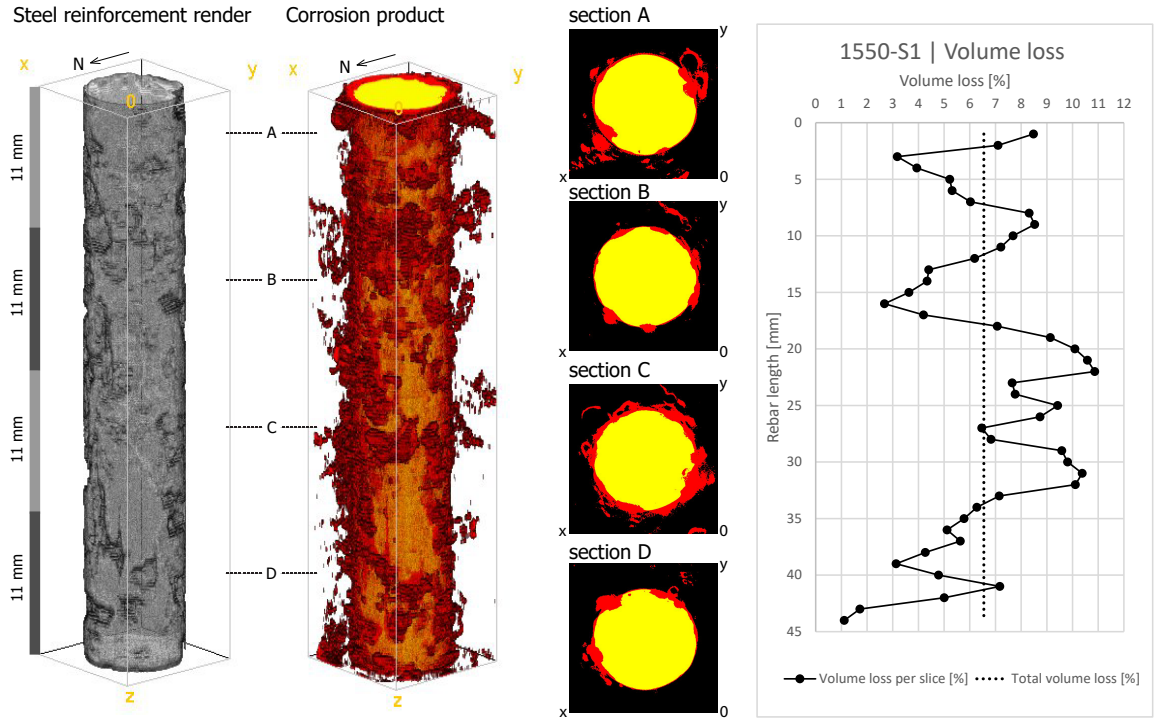


Figure 6.2: 1550-S1: steel reinforcement render (left), render highlighting corrosion product in red (center-left), 2D cross sections (center-right), volume loss per each 1-mm slice along the reinforcement length (right)

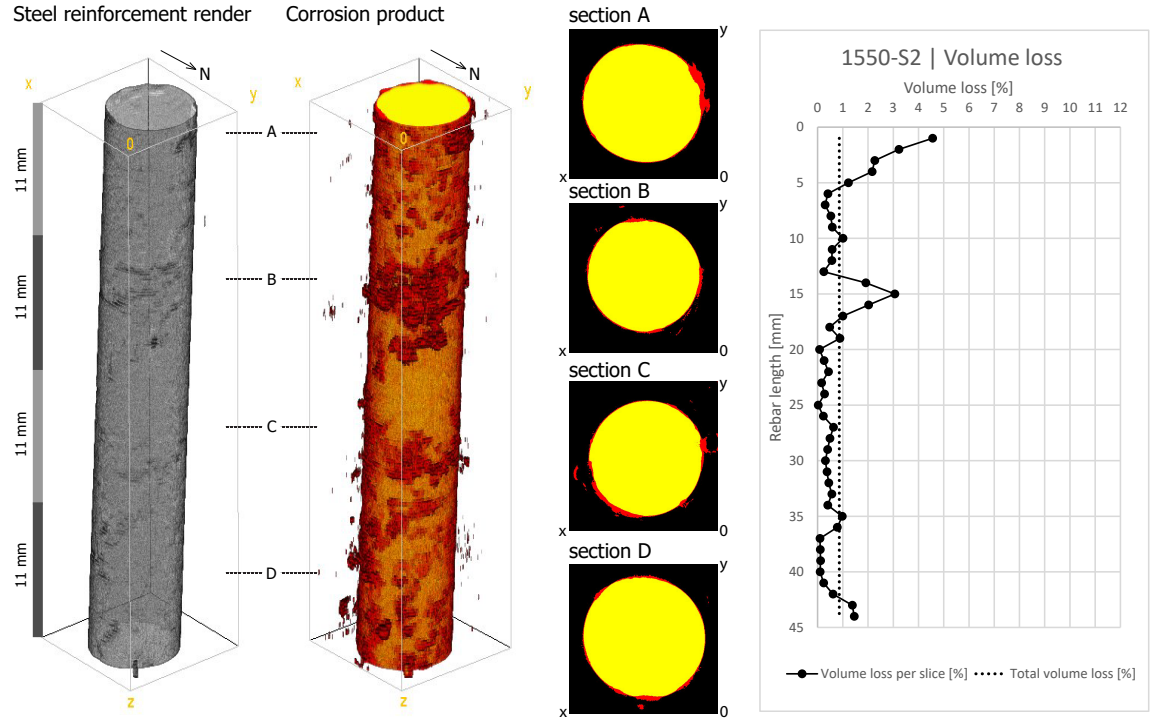


Figure 6.3: 1550-S2: steel reinforcement render (left), render highlighting corrosion product in red (center-left), 2D cross sections (center-right), volume loss per each 1-mm slice along the reinforcement length (right)

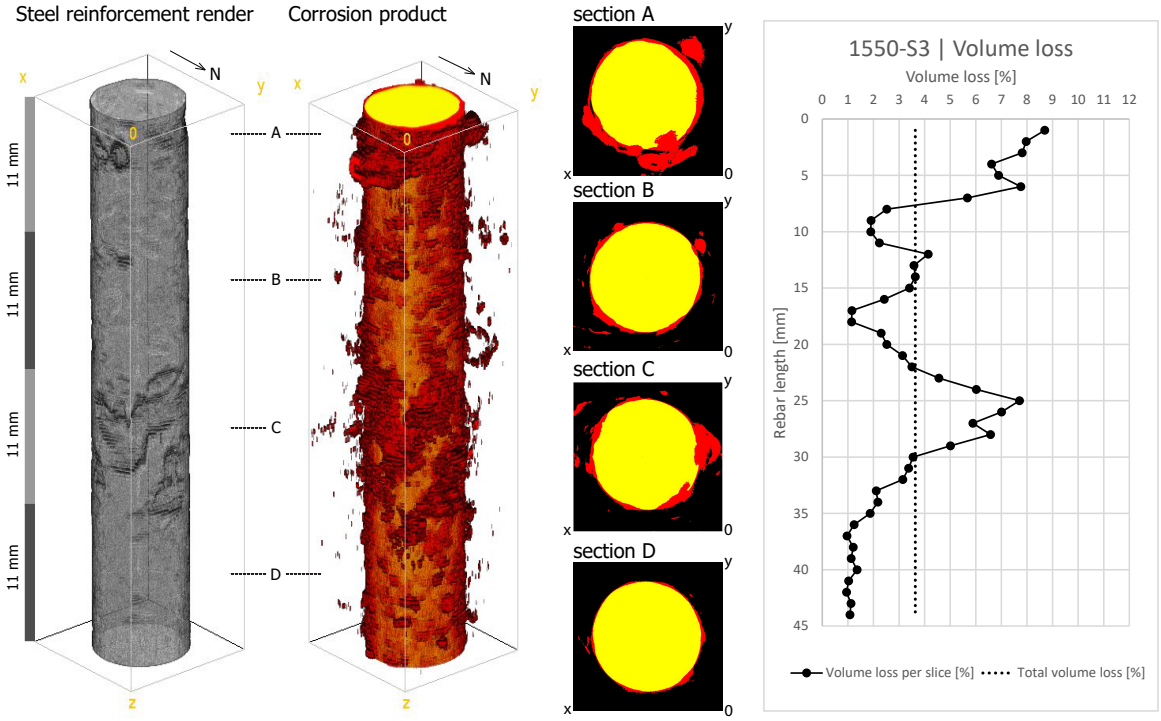


Figure 6.4: 1550-S3: steel reinforcement render (left), render highlighting corrosion product in red (center-left), 2D cross sections (center-right), volume loss per each 1-mm slice along the reinforcement length (right)

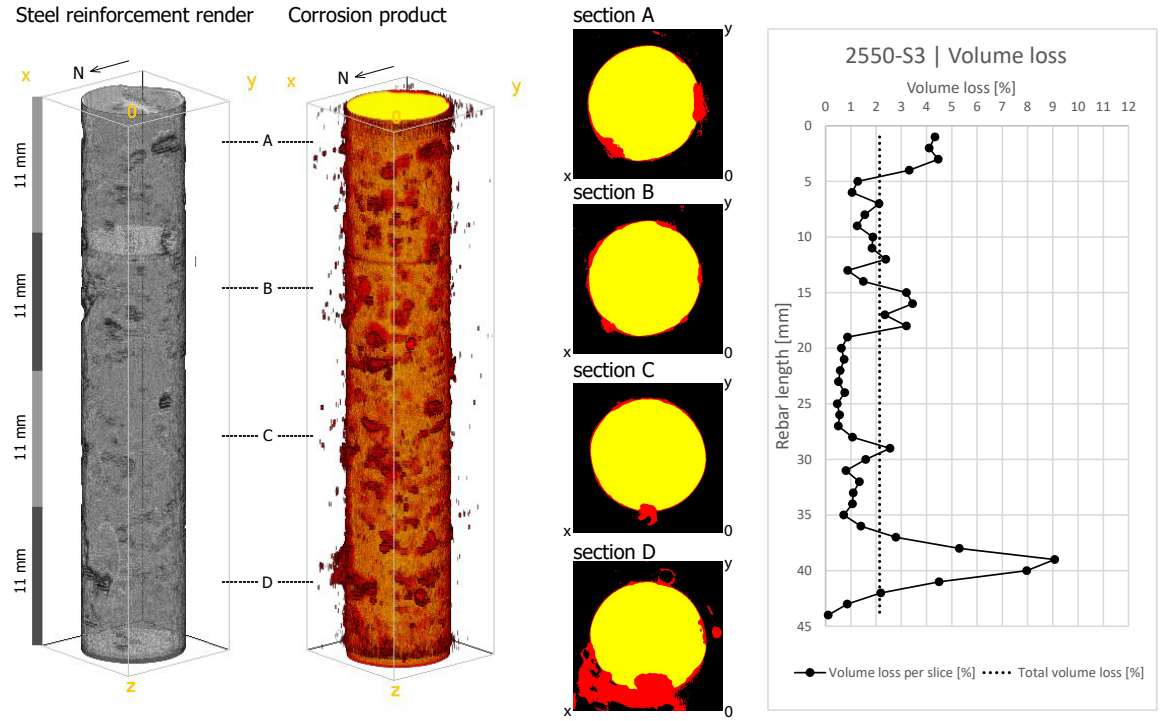


Figure 6.5: 2550-S3: steel reinforcement render (left), render highlighting corrosion product in red (center-left), 2D cross sections (center-right), volume loss per each 1-mm slice along the reinforcement length (right)

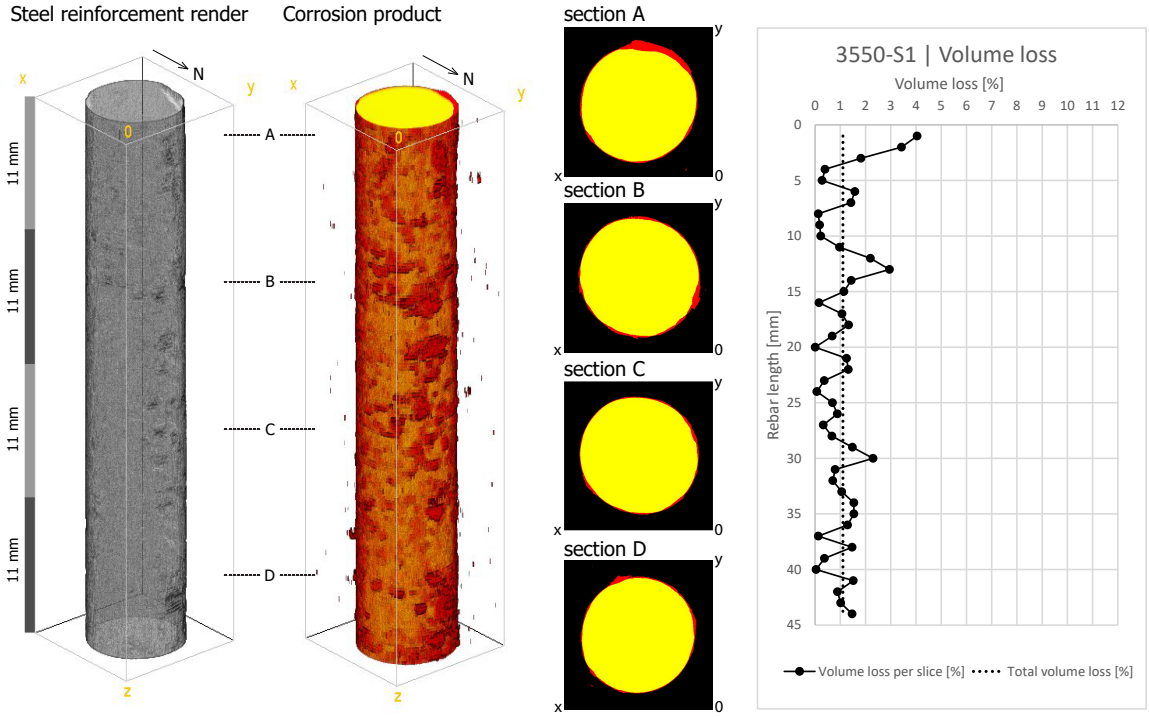


Figure 6.6: 3550-S1: steel reinforcement render (left), render highlighting corrosion product in red (center-left), 2D cross sections (center-right), volume loss per each 1-mm slice along the reinforcement length (right)

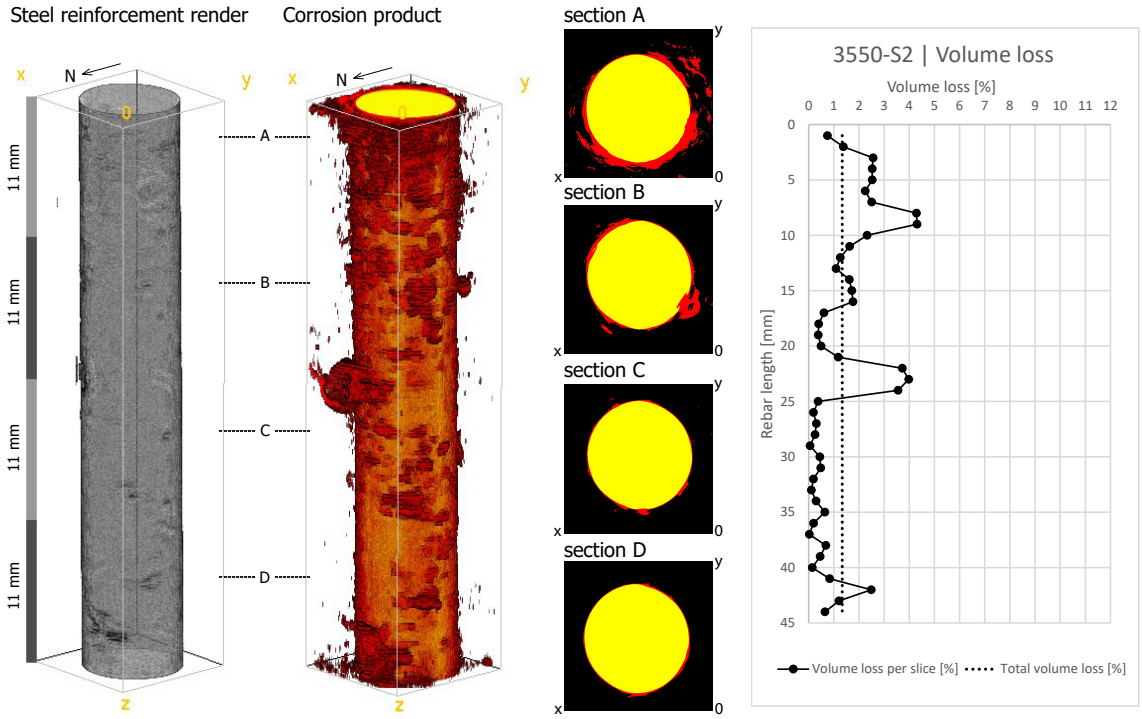


Figure 6.7: 3550-S2: steel reinforcement render (left), render highlighting corrosion product in red (center-left), 2D cross sections (center-right), volume loss per each 1-mm slice along the reinforcement length (right)

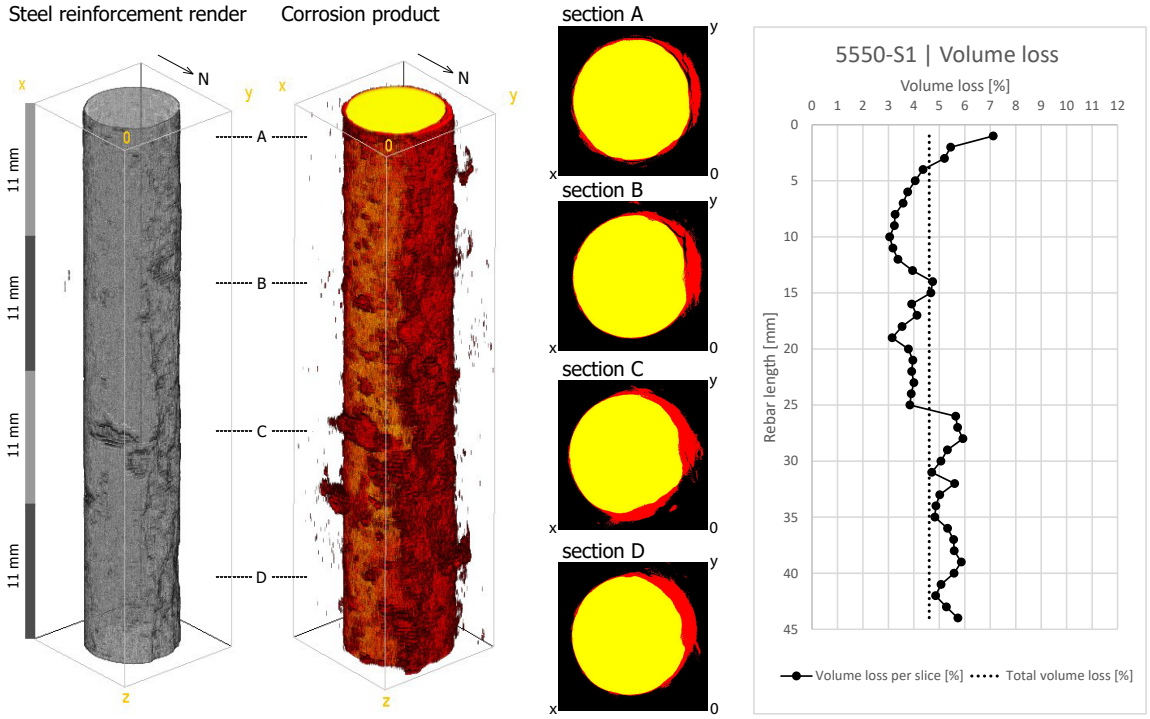


Figure 6.8: 5550-S1: steel reinforcement render (left), render highlighting corrosion product in red (center-left), 2D cross sections (center-right), volume loss per each 1-mm slice along the reinforcement length (right)

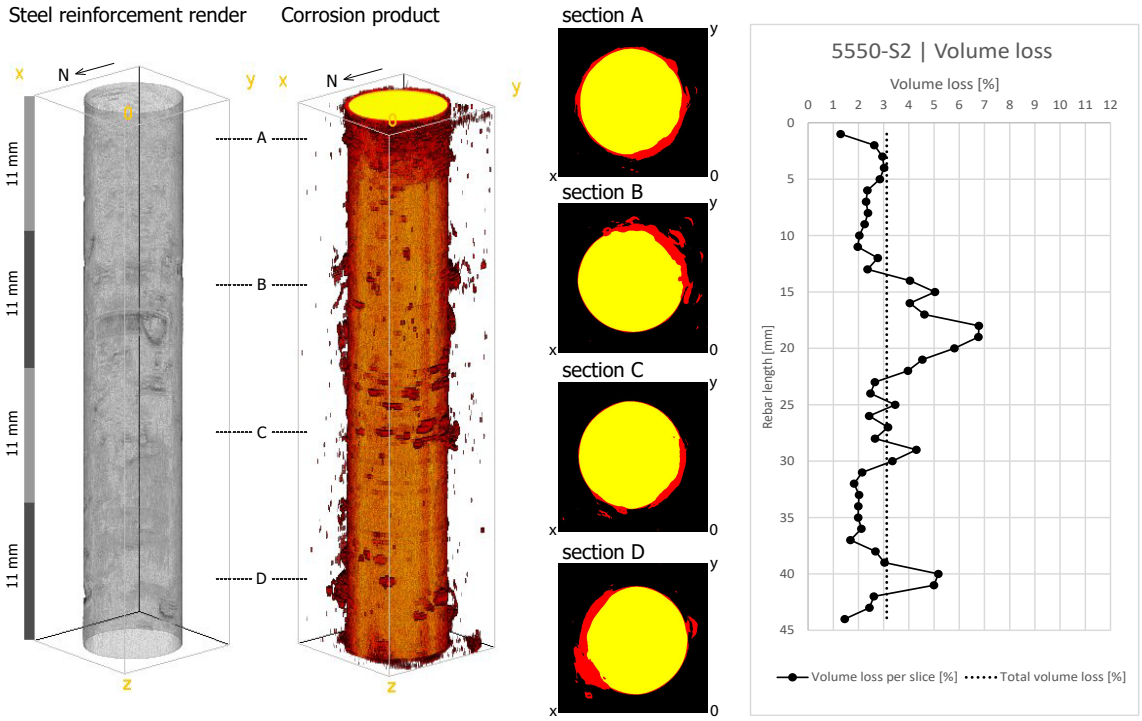


Figure 6.9: 5550-S2: steel reinforcement render (left), render highlighting corrosion product in red (center-left), 2D cross sections (center-right), volume loss per each 1-mm slice along the reinforcement length (right)

The progress the volume loss along the length of the reinforcement can be analyzed for each specimen looking at the above-reported figures (Figure 6.2 - Figure 6.9). 1550-S1 shows high volume loss due to corrosion along the whole length of the bar, with a relatively low level of volume loss (of around 1-1.5%) for only a few slices at the bottom of the bar. The presence of deep pits corresponds to the slices where steep volume loss occurs, getting to a maximum of around 11% (Figure 6.2). On the other hand, 1550-S2 shows a low level of corrosion along the whole length of the rebar (around 1%), with exceptions for only a few slices where the maximum volume loss reaches around 5% (at the top of the bar) and around 3% (at 15mm of length) (Figure 6.3).

1550-S3 and 2550-S3 show a comparable volume loss distribution along the bar length despite differences between the two total volume losses, which equal to around 3.5% and 2% respectively. Both specimens are subjected to localized relatively deep pits that cause a steep increase in the volume loss for some slices, causing a maximum localized volume loss of around 9% for both (Figure 6.4 - Figure 6.5).

3550-S1 and 3550-S2 show a similar corrosion pattern along the rebar length. For both, the total volume loss is relatively low, around 1%. Almost no corrosion for most of the length of the rebars is visible (most of the slices register volume losses lower than 1%), except for a few localized relevant pits, leading to a highest volume loss of around 4%, especially for 3550-S2 (Figure 6.6 - Figure 6.7).

5550-S1 and 5550-S2 show a different progress of corrosion along their length, both for the distribution of the corrosion pits and for the total volume loss. The former specimen lost around 4.5% of steel in total, while the latter one lost around 3%. 5550-S1 shows a relatively uniform volume loss along the whole length of the reinforcement, with lowest and highest peaks of around 3% and 7% respectively. It must be said that 5550-S1 was heavily cracked at the side exposed to the outside over the whole length of the reinforcement (N-direction). This could have led to higher ingress of aggressive components to this side, causing a more oriented corrosion distribution along the length of the reinforcement and a change of mechanism from pitting to more general corrosion (Figure 6.8). On the other hand, 5550-S2 was not heavily cracked, and the progress of volume loss (and thus of pits) along the bar is more like other specimens, with lower volume losses for most of the length (of around 2%) alternated by localized deep pits, leading to a maximum volume loss of around 7% for some slices (Figure 6.9).

For most of the specimens, it is noticeable that a significant volume loss occurs at the top of each bar (apart from 3550-S2 and 5550-S2). As it was mentioned previously, the top and the bottom of each steel reinforcement were covered with a protecting coating for 10 mm, to avoid side-effects due to the vicinity to the outside conditions (Section 3.2). The presence of this coating might have caused a localized accumulation of chlorides at the interface steel-coating, resulting in a relatively higher volume loss due to corrosion for most of the specimens at this location.

Further than the volume loss distribution along the length of the reinforcement, the total volume loss was also determined for each specimen (dotted line in Figure 6.2 - Figure 6.9), as reported below (Table 6.1).

Table 6.1: Average volume loss for 44mm-long reinforcement samples

| Specimen | Volume loss [%] |
|---|---|
| 1550-S1 | 6.55 |
| 1550-S2 | 0.86 |
| 1550-S3 | 3.64 |
| 2550-S3 | 2.14 |
| 3550-S1 | 1.10 |
| 3550-S2 | 1.33 |
| 5550-S1 | 4.60 |
| 5550-S2 | 3.12 |

Looking at Table 6.1, it is visible that steel reinforcement embedded in different concrete mixes was affected differently by corrosion. This statement sounds reasonable if thinking that the concrete micro-structure, which has a relevant impact on corrosion resistance of reinforced concrete, is mainly dependent on the used cement type. Both CEM III specimens show a very similar low level of volume loss due to corrosion, around 1%. Comparable volume loss is also found for 2550-S3, likely for the same reason already mentioned about CEM III specimens. Interesting point is that CEM III specimens and 2550-S3 were the most carbonated prisms, as described in more detail later in this report (Section 6.4). CEM V specimens show a difference of around 1% between them: for these specimens, the volume loss due to corrosion was found to be larger than the one of CEM III, up to around 4,5% for 5550-S1. Interesting results were found in CEM I specimens: on the one hand, 1550-S1 shown the highest volume loss of steel, up to around 6.5%. On the other hand, 1550-S2 shown the lowest level of corrosion, below 1%. These differences are significant if considering that specimens should have been cast with the same concrete mix (i.e. cement type and water/cement ratio) and then exposed to the same environmental conditions). Differences between these two specimens are not clarified by the volume loss of 1550-S3, which equals to around 3.5%.

It must be said that, as previously mentioned in Section 3.2, in 2010 specimens were found to be mislabeled, and a re-labeling procedure was conducted based on Non-Destructive testing, visual inspections and statistical analysis [8]. The degree of confidence of the identification procedure was equal to 95% for the specimens selected for this research. However, the data for CEM I specimens might suggest that the identification procedure was not accurate for one of them, or that these differences are governed by other factors that were not identified. Relevant differences were also found between these two prisms already in 2010 [8] when electro-chemical and carbonation depth measurements were taken (Section 5.1 - Section 5.2). It might be the case that the identification for 1550-S2 was not accurate, so that this prism could have been cast with different (lower) water/cement ratio than what is reported by the identification procedure conducted in 2010, resulting in higher corrosion (and carbonation) resistance of the concrete mix, in line with what the volume loss quantification suggests. As suggested by Pacheco [8], microscopy analysis could give insights about the composition of each specimen and thus clarify these differences. However, no water/cement ratio identification was carried out in this research.

## 6.4. Relation between intake measurements, carbonation depth and steel volume loss

Measurements related to the characterization of the whole reinforced concrete prisms (i.e. carbonation depth and intake measurements, Section 5.1 - Section 5.2) were analyzed with regard to the actual corrosion state of the steel reinforcement. The relation between the total steel reinforcement loss and carbonation depth is reported below (Figure 6.10):

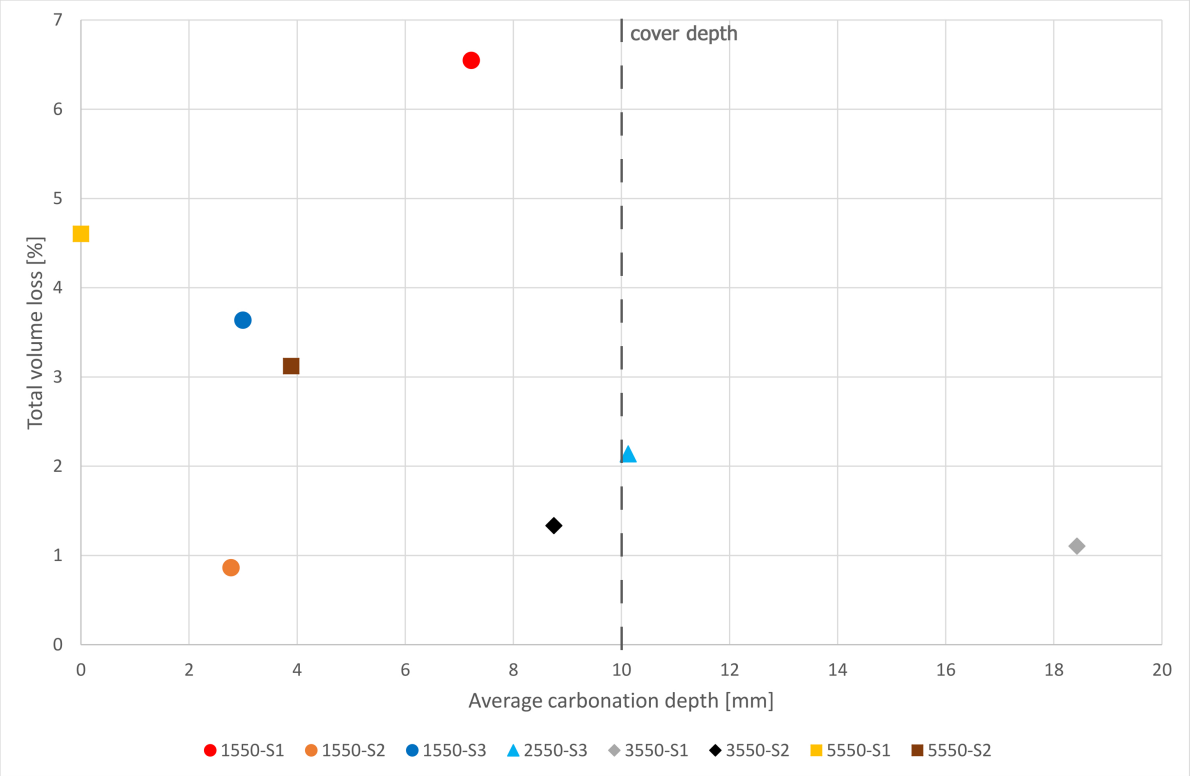


Figure 6.10: Relation between average carbonation depth [mm] and total volume loss of steel reinforcement [%]

From Figure 6.10 the relation between carbonation depth of concrete and the volume loss of steel reinforcement is visible. Two different phenomena are visible. On the one hand, steel reinforcement subjected to the highest level of corrosion (1550-S1, 1550-S3 and CEM V bars) were not reached by the carbonation of concrete. On the other hand, the most carbonated specimens were subjected to much lower volume loss due to corrosion (2550-S3 and CEM III bars). 1550-S2 shows exceptional behavior, with both low volume loss (1%) and carbonation depth (less than 3 mm). Carbonation of concrete involves the formation of $CaCO3$ according to:

$$CO_2 + Ca(OH)_2 \xrightarrow{H_2O} CaCO_3 + H_2O$$

For the specimens where carbonation reached and then overpassed the reinforcement (located at 10 mm of depth), carbonation could have also caused a "pushing" effect to the chlorides inside the concrete matrix. This migration of chlorides could have to some extent reduced the aggressivity of the concrete environment surrounding the reinforcement, thus preventing aggressive corrosion to initiate. This "pushing" effect of carbonation was already found by Pacheco [8], who also measured the chloride profiles of some specimens. For a destructively-analyzed CEM III specimen, he observed that the chloride content along the prism length was mostly lower than the chloride threshold level for corrosion initiation [3] [4] [5]), while for CEM I specimen the chloride content was mostly higher than the critical

threshold, reaching 0.8% at maximum. These values suggested that the resistance to chloride diffusion of CEM I concrete was lower than the one of CEM III concrete [8] [86]. Despite here no chloride profiles were measured, carbonation depth and related volume loss of steel reinforcement suggests the same phenomena, resulting in more aggressive corrosion state for reinforcement embedded in CEM I rather than CEM III.

It should be pointed out that the environmental conditions to which specimens were exposed between ages of 6 months and 2,5 years could not be identified. These included: fog room, 20°C and 80% RH or outside unsheltered conditions for around 2 years. Saturation of concrete due to wet environments (i.e. fog room) could have increased the carbonation resistance of prisms at an early age, thus reducing the eventual carbonation progress. This speculation might explain the relatively varying carbonation depth for specimens cast with the same mix (especially CEM I, CEM II and CEM III), which differed by more than 5 mm.

The relation between intake measurements and volume loss of steel reinforcement was also analyzed. In Table 6.2 and Figure 6.11, potential and corrosion rate of steel measured in April 2010 [8] are reported as well as the volume loss of each bar. The decision to consider these values instead of those recorded in 2018 was already discussed previously, as 2010-measurements allow for more accurate analysis and the corrosion state might have been less influenced by environmental conditions (Section 5.1).

Table 6.2: Steel potential, corrosion rate (2010) [8] and volume loss (2018)

| Specimen | E [mV] (mean value) | CR [um/year] | Volume loss [%] |
|---|---|---|---|
| 1550-S1 | -649 | 89.9 | 6.55 |
| 1550-S2 | -597 | 12.1 | 0.86 |
| 1550-S3 | -548 | 3.0 | 3.64 |
| 2550-S3 | -554 | 1.3 | 2.14 |
| 3550-S1 | -542 | 4.3 | 1.10 |
| 3550-S2 | -502 | 4.4 | 1.33 |
| 5550-S1 | -551 | 3.0 | 4.60 |
| 5550-S2 | -490 | 2.9 | 3.12 |

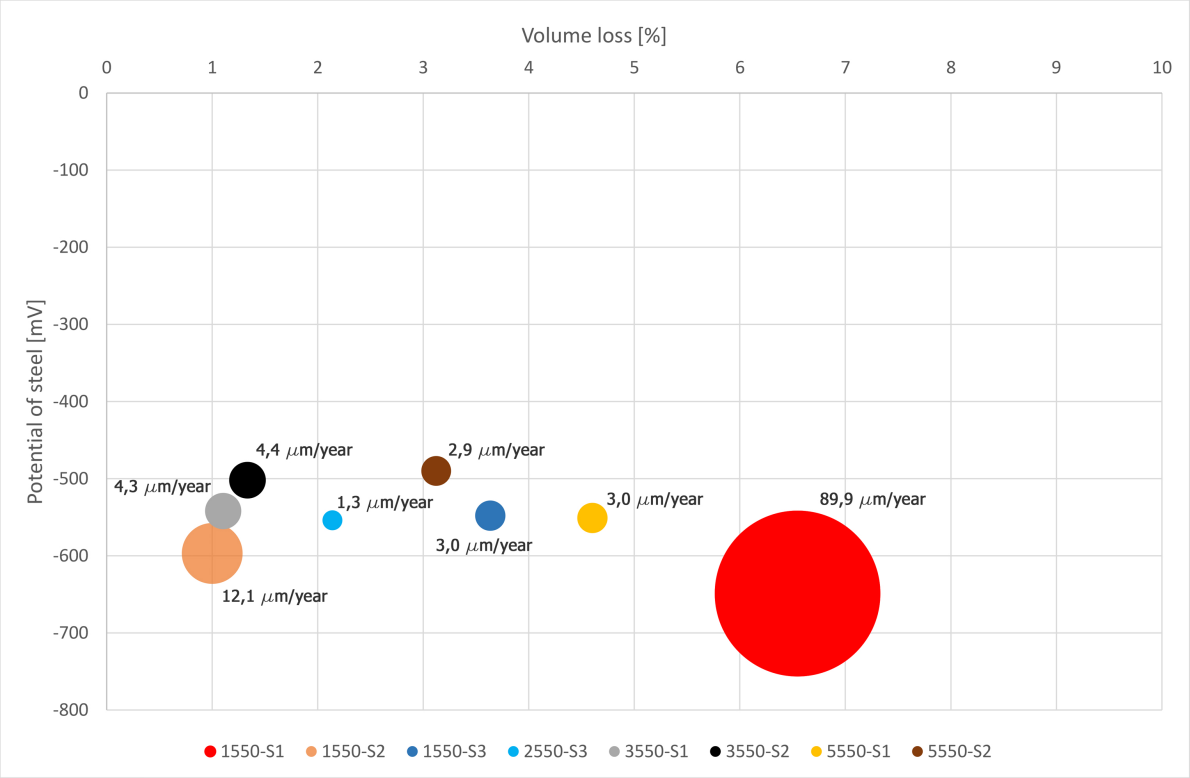


Figure 6.11: Relation corrosion rate [um/year], potential of reinforcement [mV] and total volume loss [%]

Looking at Figure 6.11 it is visible that steel potential is more negative than the characteristic threshold of on-going corrosion (-300 mV against Ti*) for all the specimens. Corrosion rate for CEM I specimens was suggesting aggressive corrosion, especially for 1550-S1. These measurements are in agreement with the corrosion state of 1550-S1, which had a volume loss equal to around 7% (the highest). On the other hand, 1550-S2 had the minimum volume loss (around 1%), suggesting low corrosion. This is in contrast to what intake measurements were suggesting. Comparable disagreement between intake measurements was found for CEM III specimens: while their potential (below -300 mV) and corrosion rate (around 4.5 um/year) were suggesting at least moderate corrosion deterioration, the volume loss was around 1% for both. For the other specimens, intake measurements of April 2010 were found to be in line with the actual state of the reinforcement.

Corrosion-related electro-chemical measurements might be heavily influenced by temperature and humidity of both the environment and the specimen, especially in relatively extreme conditions. This was the case for February 2010 and 2018, but apparently not for measurements taken in April 2010, which were indeed in line with the actual corrosion state of the reinforcement for most of the specimens. Differences found for 1550-S2 and CEM III specimens might be addressed to the principle of the measurements themselves: isolated measurements describe the state of the steel at a specific point in time, without giving further information about the accumulated volume loss. This means that E and CR might be valid for the state of the specimen in April 2010 (so they were apparently corroding intensively), but corrosion before and after these measurements cannot be evaluated. Corrosion might have become less intense or even stopped over a relatively short time due to changes in environmental conditions or saturation of specimens, for instance. For these reasons, point-in-time intake measurements should be always considered with caution, especially if isolated during a relatively long period of time.

## 6.5. Depth and orientation of corrosion pits

The quantification of total volume loss of steel reinforcement (Section 6.3) was measured for each mm of bar length without giving insight into the orientation of the corrosion pits. To quantitatively study the influence that the exposure side of the reinforcement had on the development of the degradation, the depth of corrosion pits has been evaluated according to Sun et al. [39]. For each specimen, a selection of 2D CT-images were evaluated for corrosion pit depths and orientation. This selection included CT-images taken at each (around) 5 mm of length of reinforcement. Pit depths were clock-wise measured at different angles from the centre of the bar around 360° with 30° interval. The depth of the pits, $d$, is calculated by:

$$d = R_0 - R$$

where $R_0$ represents the initial radius of steel bar before corrosion and $R$ is the radius of the steel bar that did not corrode. The range between 180° and 0° indicates the direction of the concrete cover (N-direction), as visible below (Figure 6.12):

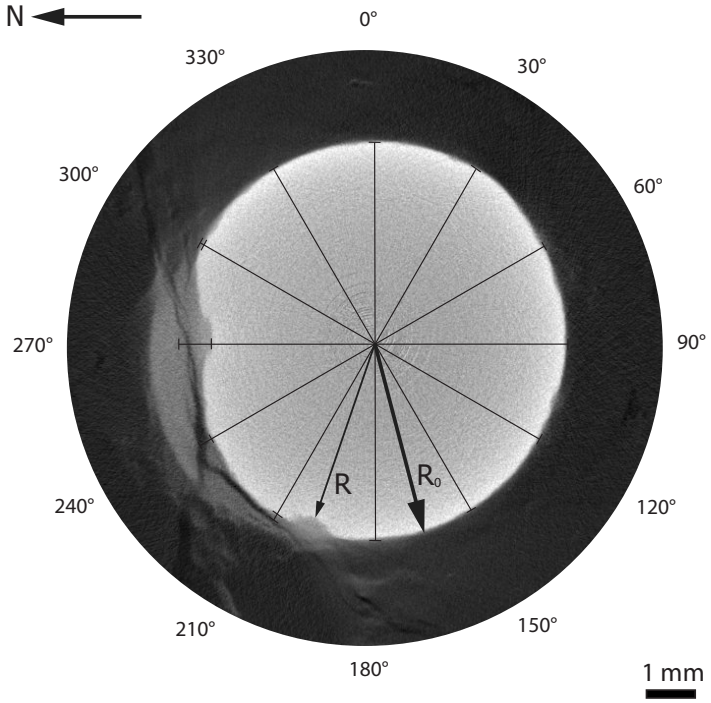


Figure 6.12: Depth and orientation of corrosion pits (from 5550-S1(R))

CT-images that were subjected to 2D processing as previously described for corrosion pit depths and orientation are visible in Appendix C.2, while pit depths at each orientation angle for all the processed 2D-images are reported below (Figure 6.13):

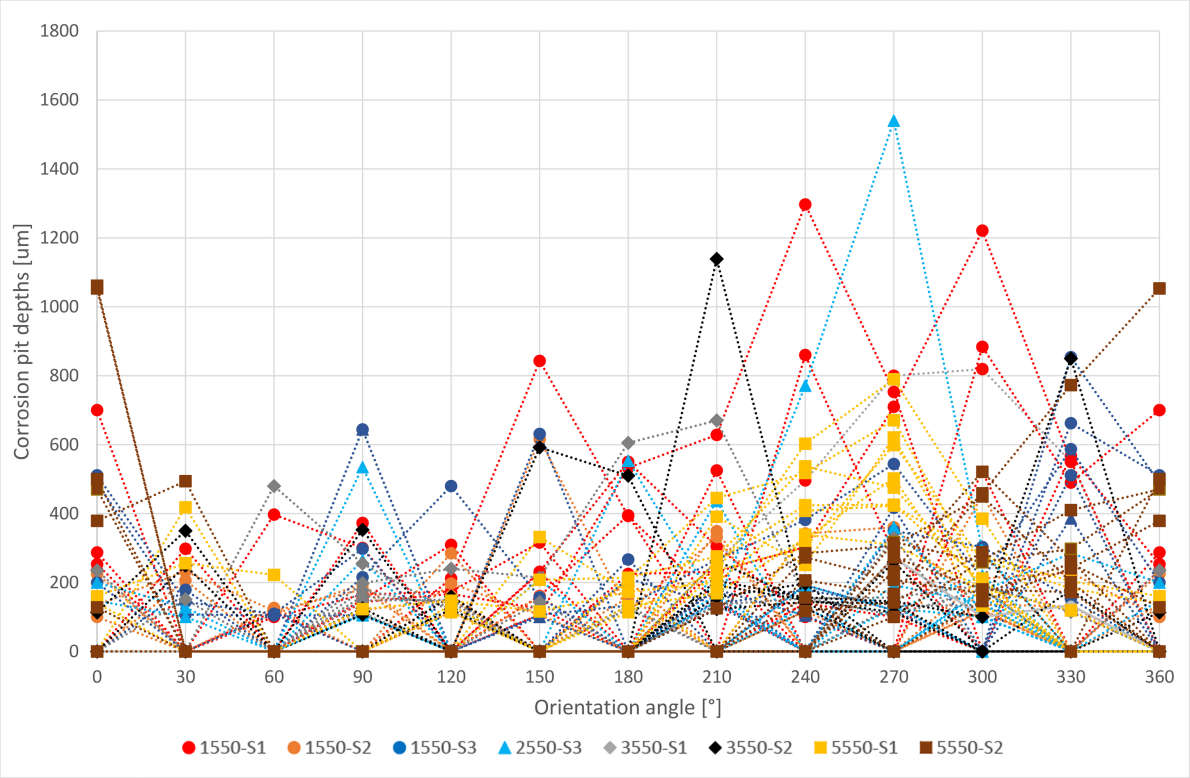


Figure 6.13: Pit depths and orientation

Figure 6.13 suggests that corrosion pits tend to get deeper at the reinforcement side exposed to the outer environment (N-direction). This statement might sound reasonable since the outer side might be subjected to higher ingress of harmful agents, such as moisture, due to the lower cover they have to travel to reach the steel. This would result in more frequent wetting and drying of the electrolyte at the out-exposed side of the reinforcement (N-direction), with likely more aggressive environment than the inside of the concrete. The influence of orientation is clearly visible for most of the specimens: N-oriented pits get to a maximum depth of 1,6 mm (for 2550-S3), with several pits between 0,8 and 1 mm deep. 5550-S1 was significantly cracked on the side exposed to outer environment, and this probably caused a marked difference between pit depths at the two sides on the reinforcement. On the other hand, it is also visible that significantly deep pits are found also at the internal side of the bars, as it is visible for 1550-S1, 2550-S3 and 3550-S1 (up to around 800 $\mu m$): these relatively deep pits at the S-oriented side generally correspond to where visible defects at the steel/concrete interface are present, as reported later: it will be shown that corrosion pits seem to be more influenced by the presence of concrete macro-defects at the steel/concrete interface, than by the orientation of the reinforcement (Section 6.6). Pit depth measurements divided per each CEM-type specimens are also visible in the Appendix C.2.

The influence of orientation for corrosion initiation of steel reinforcement has been widely studied in the literature [17]-[30]. As previously mentioned (Section 2.3), in some cases it was observed that the most corroded side of the reinforcement was the one less close to the outside conditions, thus the bottom side of the bars. This fact was caused by the casting direction and the consequent defects that were present at this side. It was concluded that more aggressive corrosion did not occur at the locations with likely highest chloride concentration and with highest ingress of electrolyte (such as the one exposed to the outside environment), but that it was more dependent on the defects present at the steel/concrete interface, hence that the orientation of the reinforcement is a secondary factor for corrosion propagation [17]. For this reason, in Section 6.6 the relation between pit depths, orientation and presence of defects (i.e. air voids) at the steel/concrete interface has been studied al the same time.

## 6.6. Influence of concrete defects on pit growth and depth

In the current literature only a few studies focused on the relation between concrete defects and presence of corrosion pits by means of X-ray computed tomography [11] [38] [39]. Savija et al. [11] accelerated corrosion of steel reinforcement embedded in cement mortar. In this paper, it is visible that corrosion was developing non-uniformly around the steel bar. The non-uniformity of rust layer was addressed to the penetration of corrosion product into open spaces, especially noticeable in presence of air voids close to the steel reinforcement or of large cracks.

In both the researches conducted by Dong et al. [38] and Sun et al. [39], it was observed that rust was penetrating into cracks when accelerating corrosion for reinforced mortar specimens. Specimens used by Sun et al. [39] were submerged into a 3.5% NaCl solution and a cathode for corrosion acceleration was located at one side of the specimen, to investigate the role that its position might have had on the pit distribution and growth. They observed that the distribution of corrosion products was not significantly related to the position of the cathode but more to the distribution of cracks. They concluded that penetrating cracks can provide a path connecting the steel reinforcement to the external environment, accelerating the transport of harmful ions to the bars and so promoting local corrosion of the steel. This last statement is in line with what was observed in this research also (Section 6.5), where more and deeper corrosion pits were found to be oriented to the outside conditions and in presence of defects at the steel/concrete interface (especially for 5550-S1).

Also in this research the influence of concrete defects on corrosion pit presence and growth was observed. Relation between macro air voids at the steel/concrete interface and corrosion pits was studied analyzing 2D CT-images, a selection of which are reported below (Figure 6.14 - Figure 6.21).

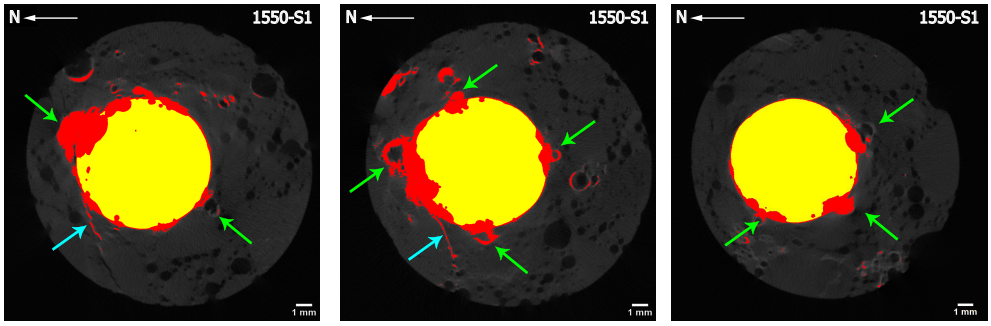


Figure 6.14: 1550-S1: Corrosion product (red) expanding into air voids (green arrow) and cracks (light-blue arrow)

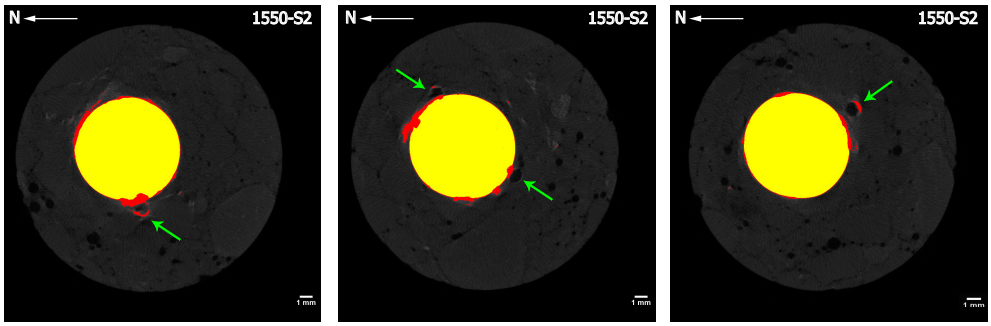


Figure 6.15: 1550-S2: Corrosion product (red) penetrating into air voids (green arrow) and cracks (light-blue arrow)

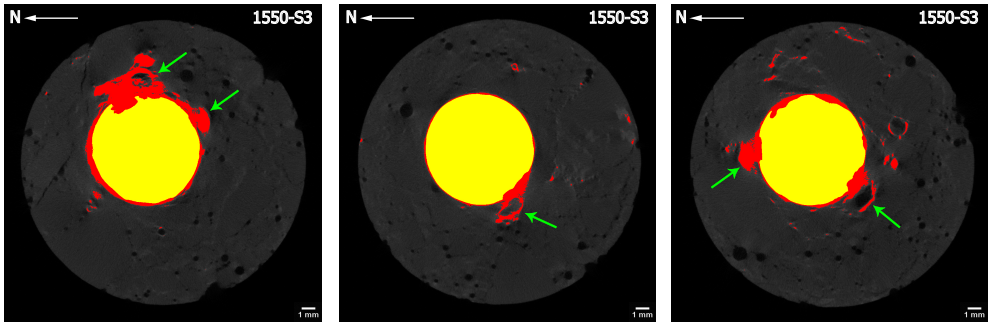


Figure 6.16: 1550-S3: Corrosion product (red) expanding into air voids (green arrow) and cracks (light-blue arrow)

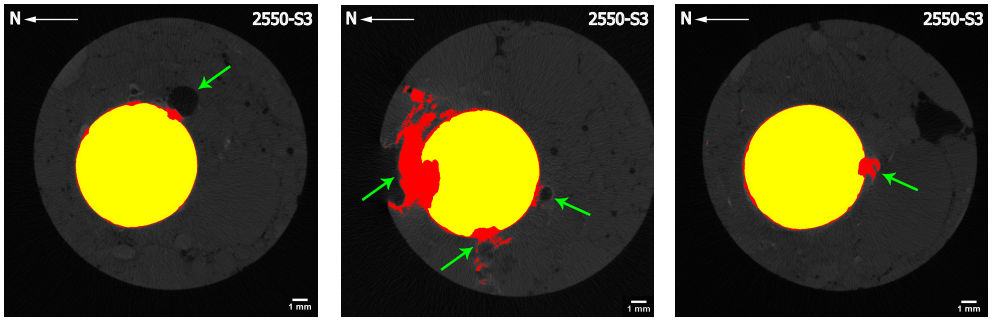


Figure 6.17: 2550-S3: Corrosion product (red) expanding into air voids (green arrow) and cracks (light-blue arrow)

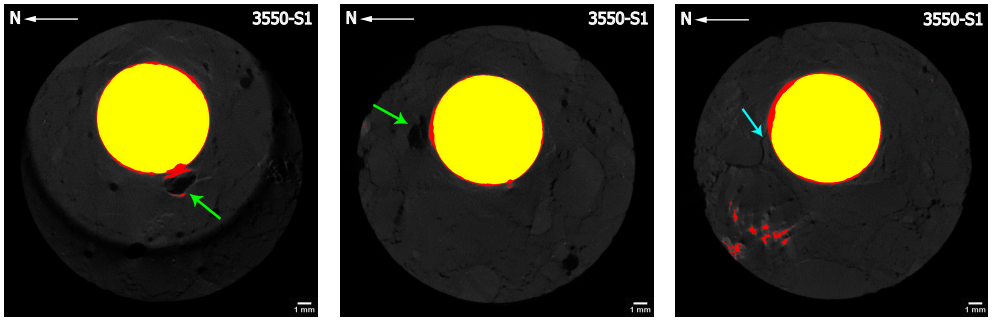


Figure 6.18: 3550-S1: Corrosion product (red) expanding into air voids (green arrow) and cracks (light-blue arrow)

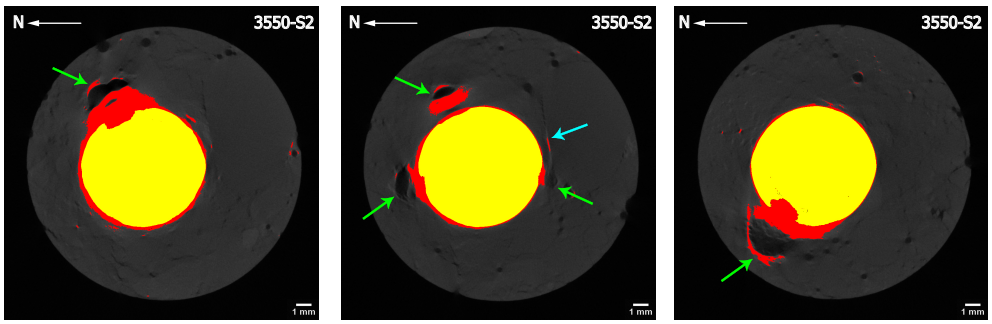


Figure 6.19: 3550-S2: Corrosion product (red) expanding into air voids (green arrow) and cracks (light-blue arrow)

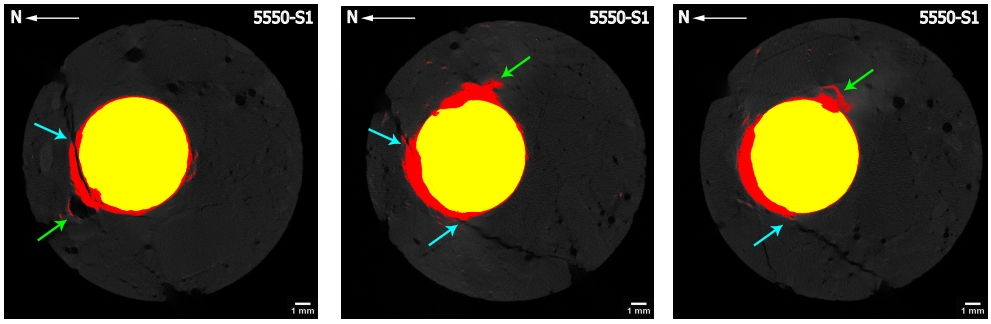


Figure 6.20: 5550-S1: Corrosion product (red) expanding into air voids (green arrow) and cracks (light-blue arrow)

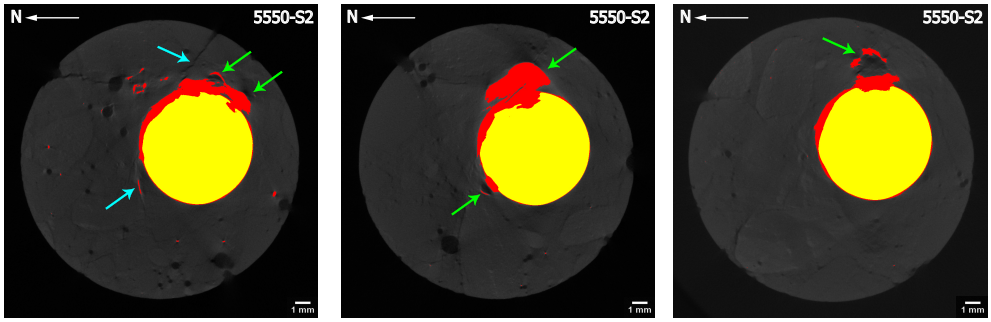


Figure 6.21: 5550-S2: Corrosion product (red) expanding into air voids (green arrow) and cracks (light-blue arrow)

From Figure 6.14-6.21, corrosion pits are generally found coincident to macro-defects at the steel/concrete interface, with consequent higher accumulation of corrosion product at those locations. When macro-air voids are present at the SCI of any specimen, one (at least) corrosion pit is also found close by. Development of corrosion pits and further accumulation of rust into air voids was observed with X-ray Computed Tomography only by Savija et al. [11]. This fact was not confirmed by any of the other researches where CT-scans were used; however, in those cases no macro-air voids were observed at the SCI [38] [39].

From visual analysis of 2D CT-images, the combination of significant concrete defects and orientation to the outside environment seems to correspond to the situation where corrosion pits get the deepest. It also seems the main influencing factor influencing pit depths is the presence of defects at the SCI rather than the orientation of the reinforcement: deeper pits are found at the S-oriented side of the reinforcement if close to air voids more than at the N-oriented side but without concrete defects at the steel/concrete interface (Figure 6.14-6.17). The relation between pit depths, presence of air voids at the SCI and orientation of the reinforcement has been quantitatively analyzed at the same time by means of processing 2D CT-images. The processed images correspond to those analyzed previously for pit depths and orientation (Section 6.5). The purpose of this procedure was to get insights about the most likely influencing factor for corrosion pits presence and depth between visible defects at the SCI and orientation of reinforcement. For this reason, corrosion pits were divided in four different groups depending on their orientation (N- and S-direction) and if close to air voids at the steel/concrete interface: type 1 (orange) and type 3 (green) were representative for corrosion pits found close to air voids at N and S direction respectively. Type 2 (yellow) and type 4 (blue) were representative for pits that were not found in proximity to air voids at the SCI at both the orientations (N and S respectively). An example of what is meant for each pit type is visible below (Figure 6.22), as well as a plot reporting corrosion pit depths, their orientation and their proximity to air voids at the steel/concrete interface (Figure 6.23).

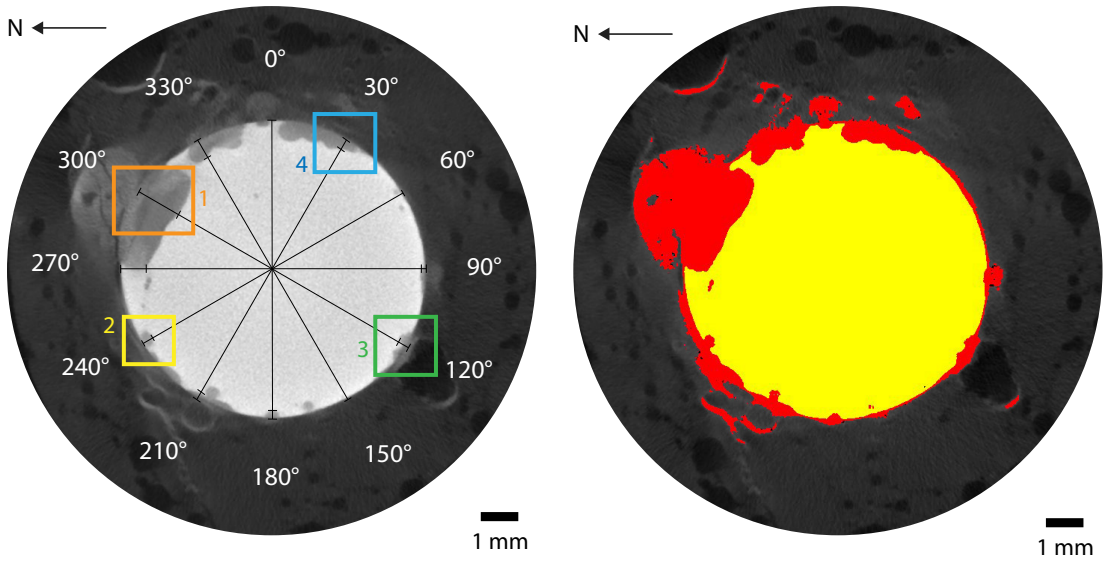


Figure 6.22: Pit depths, orientation and presence of air voids at the SCI: example from 1550-S1 with N-oriented pit coincident to an air void (orange), N-oriented pit coincident to dense cement paste at the SCI (yellow), S-oriented pit coincident to an air void (green) and S-oriented pit coincident to dense cement paste at the SCI (blue)

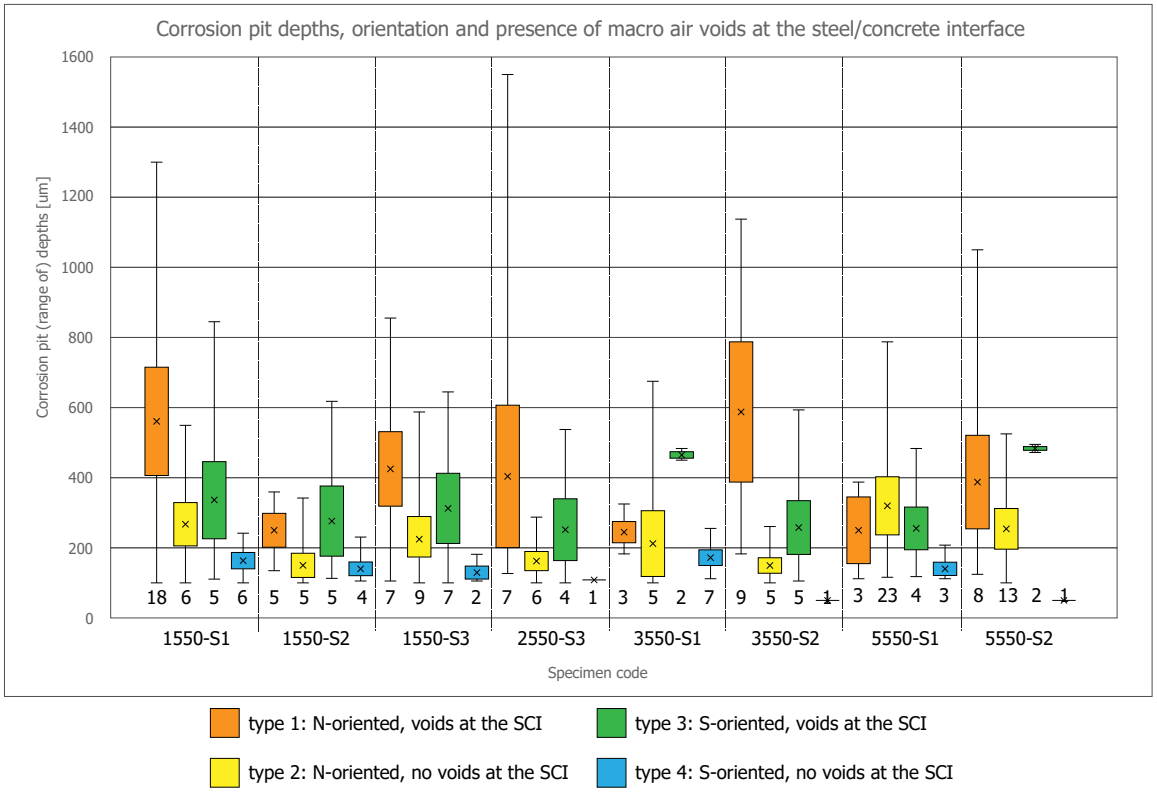


Figure 6.23: Range of depths of corrosion pits [$\mu m$] with outside/inside orientation and proximity to concrete defects at the steel/concrete interface (top bar=maximum depth, bottom bar=minimum depth, X=mean value, box length=standard deviation

From Figure 6.23, some general observations can be made. It is visible that the depth of corrosion

pits (up to around 1,6 mm at maximum) is directly depending on the presence of concrete defects at the steel/concrete interface (type 1 and type 3) rather than on the orientation of the steel (type 2 and 4), contrarily to what Figure 6.13 only suggested. This statement is markedly visible for all the analyzed specimens, for which type-1 and type-3 pits are significantly deeper than type-2 and type-4 ones. Only 5550-S1 shows similarly deep corrosion pits regardless the presence of air voids at the steel/concrete interface. However, this specimen was heavily cracked on the N-oriented side, which probably lead to higher ingress of harmful agents, causing the propagation of deep pits even if no air voids were present close to the reinforcement, or leading to a more general and distributed corrosion than pitting. In this case, cracks were the likely leading factor for corrosion propagation.

The influence of steel orientation on propagation of corrosion pits might be visible if comparing pits of type 1 and type 3. When air voids are present at the SCI, pits get deeper at the N-oriented side. This observation is markedly visible for the majority of the specimens but not for 1550-S2, 3550-S1 and 5550-S2, for which type-3 pits are found to be similar or even deeper than type-1 pits. However, for these specimens only a few air voids were present at the SCI at both sides, which could compromise the comparison of these measurements (especially for 3550-S1 and 5550-S2, where only one "type-3 pit" was found). The relatively low amount of air voids at the SCI for these specimens might be related to the relatively low volume loss due to corrosion, as previously discussed in Section 6.3.

Also type-2 and type-4 pits show dependency on the steel orientation similar to what was observed for type-1 and type-3 ones. Where no concrete defects are present at the SCI, the leading factor causing more aggressive corrosion looks to be the likely higher ingress of harmful agents from the outer environment, as expected.

The fact that corrosion of steel is more sensitive to concrete defects at the steel/concrete interface rather than the orientation of the reinforcement itself has been widely studied in the literature (Section 2.3, [17]-[30]). From previous studies, it was observed that corrosion pits are more likely to grow close to visible defects rather than at zones where the cement paste is dense and compact at the steel/concrete interface [18]-[23]. This statement is also confirmed by the analysis conducted in the present research. From previous studies, it was stated that the sensitivity of pits to air voids at the SCI is the result of the corrosion-inhibiting pH-dependant behaviour of the hydration products of the cement paste (i.e. calcium hydroxide, CH, and calcium-silica hydrates, C-S-H), resulting in its buffering effect, as well as the free chloride level necessary for corrosion to initiate. In other words, the ingress of harmful agents from the outside environment is the main cause for initiation of steel deterioration, which starts to corrode when concrete pH drops below around 11. However, CH and also C-S-H have a pH-dependent dissolution behaviour: in the case of calcium hydroxide, dissolution starts (even if relatively slowly with $K_{sp} = 5.5 * 10^{-6}$) already at a pH below 12.6, with a dissolution rate increasing in a less alkaline environment. The dissolution of calcium hydroxide occurs as defined by:

$$Ca(OH)_2 \longrightarrow Ca^{2+} + 2\,OH^-$$

The release of hydroxyl ions keeps the chloride to hydroxyl concentration ratio ($Cl^- : OH^-$) lower than the free chloride threshold level at the locations where dissolution of calcium hydroxide occurs. Metastable corrosion pits become stable if a certain metal salt concentration (which sustains iron dissolution) at the anolyte is guaranteed [89]. This pits transition can be locally mitigated by the dissolution of $Ca(OH)_2$, which lowers the local $Cl^- : OH^-$, and a reduction in the chloride ion activity in the local pore solution, which may result from the effective removal of chloride ions directly involved in the corrosion process from the pore solution. This latter in part results from their association with dissolved iron in some intermediate form of corrosion product [24]. In so doing, iron dissolution may not be sustained and pits re-passivation would occur. However, when concrete defects are present at the steel/concrete interface, no CH nor C-S-H can locally dissolve to keep the free chloride level lower than the threshold value. Furthermore, in partially or completely saturated conditions, air voids would keep electrolyte at the steel surface increasing the risk of corrosion, as observed in this research. Among others, these aspects led to the hypothesis that visible defects such as air voids at the steel/concrete interface are

more sensitive locations for corrosion initiation and further avoiding re-passivation of corrosion pits [24].

From the analysis reported above, it was observed that the combination of visible defects at the steel/concrete interface, a likely higher concentration of harmful agents and the presence and wetting/drying cycles of electrolyte creates the most aggressive environment for corrosion pits to firstly initiate and then propagate. This interrelated-dependency of corrosion pits growth was already suggested by Angst [17], who stated that de-passivation of reinforcement and then further propagation of corrosion was related to the presence of interfacial or metallurgical defects with a sufficient high local chloride concentration, as it is suggested by CT-images analysis reported here. However, contrary to what was previously observed by some authors [17] [27], in this research the most corroded side of the reinforcement is the one exposed to the outside environment (Section 6.5). These differences might be explained by the fact that in previous researches reinforcement was oriented perpendicularly to the casting direction. This procedure caused concrete defects to be at the bottom side of the reinforcement due to water bleeding and settlement [18] [27]. As previously shown, the presence of concrete defects at the SCI seems to be the main factor for corrosion initiation and pit growth. In this research, reinforcement was oriented parallel to the casting direction (Section 3.2), inhibiting the effects that bleeding and settlement might have on the quality of the steel/concrete interface.

# 7

# Micro-structural characterization of corrosion product

## 7.1. Purpose, samples preparation and equipment

After conducting CT-scan image acquisition and analysis, micro-structural characterization of both concrete and corrosion product was conducted through different techniques, such as Scanning Electron Microscope/Energy Dispersive X-Ray Spectroscopy (SEM/EDS), Nano-indentation and X-Ray Diffraction (XRD). The purposes of these analysis were:

- to determine the Elastic Modulus of corrosion product ($E_{cp}$) formed in different concrete mixes, by means of nano-indentation, and analyze differences of $E_{cp}$, if any;
- to quantify the composition of nano-indented corrosion product through SEM/EDS point analysis, and evaluate the relation between the composition of corrosion product and its $E_{cp}$;
- to characterize the crystalline phases of corrosion product formed in different concrete mixes by means of XRD;

SEM/EDS and nano-indentation were conducted on (around) 5-mm-high slices which were carefully sawn perpendicularly to the reinforcement of cores that were previously CT-scanned and laterally impregnated with fluorescent epoxy (Figure 3.4). Once sawn, slices were manually ground with #120, #220, #280, #320, #600, #800 and #1200 grinding Silcone Carbide sanding paper and polished with 6, 3, 1 and 0.25 $\mu m$ polishing Diamond paste on a lapping table. 100% ethanol and non-water based polishing paste were used for grinding and polishing respectively, to interrupt hydration and avoid further on-going corrosion. Once polished, slices were covered by commercial transparent nail polish to insulate the samples from oxygen supply. Just before conducting nano-indentaton, nail polishing was dissolved with 100% acetone and samples were re-polished with 0.25 $\mu m$ diamond paste again for around 15 minutes. Nano-indentation was conducted on suitable locations detected through optical microscopy, hence where there was a significant amount of corrosion product at the steel/concrete interface. A mark was made at the edges of the samples that helped to identify where indents were under the SEM, which was performed as soon as nano-indentation was completed.

XRD was conducted on corrosion product collected from other reinforcement bars embedded in the reinforced concrete prisms, hence on those that were not previously CT-scanned (Figure 3.1). Concrete prisms were mechanically split and corrosion product was carefully ground from the reinforcement bars and then collected in plastic containers. These containers were then kept in a desiccator to avoid any change in Iron phases due to the access of oxygen until XRD was conducted. The results of XRD are described and discussed in Section 7.5.

## 7.2. Nano-indentation

As conducted by Savija et al. [11], an Agilent Nano Indenter G200 with a diamond Berkovich tip (i.e. a three-sided pyramidal diamond) was used for nano-indentation tests. Each polished section was subjected to one grid-like series of indents, with fixed row/column number (5/20). For all the tests, the maximum indentation depth was set to 2000 nm. The Elastic modulus of corrosion product ($E_{cp}$) was determined through the Continuous Stiffness Method (CSM) developed by Oliver and Pharr [91], which provides continuous stiffness measurements as function of indentation depth. The average $E_{cp}$ was determined in the range of 1000 nm and 1800 nm. The Poisson ratio of corrosion product was set to 0.25, as used in previous studies about nano-indentation testing of corrosion product, since values between 0.2-0.3 did not give significant differences in the determination of $E_{cp}$ [11] [64]. A more detailed explanation about the test procedure and its output is given in Appendix 2.4.3. Once Nano-indentation was performed, $E_{cp}$ of each indented point was surface-plotted and overlapped to BSE images of the specimens' portion that was subjected to nano-indentation (Figure 7.1-7.8), while further BSE images are visible in Appendix D.

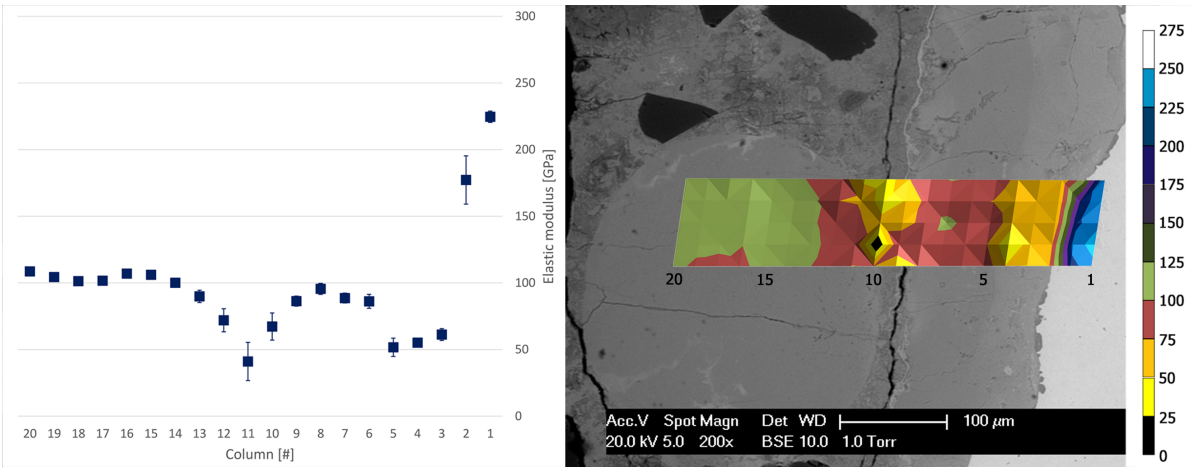


Figure 7.1: 1550-S1: range of Elastic modulus of indented columns (left) and Elastic modulus surface plot overlapping BSE image of indented location (right) - values of colorbar in GPa

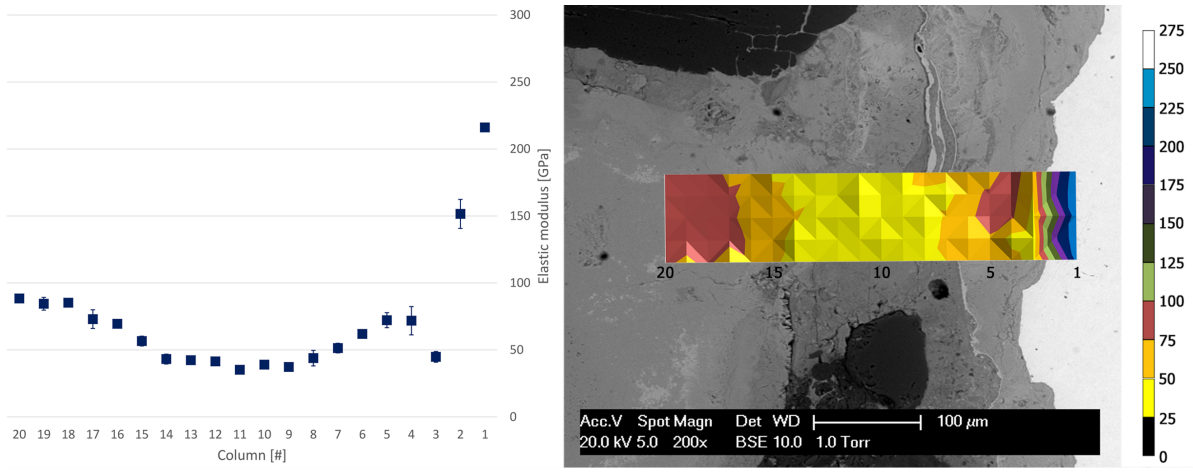


Figure 7.2: 1550-S2: range of Elastic modulus of indented columns (left) and Elastic modulus surface plot overlapping BSE image of indented location (right) - values of colorbar in GPa

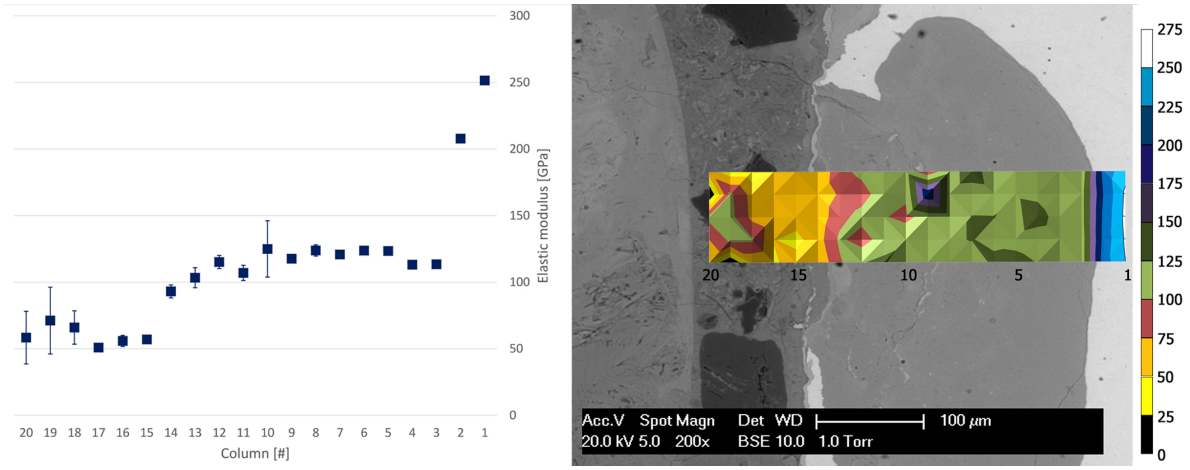


Figure 7.3: 1550-S3: range of Elastic modulus of indented columns (left) and Elastic modulus surface plot overlapping BSE image of indented location (right) - values of colorbar in GPa

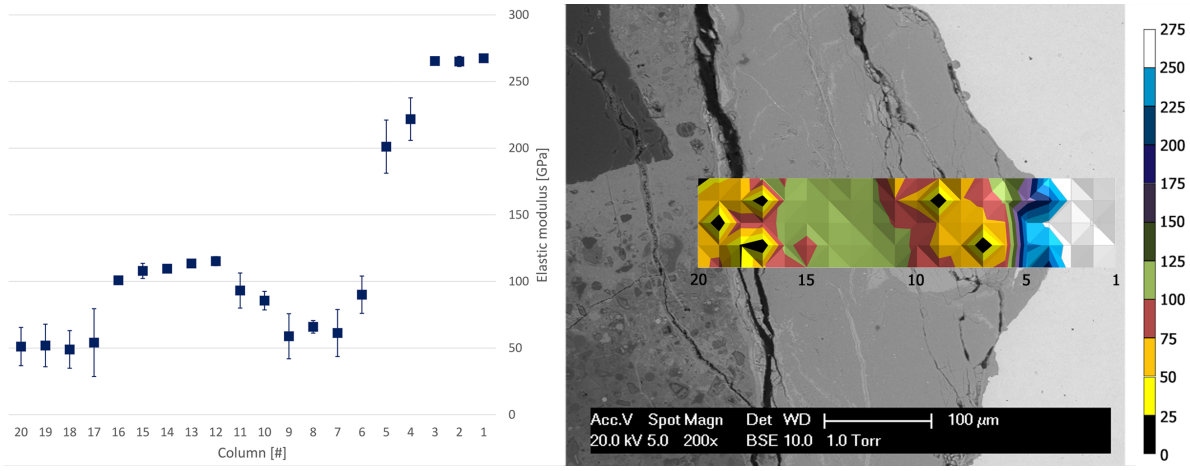


Figure 7.4: 2550-S3: range of Elastic modulus of indented columns (left) and Elastic modulus surface plot overlapping BSE image of indented location (right) - values of colorbar in GPa

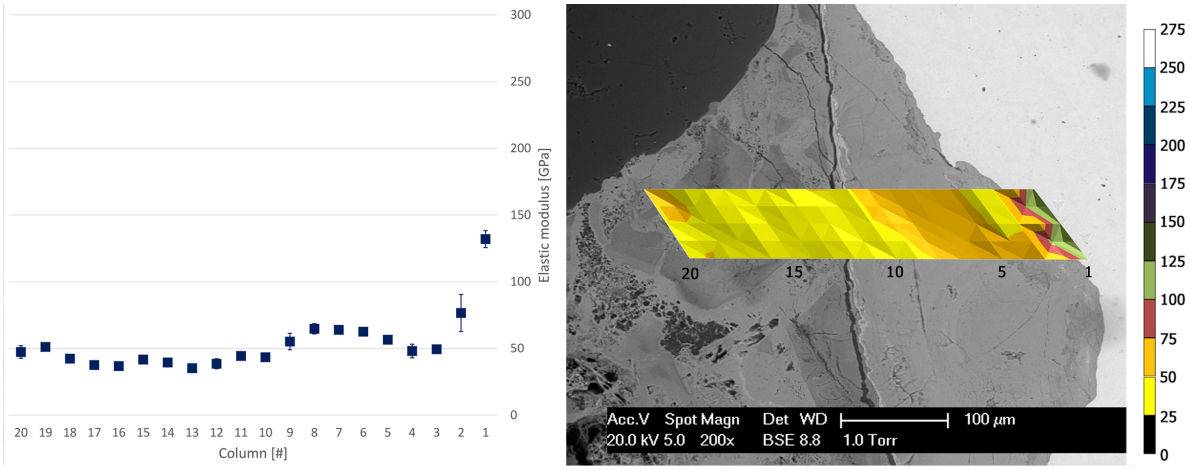


Figure 7.5: 3550-S1: range of Elastic modulus of indented columns (left) and Elastic modulus surface plot overlapping BSE image of indented location (right) - values of colorbar in GPa

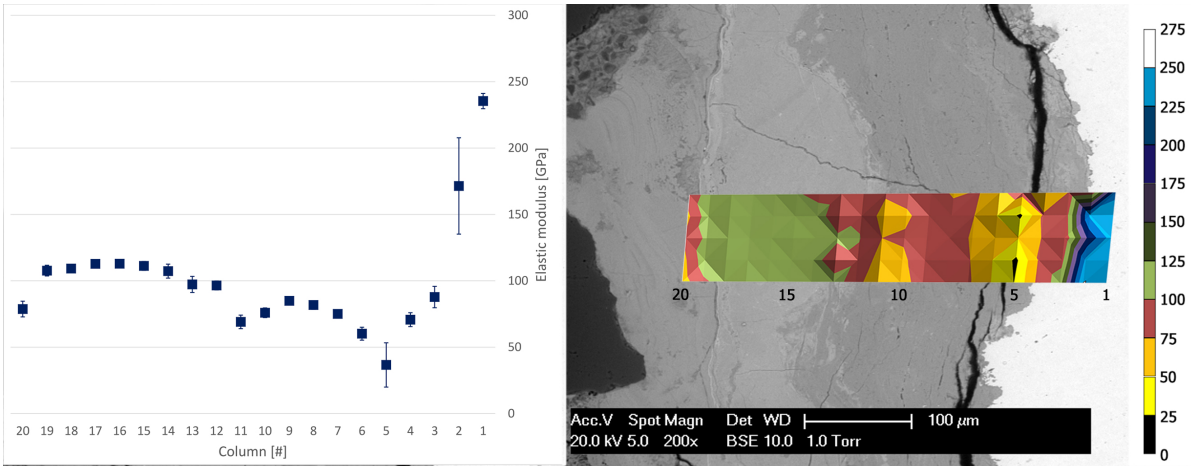


Figure 7.6: 3550-S2: range of Elastic modulus of indented columns (left) and Elastic modulus surface plot overlapping BSE image of indented location (right) - values of colorbar in GPa

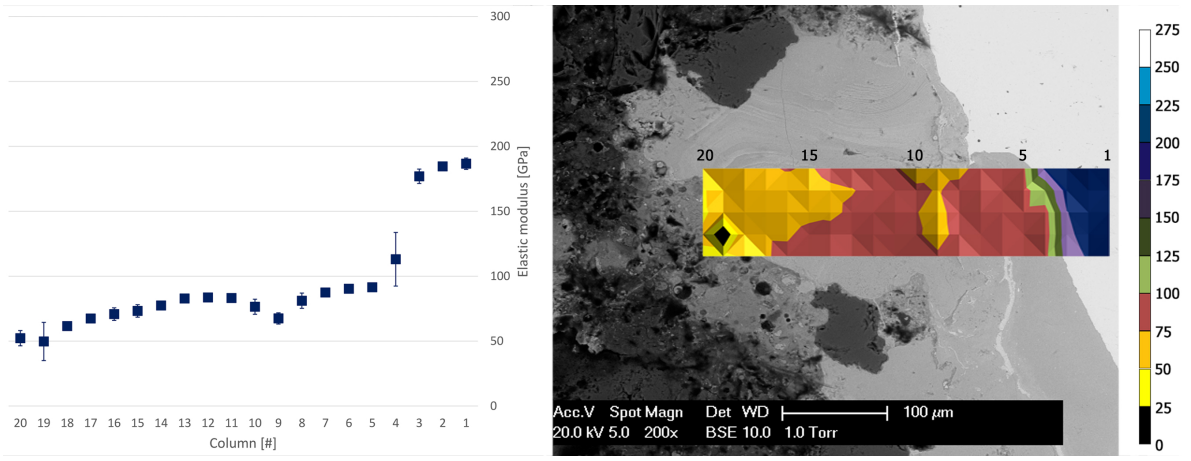


Figure 7.7: 5550-S1: range of Elastic modulus of indented columns (left) and Elastic modulus surface plot overlapping BSE image of indented location (right) - values of colorbar in GPa

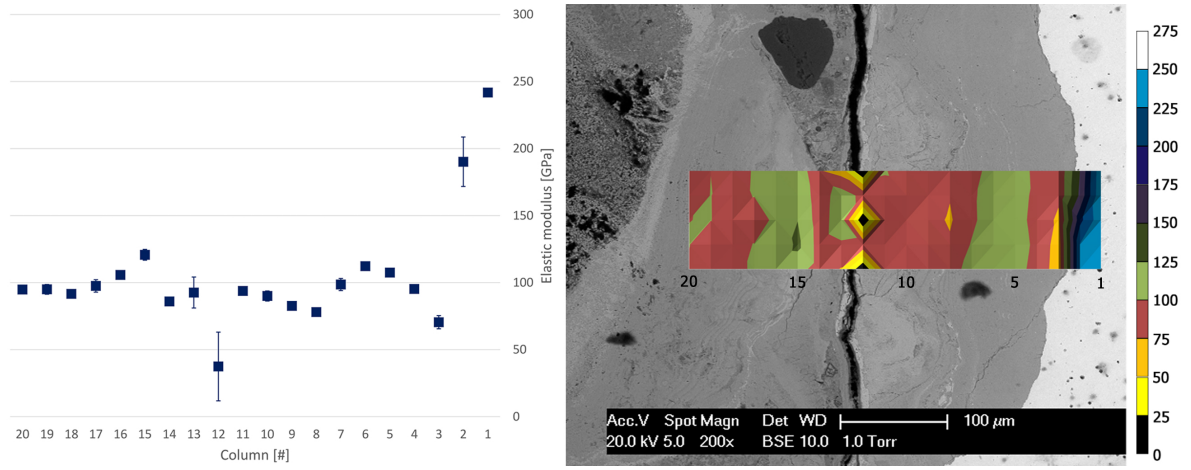


Figure 7.8: 5550-S2: range of Elastic modulus of indented columns (left) and Elastic modulus surface plot overlapping BSE image of indented location (right) - values of colorbar in GPa

Looking at Figure 7.1-7.8, many observations can be made. Areas of corrosion product with different appearance and micro-mechanical properties can be distinguished. For most of the specimens, some portions seem dense and compact, while others present visible cracks. A clear example of this distinction is 3550-S2, where these two areas are clearly marked by different appearance (but also for 1550-S1, 2550-S3 and 5550-S2). Also areas where corrosion product penetrated into the surrounding cement paste were indented (marked as CEM+CP). The Elastic modulus of these latter indents, as the one of cracked corrosion product, ranged between 0-50 GPa (black-yellow).

For most of the specimens, the Elastic modulus of uncracked corrosion product ranges between 75-125 GPa (red-green), with a few areas between 50-75 GPa (orange, i.e. 1550-S1 and 5550-S1). Only 3550-S1 did not have $E_{cp}$ higher than 75 GPa. However, as visible from Figure 7.5, the indentation grid was significantly tilted and the E modulus of steel was far from the expected value (equal to around 150 GPa instead of the expected 210 GPa). It is likely that the specimen was not properly kept in place when nano-indented, then shift during the test, or that the indentation tip was not properly calibrated, resulting in unlikely values. Results from 3550-S1 will be then taken into account with caution.

Only a few researches were conducted on the use of nano-indentation to determine $E_{cp}$. Savija et al. [11] found that corrosion product formed in a SHCC mixture (self-healing cementitious composite) had $E_{cp}$ ranging between 49.4-67.9 GPa. Zhao et al. [64] observed that corrosion product was divided into two main layers: an inner one (related to corrosion degradation) and an outer one (related to the mill scale), with this latter not derived from corrosion. The Elastic modulus of these two layers ranged between 47-86 GPa for the inner layer and between 98-122 GPa for the outer layer. In this research, $E_{cp}$ is higher than what was found by others but still in the same order of magnitude, mostly ranging between 75-125 GPa. Differences with previous studies might be explained by the different specimens that were used by Zhao et al. [64] and Savija et al. [11]. In both the cases corrosion was anodically generated, which tends to influence the formation and further distribution of corrosion product [96]. The corrosion current density at which the corrosion product is formed might be a relevant parameter influencing the micro-structure of the resulting degradation product, such as its porosity, which might influence its micro-mechanical properties. Further specimens nano-indented by Zhao et al. [64] included portions of corrosion product previously peeled from a corroding bar, thus not including the steel/concrete interface and the potential effects that this might have on corrosion product's micro-structure (i.e. due to constraint from the surrounding concrete). Nevertheless, $E_{cp}$ reported in this research are overall comparable to previous studies by nano-indentation.

The fact that the Elastic modulus of cracked portions and close to the cement paste is lower than apparently denser areas sounds reasonable. When performing nano-indentation, the presence of defects close to the indent would offer accommodating areas for the deformation of the indented material. This results in less applied stress to cause a certain strain, hence in lower Elastic modulus. If indenting more far from defects, the material is more constrained and the resulting Elastic modulus is higher. Similar values and explanation are in line with what was already pointed out by others [11] when performing nano-indentation on cracked anodically-accelerated corrosion product.

In accordance with others [96] [97], in Figure 7.1-7.8 penetration of corrosion product into the surrounding cement paste is clearly visible (see also Appendix 2.4.3). Since specimens were 20 years old and corrosion was not anodically accelerated, it is likely that corrosion progressed with relatively low current density during the years (and perhaps not continuously). This relatively in-time-distributed corrosion progress would have allowed for corrosion product to accommodate and/or penetrate where possible without causing premature cracking (i.e. in air voids at the steel/concrete interface or in the surrounding matrix). This statement is in line with what was pointed out by Savija et al. [11], who did not observe any penetration of corrosion product into the cementitious matrix because corrosion was anodically accelerated and accommodating cracks were made, with no consequent need for corrosion product to penetrate into the cementitious matrix. However, investigating the depth at which corrosion product penetrated into the surrounding cement paste was not the aim of this research.

Apart from presence of cracks and defects in the corrosion product layer, which cause localized differences in its $E_{cp}$, it is interesting to observe that corrosion product seems to be clearly made by

distinct bands, which have different micro-mechanical properties and appearance (especially 1550-S1, 3550-S2, 5550-S1 and 5550-S2, see also Appendix 2.4.3). A change in $E_{cp}$ mostly corresponds to a change in brightness of the corrosion product region. Since brightness of BSE images is, to a certain extent, representative of the micro-structure of the observed material, Figure 7.1-7.8 suggest that a relation between $E_{cp}$ and the characteristics of corrosion product (i.e. chemical composition and micro-structure) could occur. To stress the well-defined layered structure of corrosion product observed in this research, a selection of BSE images of one indented location (from 3550-S2) is reported (Figure 7.9).

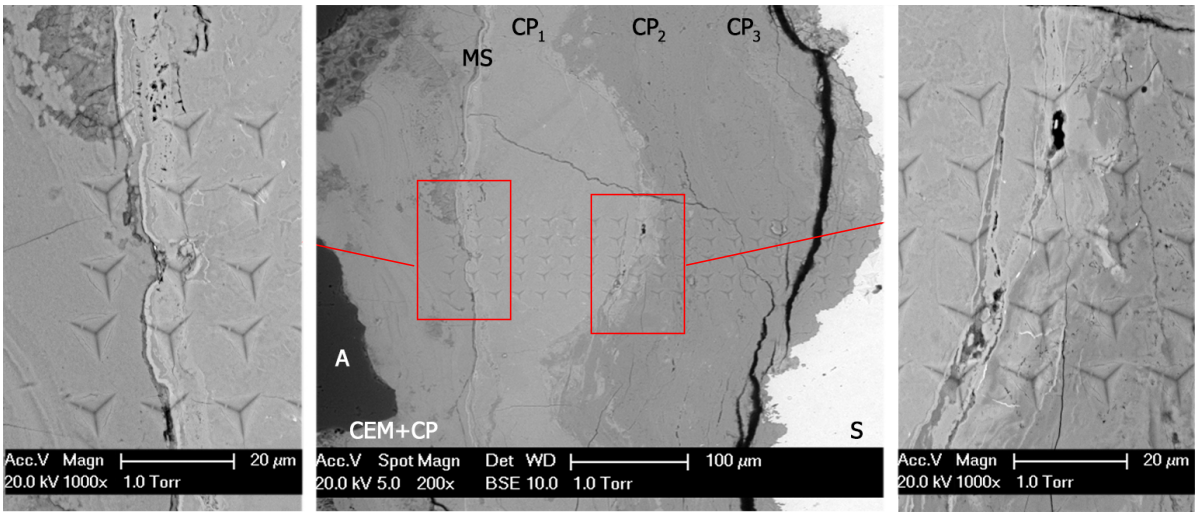


Figure 7.9: (centre) BSE image of layered structure of corrosion product with labeled components from 3550-S2 (S=steel; CP(x)=layers of corrosion product; CEM=cement; AV=air void; C=crack; A=aggregate; MS=mill scale); (left) interface between corrosion product and cement paste; (right) interface between different corrosion product layers

In Figure 7.9, different layers of corrosion product can be distinguished. A thin mill scale layer (MS) is visible at the edges of the steel reinforcement, dividing the corrosion product (on its right-hand side) and the surrounding cement paste (on its left-hand side). Getting closer to the steel bar, at least three corrosion product layers are visible: an external one (CP1), apparently dense and bright with one perpendicular crack; an intermediate one (CP2), apparently less dense and darker than CP1; an internal one (close to the steel, CP3), slightly brighter than CP2 and heavily cracked. In Figure 7.6 it is also visible that these different layers of corrosion product have mostly well-defined $E_{cp}$ (CP1=100-125 GPa; CP2=100-75 GPa; CP3=100-50 GPa), of which values change at the interface between the layers. Similar pattern is found for 1550-S1 (Figure 7.1) and 2550-S3 (Figure 7.4). Other specimens present different progress of $E_{cp}$: for 1550-S3 (Figure 7.3), an apparently homogeneous corrosion product layer is visible from the steel interface until the surrounding cement paste, with consequent homogeneous $E_{cp}$ (100-125 GPa). For 5550-S1 (Figure 7.1) and 5550-S2 (Figure 7.8) different corrosion product layers are also distinguishable based on their appearance and their micro-mechanical properties; however, the pattern of $E_{cp}$ is not similar to the one of previous specimens.

Layered corrosion product at the steel/concrete interface was already observed by others [64] [46] [96] [98]. Duffò et al. [98] performed Raman spectroscopy on different zones of layered corrosion product, which was clearly made by adjacent bands. Although they identified all the Iron compounds that corrosion product was made of, it was not possible to relate different bands to specific Iron compounds. On the contrary, Demoulin et al. [102] performed Raman spectroscopy on corrosion product formed in 46- and 260-years-old reinforced concrete structures, and differently-looking bands precisely corresponded to different corrosion products. In their research, two main corrosion product layers were identified at the steel/concrete interface of different samples: one layer made of wustite, magnetite and hematite mixed together (WMaH) and one layer mainly made of goethite, with marblings of magnetite+maghemite or maghemite+ferrihydrite. All these components could be distinguished already

based on different imaging characteristics from BSE images, and micro-Raman spectra confirmed their different mineralogy. However, it was not possible to agree about a general corrosion pattern since the order of these corrosion product layers from the steel reinforcement was variable. Wong et al. [96] found that corrosion product was generally uniform and featureless, but occasionally it appeared to be layer-structured, made of dark and bright corrosion product bands, as it was found for most of the cases in the present research. Wong et al. [96] concluded that this layered structure of corrosion product resulted from different levels of oxidation that occurred per each layer, which is dependent on the prevailing localized conditions where and when corrosion product is made (i.e. oxygen supply). This point was supported by EDS spot analysis conducted to evaluate the chemical composition of different layers of corrosion product. It was observed that darker bands had lower mean atomic Fe/O (equal to 0.56 $\pm 0.02$), which suggested formation in an oxygen-rich environment, while brighter bands had higher mean atomic Fe/O (equal to 0,84 $\pm 0.08$). The dependance of corrosion product on oxygen supply is in accordance with Cornell [46], who pointed out that corrosion product of steel exposed to atmospheric conditions is frequently formed by two distinct layers: one made of magnetite at the iron/rust interface (as a result of reduced oxygen supply) and one outer layer made of goethite and/or lepidocrocite. In his book, he also stressed the relevance that alternate cycles of wetting and drying cause periodical changes of the corrosion potential of the system, inducing cyclic changes in the composition of the rust.

From the images reported above (Figure 7.1-7.9) and from what was observed by others [64] [46] [96] [98] [102], it seems clear that corrosion product is made by different layers, one adjacent to each other. However, it is not possible to agree about a preferential pattern of corrosion product progress (in terms of its appearance, structure and, therefore, of its micro-mechanical properties) from the steel reinforcement to the surrounding cement paste. It is likely that corrosion product characteristics, such as its chemical composition, micro-structure and porosity, highly depend on the conditions and (kinetic/thermodynamic) equilibrium where and when the corrosion product is formed as well as on many inter-related parameters. Firstly, varying oxygen supply and moisture availability would result in corrosion product layers with different micro-structure and porosity. The presence of other species (i.e. chlorides content, $SO_4$ and $CO_2$) and pH gradient would also influence the solubility of iron and the stability of individual iron compounds. The differences of temperature variations and wet/dry cycles between specimens might also influence the micro-structure and composition of corrosion product. Furthermore, the quality of the steel/concrete interface might also have an influence on the structure of the corrosion product. In other words, dense cement paste at the steel/concrete interface might constrain more the forming corrosion product, thus resulting in denser layers. On the contrary, if corrosion product is formed close to air voids it would likely results in less constrained layers, due to the accommodating space that voids would offer with less constrain (at least before voids get completely filled by corrosion product). It was also previously pointed out that visible cracks seem to have significant influence on the micro-mechanical properties of corrosion products: for some of the specimens, these cracks were coincident with the mill scale layer (i.e. 1550-S1, 3550-S1 and 5550-S2), while for other specimens they were located more internally (i.e. 2550-S3 and 3550-S2). Since the characteristics of the steel/concrete interface change locally for each specimen, it was unlikely to find similar progress at locations with different characteristics in different specimens. To clarify the influence that the characteristics of the steel/concrete interface might have on the properties of corrosion product, deeper investigation would be needed. GAD images that clearly shows different local characteristics of corrosion product, such as apparent density and porosity, are reported below (Figure 7.10).

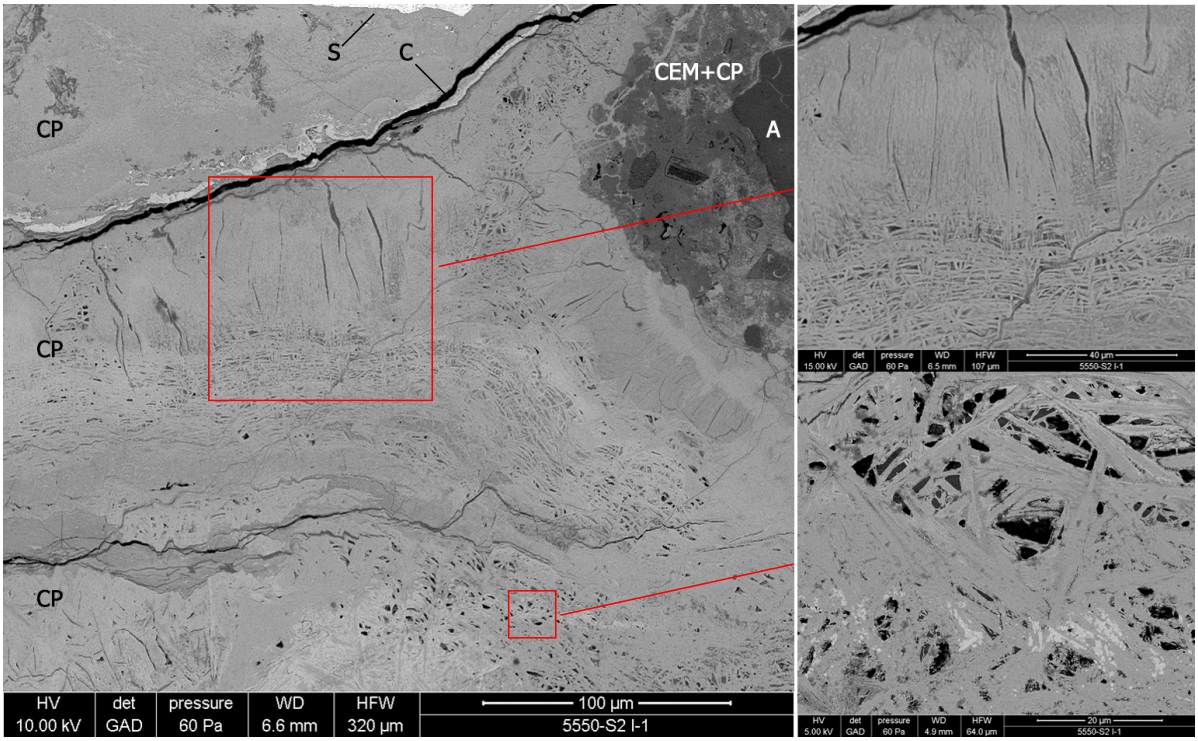


Figure 7.10: (left) GAD image of layered structure of corrosion product with labeled components from 5550-S2 (S=steel; CP(x)=layers of corrosion product; CEM=cement; AV=air void; C=crack; A=aggregate); (up-right) portion of dense corrosion product with perpendicular cracks and more porous overlapping parallel layers; (bottom-right) randomly-oriented needle structure;

On the other hand, what is common to all the specimens of the present research is that changes of local micro-mechanical properties correspond to changes in brightness and appearance of corrosion product, as visible in Figure 7.1-7.8. As already mentioned (Section 2.4.2) there is no common agreement about (i) the Elastic modulus of corrosion product and (ii) the relation between $E_{cp}$ and the micro-structure and/or chemical composition of corrosion product. Significantly different $E_{cp}$ were measured by many researchers through several techniques with scattering equal to a factor of $10^6$ (Figure 2.16), but only a few of them tried to determine the relation between $E_{cp}$ and corrosion product properties and composition. Zhao et al. [64] found that mill scale layer had higher $E_{cp}$ than corrosion-generated layer performing nano-indentation on these two. Since Cook [68] observed that mill scale-related corrosion product has higher Fe/O than corrosion-generated one, Zhao et al. [64] concluded that higher the Fe/O of corrosion product, higher its Elastic modulus. However, this relation has never been verified. Savija et al. [11] performed EDS elemental mapping of the indented locations. Even though this technique gave a general idea about the composition of the indented corrosion products, no localized relation between chemical components of corrosion product and its mechanical properties could be conducted.

To investigate the relation between the localized chemical composition of corrosion product and its micro-mechanical properties, EDS elemental mapping and spot analysis coincident to nano-indented locations were conducted, as described below (Section 7.3).

## 7.3. SEM/EDS elemental mapping and spot analysis

To evaluate the relation between the pattern of $E_{cp}$ and the profile of Fe content within the corrosion product, elemental mappings of indented steel/concrete inter-facial zones were conducted (see Appendix D.1.2). For the microanalysis, a Philips XL30 ESEM equipped with an EDAX energy-dispersive spectrometer was used in the hi-vac chamber condition. Elemental mappings were carried out at 20

kV. Out of the elemental map of the indented SCI, only the portion of the sample that was indented ("indentation grid") was first cropped and then further analyzed. For each indentation grid (highlighted in red dashed rectangle in Figure 7.11-7.18), the iron weight percentage curve was obtained through a Matlab tool for image analysis developed by Ma et al. [103], according to the following methodology. Since the intensity of the iron mapping represents the relative relationship of weight percentage of the iron only, the code was used to get the normalized weight percentage of iron at each pixel and the iron distribution along the relative coordinates of the indentation grid. This procedure consists in two steps, re-scaling and calculation, as described in detail elsewhere [103]. Output of this methodology is the average of the iron-related counted pixels at each pixel column of the indentation grid (hence one value per column). The obtained number represents the average iron weight percentage at the corresponding relative coordinate, as visible below (Figure 7.11-7.18).

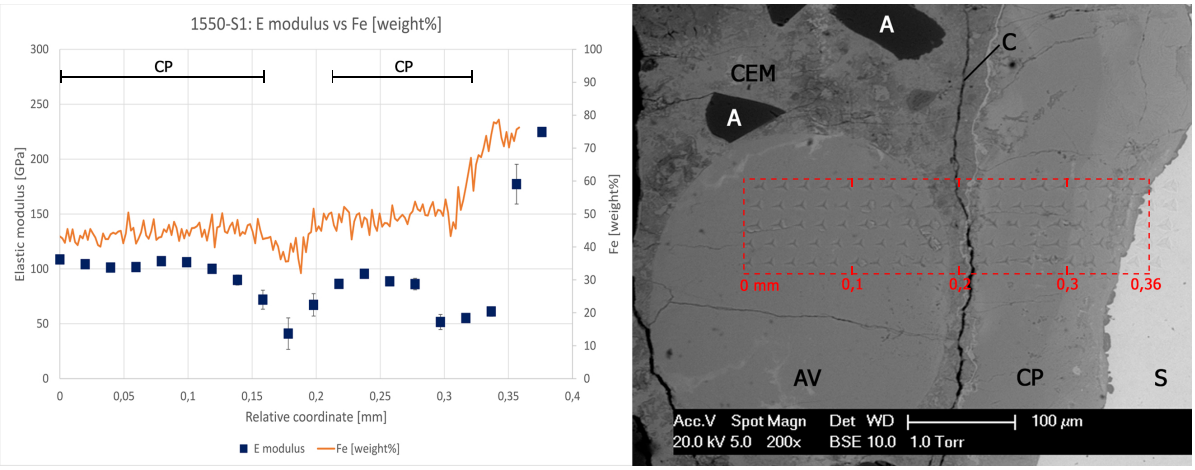


Figure 7.11: 1550-S1: (left) $E_{cp}$ [GPa] and Fe [wt%] profile within the indentation grid; (right) BSE of SCI with highlighted indentation grid (red dashed rectangle);

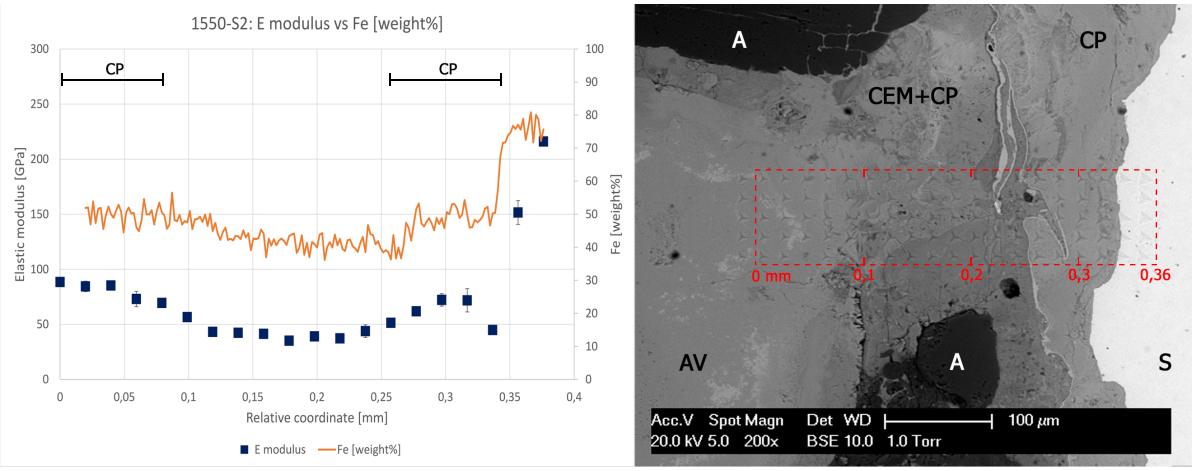


Figure 7.12: 1550-S2: (left) $E_{cp}$ [GPa] and Fe [wt%] profile within the indentation grid; (right) BSE of SCI with highlighted indentation grid (red dashed rectangle);

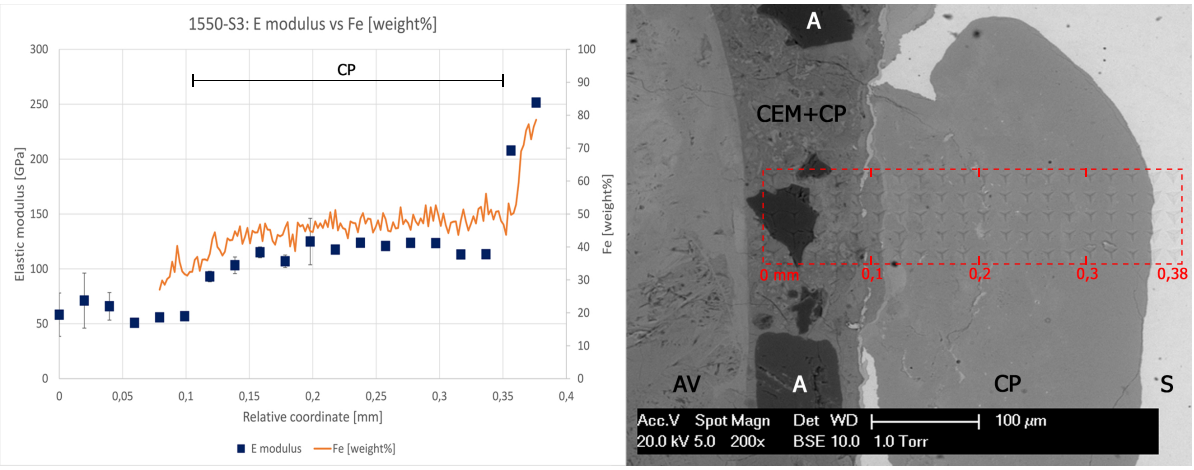


Figure 7.13: 1550-S3: (left) $E_{cp}$ [GPa] and Fe [wt%] profile within the indentation grid; (right) BSE of SCI with highlighted indentation grid (red dashed rectangle);

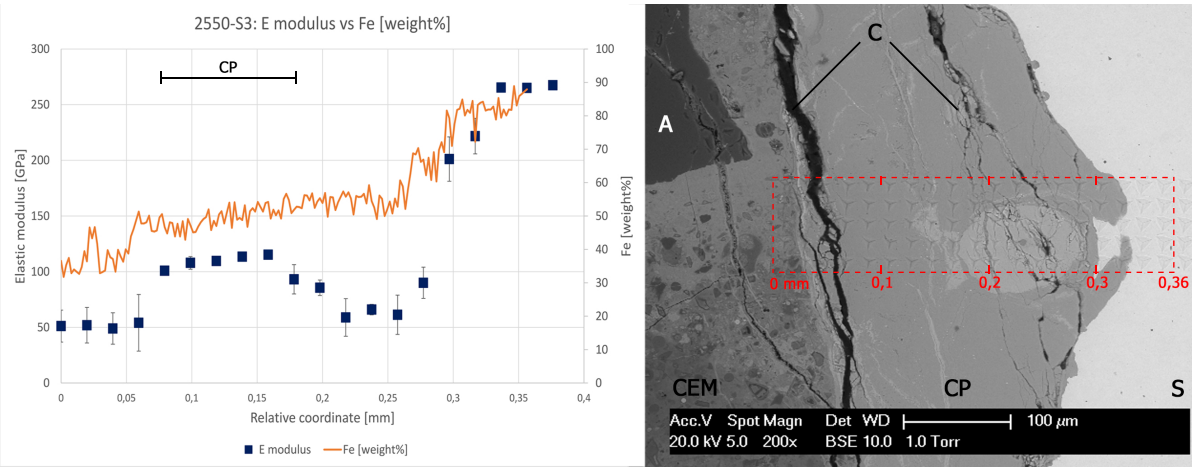


Figure 7.14: 2550-S3: (left) $E_{cp}$ [GPa] and Fe [wt%] profile within the indentation grid; (right) BSE of SCI with highlighted indentation grid (red dashed rectangle);

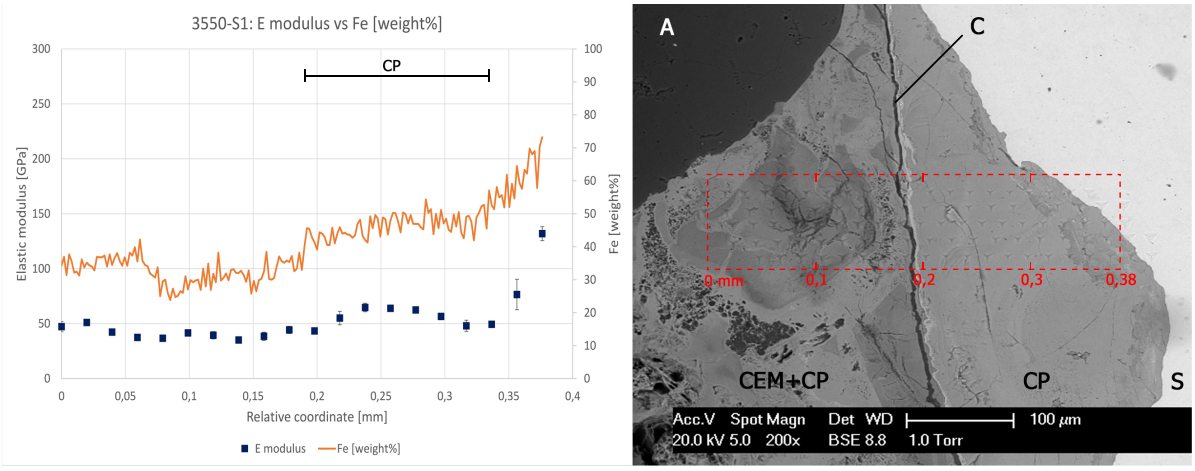


Figure 7.15: 3550-S1: (left) $E_{cp}$ [GPa] and Fe [wt%] profile within the indentation grid; (right) BSE of SCI with highlighted indentation grid (red dashed rectangle);

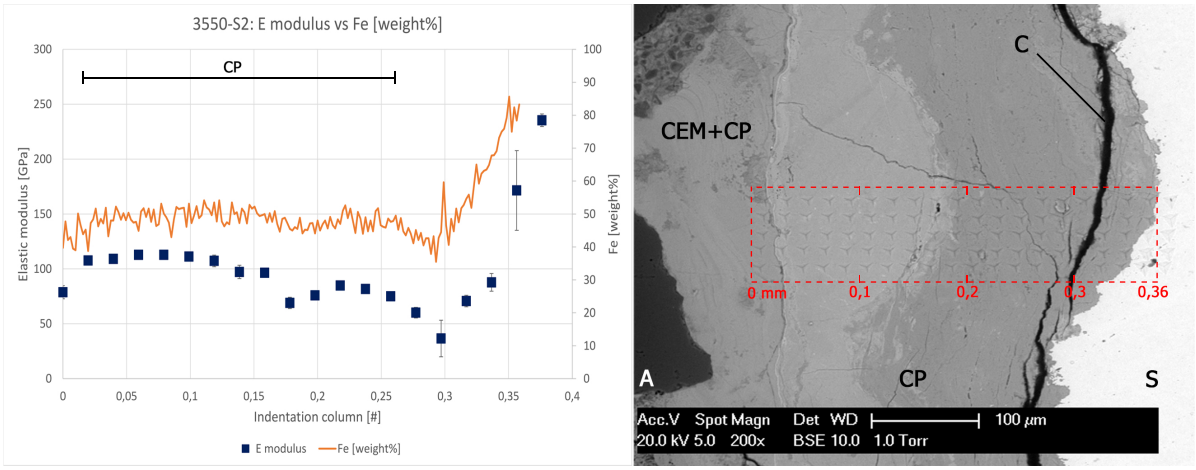


Figure 7.16: 3550-S2: (left) $E_{cp}$ [GPa] and Fe [wt%] profile within the indentation grid; (right) BSE of SCI with highlighted indentation grid (red dashed rectangle);

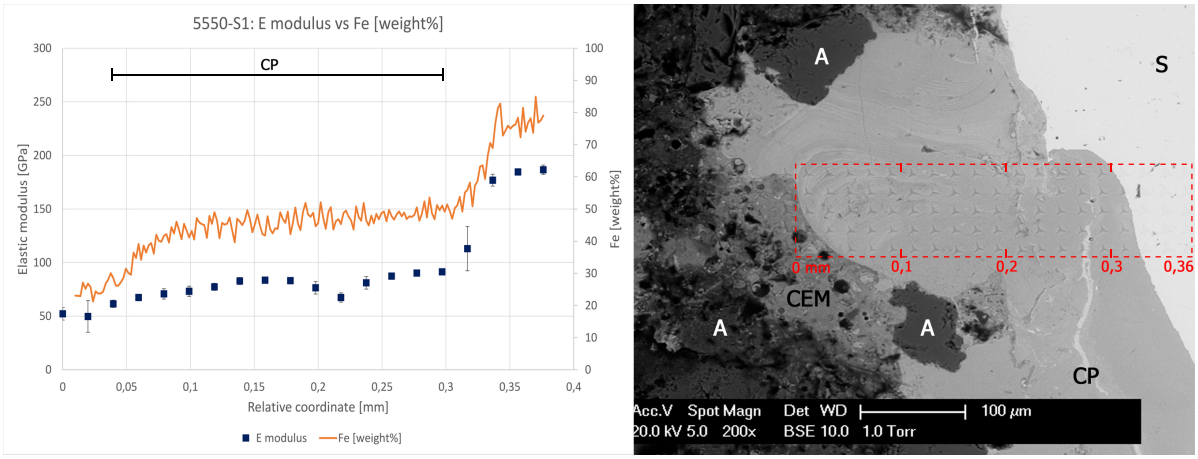


Figure 7.17: 5550-S1: (left) $E_{cp}$ [GPa] and Fe [wt%] profile within the indentation grid; (right) BSE of SCI with highlighted indentation grid (red dashed rectangle);

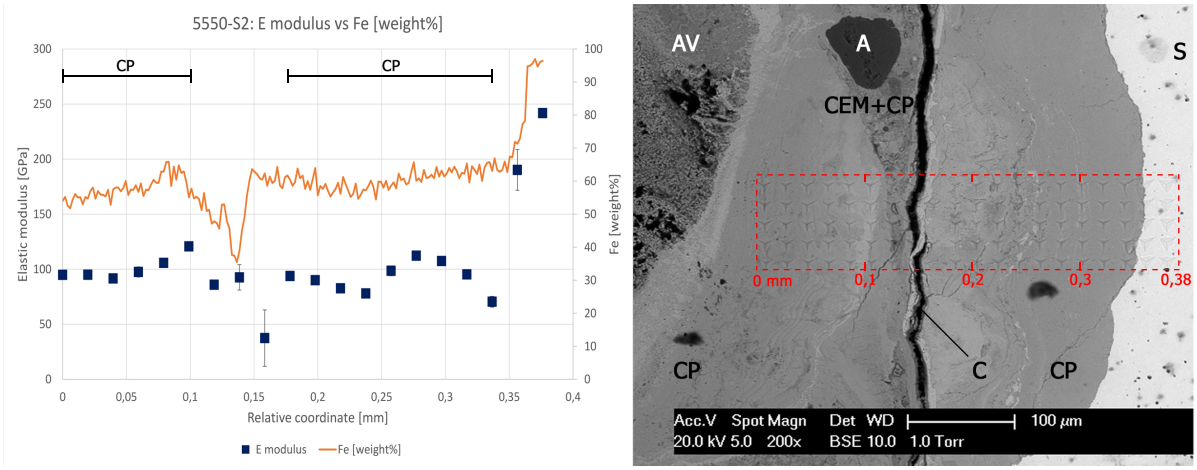


Figure 7.18: 5550-S2: (left) $E_{cp}$ [GPa] and Fe [wt%] profile within the indentation grid; (right) BSE of SCI with highlighted indentation grid (red dashed rectangle);

In Figure 7.11-7.18 the $E_{cp}$ and Fe concentration profiles within each indentation grid are plotted. For all the specimens, it is visible that the two profiles have very similar pattern. Only in some portions of 1550-S1 (between 0.32-0.35 mm), 2550-S3 (between 0.15-0.25 mm) and 5550-S2 (between 0,30-0,35 mm) the shape of the two profiles is significantly different. However, for most of these portions the standard deviation of $E_{cp}$ at those locations is relevant, which probably compromised this local comparison. For all the specimens, the Fe [wt%] increases at around 0.35 mm of relative coordinate up to around 90%, which corresponds to the steel reinforcement, as expected.

Undisturbed corrosion product portions (i.e. non-penetrating cement paste and not heavily cracked) are identified with "CP" in Figure 7.11-7.18. The Fe concentration of these portions ranges overall between around 50-65%, while $E_{cp}$ ranges between 50-125 GPa. Interestingly, also "disturbed" corrosion product has $E_{cp}$ which varies as a function of Fe concentration (i.e. in 1550-S1 between 0.18-0.22 mm; in 1550-S2 between 0.10-0.25 mm; in 5550-S2 between 0.10-0.20 mm). This finding is probably related to the working principle (and perhaps limitations) of nano-indentation, which will be discussed in more detail later in this report, as well as the relation between $E_{cp}$ and Fe [wt%].

$E_{cp}$ and Fe [wt%] profiles have similar pattern within the same indentation grid. A relative increase (or decrease) in Fe [wt%] corresponds to a consequent increase (or decrease) of $E_{cp}$ at the same locations. However, it also looks like that there is no linear relation between these two parameters if comparing different specimens. Slight variations of Fe [wt%] are found if comparing the iron concentration of corrosion product belonging to different indentation grids; on the other hand, the $E_{cp}$ of the same grids varies considerably, in some cases up to 50 GPa of difference (see for example 1550-S3 and 5550-S1). To investigate the relation between the Iron concentration at one indent and its $E_{cp}$, EDS spot analysis was also carried out. As previously visible, nano-indentation footprints were recognizable through BSE images. The equipment used for this analysis was a FEI Nova Nano SEM 650 , which has a SE/BSE (Secondary Electrons/Backscattered Electrons) in-lens detector and is coupled with a low vacuum solid-state detector BSED (GAD), as well as an EDS detector by Oxford Instrument. EDS spot analysis was conducted at 15 kV in low vacuum mode (60 Pa) for around 25 indentation points per specimen; for each spot, X-rays spectra were collected for 60 s. The spot analyzed through EDS coincided to a circular portion passing through all the three vertices of the triangular footprint of each indent, as sketched in Figure 7.19.

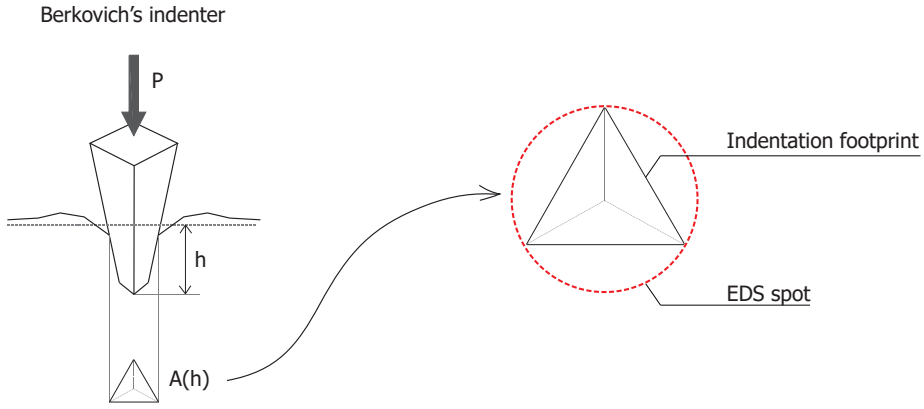


Figure 7.19: (left) footprint of Berkovich's indenter; (right) EDS circular spot;

The relation between the $E_{cp}$ and Fe concentration (in weight percentage [wt%]) for each analyzed indentation point is shown below (Figure 7.20). More information which indentation footprints were EDS analyzed are visible in Appendix D.X.

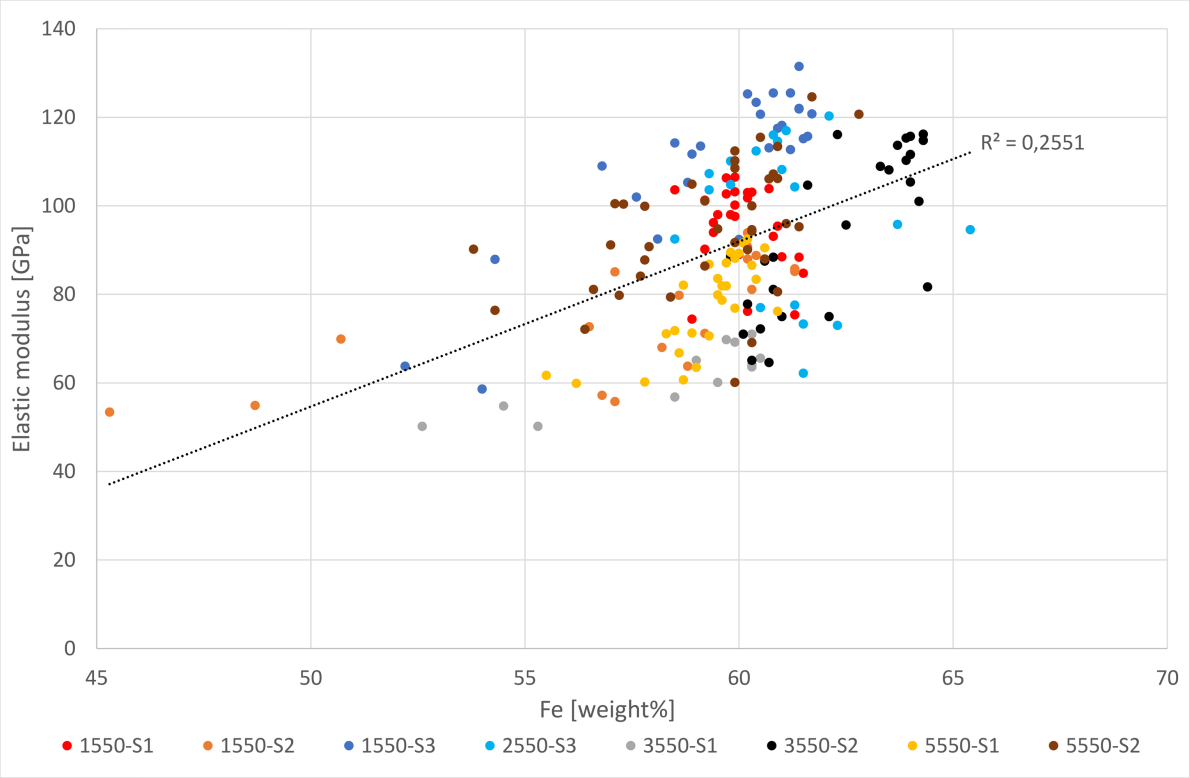


Figure 7.20: Relation between $E_{cp}$ [GPa] and Fe concentration [wt%];

In Figure 7.20 the relation between $E_{cp}$ and Fe concentration is shown. As pointed out previously, $E_{cp}$ of "undisturbed" corrosion product ranges between around 50-125 GPa, while Fe [wt%] ranges between 50-65%. The trending relation between these two parameters that was suggested by $E_{cp}$-Fe [wt%] profiles (Figure 7.11-7.18) is further confirmed here. Higher the Fe [wt%] of the indented location, higher the related $E_{cp}$. However, the $R^2$ factor clearly shows that the relation is far from accurate. This fact is explainable by the fact that standard-less analysis was used to measure the iron concentration. This implies that the Fe [wt%] should not be considered as absolute value, making the Iron concentration measured for different specimens incomparable. However, if considering specimens singularly and relative Fe [wt%], the (reliable) trend between iron concentration and $E_{cp}$ clearly shows a proportional relation, which is discussed below.

To evaluate the absolute values of $E_{cp}$ as well as the influence of Fe concentration (and wt% profiles) on $E_{cp}$, it is worthy to analyze the fundamentals of how the modulus of elasticity (E) is defined and on what parameters it depends. As well known, the modulus of elasticity is defined as the slope of the stress-strain curve in the elastic deformation region, and it is widely used in engineering to evaluate the stiffness of materials. It is also well known that E depends on micro characteristics of the material, such as its micro-structure, its chemical composition and, more precisely, on the bond (potential) energy between the atoms that the material is made of. The bond energy between atoms is defined as the bond strength in a chemical bond. Among others, these chemical bonds can be ionic, covalent or metallic, depending on the nature of the atoms. Chemical bonds between atoms are formed at a certain inter-atomic distance, $r_0$, at which there is no repulsion nor attraction between atoms due to their electromagnetic interaction. At $r_0$ atoms combine to make a compound, and energy is released (hence the compound has always lower energy than the singular atoms). To disassemble a system of particles into separate particles, an amount of energy higher than the binding (or separation) energy has to be supplied. Application of stresses imply that potential energy is supplied to the material that is stressed. The deformation behaviour of the material subjected to these stresses depends on its inter-atomic bond energy. Higher the atomic bond energy, higher binding separation energy has to be supplied to disassemble the compounds, hence higher the modulus of elasticity. At the same time, the

bond strength is built upon the charges of the atoms, so higher the valency of the atoms and greater the bond energy, hence the Elastic modulus. This mechanism can be also observed if analyzing the slopes of inter-atomic force-distance curves of two materials with different stiffness, as visible in Figure 7.21.

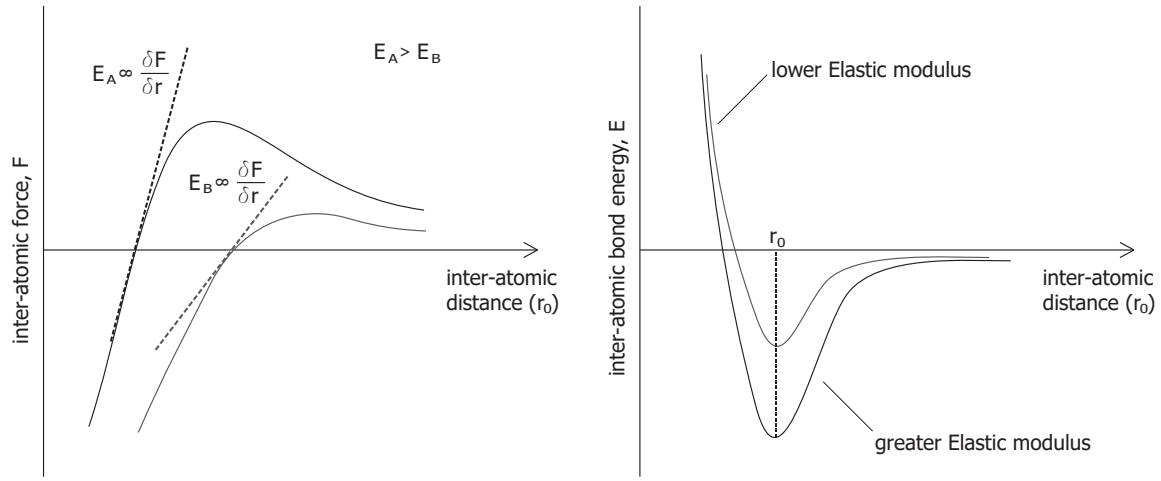


Figure 7.21: (left) Inter-atomic force-distance curves of two materials with different stiffness; (right) Bond potential energy-distance curves of two materials with different stiffness;

When performing nano-indentation test, the location that is nano-indented might be a cluster of different components, and not corrosion product only. This is also suggested by EDS elemental maps and spot analysis, where some very small amount of Ca and Si are sometimes visible in the corrosion product. Based on the results shown in Figure 7.11-7.18, it looks that Fe concentration overall makes the bond energy of indented cluster to increase, which would explain the overall proportional relation between Fe [wt%] and $E_{cp}$. Higher concentration of iron implies stronger chemical bonds between the components of the indented spot, hence increasing its elastic modulus of the whole cluster. On the contrary, cement-related components (i.e. Ca and Si) are less stiff than Fe, so higher their content then lower the modulus of Elasticity of the indented cluster. Indeed, the inter-atomic distance of CaO is equal to around 2.4 Å, which is higher than the around 2.1 Å of FeO and $Fe_2O_3$. SiO has lower inter-atomic distance, equal to around 1.60 Å [105]. However, the valency of $Fe^{III}$ is higher than the one of Si, which might cause a higher bonding energy of the iron oxides rather than silicon oxides. This might also be suggested by the higher melting temperature of iron rather than the one of silicon, equal to 1538°C and 1414°C respectively. Limitations about the adopted techniques and methodologies should be specified to stress the likely dependence of modulus of elasticity on other parameters rather than iron concentration only, as Figure 7.20 suggests. In this section, no standard-based EDS analysis was conducted, hence the content of some components (i.e. oxygen) might not be accurate, due to the porosity of the corrosion product. Although nano-indentation gives consistent results about the micro-mechanical properties of indented locations, the relation between chemical composition and modulus of elasticity reported here gives a trending dependence, which however cannot be considered as absolute.

## 7.4. Standard-based EDS spot analysis

From the analysis reported above, it was observed that E and Fe [wt%] profiles within each indentation grid had very similar pattern. For each specimen, it might be the case that higher Fe content leads to higher atomic bond energy (or higher stiffness of the cluster), hence resulting in higher elastic modulus. This statement seems to be valid for both undisturbed corrosion product but also for corrosion product mixed/penetrating into the surrounding cement paste. However, due to the well-known limitations related to standard-less EDS analysis, it was not possible to make accurate analysis about the relation between the absolute concentration of each component at certain locations and the related elastic modulus for different specimens at the same time.

To clarify some points that were left open by standard-less EDS mapping and analysis, standard-based EDS spot analysis (STD) was also conducted. These points were, for instance, if the elastic modulus of corrosion product is influenced by the Fe/O and by the likely corrosion product compound that is indented. For the microanalysis, a Philips XL30 ESEM equipped with an EDAX energy-dispersive spectrometer was used in the hi-vac chamber condition. The EDS detector used was a SUTW (sapphire) type. Only 1550-S1 was considered for this analysis. More specifically, 20 spots of the of the steel/concrete interface of 1550-S1 were EDS/STD analyzed. These points corresponded to the portion of the interfacial zone just below the last row of the indentation grid (n.1-20 black dots on the right-hand side, Figure 7.22). EDS spot analysis was conducted at 15 kV of acceleration voltage (contrarily to what Figure 7.22 suggests, which was taken for reporting only), and at each spot X-rays spectra were collected for 60 s. Based on natural minerals and pure metals, which were used as reference standards, quantitative analysis were made for Fe, O, Ca, Cl, Si. Analysis totals (i.e. the sum of all the elements present) were determined assuming that oxygen is bound by predefined stoichiometry to all the other analyzed elements. The Elastic modulus profile (on the left-hand side, Figure 7.22) corresponds to the $E_{cp}$ of the bottom indentation row only.

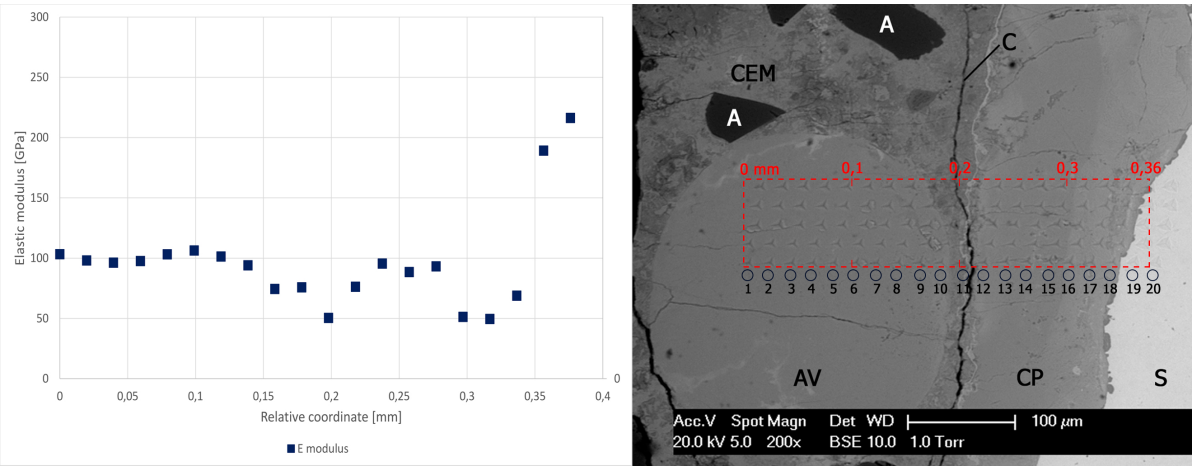


Figure 7.22: 1550-S1: (left) Elastic modulus profile of bottom indentation row; (right) indentation grid (red-dashed) and EDS/STD spot analysis (black dots n.1-20)

The relation between the Elastic modulus of each spot (n.1-20) and its concentration profiles within the indentation grid is shown and analyzed below (Figure 7.23-7.24), while relation between singular indented spots is visible in Figure 7.25-7.26.

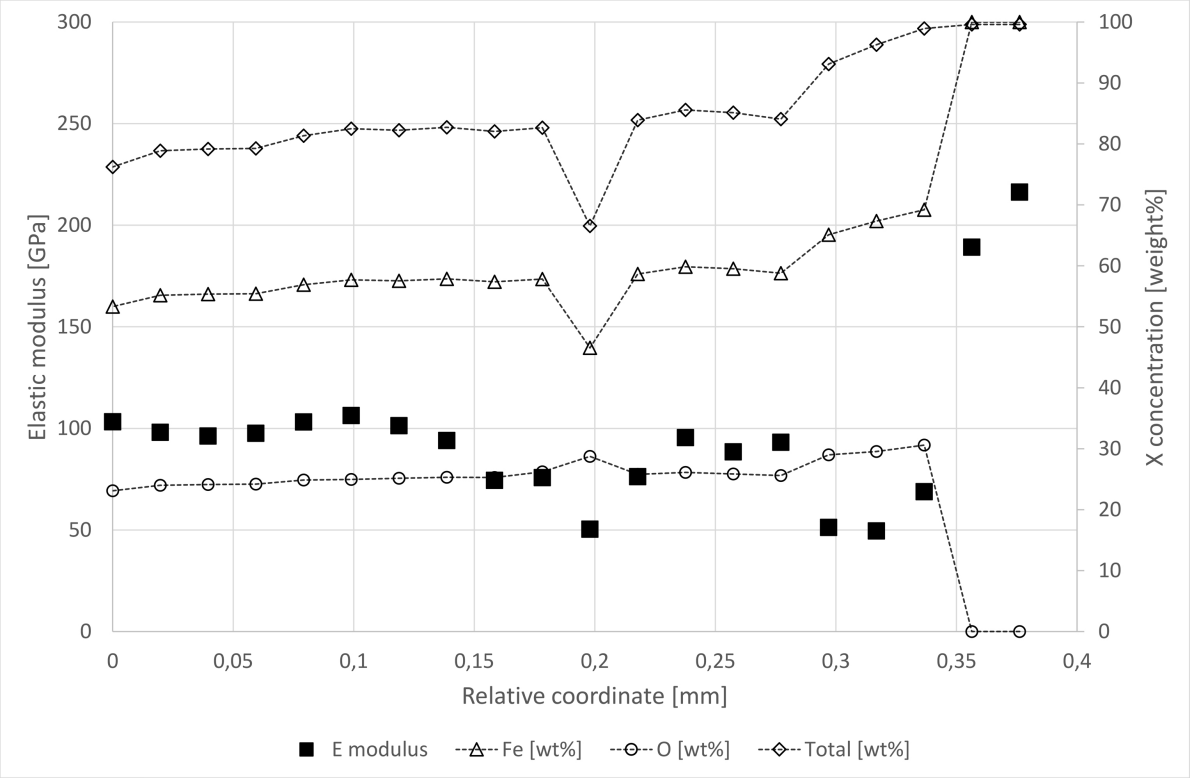


Figure 7.23: 1550-S1: Profiles within indentation grid: Elastic modulus [GPa] (squares), Fe [wt%] (triangles), O [wt%] (circles) and total [wt%] (diamonds);

In Figure 7.23, the profiles of Fe, total O and total concentration [wt%] are plotted against the related Elastic modulus [GPa] of indented spots. Interestingly, three well-defined bands of corrosion product (with different $E_{cp}$, Fe and total concentration) can be identified. Between 0.30-0.35 mm, $E_{cp}$ ranges between 50-75 GPa. At the same time, this portion has the highest concentration of Fe, O and total, ranging between 65-70 [wt%], 28-31 [wt%] and 94-98 [wt%] respectively. At 0.28 mm, $E_{cp}$ increases up to around 95 GPa, while Fe, O and total [wt%] simultaneously decrease by around 10%. At 0.2 mm, a steep decrease is visible for $E_{cp}$, Fe and total [wt%], with consequent decrease in O concentration. This portion corresponds to the presence of a visible crack (see also Figure 7.22). Between 0.15-0.0 mm, the $E_{cp}$ stabilizes at around 100 GPa, while Fe, O and total [wt%] continuously decrease down to 52 wt%, 24 wt% and 75 wt% respectively. Overall, the concentration of Fe, O and total [wt%] decrease continuously while getting far from the steel reinforcement. On the contrary, $E_{cp}$ followed the opposite pattern, decreasing if getting closer to the steel reinforcement. Apart from the relation between Fe, O and total concentration [wt%] and $E_{cp}$, also the concentration of other components within the indentation grid has been analyzed, as reported in Figure 7.24.

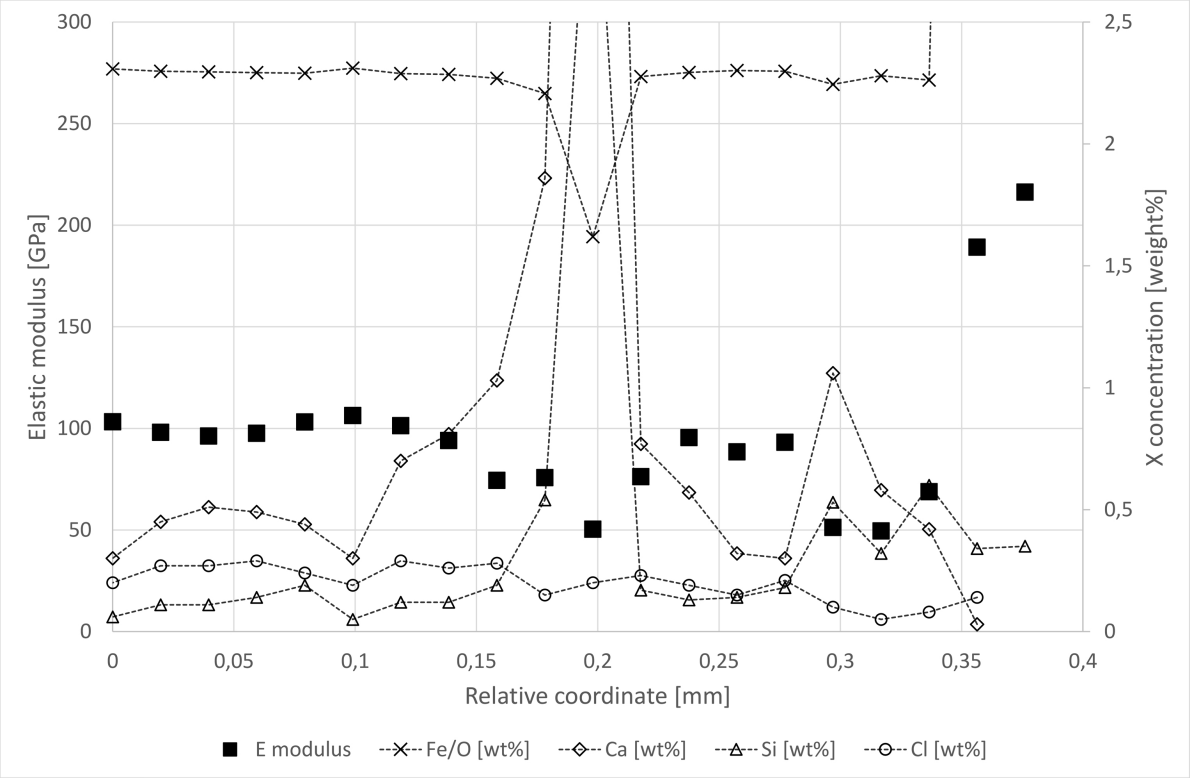


Figure 7.24: 1550-S1: Profiles within indentation grid: Elastic modulus [GPa] (squares), Fe/O [wt%] (crosses), Ca [wt%] (diamonds), Si [wt%] (triangles), Cl [wt%] (circles);

In Figure 7.24, the profiles of Fe/O, Ca, Si and Cl concentration [wt%] are plotted with the related Elastic modulus [GPa] of indented spots. Interestingly, Fe/O stays almost constant at any coordinate of the indentation grid (between 2.24-2.31 [wt%]), apart from a steep decrease close to a crack (at 0.2 mm). Similar constant progress is found also for Cl [wt%], which however is never higher than 0.5 [wt%]. Furthermore, it is also visible that higher Ca and Si concentration [wt%] roughly corresponds to lower Elastic modulus of the indented locations (especially for the cracked portion at around 0.2 mm and between 0.28-0.32 mm).

Apart from the concentration profiles as shown in Figure 7.23-7.24, also the relation between component concentration and elastic modulus of singular indented spots was analyzed, as visible below (Figure 7.25-7.26).

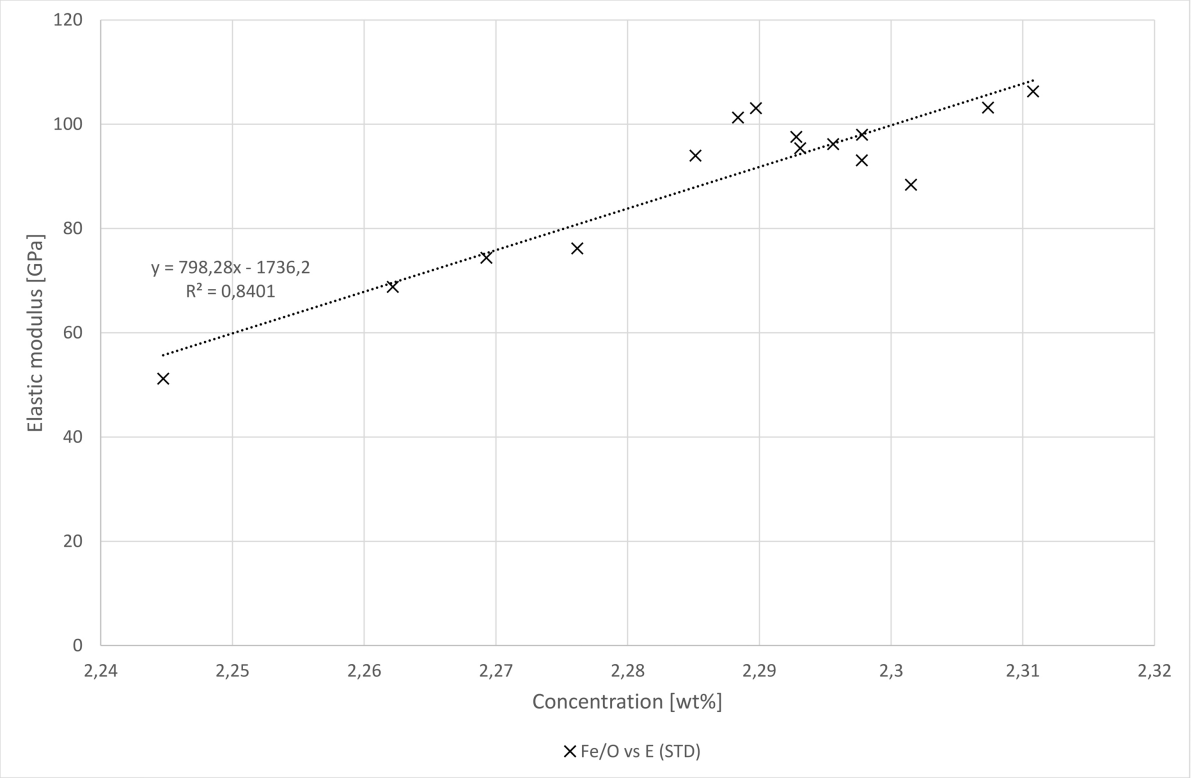


Figure 7.25: Relation between $E_{cp}$ and Fe/O [wt%], with $R^2$=0.84;

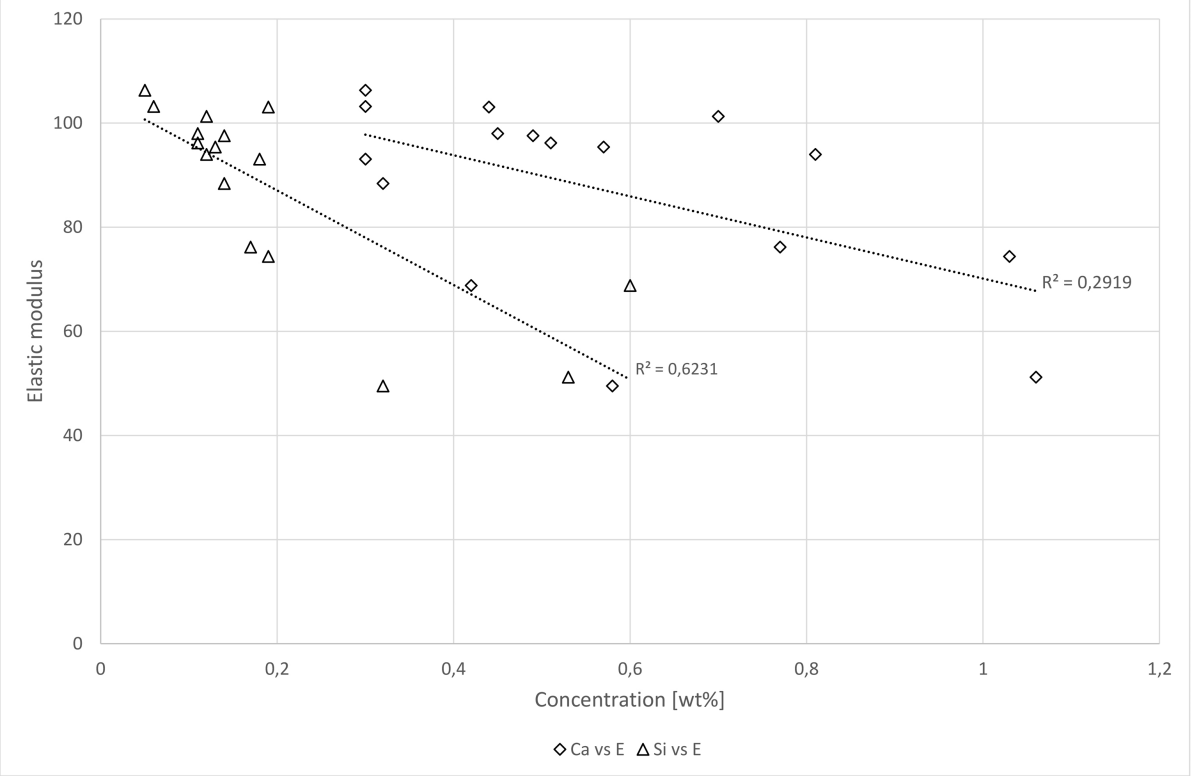


Figure 7.26: Relation between $E_{cp}$ and both Ca and Si [wt%], with $R^2$ of 0.62 and 0.29 respectvely

From Figure 7.25-7.26, interesting observations can be conducted. On the one hand, it was pointed that the Fe/O stays almost constant within the indentation grid, with values between 2.24-2.31 wt% (or 0.64-0.66 at%). Even though the range of variation of Fe/O is relatively slight, it almost linearly corresponds to a related variation of Elastic modulus, with $R^2$ of 0.84. On the other hand, in Figure 7.26 it is visible how higher concentration of cement-related components (i.e. Ca and Si) roughly corresponds to a decrease in the elastic modulus of the related indented locations.

From the analysis reported above and earlier in this report, many points can be discussed. At first, indents with higher concentration of cement-related components (i.e. Ca and Si) have lower Elastic modulus. This finding is in line with what was already observed and discussed previously, sounding reasonable if considering the working principle of techniques used here. In other words, when performing nano-indentation, the output modulus of Elasticity is representative of the indented location, which is likely to be a cluster of different compounds. When indenting the portion of corrosion product penetrating into the cement paste, the related Elastic modulus is lower than the one of the "undisturbed" corrosion product. This is because the former locations have higher Ca and Si concentration (and so lower Fe), resulting in a less stiff cluster. However, different amounts of Ca, Si and Cl [wt%] are also found in portions of "undisturbed" corrosion product. Overall, higher the quantity of these components, lower the related $E_{cp}$.

Even though the Fe/O along the indentation grid was almost constant (2.24-2.31 wt%, equivalent to 0.64-0.66 at%), slight variations of Fe/O corresponds to significant variations of $E_{cp}$. The relation between these two parameters appear to be relatively linear, with a $R^2$ of 0.84. The proportional relation between Fe/O and $E_{cp}$ was already suggested by Zhao et al. [64]; however, they based this suggestion on Fe/O measured through standard-less EDS analysis and this relation was never investigated more in depth according to the present literature. The results reported here seem to confirm this relation, which is likely to happen for the lower bond energy of the compound if the oxygen concentration is higher. However, it must be specified that in this section of the report only a few locations were both nano-indented and EDS/STD analyzed. To make this relation more consistent, more data would be needed.

It is interesting to notice that Fe/O did not vary for differently-looking corrosion product bands. This finding is contrary to what was observed by others [67] [96]. Wong et al. [96] observed that different corrosion product bands had Fe/O varying of around 0.30 at% (0.84 at% for the lighter bands, 0.55 at% for the darker bands). They stated that different Fe/O ratios were representative for different oxygen supplementation of the environment where the corrosion product was formed (higher when Fe/O is lower). In this research, no significant variations of Fe/O were observed (between 0.64-0.66 at%). On the contrary, it is the total wt% which varies significantly within the indentation grid (hence getting more distant from the steel). It is indeed visible from Figure 7.22-7.23 that differently-looking portions of corrosion product have relatively different total concentration. The light corrosion product band close to the steel (between 0.30-0.35 mm) have 92-97 wt%; between 0.24-0.30 a darker band is clearly visible, with related total that varies between 83-86 wt%; a total of 78-82 wt% is then coincident for the portion of corrosion product between 0-0.15 mm. These three bands have different ranges elastic modulus of 50-75 GPa, 80-95 GPa and 90-110 GPa respectively. In other words, appearance, total [wt%] and $E_{cp}$ of corrosion product vary simultaneously, and the latter two are inversely proportional. The variations of total [wt%] are likely to be related to the carbon and water content of different corrosion product bands. Corrosion product between 0-0.15 mm is the portion with highest water content (or lowest total [wt%], getting denser if closer to the steel reinforcement. Finding higher water content for corrosion product more far from the steel sounds reasonable because of the likely higher availability of water and oxygen of the former portion rather than the one expected if attached to the steel (because of the more components oxygen and water would have to overpass in this latter case). However, it was also observed that the portion with higher water content is the one with higher Elastic modulus (between 90-110 GPa). Since higher water content would probably lower the inter-atomic bonding energy of the corrosion product cluster, this finding is unexpected. It might be the case that penetrating epoxy disturbed the measurements of Elastic modulus at the locations where higher content of epoxy is found, of which $E_{cp}$ would have been lower if pores were not filled.

Furthermore, it was previously mentioned that corrosion product compounds probably have different Elastic modulus because of their own inter-atomic bonding energy. Also in previous researches, different appearance of corrosion product bands was related to different corrosion product compounds that the bands were made of and also of their Fe/O. For this reason, in Figure 7.27 Elastic modulus of each indent is plotted against its Fe/O, highlighting which Fe/O belongs to which compound of corrosion product.

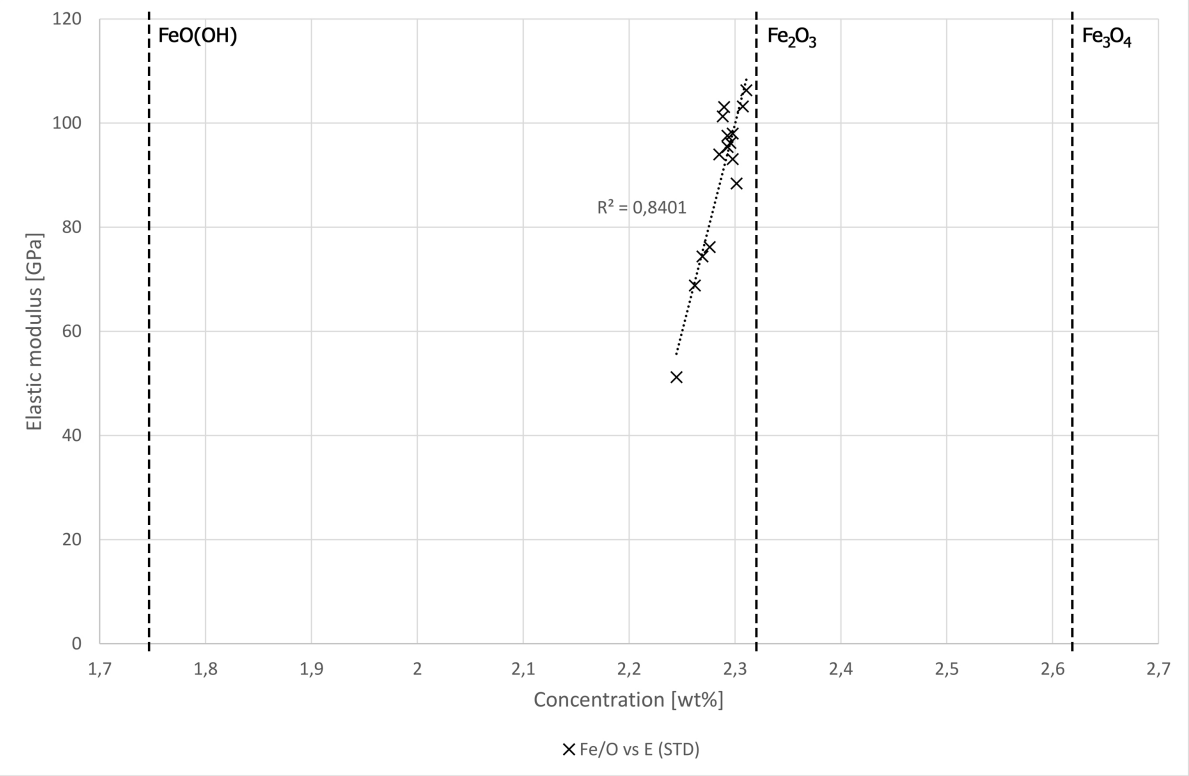


Figure 7.27: Elastic modulus [GPa] against Fe/O [wt%] of corrosion product with highlighted Fe/O of different compounds

Looking at Figure 7.27, it is visible that the corrosion product that was EDS/STD analyzed might belong to a mix of compounds with main presence of $Fe_2O_3$. Most of the indented locations have Fe/O that suggest they are made of $Fe_2O_3$ (which has Fe/O equal to 2.32 wt%), with Elastic modulus ranging between 90-110 GPa. A few locations have also lower Fe/O, that might suggest that these locations are made of a mix of different compounds. Since 1550-S1 was also analyzed through XRD (as reported later in Section 7.5) and goethite was identified, it might be the case that the indents with lower Ecp are formed by a combination of $FeOOH$ and $Fe_2O_3$. Since FeOOH has lower inter-atomic bonding energy (due to the presence of hydrogen, for instance) than $Fe_2O_3$, higher content of goethite (so lower Fe/O) would explain the lower Elastic modulus. However, Fe/O stays always higher than 2.22 wt%, which is relatively far from the 1.74 wt% representative for goethite, hence the lower Elastic modulus of some locations cannot be clearly explained by the fact that those locations are formed by a mix of compounds. Although it seems clear that differently-looking corrosion product bands have different Elastic modulus, the main factor that causes these differences remains an open question for future research. It might be the case that different appearance of corrosion product bands belongs to the time at which corrosion product was formed rather than its chemical composition. Another factor that might have influenced the properties of the corrosion product bands is the pH gradient at the location where corrosion product is formed. Indeed, the pH close to the corrosion pit is likely lower than the pH more far from the reinforcement. Different pH might have affected the precipitation of components when corrosion product is formed, resulting in, for example, different grain size and hence different appearance. Since in this study it was not possible to clarify this dependency, further research about this topic is needed.

## 7.5. X-ray Diffraction

Eight corrosion product samples were peeled from the steel bars and characterized through a Bruker D8 Advance diffractometer equipped with a Lynxeye detector with opening angle of 2.94°. with working at 40 kV and 40 mA. The data of the experiment were collected at room temperature using Cu Kα radiation (λ = 1.5406 Å) over a 2θ range of 10°-40°, step size 0.02 degrees 2θ. The sample was deposited on a zero background holder and was rotated at 15 rpm during the measurement. Generator settings were 40 kV and 40 mA. After data collection, phase identification was carried out with the Bruker program "EVA4.2." and based on the judgment of the expert. The XRD patterns for the eight corrosion product samples is visible in Appendix D, Figure D.27-D.34. For each sample, a summary of the main phases identified through XRD is reported in Table 7.1 as well as the code of the sample. The bars from which the corrosion product was peeled did not correspond to the bars analyzed through Nano-indentation nor SEM/EDS, but they were belonging to the same concrete specimen and they had equal cover depth. The letter C, R and L indicate the location of the bar with regard to the whole concrete specimen, as visible in Figure 5.5.

Table 7.1: Main identified crystalline phases for each corrosion product powder sample

| **Sample** | **Main crystalline phases** |
|---|---|
| 1550-S1(C) | Quartz; Goethite; Calcite |
| 1550-S2(R) | Quartz; Goethite; Calcite; Maghemite |
| 1550-S3(C) | Quartz; Calcite; Portlandite |
| 2550-S3(L) | Quartz; Portlandite; Goethite; Lepidocrocite |
| 3550-S1(L) | Quartz; Goethite; Calcium Carbonate |
| 3550-S2(R) | Quartz; Goethite; Lepidocrocite; Portlandite |
| 5550-S1(L) | Quartz; Goethite; Calcite |
| 5550-S2(L) | Quartz; Goethite; Portlandite; Lepidocrocite; Calcite |

For the components that belong to corrosion product, goethite (α-FeOOH) was qualitatively identified in all the samples. Further lepidocrocite (ɣ-FeOOH) was identified in 2550-S3, 3550-S2 and 5550-S2, while maghemite (γ-$Fe_2O_3$) was identified in 1550-S2. The presence of α-FeOOH only for some of the samples might be related to the transformation of lepidocrocite into goethite during the years, as found by [92] [93], thus resulting in no ɣ-FeOOH identified. Maghemite was also identified for 1550-S2 only. However, $Fe_2O_3$ is considered a component of the mill scale which formed along the steel reinforcement before corrosion initiation, due to the high temperature that it needs to be formed that are rarely reached during service in structures [46] [70]. Mill scale portions were probably collected when peeling corrosion product from the steel reinforcement.

An interesting point of XRD patterns is that no β-FeOOH was identified in any of the samples. Based on the literature, akageneite is generally found in reinforcement exposed to environment with relative high concentration of $Cl^-$. This is due to the fact that the formation of β-FeOOH needs halogen ions (i.e. chloride ions) to stabilize the tunnel structure of the akageneite crystals [46] [47] [50] [51] [92]. Same presence of β-FeOOH was also found by Zhao et al. [70], Zitrou et al. [94] and De la Fuente et al. [95]. Nishimura et al. [51] observed that the content of β-FeOOH increased with increasing the concentration of $Cl^-$ in the environment and the exposure time. In this research, specimens were exposed to salt wet/dry cycles for 6 months only out of 20 years of "service-life", which was probably not permanent enough to imply a relevant formation of β-FeOOH. Chloride profiles were also measured by Guerreri et al. [81] when specimens were 2,5 years old: it was observed that the concentration at the reinforcement location was lower than expected, suggesting that chlorides migrated through the specimens without stabilizing at the steel location, which would have probably led to the formation of β-FeOOH.

Other components, such as quartz, calcite and portlandite were identified for most of the samples; these latter ones are likely belonging to concrete portions attached to the steel reinforcement (perhaps carbonated for 2550-S3 and CEM III specimens). Moissanite-3C and silicon carbide are also identified for most of the samples, which are related to the grinding sander paper that was used to clean the reinforcement mechanically.

## 7.6. Propagation of corrosion product into air voids

Even though some researches focused on the influence that air voids at the steel/concrete interface might have on the initiation of corrosion of the steel reinforcement (as reported in Section 2.3), only a few authors focused their attention into investigating how corrosion product propagates into these macro-defects [11] [96]. In the present research, penetration of corrosion product into air voids was qualitatively observed through BSE images of the steel/concrete interface of different specimens, some of which are reported below (Figure 7.28-7.29, see also Appendix D.4).

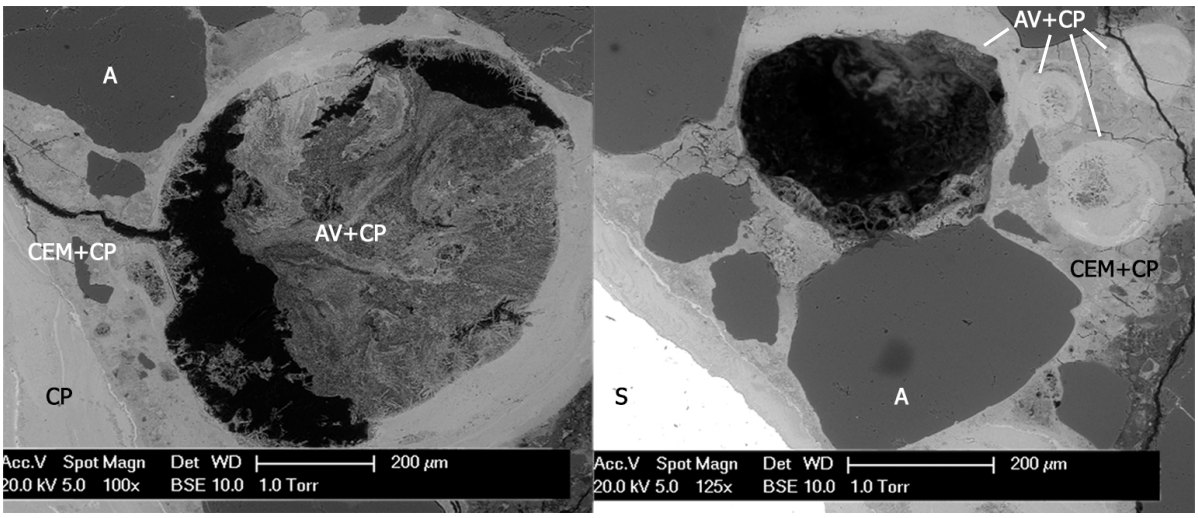


Figure 7.28: BSE image of corrosion product penetrating into air voids at the steel/concrete interface with labeled components (S=steel; CP=corrosion product; CEM=cement; AV=air void; C=crack; A=aggregate)

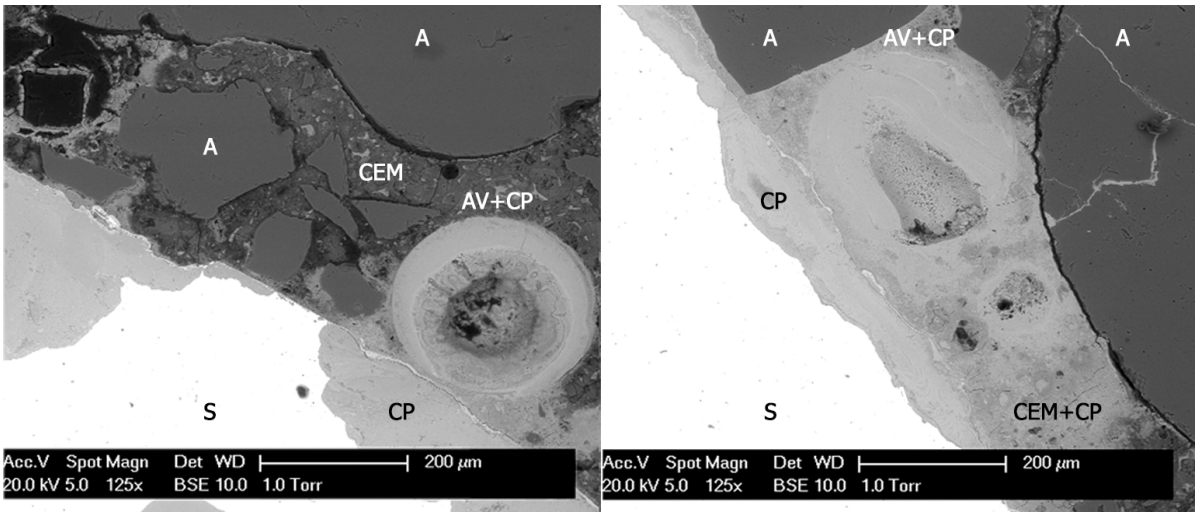


Figure 7.29: BSE image of corrosion product penetrating into air voids at the steel/concrete interface with labeled components (S=steel; CP=corrosion product; CEM=cement; AV=air void; C=crack; A=aggregate)

In Figure 7.28-7.29, it is interestingly visible how corrosion product penetrates into air voids at the steel/concrete interface. In most of the voids, corrosion product seems to be concentrically stratified, following the circumference of the void itself. In Figure 7.28-7.29 (left BSE images), partially filled voids are visible, with apparently compact corrosion product at the edges of the defects while more porous corrosion product in the centre. Similar pattern is visible also in completely filled air voids (Figure 7.28-7.29, right BSE images), where the defects appear filled from the edges to the center. It is also interesting to note that the thickness of the corrosion product layer of completely filled voids concentrically diminishes if getting closer to the steel reinforcement, while it stays thicker at the most far edge from the reinforcement (see especially Figure 7.29 (right BSE image)).

Similar penetration of corrosion product into air voids at the steel/concrete interface was already observed by Wong et al. [96]: in that research, similar concentrically stratified pattern of corrosion product is visible through BSE images of the SCI, as well as less dense portion of corrosion product in the center of air voids. However, no deeper investigations about the penetration of corrosion product into air voids was conducted.

Savija et al. [11] observed corrosion product penetration into air voids by means of CT-scan when corrosion was anodically accelerated. In his research, it is interesting to observe how corrosion product propagates into inter-facial defects: from the reinforcement edge, corrosion product is formed and expands in volume, gradually starting to fill the void from the location where a corrosion pit is growing. However, based on the above-reported BSE images and what was observed by Wong et al. [96], it is unlikely to think that corrosion would propagate continuously following that ”cauliflower-like” progress. If this was the case, the edges of air voids far from the reinforcement would be the last-in-time locations where corrosion product would get to, and the void would be filled gradually from the steel. This behaviour is different from what that these images suggest, where the center of the voids seem to be the last-in-time place to be filled by corrosion product expansion.

The concentrically stratified filling of air voids suggest that corrosion product migrates to the edges, probably being transported by liquid solution. In other words, it might be the case that air voids get (partially or completely) saturated by watery solution (i.e. wet/dry cycles due to environmental precipitations). Getting saturated, corrosion product would mix with the saturating solution, thus migrating from the edges of the reinforcement. However, if drying of the solution occurs, the dissolved corrosion product would then precipitate at the edges of the air void. A series of this dissolution/precipitation of corrosion product due to wet/dry cycles of air voids would imply that air voids at the steel/concrete interface would be filled concentrically stratified, as observed in this research.

It must be specified that this progress of corrosion product penetrating and filling air voids was based on observations only. No experiments nor other literature was found that could clarify (or reject) this phenomena. How corrosion product propagates into concrete defects at the SCI might play an important rule when modelling corrosion propagation of reinforced concrete structures. If this was the case, pressure due to volume expansion would be exerted through each corrosion product’s layer and finally released to the surrounding concrete. Since different layers have clearly different appearance and likely different properties (i.e. Elastic modulus), speculating how the stresses would be transferred from layer to layer is a challenging issue. Further research is needed in order to clarify this behaviour.

# 8

# Conclusions and recommendations

## 8.1. Conclusions

The state of naturally-generated corrosion of steel reinforcement embedded in 20 years old concrete specimens has been studied in this research. This project carried out three main levels of characterization. The macro-scale level consisted of characterizing the corrosion state of specimens after almost 20 years of outside exposure, by means of destructive techniques and microscopy analysis. The meso-scale level consisted of quantifying the volume loss due to corrosion and the relation between corrosion pits, defects at the steel concrete interface (i.e. air voids) and orientation of the reinforcement through X-ray Computed Tomography. The micro-scale level consisted of evaluating the modulus of elasticity, micro-structure and chemical composition of corrosion product by means of Nano-indentation and SEM/EDS elemental mapping and spot analysis and XRD. Conclusions for each characterization level are reported as follows:

### Macro-scale characterization of reinforced concrete specimens

- The combination of analysis of BSE images and Non-destructive electro-chemical measurements is an effective way for identifying the cement type that concrete mixes are made of. The identification carried out in this research confirmed the identification made in 2010 through visual inspection and statistical analysis of electro-chemical measurements for 7 out of 8 specimens according to Pacheco [8]. The number of specimens for each cement type that were analyzed in this research was then as follows: 3 for CEM I (1550-S1, 1550-S2, 1550-S3), 1 for CEM II (2550-S3), 2 for CEM III (3550-S1, 3550-S2) and 2 for CEM V (5550-S1, 5550-S2).
- Electro-chemical measurements recorded in 2018 suggested a less aggressive on-going corrosion than historical measurements. When measurements were recorded the low outside temperature might have influenced the corrosion state of the reinforcement, resulting in values non representative for the long-term corrosion state of the bars. Since electro-chemical measurements represent the on-going corrosion state of the reinforcement at the time of measuring only, isolated-in-time values should be always considered with caution.
- Carbonation depth was destructively measured for all prisms. CEM II and CEM III specimens showed to be the most carbonated ones, with carbonation depth up to 10 mm (2550-S3) and to 18 mm (3550-S1). Lower carbonation resistance of blended cement concrete is in accordance to the lower CH content of these mixes after their hydration thanks to the pozzolanic behaviour of their fillers. On the other hand, CEM I and CEM V specimens had carbonation depth lower than 10 mm. The higher carbonation resistance of the former ones is likely related to the higher amount of CH resulting from hydration of Portland cement if compared to blended cements. For CEM V specimens, the combination of dense micro-structure and higher CH content than CEM III might have provided an improvement of the their carbonation resistance, resulting in carbonation depth lower than 5 mm after 20 years of exposure. Differences between specimens with same

cement type might be caused by different exposure conditions to which specimens were exposed between 6 months and 2,5 years old, which remain unknown.

### Meso-scale characterization of steel reinforcement

- X-ray Computed Tomography proved to be a powerful Non-Destructive tool to quantify the volume loss of reinforcement due to corrosion, to evaluate the distribution of corrosion pits along the length of the reinforcement and to analyze the most sensitive locations at the steel/concrete interface for corrosion to initiate.

- The volume loss due to corrosion quantified through X-ray Computed Tomography was mostly in line with what suggested by historical electro-chemical measurements. Only 1550-S2 had differences between the results of these two techniques. This difference might be explained by the fact that electro-chemical measurements were taken every several years, thus they might have been not really representative for the corrosion progress during the whole service life.

- Specimens with higher carbonation depth were found to be the least corroded (i.e. 2550-S3, 3550-S1, 3550-S2). In this sense, it is likely that the formation of $CaCO_3$ (from the reaction between $Ca(OH)_2$ and $CO_2$) densified the micro-structure of the concrete, thus improving the corrosion resistance of the mix.

- Defects at the steel/concrete interface are the leading factor which causes deep corrosion pits to grow. On the one hand, when significant cracks are present, the volume loss of reinforcement is mainly found at the steel portion oriented to the outside environment (i.e. 5550-S2). On the other hand, when macro-voids are present at the steel/concrete interface also one (at least) corrosion pit is visible nearby. Corrosion pits are also found nearby dense cement paste surrounding the steel: however, these pits were found to be more superficial than those found nearby defects. This fact might be explained by the buffering effect provided by the dense cement paste surrounding the steel, keeping the local chloride concentration lower than the threshold level for corrosion to initiate and then propagate. The combination of concrete defects at the steel/concrete interface and orientation to the outside environment was found to be the case where deepest corrosion pits were measured. This statement sounds reasonable considering that, firstly, defects cannot provide buffering effect for corrosion to initiate and, secondly, wet/dry cycles of solution are likely to be more frequent at the outside-exposed portion of the steel, due to the lower concrete cover that the water has to penetrate.

### Micro-scale characterization of corrosion product

- The Elastic modulus of undisturbed corrosion product ranged between 60-120 GPa for all the specimens (except for 3550-S1, of which results were compromised but the test procedure also looking at the non-accurate E of un-corroded steel). Presence of cracks as well as concentration of Ca and Si higher than 5 wt% (representative for corrosion product mixed with/penetrating into the surrounding cement paste) cause a decrease of E (as already pointed out by Savija et al. [11]), which ranged between 25-55 GPa.

- From a Civil Engineering point of view, no significant differences have been found between $E_{cp}$ measured in different specimens. To model corrosion progress of reinforced concrete structures, $E_{cp}$ equal to 80-90 GPa is suggested. This value does not significantly differ from values of $E_{cp}$ found by others through nano-indentation [11] [64]. However, contrarily to what was previously done, in this research only naturally generated corrosion product was analyzed, which is a point in favor to use $E_{cp}$ reported here.

- Corrosion product penetrating into the surrounding cement paste was observed. Penetration of corrosion product probably happened before cracks were induced, with these latter ones becoming preferable accommodating regions for corrosion product to expand as soon as they were formed. Since no anodic accelerated corrosion was induced to the specimens in this research, corrosion likely proceeded during time in a gradual way, allowing the surrounding cement paste to accommodate it without premature cracking. This finding confirms again the need of including a certain accommodating region for corrosion product when modelling cracking of reinforced concrete due to corrosion.

- Corrosion product clearly appeared to be made of distinct and adjacent bands, well-defined by different appearance (in BSE mode) and $E_{cp}$. However, as already pointed out by others [102], no agreement about one specific pattern of these layers could be made.

- Through processing EDS elemental mapping, it was observed that higher the Fe concentration [wt%] of the indented locations (for both "undisturbed" and corrosion product mixed with cement paste), higher the related $E_{cp}$. This finding might be related to the likely higher atomic bond energy and stiffness of the indented cluster with higher Fe concentration.

- Confirming what was previously speculated by Zhao et al. [64], based on the standard-based EDS analysis it looks that $E_{cp}$ is (linearly) dependent on Fe/O, with a $R^2$ of 0,84. However, since relatively slight variations of Fe/O (equal to 0,07 [wt%]) coincided to much more significant variations of $E_{cp}$ (which ranged between 50-125 GPa), to make this relation more consistent more data and investigation would be needed.

- The Fe/O of corrosion product formed in 1550-S1 suggested that corrosion product was made of a mix of compounds, with likely dominant content of $Fe_2O_3$ but also containing $FeOOH$. This is also suggested by XRD diffractograms since for 1550-S1 only α-FeOOH was identified. Lower the Fe/O, which is probably representative for higher content of $FeOOH$, lower the $E_{cp}$: this finding sounds reasonable considering that iron hydroxides are less stiff than iron oxides [46].

- Performing standard-based EDS spot analysis, it was observed that portions of corrosion with total [wt%] ranging between 75-85% had $E_{cp}$ of 90-110 GPa, while portions with 85-95% had $E_{cp}$ of 60-85 GPa. These portions were also clearly distinguishable by their different appearance (i.e. brightness). Different total [wt%] is representative for different corrosion product compound since the concentration difference between the measured total and 100% relies on hydrogen, carbon and water content. In this way of thinking, corrosion product with higher water content has higher Elastic modulus. However, since $H_2O$ would likely lower the bonding energy of the indented cluster, this finding is unexpected and raises questions for future research.

- Through XRD on corrosion product powder, goethite was identified for most of the specimens (except for 1550-S3, for which no iron-related compound were identified likely due to specimen manipulation or due to amorphous state of corrosion product). Lepidocrocite (for 2550-S3, 3550-S2 and 5550-S2) and maghemite (for 1550-S2 only) were also identified, with this latter one probably belonging to the mill scale layer of corrosion product. Even though specimens were exposed to 6-months accelerated NaCl cycles and contrary to previous studies, no akageneite was identified (which is frequently found in chloride rich environments), probably due to the relatively short time of exposure to NaCl solution if related to the whole 20-years service-life.

- Qualitatively analyzing BSE images of the steel/concrete interface of different specimens, corrosion product penetrating into air voids at the SCI was interestingly observed to be concentrically-layered. It is speculated that corrosion product migrates from the corrosion pit to the edges of the air void at first, gradually filling the void from the outer walls to the inside. Transport of corrosion product from the corrosion pit might be caused by wetting-drying cycles of watery solution which could wet the concrete environment (and so the voids) under wet conditions, mixing with corrosion product and then precipitating to the edges of the void when the concrete would dry out.

## 8.2. Implications for practice

The concept of "sustainability" defines the "the ability to maintain changes of processes and objects at a certain rate or level and in a balanced fashion, in which the exploitation of resources, the direction of investments, the orientation of technological development and institutional change are all in harmony and enhance both current and future potential to meet human needs and aspirations". When dealing with sustainability in the field of degradation of construction materials, the term has the meaning of the ability to predict the long-term performance of different systems and structures in their actual exposure environment. For this aim, many analytical and numerical models have been proposed in the literature that aspire to simulate how corrosion affects certain reinforced concrete structures as well as what are the consequences of corrosion. However, due to the dependency on many inter-related parameters, these models are still far from being accurate. In this research, the characterization of corrosion product formed in different concrete mixes was carried out, since characteristics of corrosion product are a relevant parameter for modelling how corrosion affects a structure. Differently to what previously done in the literature, in this study naturally-generated specimens and corrosion product were analyzed, excluding any possible approximations and artefacts related to accelerating corrosion in laboratory conditions. Among other results, an Elastic modulus of corrosion product equal to 80-90 GPa is suggested to be used in numerical models about corrosion of reinforced concrete, regardless the cement type of the structures. Ideally in the future, the corrosion state and structural capacity of a structure affected by corrosion could be assessed by these models, and a precise maintenance and repair plan would be possible without time- and money-consumes that are generally needed when inspecting and repairing a structure nowadays.

Generally in practice, the main factor that is under investigation when analyzing the corrosion state of a structure is the chloride content at different depths in the concrete. If the chloride content is higher than the chloride threshold level (equal to 0,4 wt%) at the depth where reinforcement is located, it is advised that corrosion could initiate at that location. However, it was observed by some researchers that the critical chloride content for corrosion initiation might be dependent on the localized conditions of the steel/concrete interface. More precisely, at the locations with defects at the SCI it seems that, to initiate corrosion, it is needed a chloride content lower than the one at the location where the cement paste is dense around the reinforcement In this research, it was observed that any time an air void was present at the SCI, a corrosion pit coincident to this void was also present. Practically speaking, it was observed that air voids at the steel/concrete interface seem to be the main factor that would cause the initiation of corrosion and further localized volume loss. If defects at the SCI will be proved to be the main factor on which corrosion initiation would be dependent, it might be the case that, in the future, investigations on the corrosion state of existing structures would not include chloride profiles as it does now, but attention would be more spent on the state of the steel/concrete interface as well as of the air content at the depth where the reinforcement is located. The relevance of this topic and the need of further research is also confirmed by the fact that many researchers and scientists are currently working on it (i.e. RILEM TC 262-SCI on the "Characteristics of the steel/concrete interface and their effect on initiation of chloride-induced reinforcement corrosion"), from which the scientific community of construction materials would benefit from.

In this study, corrosion product expanding into air voids at the steel/concrete interface was also observed. More precisely, it was observed that corrosion product precipitates at the edges of air voids at the SCI before filling the voids completely (see Section 7.6 for more details). The BSE images reported in this study suggest that corrosion product is transported to the edges of the reinforcement, likely by solution that might be present (or penetrate) inside the concrete. In the current literature, attention is generally focused on the study of corrosion initiation of the reinforcement, while only small research has been focused on the propagation phase. Even though corrosion propagation remains an important open point for the scientific and practice community dealing with construction materials, observations reported here might be useful for future research about understanding how corrosion propagates depending on the presence of defects at the steel/concrete interface. How corrosion product expands in the concrete surrounding the steel reinforcement remains an open question, which definitely needs further research to be better understood.

## 8.3. Recommendations for future research

In this project, the corrosion state and products of 20-years-old reinforced concrete specimens were characterized through several techniques. Since many questions regarding corrosion initiation and propagation in reinforced concrete are still open, there are many possibility for future research based on the findings of this research.

At first, the non-destructive nature and the analysis that X-ray Computer Tomography allows to conduct make this technique valuable when studying corrosion of steel in concrete. In this research, specimens were significantly corroded, so it was not possible to evaluate during time how and where corrosion inititates and the propagate. It would be interesting to evaluate the corrosion progress collecting scans at a certain time interval for specimens for which corrosion did not propagate yet, to evaluate the sensitivity of corrosion initiation to steel/concrete defects as well as how corrosion product penetrate into air voids and cracks. The regular monitoring of corrosion progress through CT-scans could give relevant insights about the fundamentals related to this mechanism.

In this research, it was observed that the type of cement used to cast the concrete did not overall influence the $E_{cp}$ of corrosion product formed in different mixes. Since corrosion product compounds are, to a certain extent, dependent on environmental factors such as oxygen supply, it might be interesting to investigate if different compounds (with different $E_{cp}$) would be found if analyzing specimens cast with different w/c but same cement type, according to the same experimental procedure conducted here in this study. Furthermore, as previously pointed out by Savija et al. [11] and confirmed in this research, it was observed that $E_{cp}$ measured through Nano-indentation is highly dependent on the level of confinement provided by the surrounding cement paste and/or by the presence of cracks. In this way of thinking, corrosion product formed in the same specimen would likely have different Elastic modulus depending on the local conditions at the steel/concrete interface, rather than depending on the different chemical composition or micro-structure. It would be then interesting to perform Nano-indentation on different locations at the same SCI, potentially with/without air voids and cracks close to the reinforcement, to evaluate the influence of the level of confinement provided by the cement paste on the Elastic modulus of corrosion product.

According to Angst et al. [104], comparing the chloride content at the steel to the critical threshold level ($C_{crit}$) of chlorides for predicting corrosion initiation does not adequately described reality. Hypothesis of some scientists is that local conditions at the steel/concrete interface strongly affect the location and tolerable chloride concentration for initiation of pitting corrosion. In other words, it is thought that defects at the steel/concrete interface (i.e. air voids) lower the chloride content necessary for corrosion of steel to initiate. Through EDS analysis, it would be interesting to quantify the chloride content at different locations of the steel/concrete interface with and without voids, and evaluate the presence of corrosion pits at the same time. This hypothesis could be made consistent if at the locations without defects at the SCI no corrosion pits would be present with equal chloride content of the locations with defects, assuming that pits would be visible in the latter case.

Finally, based on the results reported in this research, it would be interesting to investigate the $E_{cp}$ of specific corrosion product compounds to know their absolute Elastic modulus by means, for example, of nano-indentation and Raman spectroscopy at the same time. Since the formation of specific compounds is mainly dependent on the environmental conditions that the structures are exposed to, knowing the mechanical properties of each type of corrosion product (or mixes of them) would allow experts to model degradation of reinforced concrete structures located in a certain environment more accurately. For the compelling open questions that are still present as well as the huge social, political and economical consequences that degradation of infrastructures due to corrosion might have in a big scale, more research related to this topic is definitely needed.

# A

# Cement type identification

## A.1. ESEM/BSE images for cement type identification

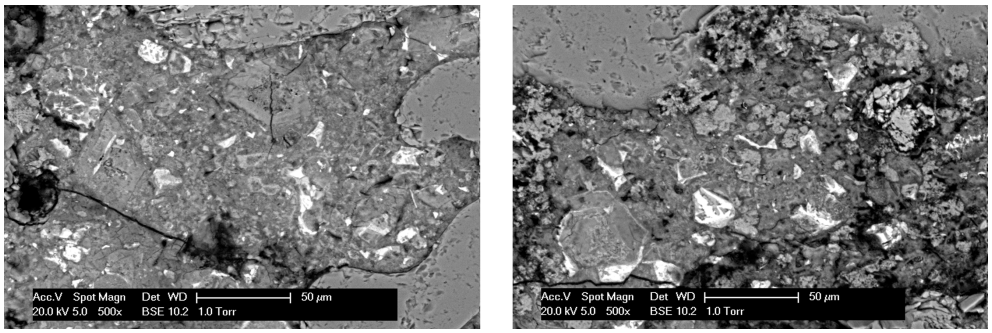


Figure A.1: 1550-S1 BSE images

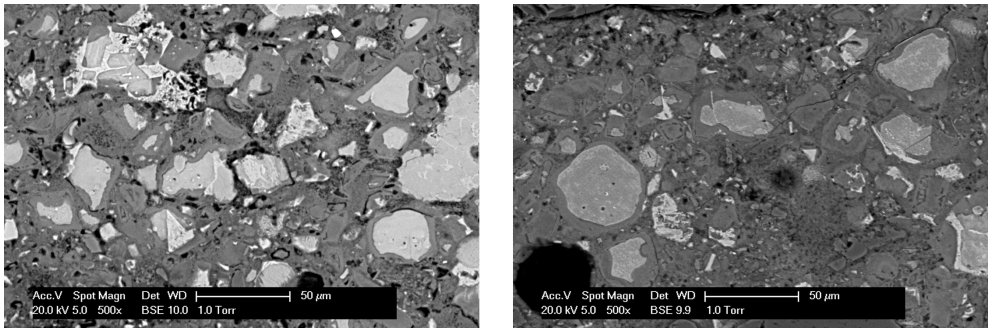


Figure A.2: 1550-S2 BSE images

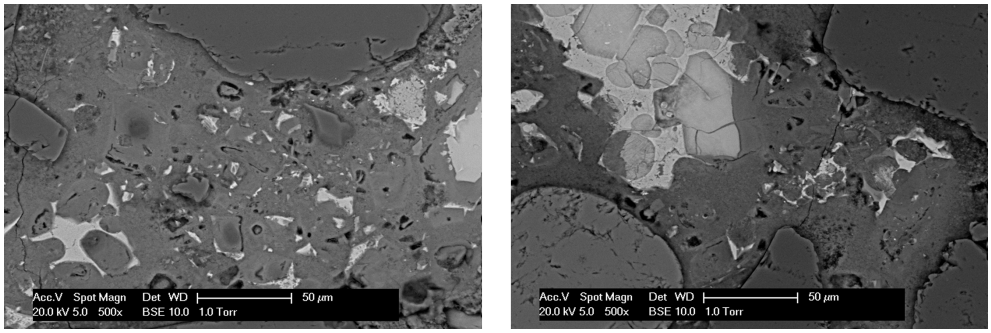


Figure A.3: 1550-S3 BSE images

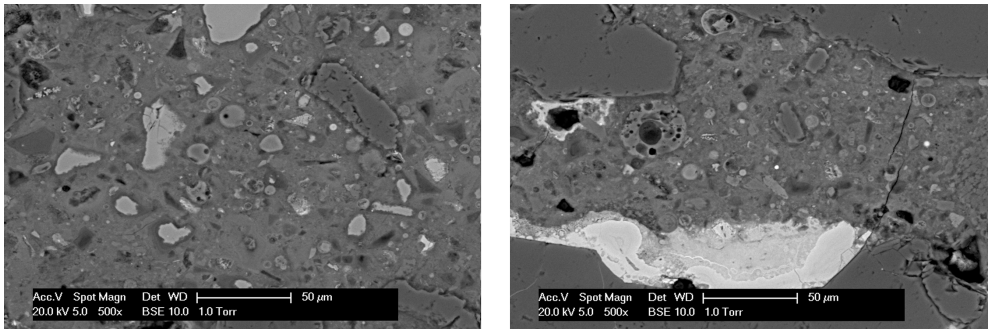


Figure A.4: 2550-S3 BSE images

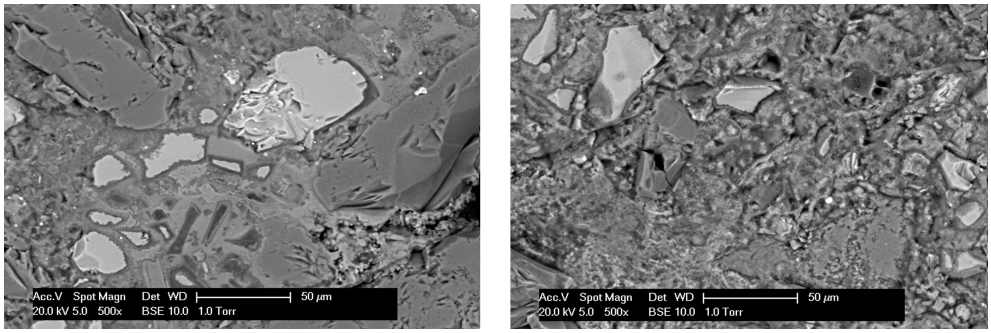


Figure A.5: 3550-S1 BSE images

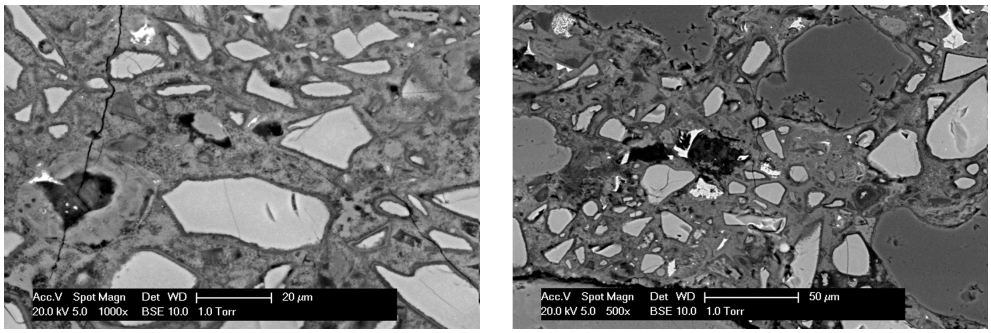


Figure A.6: 3550-S2 BSE images

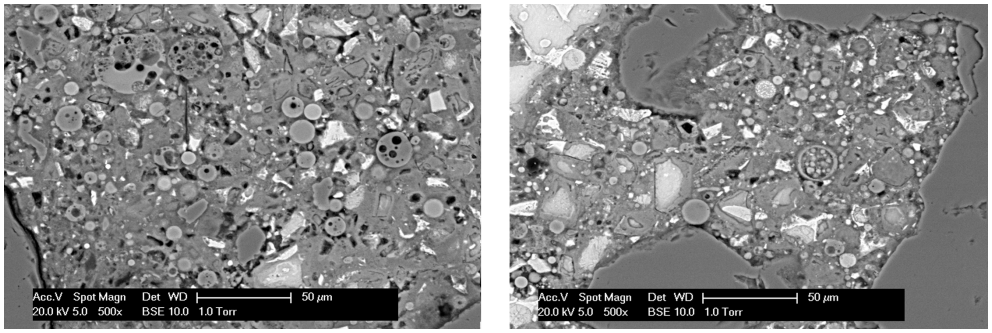


Figure A.7: 5550-S1 BSE images

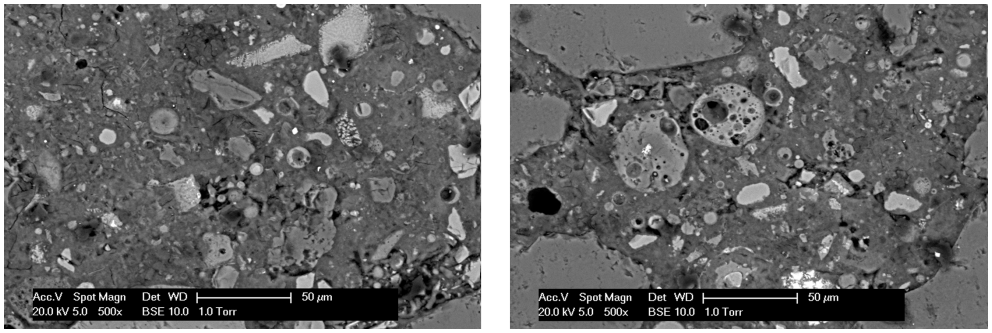


Figure A.8: 5550-S2 BSE images

# B

# (Macro-scale) characterization of reinforced concrete prisms

## B.1. Potential and resistivity measurements (2010-2018)

| | Mix 1550-S1 | | Old label: 7-9 (1550-A) | | | | | | | | | |
|---|---|---|---|---|---|---|---|---|---|---|---|---|
| | Steelpotential (E) [mV] vs Ti* | | | | Resistance 2-point (ESCORT 120Hz) | | | | Corrosion rate [um/year] | | | |
| | 10 mm | | 30 mm | | | | | | 10 mm | | 30 mm | |
| Date | Mean | STD | Mean | STD | R2-10 [kOhm] | ρ-10 [kOhm*m] | R2-50 [kOhm] | ρ-50 [kOhm*m] | Mean | STD | Mean | STD |
| November 2009 | -482 | 40 | -485 | 40 | 3,2 | 0,3 | 2,2 | 0,2 | | | | |
| February 2010 | -532 | 56 | -503 | 17 | 1,1 | 0,1 | 2,2 | 0,2 | 0,1 | 0,1 | 0,2 | 0,1 |
| April 2010 | -649 | 53 | -629 | 127 | 3,2 | 0,3 | 2,2 | 0,2 | 89,9 | 59,0 | 64,7 | 110,3 |
| February 2018 | -380 | 8 | -361 | 31 | 2,0 | 0,2 | 1,4 | 0,1 | | | | |

| | Mix 1550-S2 | | Old label: 6-8 (1550-B) | | | | | | | | | |
|---|---|---|---|---|---|---|---|---|---|---|---|---|
| | Steelpotential (E) [mV] vs Ti* | | | | Resistance 2-point (ESCORT 120Hz) | | | | Corrosion rate [um/year] | | | |
| | 10 mm | | 30 mm | | | | | | 10 mm | | 30 mm | |
| Date | Mean | STD | Mean | STD | R2-10 [kOhm] | ρ-10 [kOhm*m] | R2-50 [kOhm] | ρ-50 [kOhm*m] | Mean | STD | Mean | STD |
| November 2009 | -474 | 75 | -407 | 87 | 8,6 | 0,8 | 6,5 | 0,6 | | | | |
| February 2010 | -480 | 81 | -395 | 69 | 6,5 | 0,6 | 6,5 | 0,6 | 0,6 | 0,6 | 0,2 | 0,1 |
| April 2010 | -597 | 165 | -651 | 106 | 7,5 | 0,7 | 6,5 | 0,6 | 12,1 | 8,3 | 1,7 | 1,3 |
| February 2018 | -159 | 28 | -221 | 23 | 10,8 | 1,0 | 8,1 | 0,9 | | | | |

| | Mix 2550-S2 | | Old label: 4-5 (2550-A) | | | | | | | | | |
|---|---|---|---|---|---|---|---|---|---|---|---|---|
| | Steelpotential (E) [mV] vs Ti* | | | | Resistance 2-point (ESCORT 120Hz) | | | | Corrosion rate [um/year] | | | |
| | 10 mm | | 30 mm | | | | | | 10 mm | | 30 mm | |
| Date | Mean | STD | Mean | STD | R2-10 [kOhm] | ρ-10 [kOhm*m] | R2-50 [kOhm] | ρ-50 [kOhm*m] | Mean | STD | Mean | STD |
| November 2009 | -324 | 26 | -419 | 24 | 9,7 | 0,9 | 6,5 | 0,6 | | | | |
| February 2010 | -412 | 35 | -421 | 67 | 8,6 | 0,8 | 7,5 | 0,7 | 0,2 | 0,1 | 0,3 | 0,0 |
| April 2010 | -548 | 21 | -456 | 50 | 1,1 | 0,1 | 9,7 | 0,9 | 3,0 | 1,4 | 0,9 | 0,2 |
| February 2018 | -184 | 18 | -192 | 85 | 16,7 | 1,6 | 10,7 | 1,1 | | | | |

Figure B.1: Steel potential and concrete resistivity measurements (2010-2018)

| Mix 2550-S3 | Old label: 3-3 (2550-C) | | | | | | | | | | | |
|---|---|---|---|---|---|---|---|---|---|---|---|---|
| | Steelpotential (E) [mV] vs Ti* | | | | Resistance 2-point (ESCORT 120Hz) | | | | Corrosion rate [um/year] | | | |
| | 10 mm | | 30 mm | | | | | | 10 mm | | 30 mm | |
| Date | Mean | STD | Mean | STD | R2-10 [kOhm] | ρ-10 [kOhm*m] | R2-50 [kOhm] | ρ-50 [kOhm*m] | Mean | STD | Mean | STD |
| November 2009 | -433 | 37 | -322 | 64 | 19,4 | 1,8 | 17,2 | 1,6 | | | | |
| February 2010 | -484 | 19 | -335 | 15 | 14,0 | 1,3 | 16,1 | 1,5 | 0,3 | 0,0 | 0,4 | 0,0 |
| April 2010 | -554 | 55 | -450 | 13 | 5,4 | 0,5 | 44,1 | 4,1 | 1,3 | 0,5 | 0,7 | 0,3 |
| February 2018 | -237 | 10 | -234 | 40 | 61,3 | 5,7 | 44,2 | 4,7 | | | | |

| Mix 3550-S1 | Old label: 8-8 (3550-B) | | | | | | | | | | | |
|---|---|---|---|---|---|---|---|---|---|---|---|---|
| | Steelpotential (E) [mV] vs Ti* | | | | Resistance 2-point (ESCORT 120Hz) | | | | Corrosion rate [um/year] | | | |
| | 10 mm | | 30 mm | | | | | | 10 mm | | 30 mm | |
| Date | Mean | STD | Mean | STD | R2-10 [kOhm] | ρ-10 [kOhm*m] | R2-50 [kOhm] | ρ-50 [kOhm*m] | Mean | STD | Mean | STD |
| November 2009 | -458 | 17 | -376 | 38 | 21,5 | 2,0 | 20,4 | 1,9 | | | | |
| February 2010 | -524 | 20 | -430 | 51 | 19,4 | 1,8 | 20,4 | 1,9 | 0,4 | 0,0 | 0,4 | 0,0 |
| April 2010 | -542 | 26 | -477 | 42 | 197,8 | 18,4 | 89,2 | 8,3 | 4,3 | 5,2 | 1,2 | 0,6 |
| February 2018 | -336 | 43 | -332 | 25 | 55,1 | 5,1 | 52,1 | 5,5 | | | | |

| Mix 3550-S2 | Old label: 4-7 (3550-D) | | | | | | | | | | | |
|---|---|---|---|---|---|---|---|---|---|---|---|---|
| | Steelpotential (E) [mV] vs Ti* | | | | Resistance 2-point (ESCORT 120Hz) | | | | Corrosion rate [um/year] | | | |
| | 10 mm | | 30 mm | | | | | | 10 mm | | 30 mm | |
| Date | Mean | STD | Mean | STD | R2-10 [kOhm] | ρ-10 [kOhm*m] | R2-50 [kOhm] | ρ-50 [kOhm*m] | Mean | STD | Mean | STD |
| November 2009 | -462 | 53 | -321 | 36 | 29,0 | 2,7 | 30,1 | 2,8 | | | | |
| February 2010 | -472 | 46 | -338 | 41 | 26,9 | 2,5 | 30,1 | 2,8 | 0,7 | 0,4 | 0,4 | 0,3 |
| April 2010 | -502 | 41 | -369 | 37 | 107,5 | 10,0 | 79,6 | 7,4 | 4,4 | 5,4 | 2,9 | 3,2 |
| February 2018 | -300 | 22 | -300 | 30 | 101,4 | 9,4 | 76,7 | 8,1 | | | | |

| Mix 5550-S1 | Old label: 5-10 (5550-F) | | | | | | | | | | | |
|---|---|---|---|---|---|---|---|---|---|---|---|---|
| | Steelpotential (E) [mV] vs Ti* | | | | Resistance 2-point (ESCORT 120Hz) | | | | Corrosion rate [um/year] | | | |
| | 10 mm | | 30 mm | | | | | | 10 mm | | 30 mm | |
| Date | Mean | STD | Mean | STD | R2-10 [kOhm] | ρ-10 [kOhm*m] | R2-50 [kOhm] | ρ-50 [kOhm*m] | Mean | STD | Mean | STD |
| November 2009 | -486 | 19 | -221 | 86 | 39,8 | 3,7 | 45,2 | 4,2 | | | | |
| February 2010 | -529 | 43 | -297 | 107 | 38,7 | 3,6 | 45,2 | 4,2 | 0,5 | 0,1 | 0,3 | 0,1 |
| April 2010 | -551 | 46 | -363 | 64 | 45,2 | 4,2 | 53,8 | 5,0 | 3,0 | 1,9 | 1,4 | 1,2 |
| February 2018 | -350 | 45 | -145 | 16 | 79,4 | 7,4 | 101,8 | 10,8 | | | | |

| Mix 5550-S2 | Old label: 2-4 (5550-D) | | | | | | | | | | | |
|---|---|---|---|---|---|---|---|---|---|---|---|---|
| | Steelpotential (E) [mV] vs Ti* | | | | Resistance 2-point (ESCORT 120Hz) | | | | Corrosion rate [um/year] | | | |
| | 10 mm | | 30 mm | | | | | | 10 mm | | 30 mm | |
| Date | Mean | STD | Mean | STD | R2-10 [kOhm] | ρ-10 [kOhm*m] | R2-50 [kOhm] | ρ-50 [kOhm*m] | Mean | STD | Mean | STD |
| November 2009 | -401 | 12 | -242 | 13 | 35,5 | 3,3 | 39,8 | 3,7 | | | | |
| February 2010 | -460 | 40 | -342 | 72 | 33,3 | 3,1 | 37,6 | 3,5 | 0,3 | 0,0 | 0,3 | 0,0 |
| April 2010 | -490 | 28 | -344 | 36 | 59,1 | 5,5 | 60,2 | 5,6 | 2,9 | 2,7 | 3,7 | 2,0 |
| February 2018 | -316 | 57 | -161 | 21 | 78,1 | 7,3 | 83,5 | 8,9 | | | | |

Figure B.2: Steel potential and concrete resistivity measurements (2010-2018)

## B.2. Reinforced concrete prisms

| 1550-S1 | 1550-S2 |
|---|---|
|  |  |

| 1550-S3 (ex 2550-S2) | 2550-S3 |
|---|---|
|  | 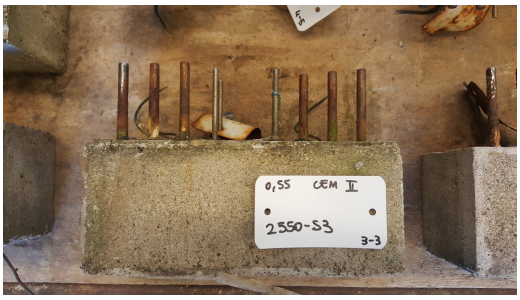 |

| 3550-S1 | 3550-S2 |
|---|---|
|  |  |

| 5550-S1 | 5550-S2 |
|---|---|
|  |  |

## B.3. Carbonation depth measurements

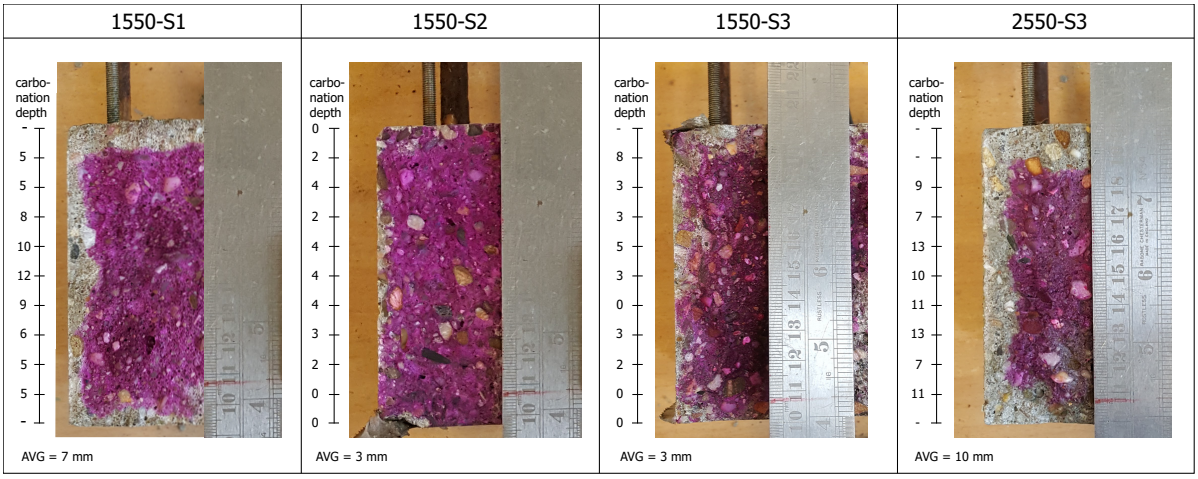


Figure B.3: Carbonation depth measurements of CEM I and CEM II prisms

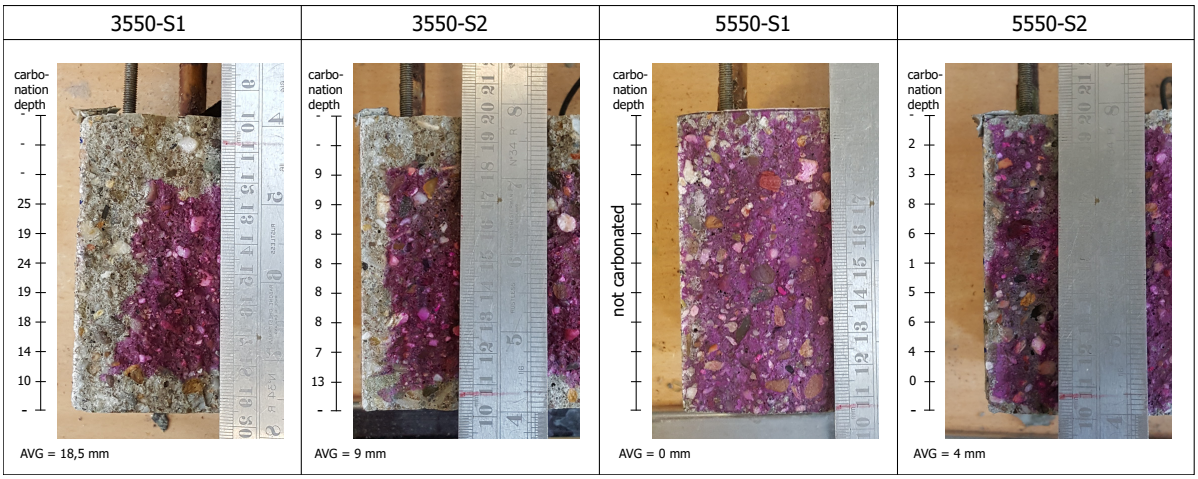


Figure B.4: Carbonation depth measurements of CEM III and CEM V prisms

# C

# (Meso-scale) characterization of steel reinforcement

# C.1. Grey scale values histograms of CT-scan image stacks

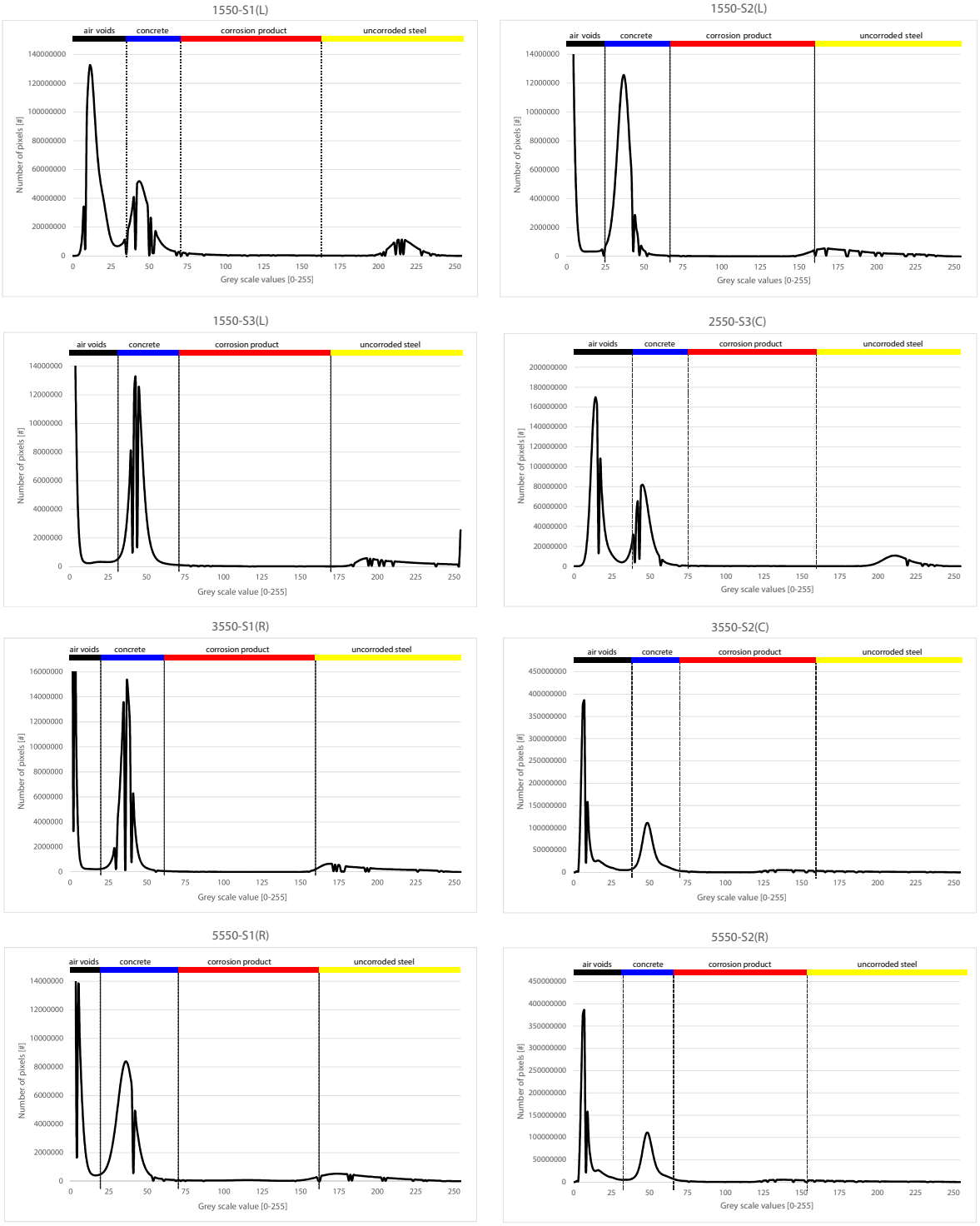


Figure C.1: GSV histograms of CT-scanned reinforced concrete cores

# C.2. Corrosion pit depths and orientation

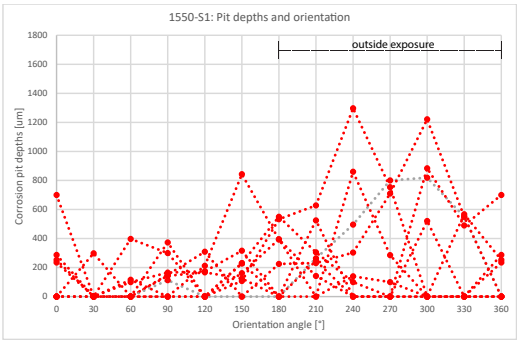


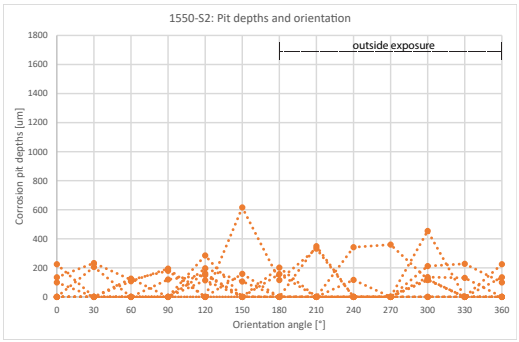


Figure C.2: 1550-S1 (left) and 1550-S2 (right) corrosion pit depths and orientation

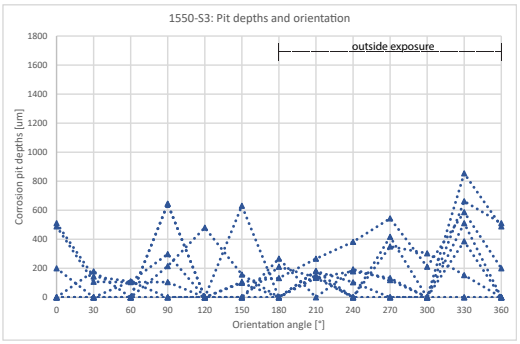


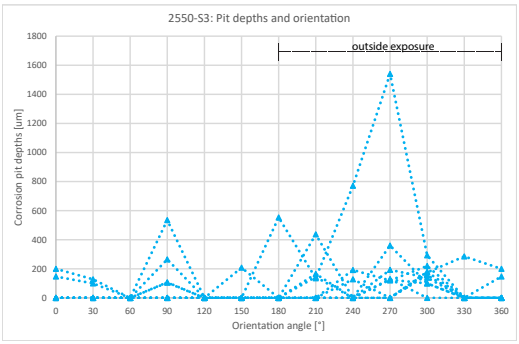


Figure C.3: 1550-S3 (left) and 2550-S3 (right) corrosion pit depths and orientation

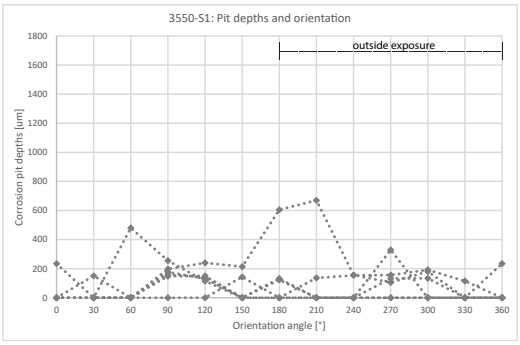


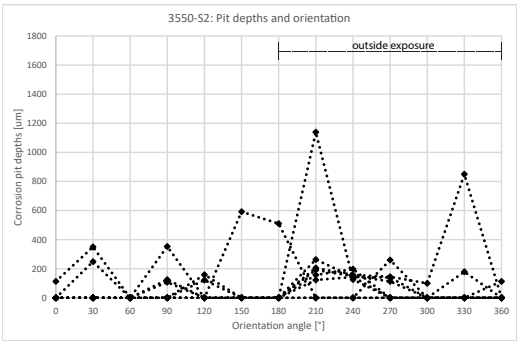


Figure C.4: 3550-S1 (left) and 3550-S2 (right) corrosion pit depths and orientation

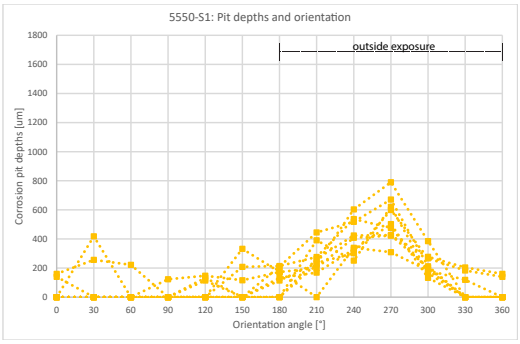


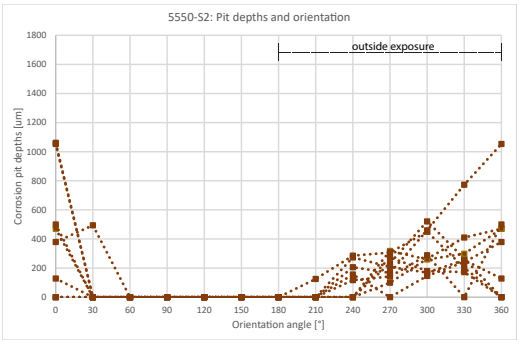


Figure C.5: 5550-S1 (left) and 5550-S2 (right) corrosion pit depths and orientation

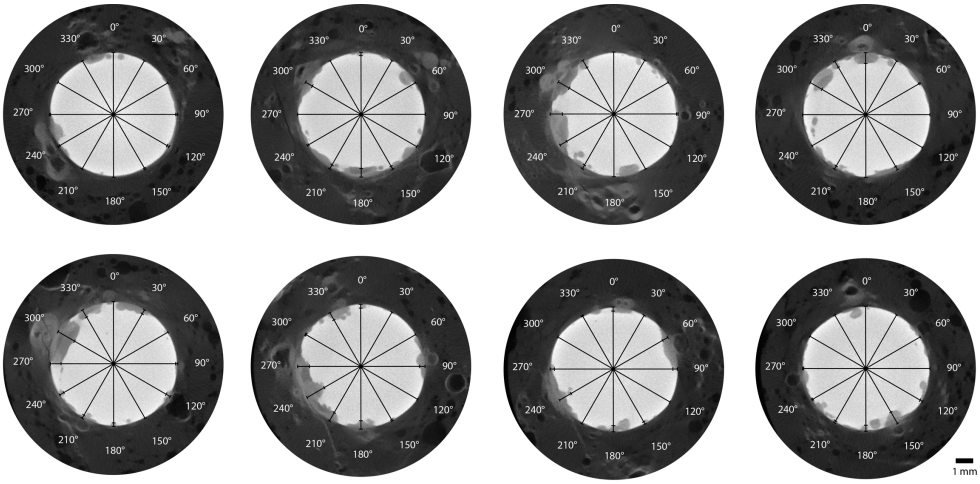


Figure C.6: 1550-S1: 2D CT-images to analyze pit depths and orientation

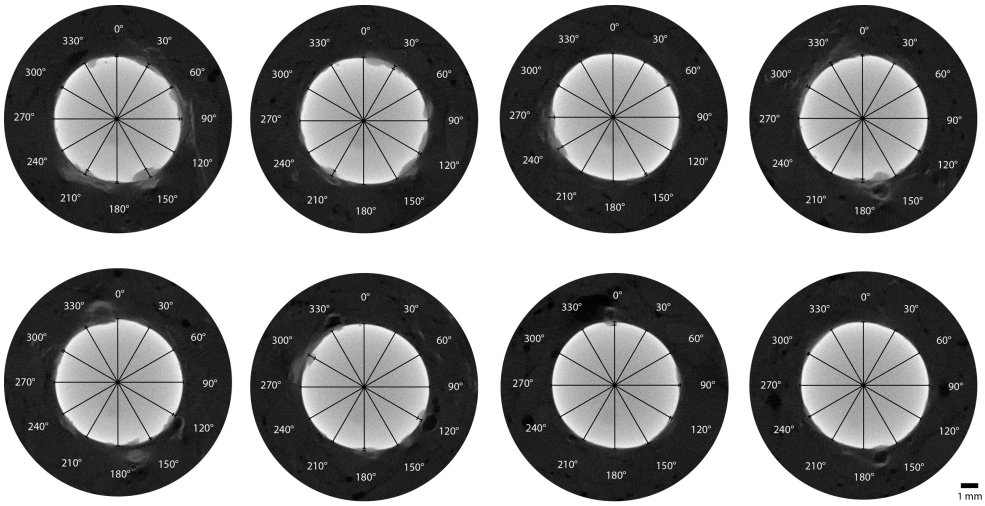


Figure C.7: 1550-S2: 2D CT-images to analyze pit depths and orientation

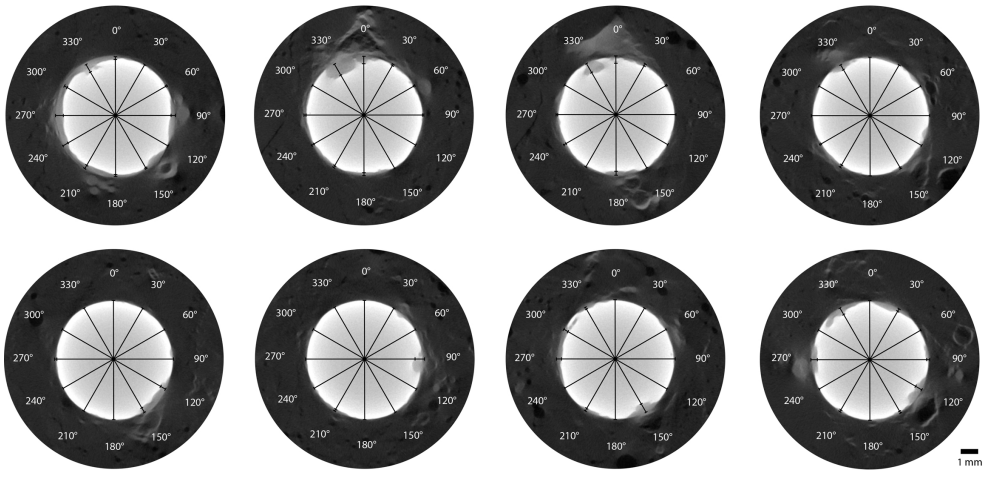


Figure C.8: 1550-S3: 2D CT-images to analyze pit depths and orientation

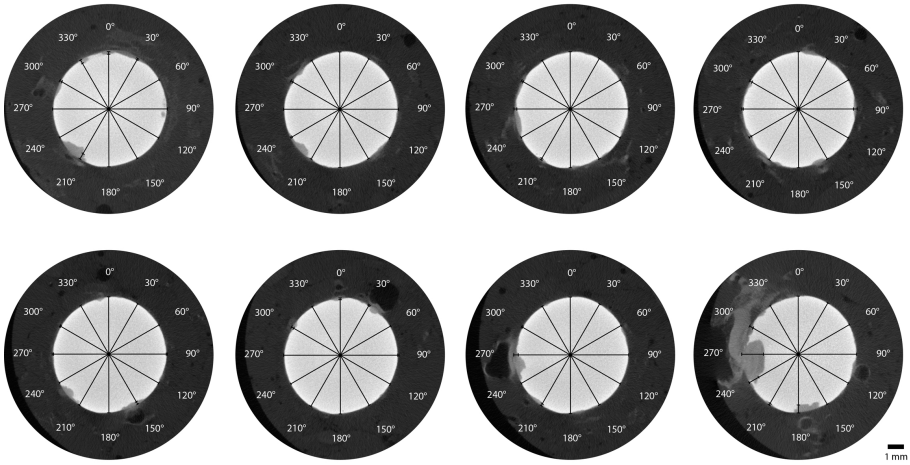


Figure C.9: 2550-S3: 2D CT-images to analyze pit depths and orientation

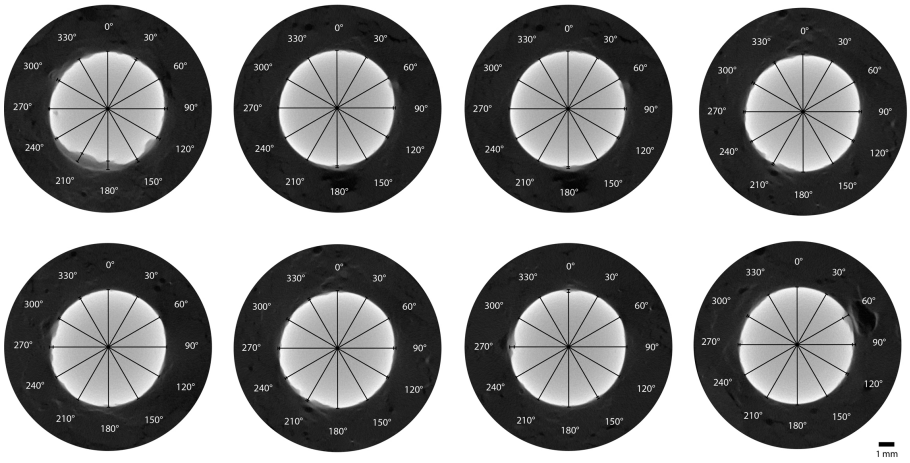


Figure C.10: 3550-S1: 2D CT-images to analyze pit depths and orientation

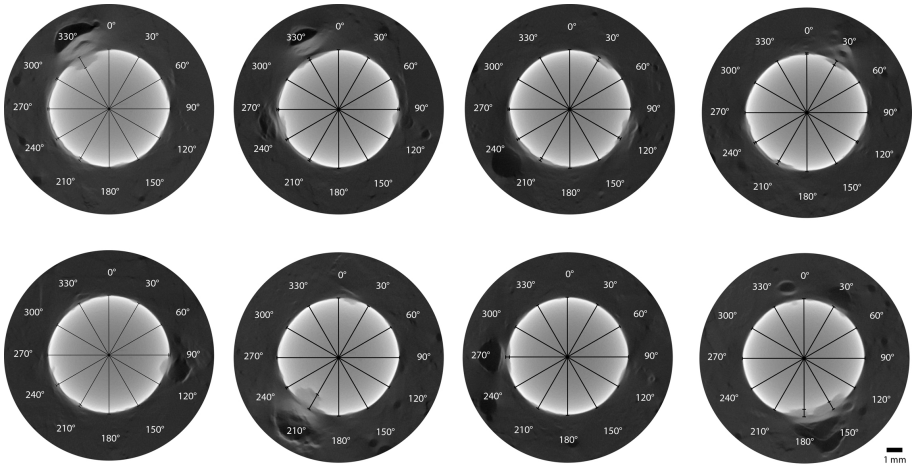


Figure C.11: 3550-S2: 2D CT-images to analyze pit depths and orientation

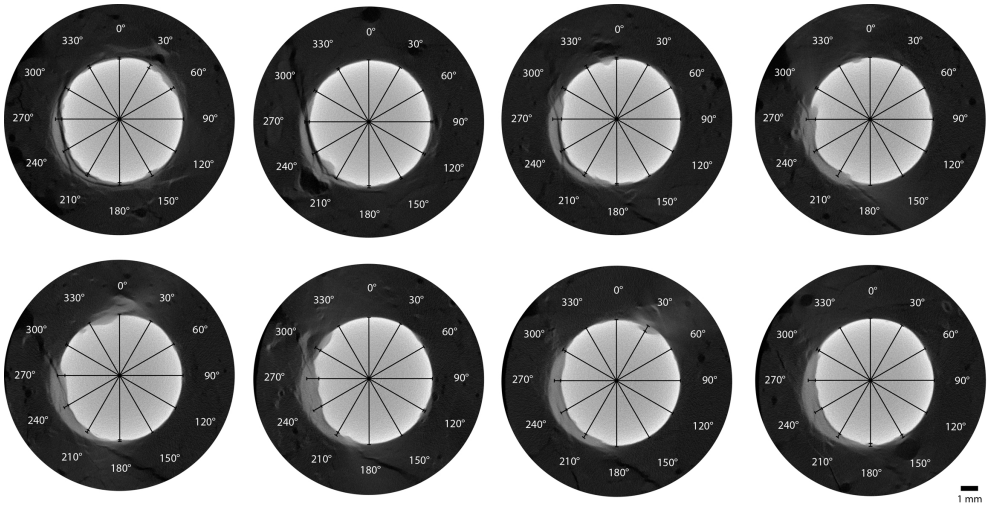


Figure C.12: 5550-S1: 2D CT-images to analyze pit depths and orientation

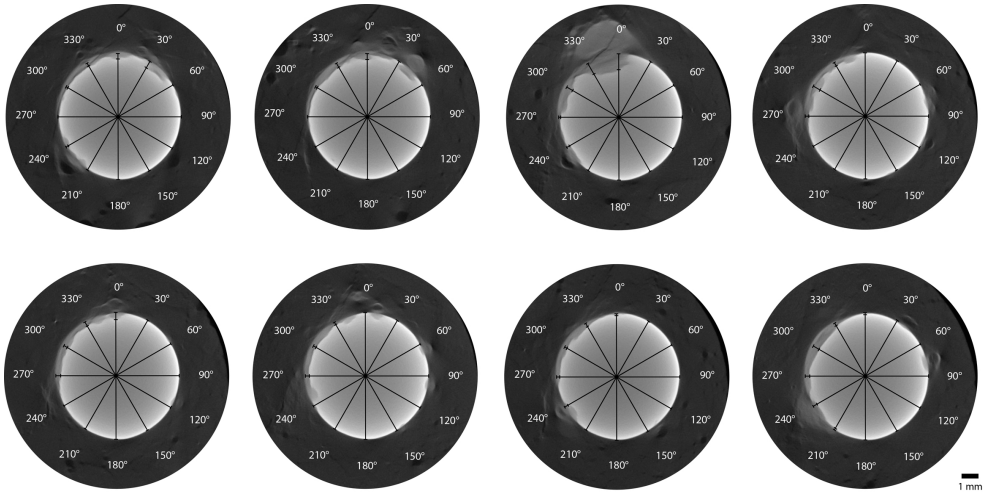


Figure C.13: 5550-S2: 2D CT-images to analyze pit depths and orientation

# D

# (Micro-scale) characterization of corrosion product

## D.1. Nano-indentation: technique and methodology

Each reinforced concrete polished section was subjected to one grid-like series of indents. The location where to perform nano-indentation was identified by means of Optical microscopy which the Agilent Nano Indenter G200 was furnished of. The distance between each consecutive indent was set at 20 $\mu m$. A portion of un-corroded steel was also indented, working as reference locations.

When nano-indentation was concluded, samples were analyzed through ESEM, where the indents were visible and elemental quantification could be conducted by means of standard-based EDS analysis. A SEM/BSE image where one (5x20) grid-like series of indents is visible is given below: in this case, #1 was the starting indent while #100 was the last one. More intermediate indentation numbers are also specified to clarify what path was followed by the Berkovich's indenter during the test (Figure D.1).

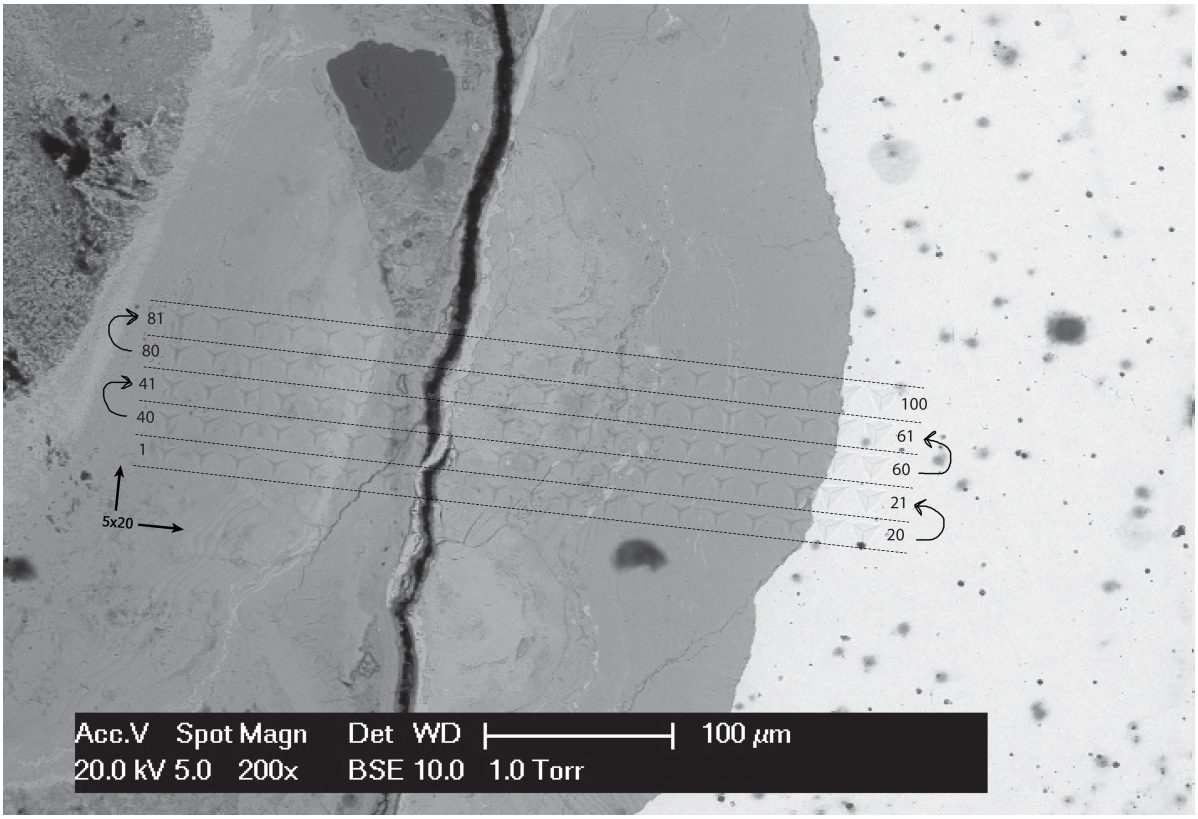


Figure D.1: grid-like series of indents for 5550-S2, with #1=starting indent (corrosion product) - #100=last indent (steel)

The Elastic Modulus of the indented elements was determined through the Continues Stiffness Method (CSM), which provides continuous stiffness measurements as function of indentation depth. The maximum indentation depth was set at 2000 nm: however, Elastic Modulus was determined in the range of 1000-1800 nm, hence where it stabilized. In Figure D.2, an example of the relation between E modulus and indentation depth for some indentation points of both steel and corrosion product is given. In Figure D.3, the E modulus determined for each indentation point is shown. Values given by Figure D.3 were then 2D-plotted in different colors and overlapped to the original BSE image, as visible in Section D.1.1.

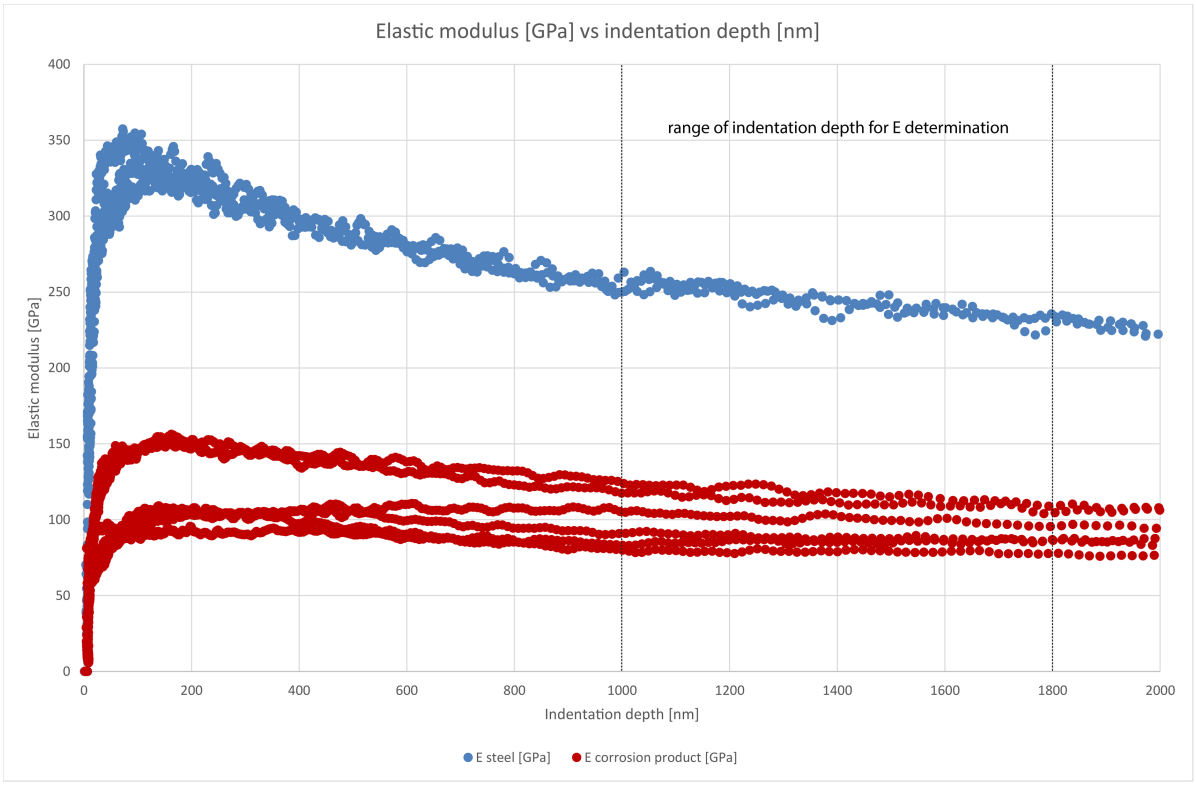


Figure D.2: Elastic modulus [GPa] determined through CSM as function of indentation depth [nm] for a selection of indents (red=corrosion product; blue=steel)

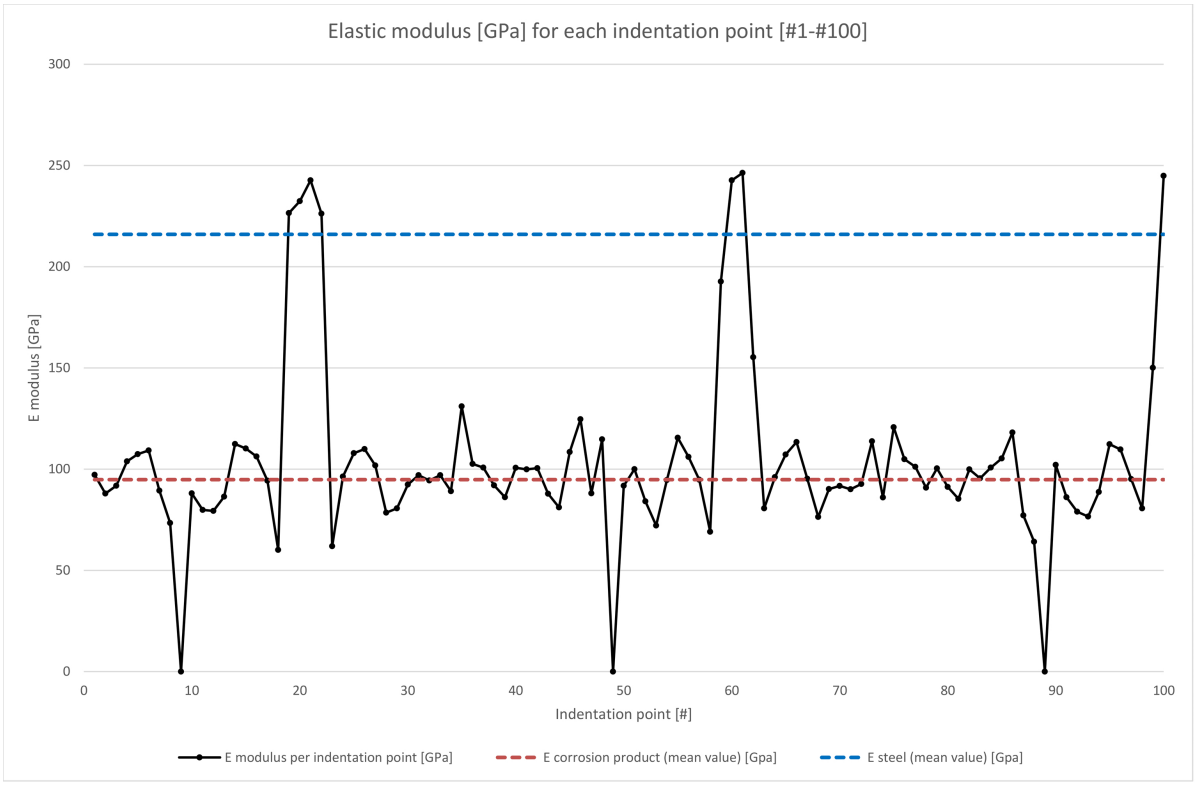


Figure D.3: Elastic modulus [GPa] determined in the range of 1000-1800 nm for each indentation point (as labeled in Figure D.1)

### D.1.1. Nano-indentation results

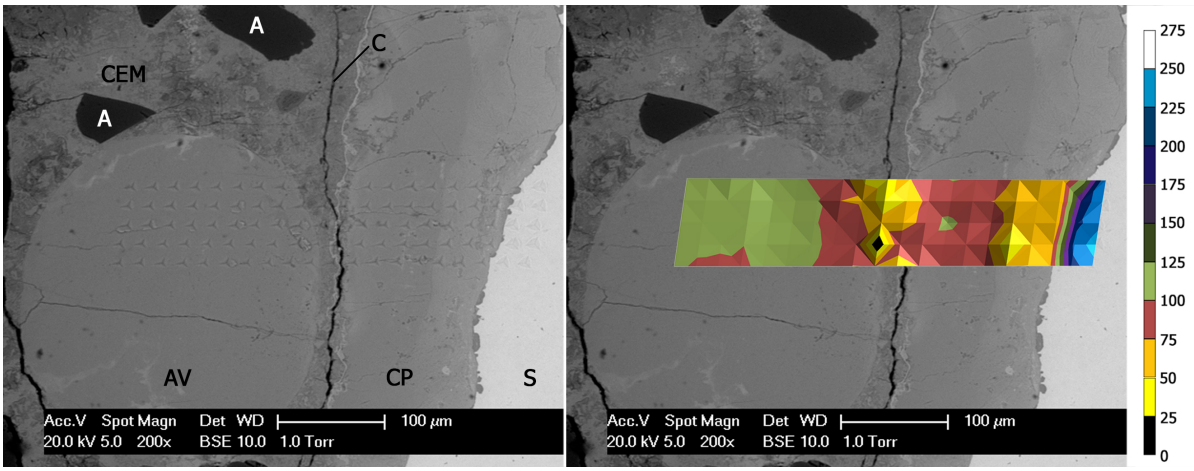


Figure D.4: 1550-S1: (left) BSE image of indented locations with labeled components (S=steel; CP=corrosion product; CEM=cement; AV=air void; C=crack; A=aggregate); (right) Elastic modulus of indented locations (values in GPa)

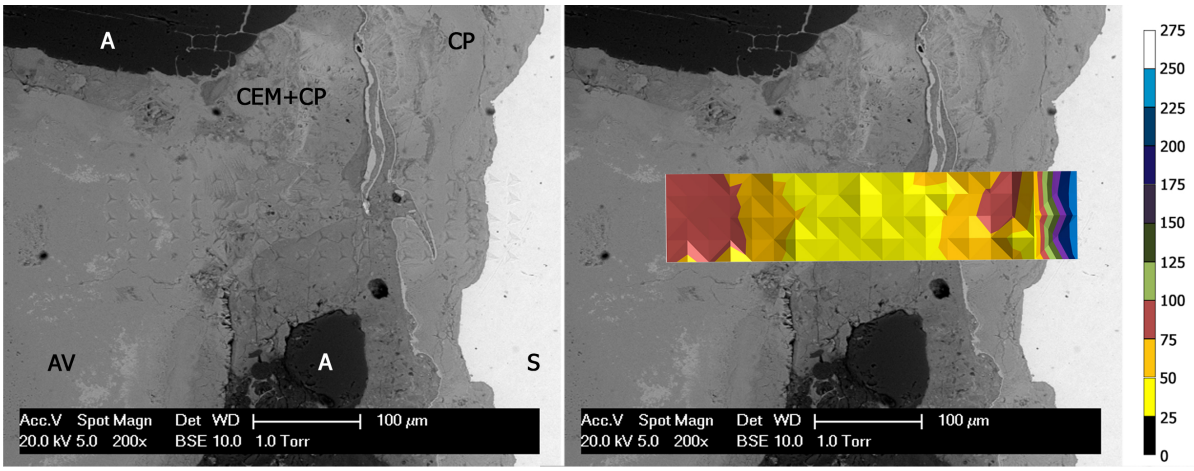


Figure D.5: 1550-S2: (left) BSE image of indented locations with labeled components (S=steel; CP=corrosion product; CEM=cement; AV=air void; C=crack; A=aggregate); (right) Elastic modulus of indented locations (values in GPa)

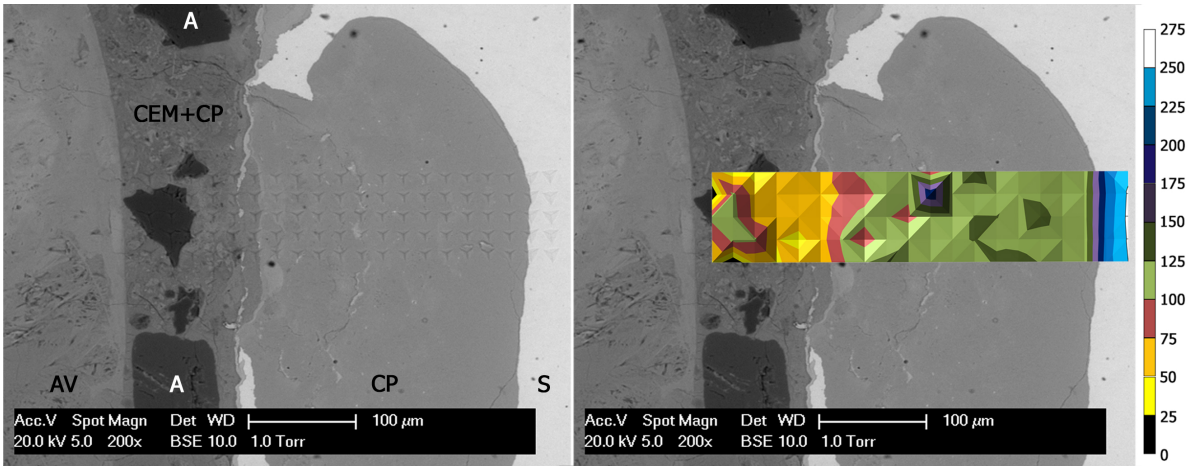


Figure D.6: 1550-S3: (left) BSE image of indented locations with labeled components (S=steel; CP=corrosion product; CEM=cement; AV=air void; C=crack; A=aggregate); (right) Elastic modulus of indented locations (values in GPa)

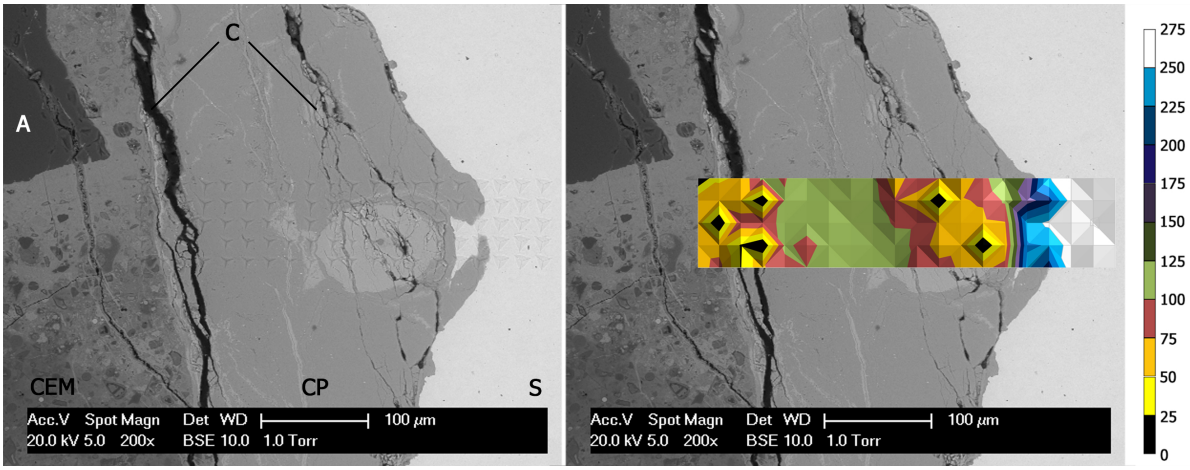


Figure D.7: 2550-S3: (left) BSE image of indented locations with labeled components (S=steel; CP=corrosion product; CEM=cement; AV=air void; C=crack; A=aggregate); (right) Elastic modulus of indented locations (values in GPa)

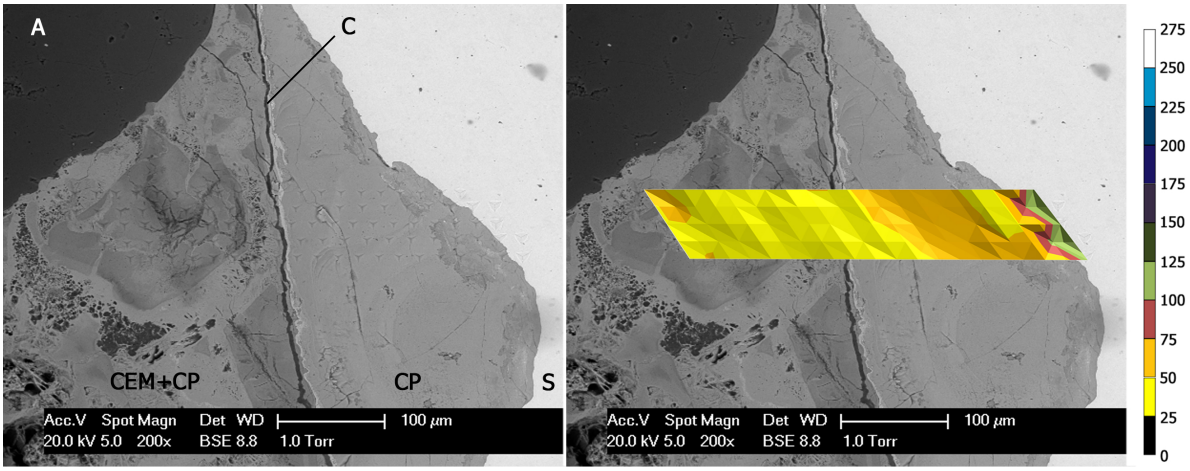


Figure D.8: 3550-S1: (left) BSE image of indented locations with labeled components (S=steel; CP=corrosion product; CEM=cement; AV=air void; C=crack; A=aggregate); (right) Elastic modulus of indented locations (values in GPa)

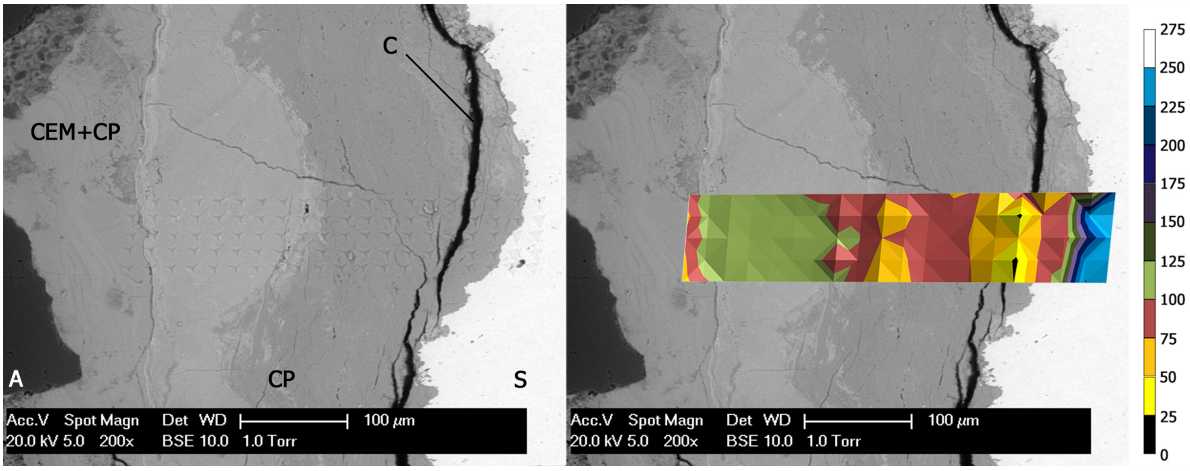


Figure D.9: 3550-S2: (left) BSE image of indented locations with labeled components (S=steel; CP=corrosion product; CEM=cement; AV=air void; C=crack; A=aggregate); (right) Elastic modulus of indented locations (values in GPa)

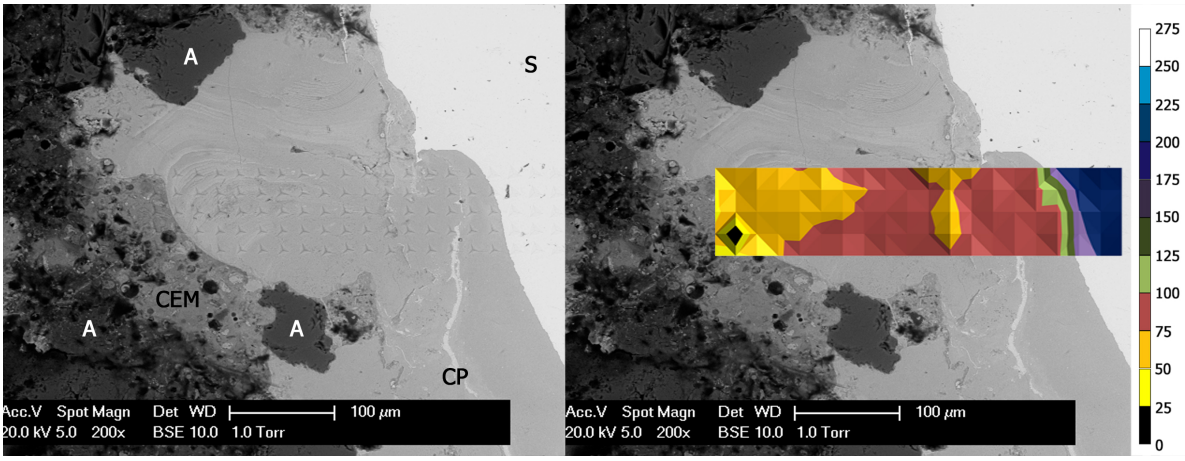


Figure D.10: 5550-S1: (left) BSE image of indented locations with labeled components (S=steel; CP=corrosion product; CEM=cement; AV=air void; C=crack; A=aggregate); (right) Elastic modulus of indented locations (values in GPa)

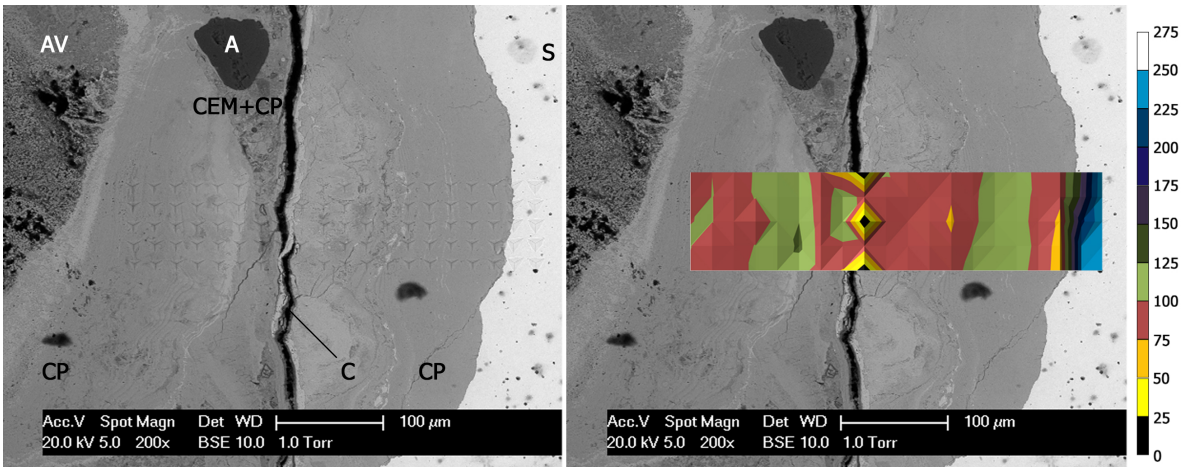


Figure D.11: 5550-S2: (left) BSE image of indented locations with labeled components (S=steel; CP=corrosion product; CEM=cement; AV=air void; C=crack; A=aggregate); (right) Elastic modulus of indented locations (values in GPa)

## D.1.2. EDS elemental mapping

### 1550-S1

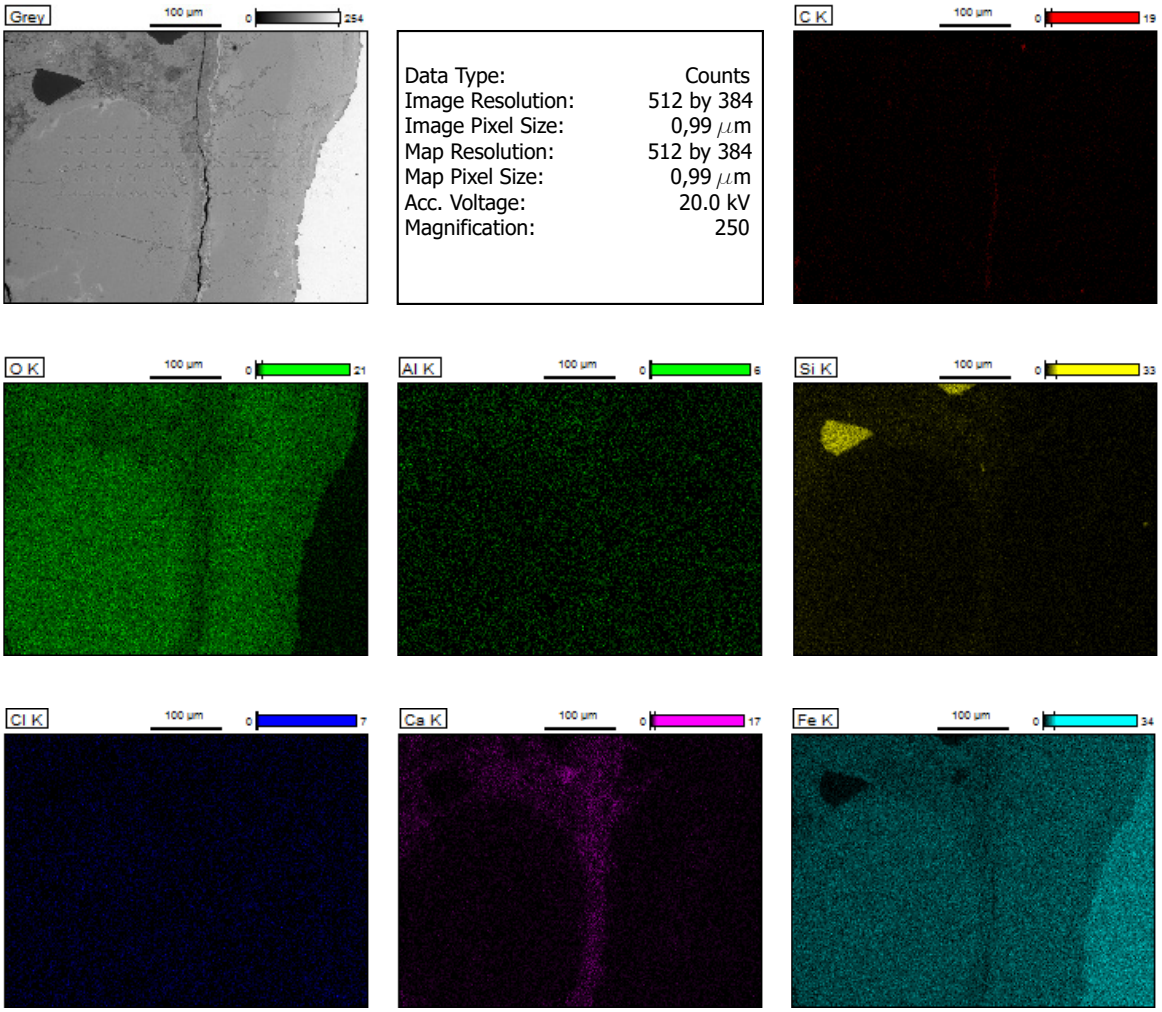


Figure D.12: 1550-S1: EDS elemental mapping

## 1550-S2

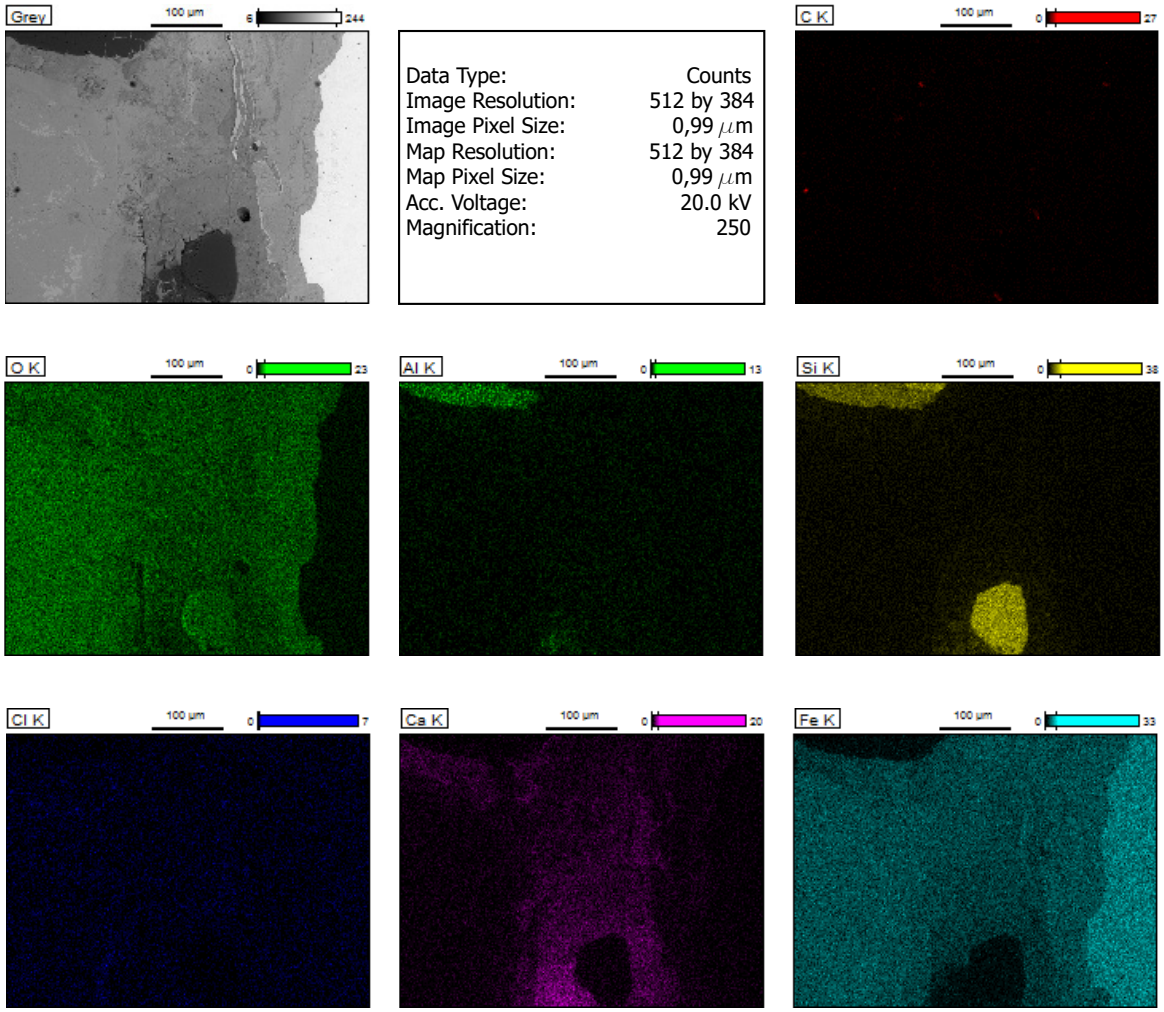


Figure D.13: 1550-S2: EDS elemental mapping

## 1550-S3

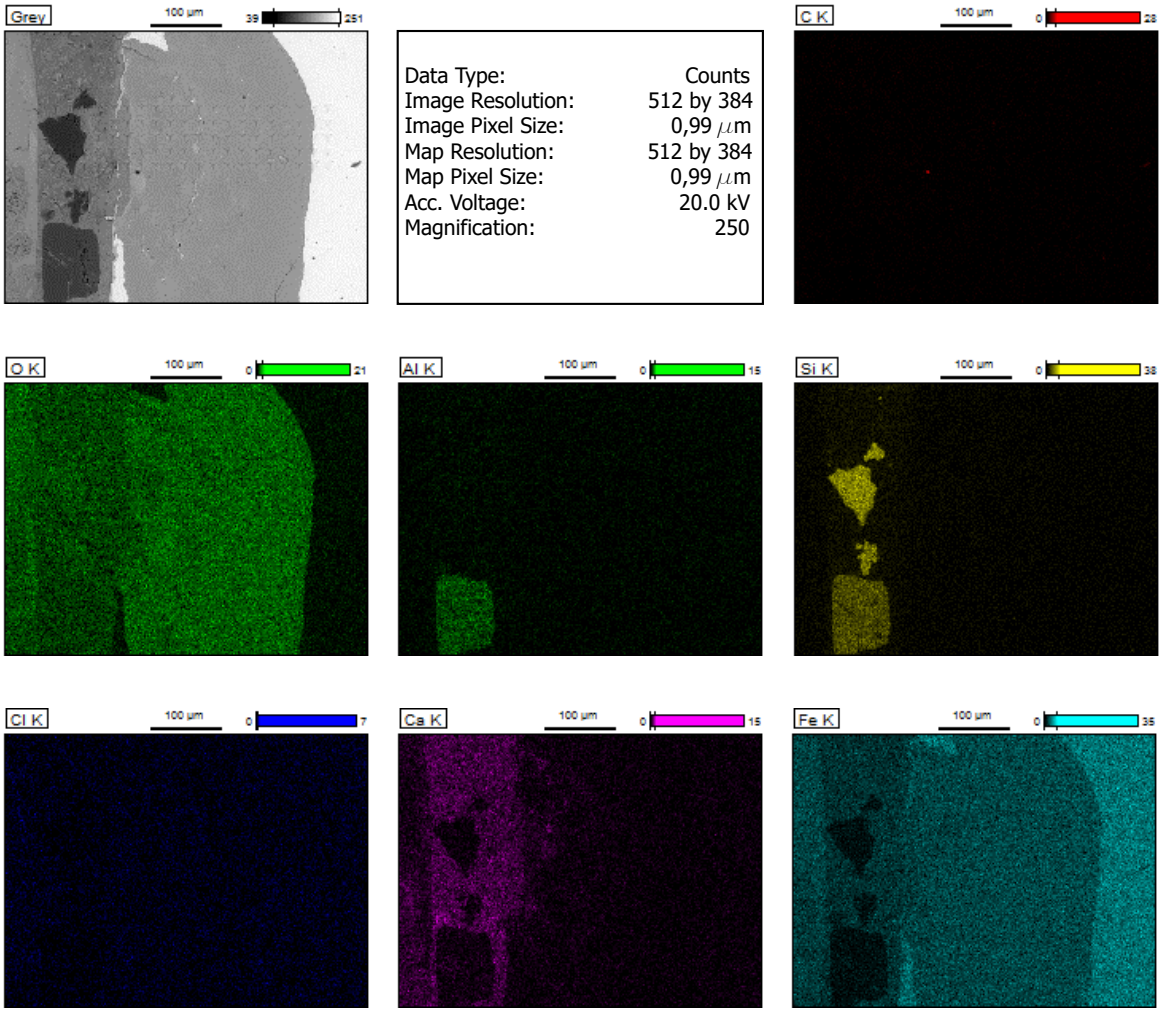


Figure D.14: 1550-S3: EDS elemental mapping

## 3550-S1

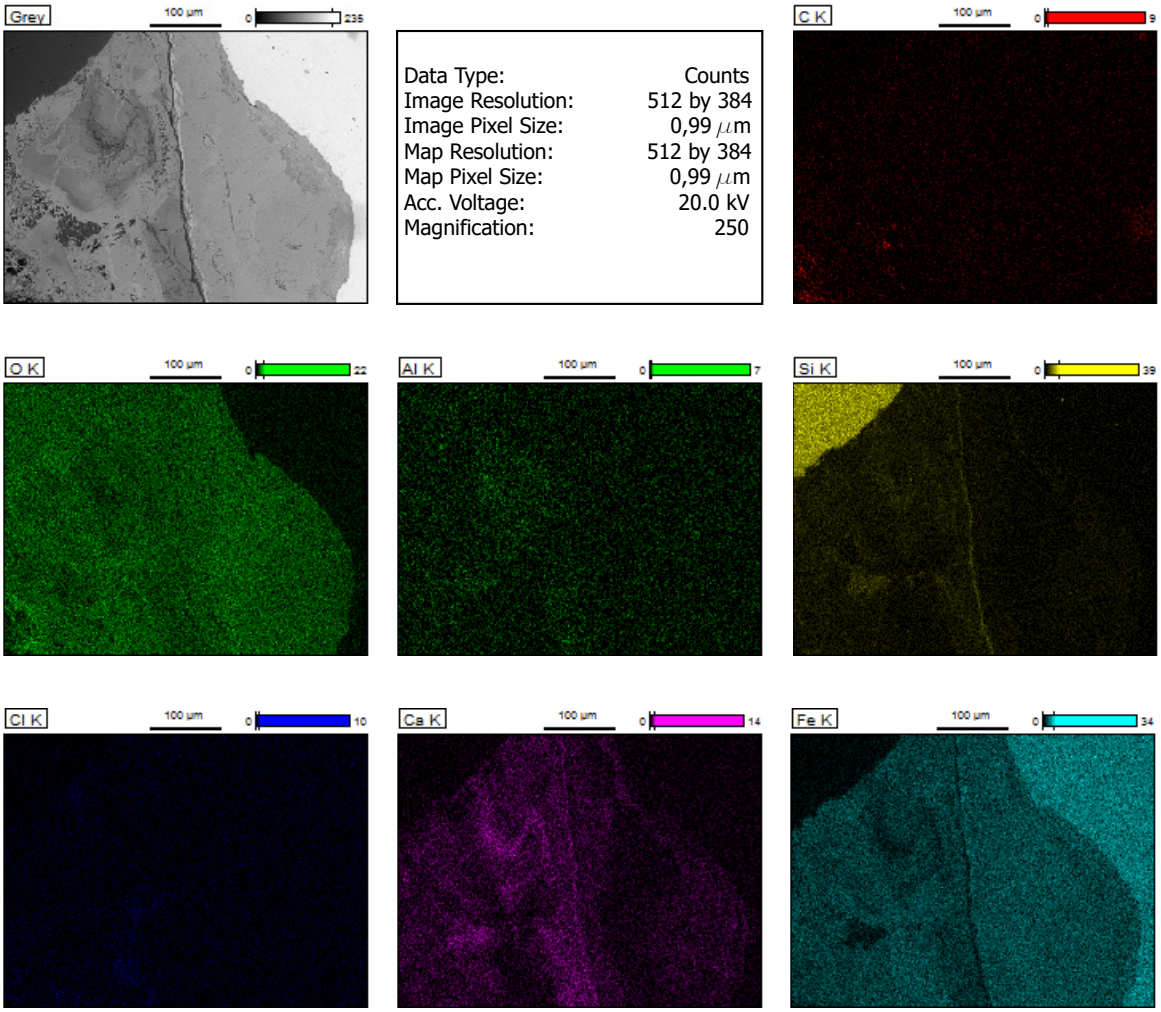


Figure D.15: 3550-S1: EDS elemental mapping

## 3550-S2

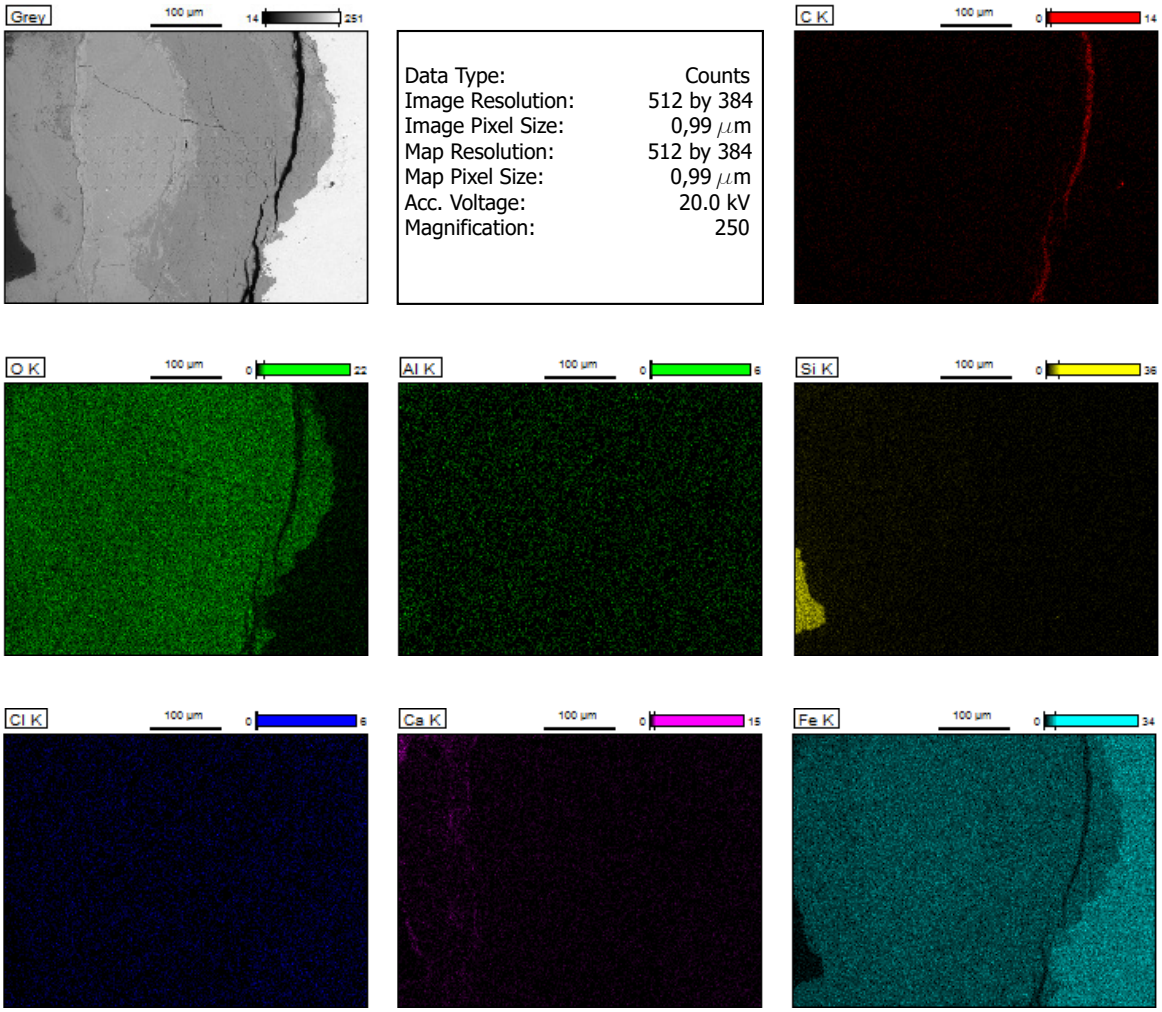


Figure D.16: 3550-S2: EDS elemental mapping

## 5550-S1

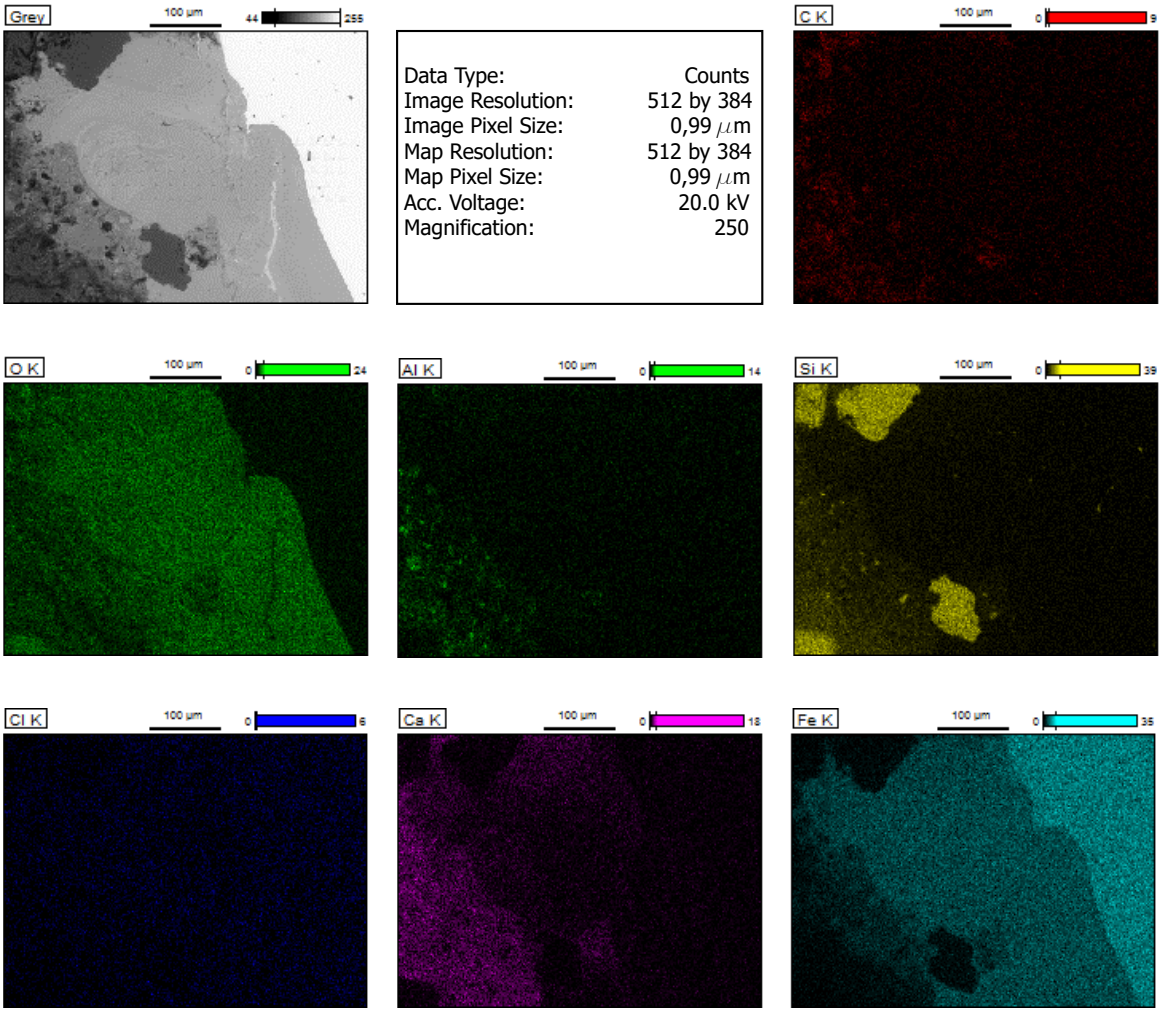


Figure D.17: 5550-S1: EDS elemental mapping

## 5550-S2

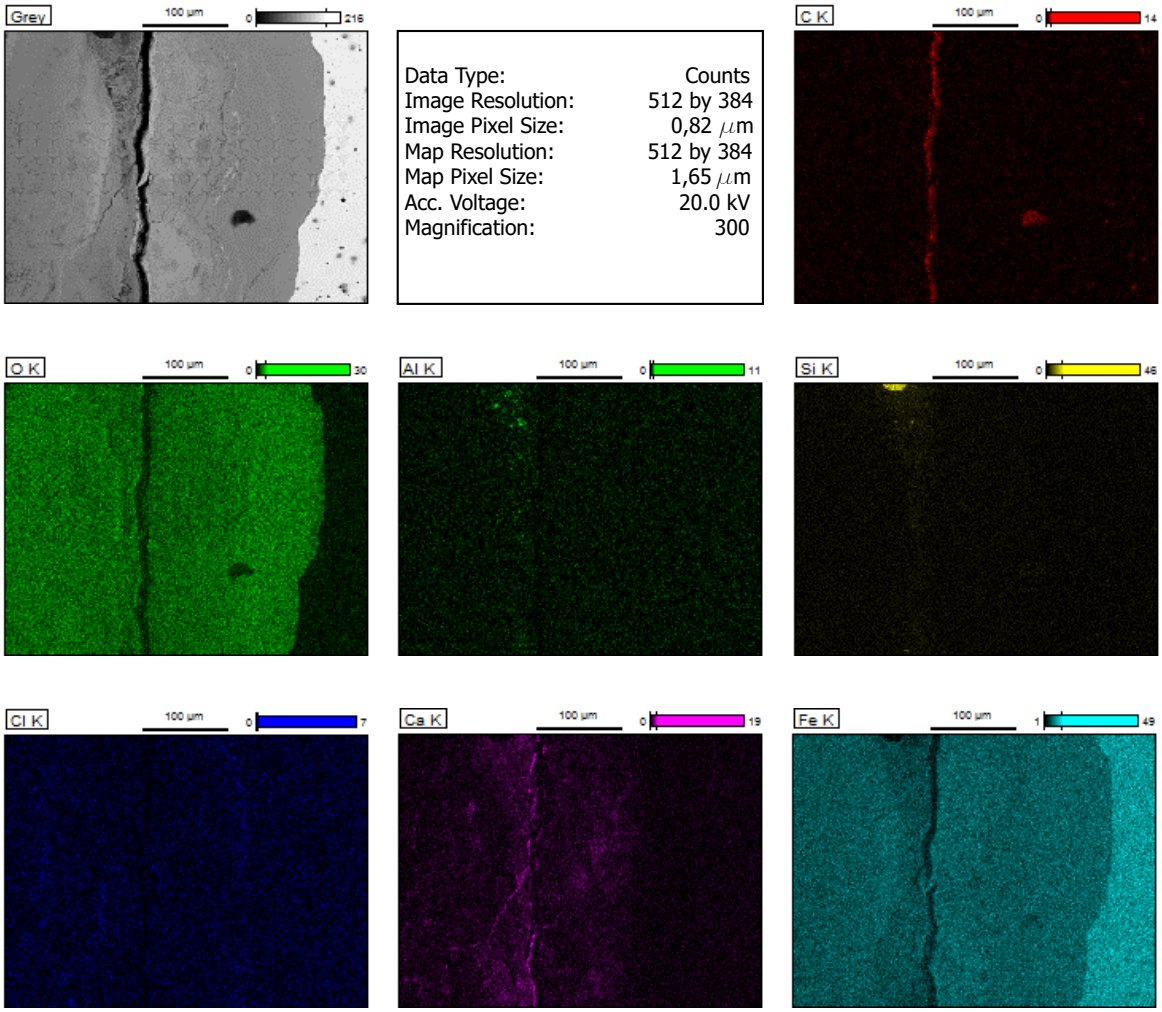


Figure D.18: 5550-S2: EDS elemental mapping

## D.2. EDS spot analysis

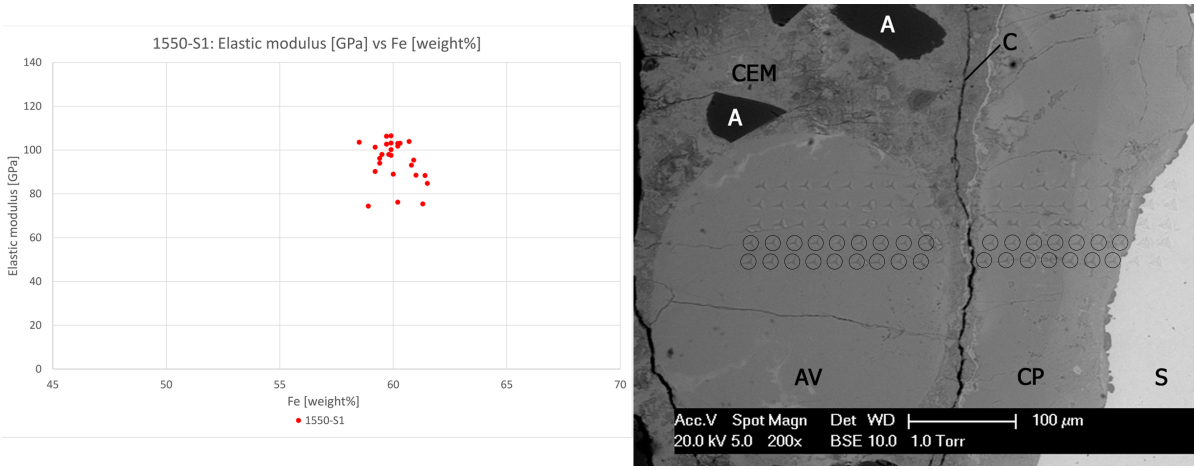


Figure D.19: 1550-S1: (left) E modulus [GPa] vs Fe concentration [wt%] of indented spots; (right) BSE image with indents analyzed through EDS spot analysis (in circles)

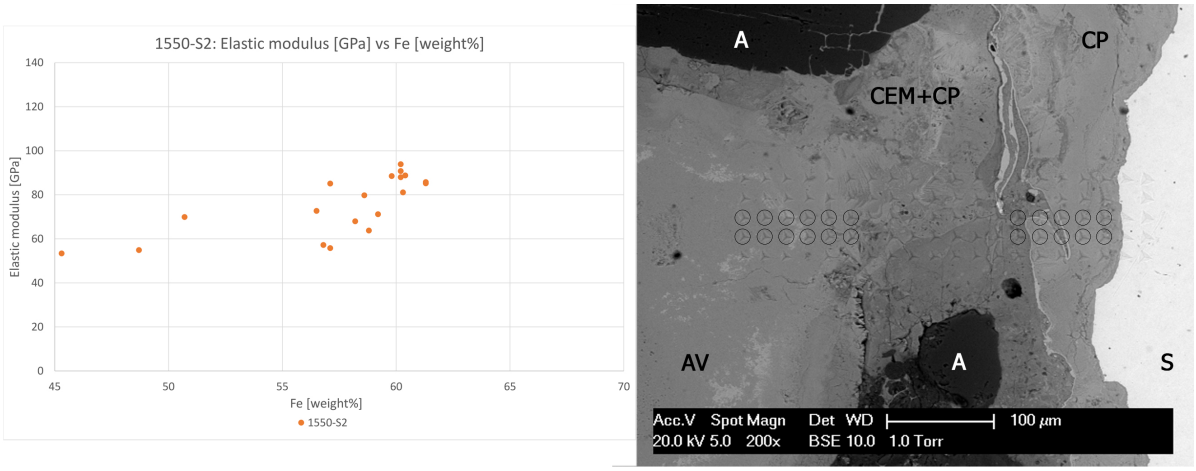


Figure D.20: 1550-S2: (left) E modulus [GPa] vs Fe concentration [wt%] of indented spots; (right) BSE image with indents analyzed through EDS spot analysis (in circles)

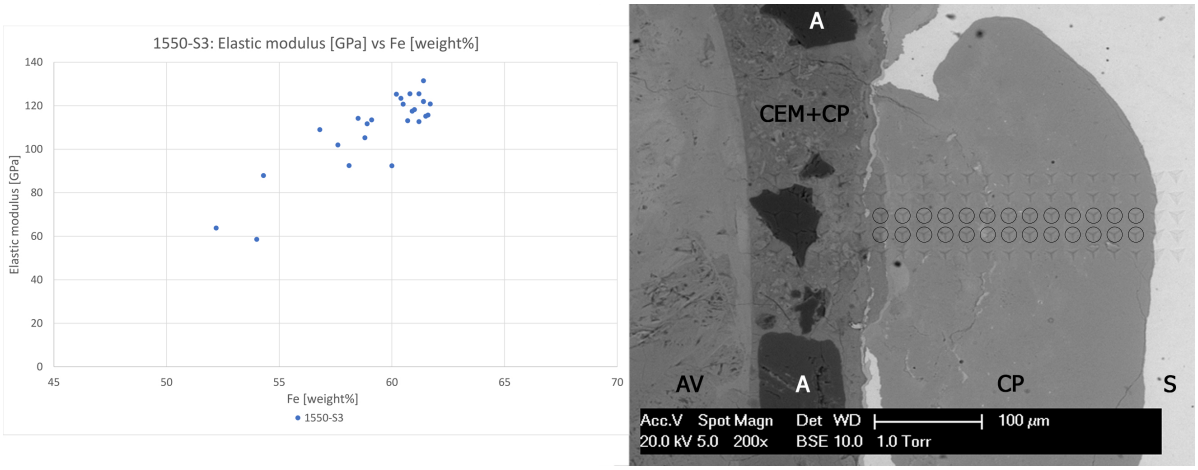


Figure D.21: 1550-S3: (left) E modulus [GPa] vs Fe concentration [wt%] of indented spots; (right) BSE image with indents analyzed through EDS spot analysis (in circles)

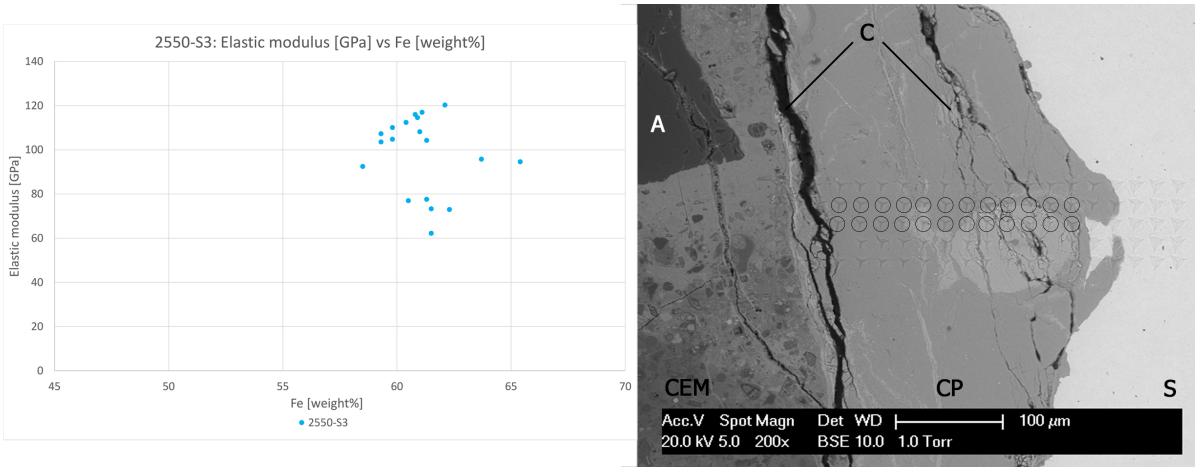


Figure D.22: 2550-S3: (left) E modulus [GPa] vs Fe concentration [wt%] of indented spots; (right) BSE image with indents analyzed through EDS spot analysis (in circles)

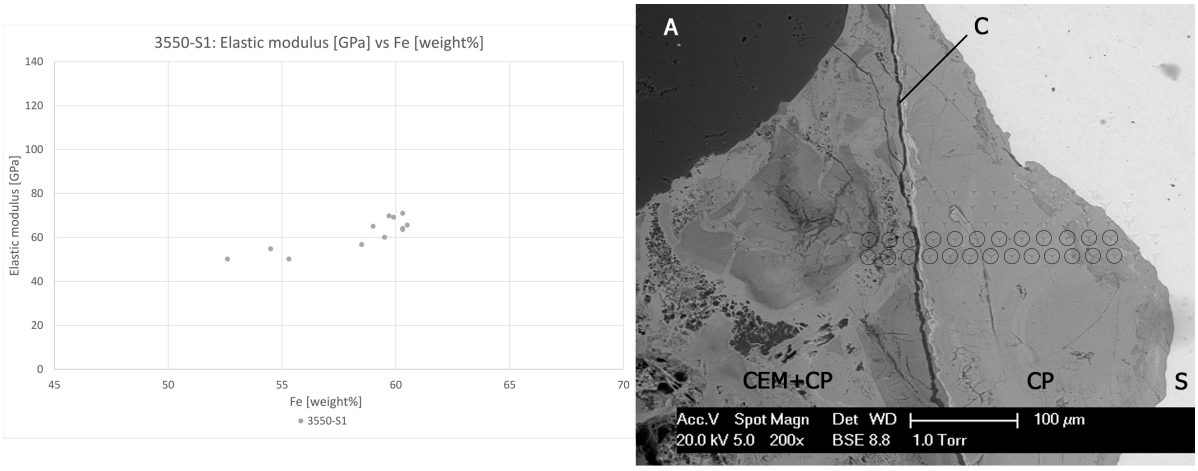


Figure D.23: 3550-S1: (left) E modulus [GPa] vs Fe concentration [wt%] of indented spots; (right) BSE image with indents analyzed through EDS spot analysis (in circles)

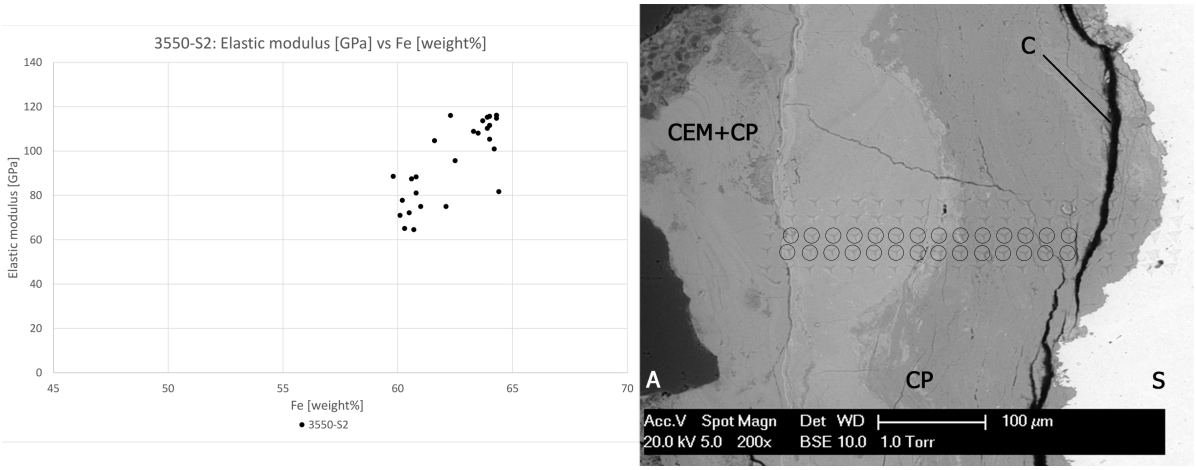


Figure D.24: 3550-S2: (left) E modulus [GPa] vs Fe concentration [wt%] of indented spots; (right) BSE image with indents analyzed through EDS spot analysis (in circles)

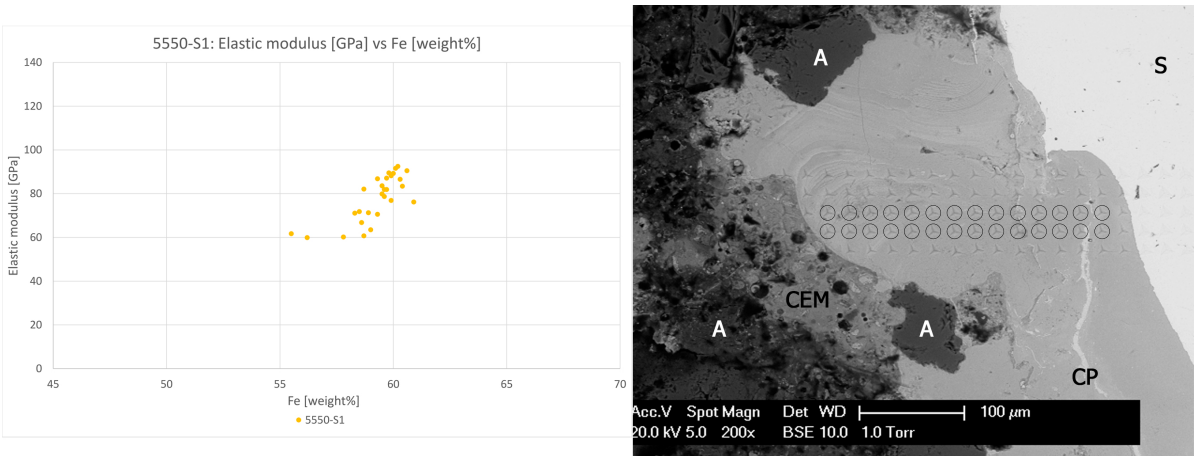


Figure D.25: 5550-S1: (left) E modulus [GPa] vs Fe concentration [wt%] of indented spots; (right) BSE image with indents analyzed through EDS spot analysis (in circles)

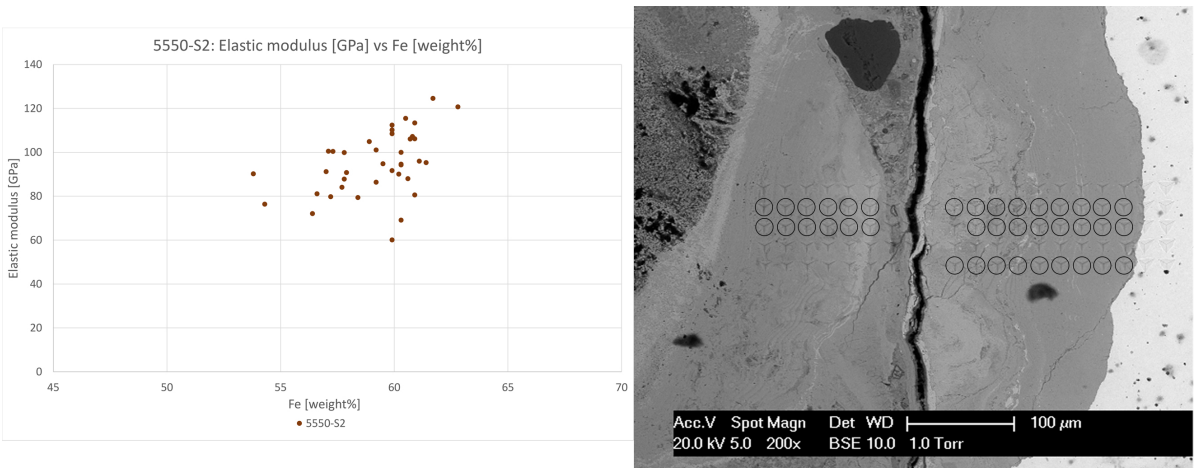


Figure D.26: 5550-S2: (left) E modulus [GPa] vs Fe concentration [wt%] of indented spots; (right) BSE image with indents analyzed through EDS spot analysis (in circles)

# D.3. X-ray Diffraction patterns

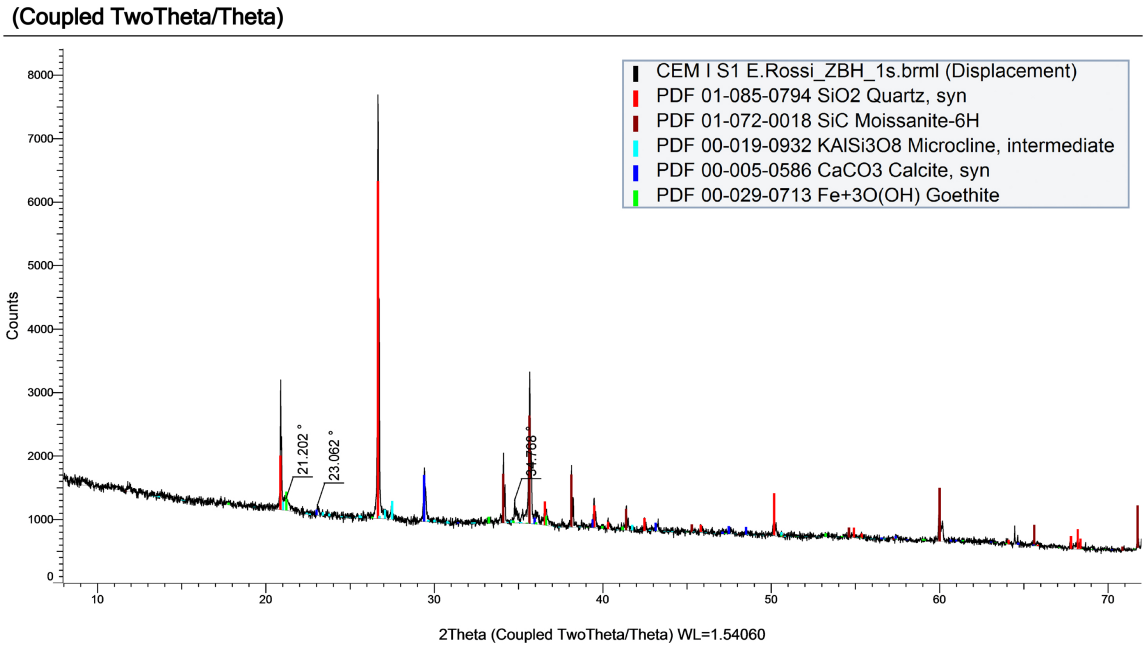


Figure D.27: XRD pattern of corrosion product sample formed in 1550-S1

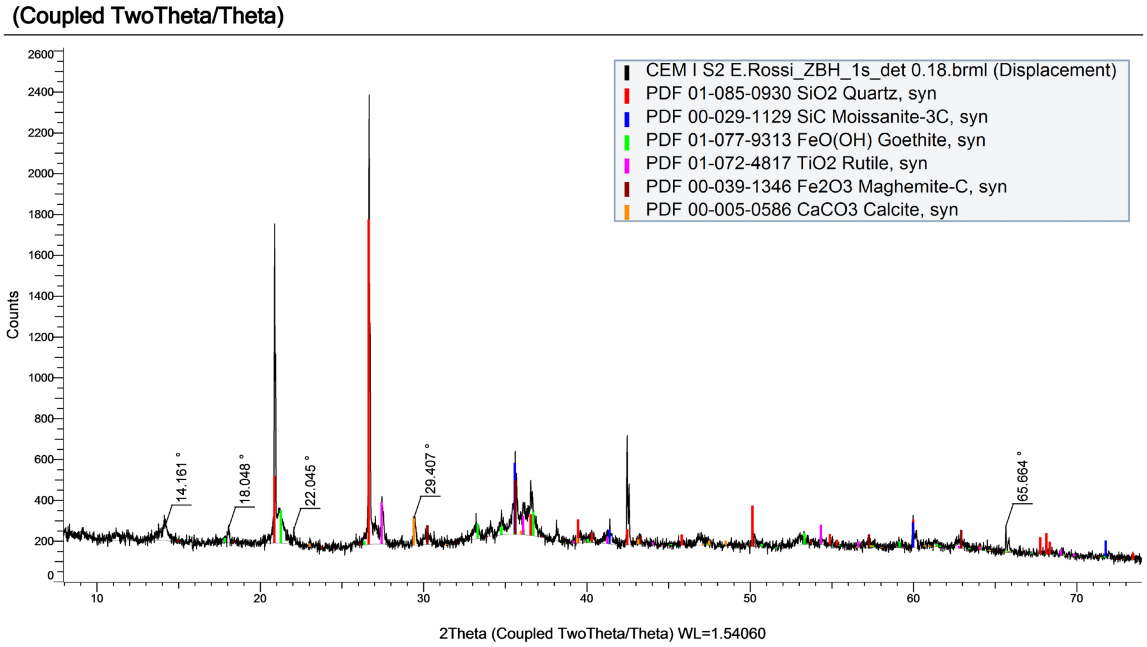


Figure D.28: XRD pattern of corrosion product sample formed in 1550-S2

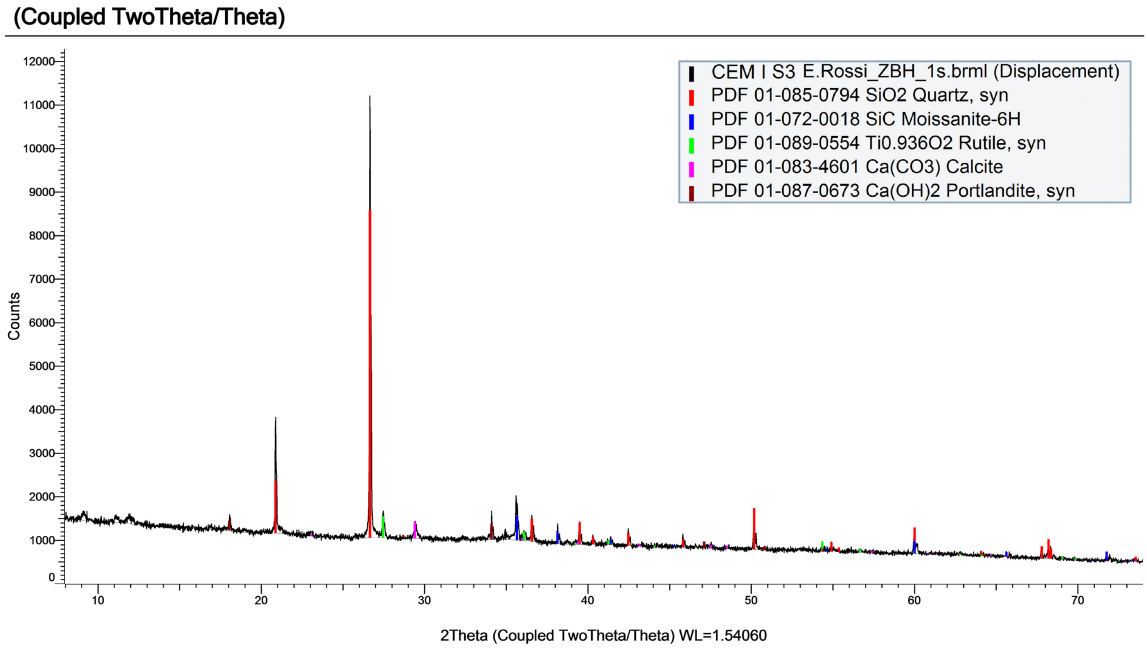


Figure D.29: XRD pattern of corrosion product sample formed in 1550-S3

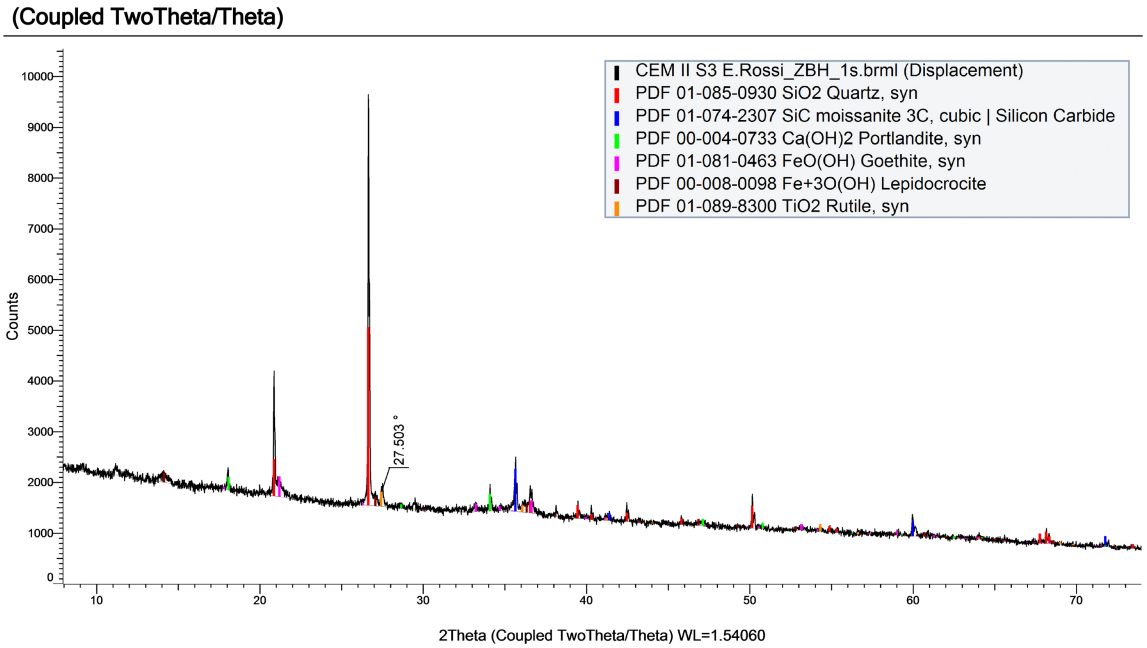


Figure D.30: XRD pattern of corrosion product sample formed in 2550-S3

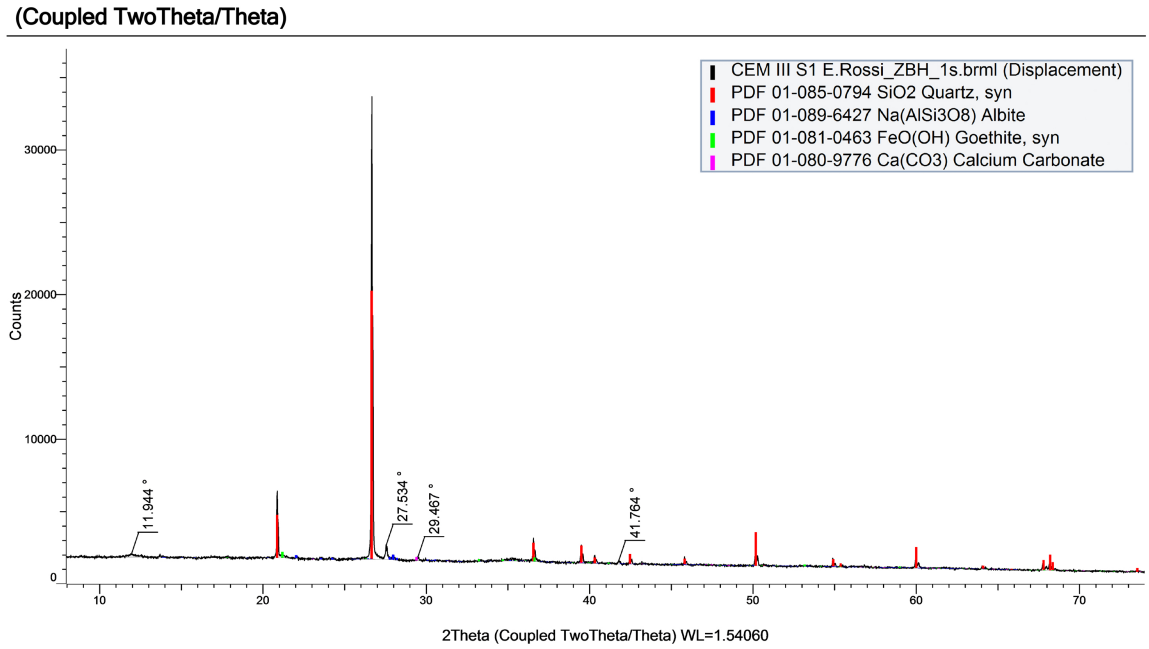


Figure D.31: XRD pattern of corrosion product sample formed in 3550-S1

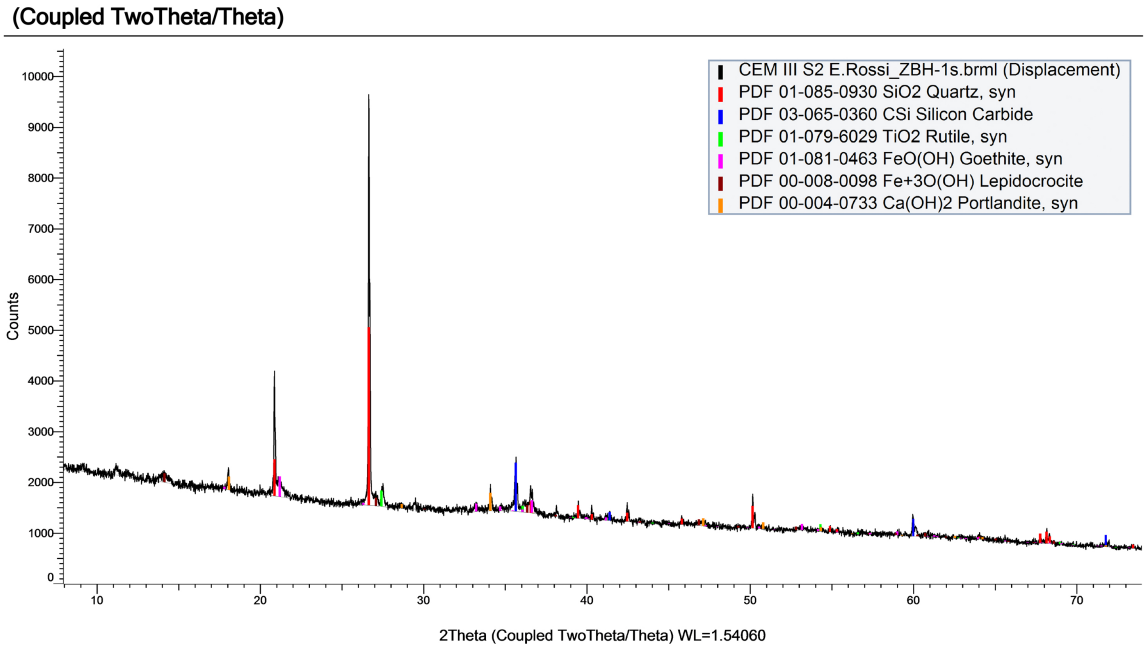


Figure D.32: XRD pattern of corrosion product sample formed in 3550-S2

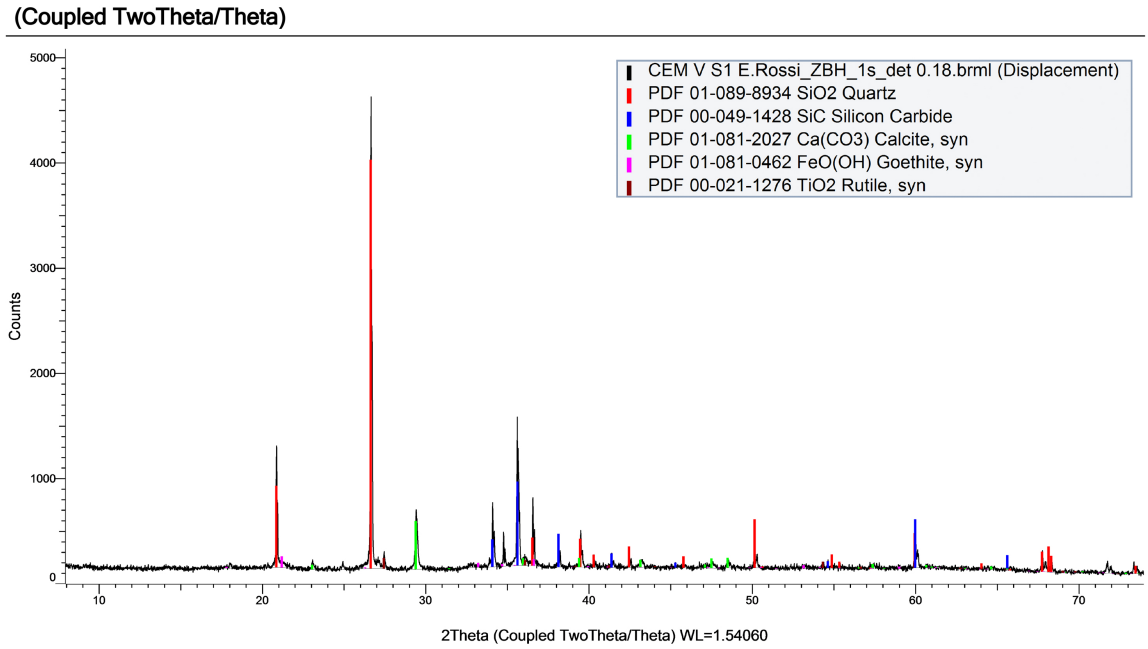


Figure D.33: XRD pattern of corrosion product sample formed in 5550-S1

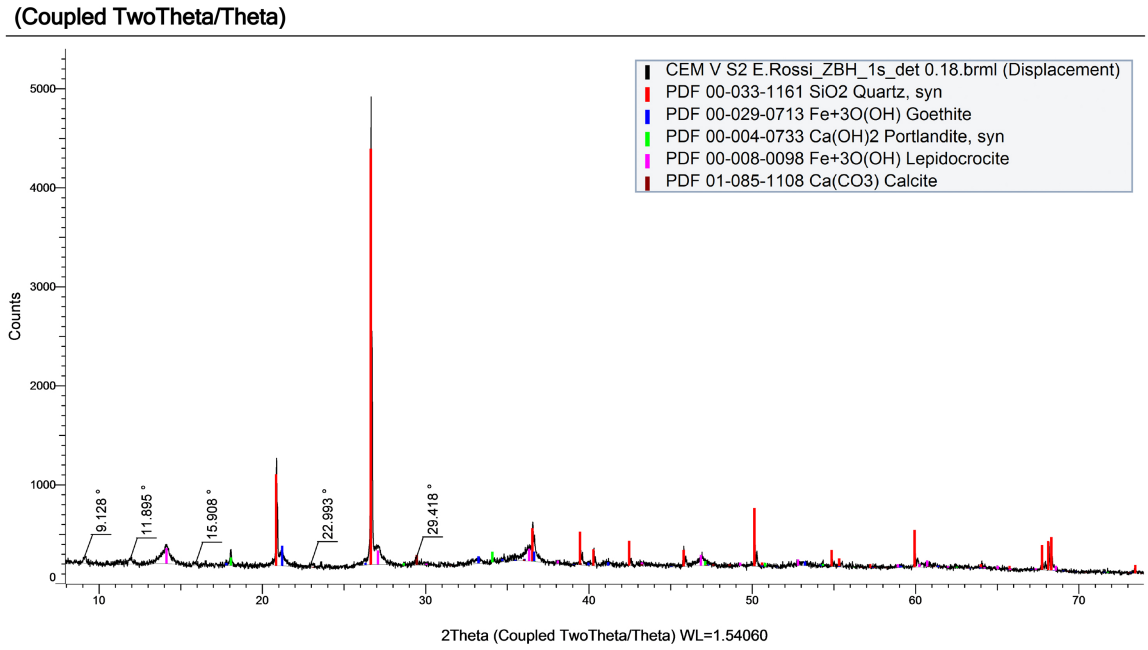


Figure D.34: XRD pattern of corrosion product sample formed in 5550-S2

# D.4. Corrosion product penetrating into air voids at the SCI

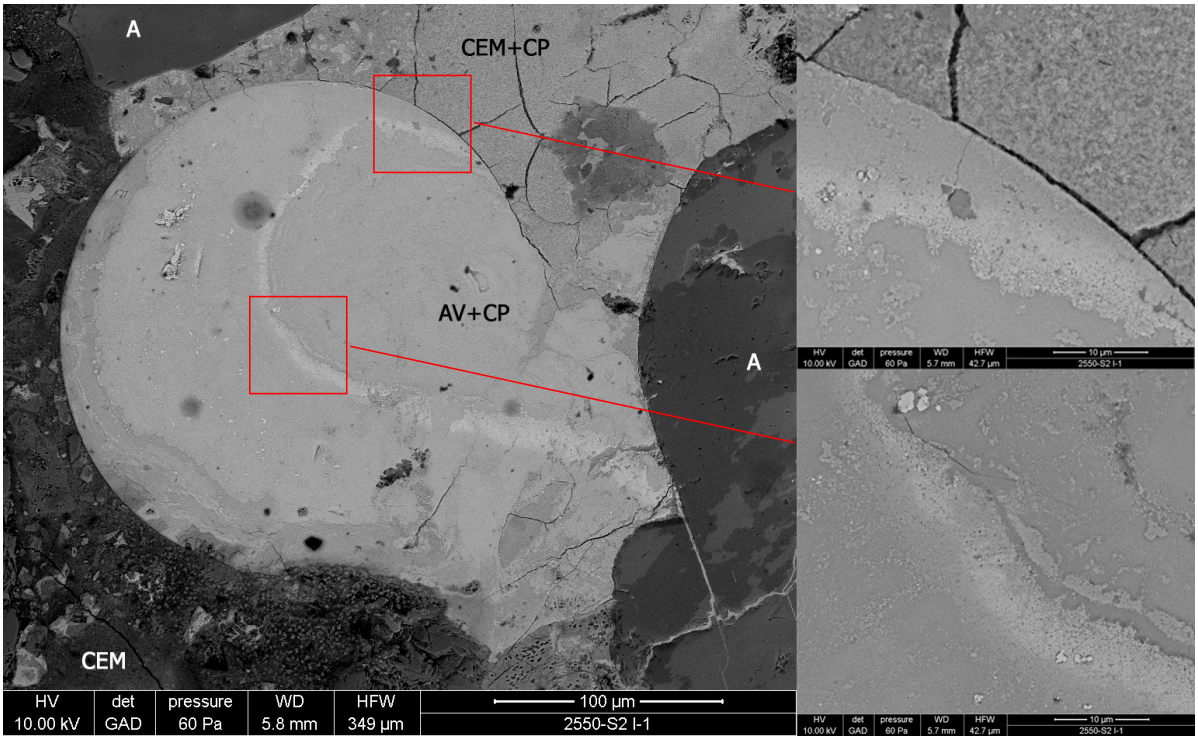


Figure D.35: BSE image of corrosion product penetrating into air voids at the steel/concrete interface with labeled components (S=steel; CP(x)=layers of corrosion product; CEM=cement; AV=air void; C=crack; A=aggregate)

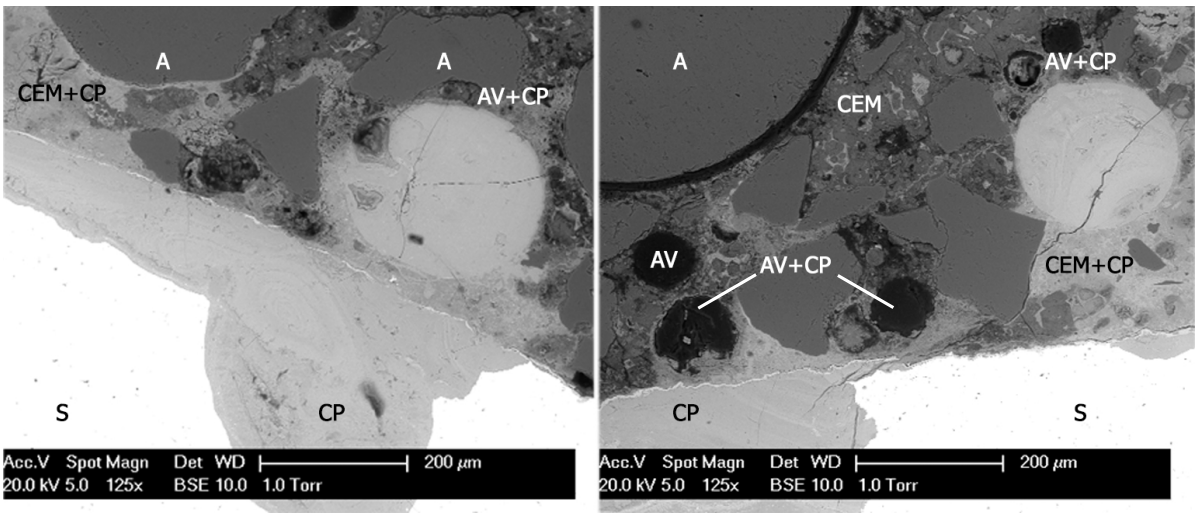


Figure D.36: BSE image of corrosion product penetrating into air voids at the steel/concrete interface with labeled components (S=steel; CP(x)=layers of corrosion product; CEM=cement; AV=air void; C=crack; A=aggregate)

# Bibliography


[1] ACI-201 (1991). *Proposed revision of guide to durable concrete*. ACI Journal of Materials 88(5).

[2] RILEM (1996). *REPORT 14: Durability design of concrete structures*. London, E&FN SPON.

[3] ACI 365 (2000). *Service-life Prediction*. 365.1R-00, American Concrete Institute.

[4] Bertolini L (2004). *Corrosion of steel in concrete*. Wiley-VCH.

[5] Broomfield JP (2007). *Corrosion of steel in concrete: understanding, investigation and repair*. London, Taylor & Francis.

[6] Bertolini L, Elsener B, Pedeferri P, Redaelli E, Polder RB (2014). *Corrosion of steel in concrete: Prevention, Diagnosis, Repair*. Wiley-VCH.

[7] Jones DA (1996). *Principles and prevention of corrosion*. Upper Saddle River: Prentice Hall.

[8] Pacheco J (2010). *Corrosion of steel reinforcement in 12 years old concrete: Inspection, evaluation and electrochemical repair of corrosion*. Delft University of Technology, Materials & Environment, Delft.

[9] Tuutti K (1982). *Corrosion of steel in concrete*. Swedish Cement and Concrete Research.

[10] Andrade C, Alonso C (1996). *Corrosion rate monitoring in the laboratory and on-site*. Construction and Building Materials 10(5): 315-328.

[11] Savija B, Lukovic M, Hosseini SAS, Pacheco J, Schlangen E (2015). *Corrosion induced cover cracking studied by X-ray computed tomography, nanoindentation and energy dispersive X-ray spectrometry (EDS)*. Mater. Struct. 48 (2043-2062).

[12] Polder RB (2001b). *Test methods for on-site measurement of resistivity of concrete – a RILEM TC-154 technical recommendation*. Construction and Building Materials 15: 125-131.

[13] Andrade C, Alonso C, Gulikers J, Polder RB, Cigna R, Vennesland O, Salta M, Raharinaivo A, Elsener B (2004). *Test methods for on-site corrosion rate measurement of steel reinforcement in concrete by means of the polarization resistance method*. RILEM TC 154-EMC, Materials and Structures, Vol.37, 623-643.

[14] Stern M, Geary AL (1957). *A theoretical analysis of the shape of polarization curves*. Journal of Electrochemical Society (104): 56.

[15] Rodriguez J, Ortega LM, Garcia AM, Johansson L, Petterson K (1994). *On site corrosion measurements in concrete structures using a device developed under the Eureka project EU-401*. International Conference, Concrete across borders, Odense.

[16] COST 509 (1997). *Corrosion and Protection of Metals in Contact with Concrete – Final Report*. R. C. Cox RN, Vennesland O, Valente T, COST.

[17] Angst UM, Elsener B, Larsen CK, Vennesland O (2011). *Chloride induced reinforcement corrosion: Electrochemical monitoring of initiation stage and chloride threshold value*. Corrosion Science 53:1451-1464.

[18] Soylev TA, Francois R (2005). *Corrosion of reinforcement in relation to presence of defects at the interface between steel and concrete*. J. Mater. Civ. Eng. 17:447-455.

[19] Christodoulou C, Glass GK (2012). *Towards rendering steel reinforced concrete immune to corrosion*. Australasian Corrosion Association 2012 Annual Meeting, Melbourne, Australia, 11-14 November, paper 159, 11pp.

[20] Page CL (1975). *Mechanism of corrosion protection of reinforced concrete marine structures*. Nature (London), 258(11):514-515.

[21] Yonezawa T, Ashworth V, Procter RPM (1988). *Pore solution composition and chloride effects on corrosion of steel in concrete*. Corros. Eng. 44(7):489-499.

[22] Mohammed TU, Otsuki N, Hisada M (1999). *Corrosion of steel bars with respect to orientation in concrete*. ACI Mater. J. 96(2):154-159.

[23] Mohammed TU, Otsuki N, Hamada H, Yamaji T (2002). *Chloride-induced corrosion of steel bars in concrete with presence of gap at the steel-concrete interface*. ACI Mater. J. 99(2):149-156.

[24] Glass GK, Reddy B, Clark LA (2007). *Making reinforced concrete immune from chloride corrosion*. Constr. Mat. 160:155-164.

[25] Mohammed TU, Hamada H (2006). *Corrosion of steel bars in concrete with various steel surface conditions*. ACI Mater. J. 103(4):233-242.

[26] Angst UM (2011). *Chloride induced reinforcement corrosion in concrete; concept of critical chloride content - methods and mechanisms*. PhD thesis, Norwegian University of Science and Technology, NTNU, Trondheim.

[27] Angst UM, Geiker MR, Michel A, Gehlen C, Wong H, Burkan Isgor O, Elsener B, Hansson CM, Francois R, Hornbostel K, Polder R, Alonso MC, Sanchez M, Correia MJ, Criado M, Sagues A, Buenfeld N (2017). *The steel-concrete interface*. Mater Struct 50:143.

[28] Soylev TA, Francois R (2003). *Quality of steel-concrete interface and corrosion of reinforcing steel*. Cem Concr Res 33:1407-1415.

[29] Page CL (2009). *Initiation of chloride-induced corrosion of steel in concrete: role of the interfacial zone*. Mater Corros 60:586-592.

[30] Horne AT, Richardson IG, Brydson RMD (2007). *Quantitative analysis of the microstructure of interfaces in steel reinforced concrete*. Cem Concr Res 37:1613-1623.

[31] Herman GT (2009). *Fundamentals of computerized tomography: image reconstruction from projections*. Springer, London.

[32] Trainor KJ, Foust BW, Landis EN (2013). *Measurement of energy dissipation mechanisms in fracture of fiber-reinforced ultrahigh-strength cement-based composites*. J. Eng. Mech. 139(7):771-779.

[33] Landis EN, Zhang T, Nagy EN, Nagy G, Franklin WR (2005). *Cracking damage and fracture in four dimensions*. Mater Struct 40:357-364.

[34] Henry M, Darma I, Sugiyama T (2014). *Analysis of the effect of heating and re-curing on the microstructure of high-strength concrete using X-ray CT*. Constr Build Mater 67:37-46.

[35] Yang Z, Ren W, Sharma R, et al. (2017). *In situ X-ray computed tomography characterisation of 3D fracture evolution and image-based numerical homogenisation of concrete*. Cem Concr Compos 75:74-83.

[36] Mendonca Filho F, Savija B, Schlangen E (2018). *Quantification of material loss due to corrosion through X-ray micro-tomography*. Corros Sci.

[37] Mendonca Filho F (2016). *Master of Science thesis: The effects of carbonation and compressive stresses on chloride ingress reinforced mortars*. Master of Science, TU Delft, Delft, the Netherlands.

[38] Dong B, Ding W, Qin S, Fang G, Liu Y, Dong P, Han S, Xing F, Hong S (2018). *3D visualized tracing of rebar corrosion-inhibiting features in concrete with a novel chemical self-healing system*. Constr Build Mater 168:11-20.

[39] Sun H, Zhao D, Gu Y, Memon SA, Ren Z, Liu B, Zhang X, Xing F, Li D (2017). *Three-dimensional characterization of steel corrosion embedded in cement paste*. Constr Build Mater 143:24-32.

[40] Itty PA, Serdar M, Meral C, et al. (2014). *In situ, 3D moniroting of corrosion on carbon steel and ferritic stainless steel embedded in cement paste*. Corros Sci 83:409-418.

[41] Ghahari SM, Davenport AJ, Rayment T, et al. (2011). *In situ synchrotron X-ray micro-tomography study of pitting corrosion in stainless steel*. Corros Sci 53:2684-2687.

[42] Cesen A, Kosec T, Legat A (2013). *Characterization of steel corrosion in mortar by various electrochemical and physical techniques*. Corros Sci 75:74-83.

[43] Ozbolt J, Orsanic F, Balabanic G, Kuster M (2013). *Modelling damage in concrete caused by corrosion of reinforcement: coupled 3D FE model*. Int J Fract 178(1-2): 233-244.

[44] Savjia B, Lukovic M, Pacheco J, Schlangen E (2013). *Cracking of the concrete cover due to reinforcement corrosion: a two-dimensional lattice model study*. Constr Build Mater 44:626-638.

[45] Zhao Y, Ren H, Dai H, Jin W (2011). *Composition and expansion coefficient of rust based on X-ray diffraction and thermal analysis*. Corros. Sci. 53:1646-1658.

[46] Cornell RM, Schwertmann U (1996). *The Iron Oxides*. VHC Verlagsgesellschaft, Weinhaim, Germany.

[47] Li QX, Wang ZY, Han W, Han EH (2008). *Characterization of the rust formed on weathering steel exposed to Qinghai salt lake atmosphere for 17 year*. Corrosion Science 50:365-371.

[48] Yamashita M, Konishi H, Kozakura T, Mizuki J, Uchida H (2005). *In situ observation of initial rust formation process on carbon steel under Na2SO4 and NaCl solution films with wet/dry cycles using synchrotron radiation X-rays*. Corrosion Science 47:2492-2498.

[49] Oh SJ, Cook DC, Townsend HE (1999). *Atmospheric corrosion of steels in marine, rural and industrial environments*. Corrosion Science 41:1687-1702.

[50] Asami K, Kikuchi M (2003). *In-depth distribution of rusts on a plain carbon steel and weathering steel exposed to coastal-industrial atmosphere for 17 years*. Corrosion Science 45:2671-2688.

[51] Nishimura T, Katamaya H, Noda K, Kodama T (2000). *Electrochemical behaviour of rust formed on carbon steel in a wet/dry environment containing chloride ions*. Corrosion 56:935-941.

[52] Townsend EH, Simpson TC, Johnson GL (1994). *Structure of rust on weathering steel in rural and industrial environment*. Corrosion 50:546-554.

[53] Wang JH, Wei FI, Shih HC (1996). *Modelling of atmospheric corrosion behaviour of weathering steel in sulfur dioxide-polluted atmospheres*. Corrosion 52:900-909.

[54] Carè S, Nguyen QT, L'Hostis V, Berthaud Y (2008). *Mechanical properties of the rust layer induced by impressed current method in reinforced mortar*. Cement and Concrete Research 38, 1079-1091.

[55] Molina FJ, Alonso C, Andrade C (1993). *Cover cracking as a function of rebar corrosion. Part 2: Numerical-model*. Mater. Struct. 163(532-548).

[56] Noghabai K (1998). *Effect of tension softening on the performance of concrete structures*. PhD thesis 1998:21, Division of Structural Engineering, Lulea University of Technology, Lulea, 1998.

[57] Lundgren K (2002). *Modelling the effect of corrosion on bond in reinforced concrete*. Magazine of Concrete Research 54 (3) 165-173.

[58] Wang HL, Jin WL, Sun XY (2008). *Fracture model for protective layer cracking of reinforced concrete structure due to rebar corrosion*. Journal of Hydraulic Engineering 39 (4) 863-869.

[59] Lu CH, Zhao YX, Jin WL (2010). *Modelling of time to corrosion-induced cover cracking in reinforced concrete structures*. Journal of Building Structures 31 (2) 85-92.

[60] Zhao YX, Jin WL (2006). *Modelling the amount of steel corrosion at the cracking of concrete cover*. Advances in Structural Engineering 9 (5) 687-696.

[61] Val DV, Chernin L, Stewart MG (2009). *Experimental and numerical investigation of corrosion-induced cover cracking in reinforced concrete structures*. Journal of Structural Engineering ASCE 5:376-385.

[62] Liu Y, Weyers RE (1998). *Modelling the time to corrosion cracking in chloride contaminated reinforced concrete structures*. ACI Materials Journal 95 (6) 675-681.

[63] Bhargava K, Ghosh AK, Mori Y, Ramanujam S (2006). *Analytical model for time to cover cracking in RC structures due to rebar corrosion*. Nucl. Eng. Des. 11 (1123-1139).

[64] Zhao Y, Dai H, Jin W (2012). *A study of the elastic moduli of corrosion products using nano-indentation techniques*. Corros Sci 65:163-168.

[65] Samsonov GV (1973). *The oxide handbook*. (IFI/Plenum).

[66] Ouglova A, Berthaud Y, Francois M, Foct F (2006). *Mechanical properties of an iron oxide formed by corrosion in reinforced concrete structures*. Corros. Sci. 12 (3988-4000).

[67] Shahzma J. Jaffer, Carolyn M. Hansson (2009). *Chloride-induced corrosion products of steel in cracked-concrete subjected to different loading conditions*. Cem. Concr. Res. 116-125.

[68] Cook DC (2005). *Spectroscopic identification of protective and non-protective corrosion coatings on steel structures in marine environments*. Corros. Sci. 2250-2570.

[69] Hosemann P, Swadener JG, Welch J, Li N (2008). *Nano-indentation measurement of oxide layers formed in LBE on F/M steels*. J. Nucl. Mater. 201-205.

[70] Zhao YX, Dai H, Ren HY, Lin WL (2011). *Experimental study of the modulus of steel corrosion in a concrete port*. Corros Sci. 17-25.

[71] Lundgren K (2005). *Bond between ribbed bars and concrete. Part 2: the effect of corrosion*. Mag. Concr. Res. 7 (383-395).

[72] Suda K, Misra S, Motohashi K (1993). *Corrosion products of reinforcing bars embedded in concrete*. Corros. Sci. 5-8 (1543-1549).

[73] Balasaf I, Burgoyne CJ (2013). *Modelling the structural effects of rust in concrete cover*. J. Eng. Mech. 137(3):175-185.

[74] Costantinides G, Ulm F-J, Van Vliet K (2003). *On the use of nanoindentation for cementitious materials*. Mater Struct 36:191-196.

[75] Brinell JA (1901). *Congrès International des Méthdes d'Essai des Matériaux de Construction*. Paris, Tome 2, 83-94.

[76] O'Neill H (1944). *Proc. Instn. Mech. Engineers*. 151 (116-130).

[77] Tabor D (1951). *The hardness of metals*. Oxford classical texts in the physical sciences.

[78] Polder RB, Russo P (1998) *Concrete resistivity, corrosion potential and corrosion rate at young age as a function of cement type*. 98-BT-R1664. TNO Building and Construction Research. Rijswijk, TNO.

[79] Polder RB (2000) *Corrosion protection of concrete with fly ash cement and other binders*. 2000-BT-MK-R0018/02. TNO Building and Construction Research. Rijswijk, TNO.

[80] Polder RB (2001a) *Corrosion protection of reinforcement in concrete with fly ash cement and other binders subjected to salt/dry loading, accelerated carbonation and addition of chloride: Results until 2.5 years age and destructive analysis*. 2001-CI-R1029-02. TNO Building and Construction Research, Delft, TNO.

[81] Guerreri M, Polder RB (2002) *Comparison of corrosion of steel bars in blended cement concrete from linear polarization resistance and visual examination afer destructive analysis*. TNO Bouw. Delft, TNO.

[82] Peelen W, Polder RB (2003) *Accelerated aging tests of the zinc-hydrogel anode for galvanic cathodic protection of steel in concrete*. 2003-CI-R0033. TNO Building and Construction Research. Delft, TNO.

[83] Kolek J (1958). *An appreciation of the Schmidt Rebound Hammber*. Magazine of Concrete Research. London. 10:27-36.

[84] Malhotra VM (1968). *Nondestructive Methods for testing concrete*. Mines Branch Monograph. Ottawa:66.

[85] Bier AT (1987). *Influence of type of cement and curing on carbonation progress and pore structure of hydrated cement paste*. Materials Research Society Symposium, 85:123–34.

[86] Neville A (1995). *Properties of concrete*. Harlow Longman.

[87] Kosmatka SH, Kerkhoff B, Panarese WC, Tanesi J (2004). *Design and control of concrete mixes*. Skokie, IL, Portland Cement Association.

[88] Aitcin PC (2008). *Binders for Durable and Sustainable Concrete*. New York, Taylor & Francis.

[89] Burstein GT, Pistorius PC, Mattin SP (1993) *The nucleation and growth of corrosion pits on stainless steel*. Corros Sci. 35:57-62.

[90] Glass GK, Buenfeld NR (1997) *The presentation of the chloride threshold level for corrosion of steel in concrete*. Corros Sci. 39:1001-1013.

[91] Oliver WC, Pharr GM (2004) *Mesurement of hardness and elastic modulus by instrumented indentation: advances in understanding and refinements to methodology*. J Mater Res 19(1):3–20

[92] Misawa T, Asami K, Hashimoto K, Shimodaira S (1973). *The mechanism of atmospheric rusting and the protective amorphous rust on low alloy steel*. Corros. Sci. 13: 279-289.

[93] Yamashita M, Miyuki H, Matsuda Y, Nagano H, Misawa T (1994). *The long-term growth of the protective rust layer formed on weathering steel by atmospheric corrosion during a quarter of a century*. Corros. Sci. 36: 283-299.

[94] Zitrou E, Nikolaou J, Tsakiridis PE, Papadimitriou GD (2007). *Atmospheric corrosion of steel reinforcing bars produced by various manufacturing processes*. Construction and Building Materials 21.

[95] De la Fuente D, Diaz I, Simancas J, Chico B, Morcillo M (2010). *Long-term atmospheric corrosion of mild steel*. Corrosion Science.

[96] Wong HS, Zhao YX, Karimi AR, Buenfeld NR, Jin WL (2010). *On the penetration of corrosion products from reinforcing steel into concrete due to chloride-induced corrosion*. Corros. Sci. 52(7):2469-2480.

[97] Michel A, Pease BJ, Geiker MR, Stang H, Olesen JF (2011). *Monitoring reinforcement corrosion and corrosion-induced cracking using non-destructive X-ray attenuation measurements*. Cement Concr Res 41:1085–1094.

[98] Duffò GF, Reinoso M, Ramos CP, Farina SB (2012). *Characterization of steel rebars embedded in a 70-year old concrete structure*. Cement Concr Res 42:111-117.

[99] Chitty WJ, Dillmann P, L'Hostis V, Lombard C (2005). *Long-term corrosion resistance of metallic reinforcements in concrete—a study of corrosion mechanisms based on archaeological artefacts*. Cement Concr Res 47:1555–1581.

[100] Chitty WJ, Berger P, L'Hostis V, Lombard C (2008). *Long-term corrosion of rebars embedded in aerial and hydraulic binders – Mechanisms and crucial physico-chemical parameters*. Cement Concr Res 50:2117–2123.

[101] Neff D, Saheb M, Monnier J, Perrin S, Descostes M, L'Hostis V, Crusset D, Millard A, Dillmann P (2010). *A review of the archaeological analogue approaches to predict the long-term corrosion behaviour of carbon steel overpack and reinforced concrete structures in the French disposal systems*. Journal of Nuclear Materials 402:196–205.

[102] Demoulin A, Trigance C, Neff D, Foy E, Dillmann P, L'Hostis V (2010). *The evolution of the corrosion of iron in hydraulic binders analysed from 46- and 260-year-old buildings*. Corrosion Science 52:3168–3179

[103] Ma X, Copuroglu O, Schlangen E, Han N, Xing F (2018). *Expansion and degradation of cement paste in sodium sulfate solutions*. Construction and Building Materials 158:410-422.

[104] Angst U, Geiker M, Michel A, and others (2017). *The steel-concrete interface*. Materials and Structures 50(2):143.

[105] Shannon RD, Prewitt CT (1969). *Effective Ionic Radii in Oxides and Fluorides*. Acta Cryst. B25, 925